UCLA
UCLA Electronic Theses and Dissertations

Title

High Frequency Dynamics of Magnetoelastic Composites and Their Application in Radio Frequency Sensors

Permalink

https://escholarship.org/uc/item/7zh1h8wj

Author

Nordeen, Paul

Publication Date

2016

Peer reviewed|Thesis/dissertation

eScholarship.org Powered by the California Digital Library
University of California

UNIVERSITY OF CALIFORNIA

Los Angeles

High Frequency Dynamics of Magnetoelastic Composites and their Application in Radio Frequency Sensors

A dissertation submitted in partial satisfaction of the

requirements for the degree Doctor of Philosophy

in Mechanical Engineering

by

Paul Killian Nordeen

2016

© Copyright by

Paul Killian Nordeen

2016

ABSTRACT OF THE DISSERTATION

High Frequency Dynamics of Magnetoelastic Composites and their Application in Radio Frequency Sensing

By

Paul Killian Nordeen

Doctor of Philosophy in Mechanical Engineering

University of California, Los Angeles, 2016

Professor Gregory P. Carman, Chair

Recently the consumer electronics market has experienced a major demand for autonomous, networked devices which can collect and process information independently from the operator. These “smart” devices are the constituents of a larger computing paradigm known as the internet of things which seeks to combine environmental sensing, communication and computing technologies into an intelligent, all-in-one platform. Driven by advances in the reduction in the size and power consumption of computing technology, this expansion of the smart device market has created a need for new sensors which can be integrated onto compact and robust chip level systems. The success of these devices leverages the scaling of existing sensor technologies to improve the footprint and efficiency of the overall electronics package while maintaining compatibility with current manufacturing processes. This size reduction of current sensor technology often presents immense engineering challenges which stem from the undesirable scaling of the physical phenomena upon which the sensor operates. The scaling of electrically

controllable magnetic field devices is one such category which demands an alternative approach at small length scales to achieve practical efficiencies. In this work an approach is taken to design small scale electrically controlled magnetic field sensors which sharply deviates from the traditional Oersted field devices typical of macroscale systems. Strain mediated multiferroic composites, which couple the intrinsic magnetic and electric degrees of freedom inside the material through mechanical strains, are explored in the context of antennas and static magnetic field sensors. An analysis of the radiation efficiency of a multiferroic antenna is presented and steps are taken to realize a practical experimental device. Two types of magnetometers are studied which use multiferroic composites to improve the sensitivities and measurement accessibility of such devices. The results of this work clearly demonstrate the significant advantages offered by strain mediated multiferroic materials for use in chip-scale sensor technologies which have significant potential to advance the capabilities of integrated “smart” electronic systems.

The dissertation of Paul Nordeen is approved.

Pei-Yu Chiou

Robert N. Candler

Christopher S. Lynch

Gregory P. Carman, Committee Chair

University of California, Los Angeles

2016

For my family,

Mom, Dad, Anna, Eir, Nick, Aubrey, Catherine, James and Jake.

Table of Contents

List of Figures

List of Tables

VITA

Education

2010-2016 M.S. – Mechanical Engineering

University of California, Los Angeles

2005-2010 B.S. – Mechanical Engineering

California State University, Fullerton

Employment History

2011-2016 Graduate Student Researcher

The Active Materials,

University of California, Los Angeles

Publications and Conference Presentations

Paul Nordeen, Mohanchandra Kotekar, Gregory Carman. Surface Wave Propagation on <111> Oriented PMN-(0.32)PT Crystals. Applied Physics Letters. *Manuscript (2016)*

Paul Nordeen, Gregory Carman. A MULTIFERROIC TRANSDUCER FOR AUDIO APPLICATIONS. US Patent 14/919,655

Paul Nordeen, Eugene Freeman, Gohkan Hatipoglu, Srinivas Tadigadapa, Gregory Carman. Passively Powered Wireless Micromachined Magnetoflexoelastic Magnetometer Based on the Quartz Force Frequency Effect. IEEE Sensors Proceedings (2016)

Scott Keller, *Paul Nordeen*, Kyle Wetzlar, Michael Moon, Gregory Carman, Scott Burnside. MULTIFERROIC SURFACE ACOUSTIC WAVE ANTENNA. US Patent Applied For.

K.P. Mohanchandra, S.V. Prikhodko, K.P. Wetzlar, W.Y. Sun, *P. Nordeen*, and G.P. Carman. Sputter Deposited Terfenol-D Thin Films for Multiferroic Applications. AIP Advances. **5**, 097119 (2015)

G. Yu, Z. Wang, M. Abolfath-Beygi, C. He, X. Li, K.L. Wong, P. Nordeen, H. Wu, P.V. Ong, N. Kioussis, G.P. Carman, X. Han, I.A. Alhomoudi, P.K. Amiri and K.L. Wang. Strain Induced Modulation of Perpendicular magnetic anisotropy in Ta/CoFeB/MgO Structures Investigated by Ferromagnetic Resonance. Applied Physics Letters **106,** 072402 (2015)

J. Cui, J.L. Hockel, P.K. Nordeen, D.M. Pisani, C.Y. Liang, G.P. Carman, C.S. Lynch. A Method to Control Magnetism in Individual Strain-Mediated Magnetoelectric Islands. Applied Physics Letters. **103** 232905 (2013)

S.M. Fashami, M.M. Al-Rashid, W.Y. Sun, *P. Nordeen*, S. Bandyopadhyay, A. Chavez, G.P. Carman. Binary Information Propagation in Circular Magnetic Nanodot Arrays using Strain Induced Magnetic Anisotropy. Nature Nanotechnology *(Submitted 2016)*

Paul Nordeen, C.Y. Liang, C.J. Hsu, J.L. Hockel, G.P. Carman. Electric Field Induced Domain Wall Transitions in Thin Film Ni/PMN-PT (001) Heterostructures. IEEE/INTERMAG Annual Meeting. Chicago (2013) (*Presentation)*

Chapter 1: Introduction

With the density of complementary metal oxide semiconductor (CMOS) devices approaching 1.6 billion/cm^2 [1] there is significant demand for the development of adjacent sensor, communications and memory technologies which are able perform with high sensitivity and efficiency. Because the barrier to overcome the scaling of the governing physical phenomena of these devices is often times quite large, the reduction in the physical size of these technologies has, in many cases, not experienced the same rate as CMOS technology. One such phenomenon, the electrical manipulation of magnetic fields, presents engineers with major challenges when making the transition to small length scales. The macroscale approach to this problem is a familiar one which finds ubiquitous application in modern technology. The generation of Oersted fields (so named for Hans Christian Oersted 1820 who discovered this effect), finds its way into many useful devices such as the electric motor or the electromechanical relay (on which the first computers were based). These technologies offer reasonable efficiencies, approaching 85% in some cases [2], and are inexpensive to manufacture. Oersted magnetic fields are created by moving charged particles, usually electrons, through a medium. This most often takes the form of current travelling inside of a conductor where the magnetic field generated curls around the direction of current. A simplification of Maxwell's equations, referred to as Amperes Circuital Law, provides an analytical description of such fields B as a function of current density J.

$$\nabla \times B = \mu_0 J \qquad [Eq. 1.1]$$

Where μ_0 is the free space permeability. An elementary level visualization, shown in figure 1.2, of the influence on iron filings from these Oersted fields can be seen in the common experiment using an electrified copper wire wrapped around a nail.

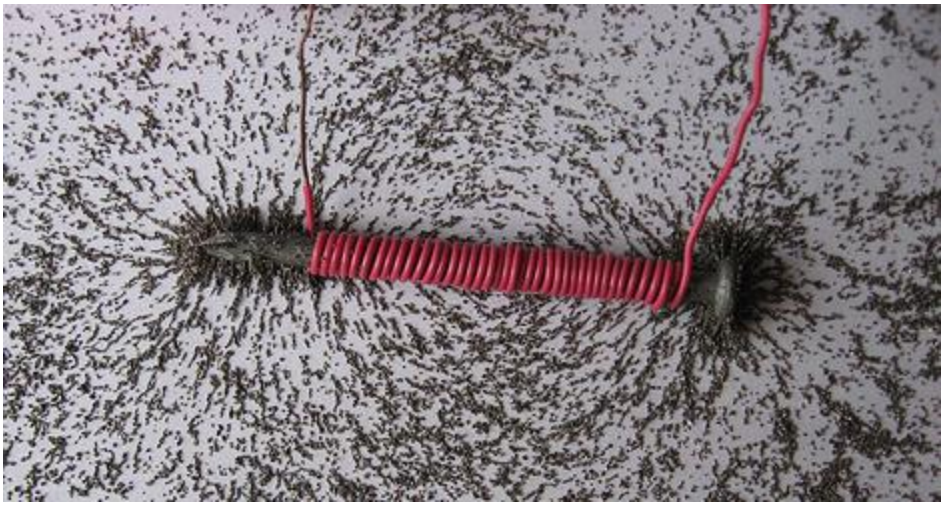

Figure 1.1 - An iron nail wrapped with a current carrying wire aligns surrounding ferromagnetic iron filings to equipotential magnetic field lines [Google Images]

To demonstrate the scaling potential of an Oersted field generator, it is convenient to define the system as a single loop of copper wire whose wire diameter is $1/10^{th}$ that of the annular loop diameter as is illustrated in figure 1-3.

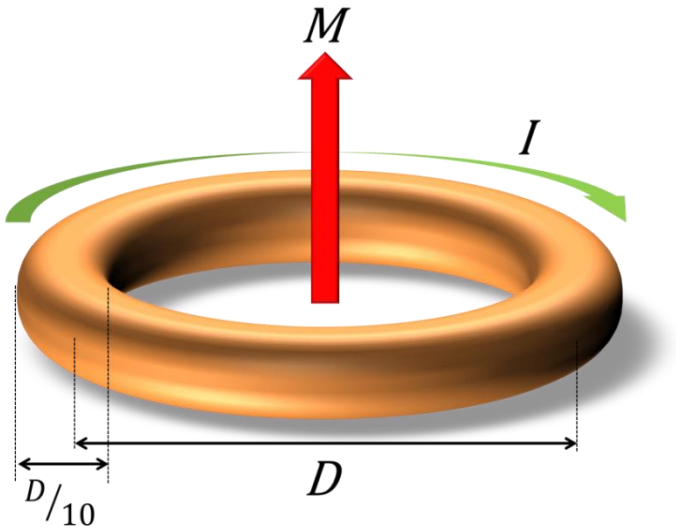

Figure 1.2 - A single turn of copper wire of annular diameter D and wire diameter D/10 which carries a current on I.

This loop carries current I and the current distribution is assumed uniform throughout the loop diameter. The magnetic dipole moment of this system can be written as

$$m = IA \qquad [Eq. 1.2]$$

Where A is the area of the loop ($0.25\pi D^2$). The magnetic potential energy of the dipole can be written simply as

$$E_m = \frac{1}{2}\mu_0 m^2 \qquad [Eq. 1.3]$$

Substitution of equation 1.3 into 1.4 and using the general form of loop area gives the magnetic potential energy as a function of the loop diameter.

$$E_m = \frac{\pi^2}{32}\mu_0 I^2 D^4 \qquad [Eq. 1.4]$$

It becomes apparent that as the size of the loop is scaled to small values, generation of an equivalently large magnetic dipole moment requires significantly more current as is evident by the fourth power variation of energy with the loop diameter. To examine how the magnetic potential energy scales with the other loss mechanisms found in the loop system, the ohmic power dissipation in the wire for current I is defined as

$$P_r = \frac{400 I^2 \rho}{D} \qquad [Eq. 1.5]$$

Taking the ratio between the magnetic potential energy (equation 1.4) after conversion to a time averaged power (multiplying by frequency for a sinusoidal current) and the ohmic dissipation (equation 1.5) yields a metric similar to the Reynolds number defined for fluid flowing inside of a hollow tube. By examining the properties of this ratio as a function of the loop diameter, it is

shown that the efficiency of the system scales as D^5. This indicates that as the loop becomes small, manipulation of magnetic fields using the electric current approach becomes extremely inefficient and is dominated primarily by ohmic power loss in the conductor (Joule heating). The practical impact of this inefficiency is evidenced clearly in the lack of micro and nanoscale devices which use Oersted magnetic field generation to operate.

In this work an intrinsic approach to controlling magnetization is explored which removes the large electrical currents, required by those of Oersted devices, from the transduction process improving efficiency at small device sizes. This technique leverages an intrinsic coupling, found in certain types of magnetic materials, between magnetic and mechanical energy. This effect, called the magnetoelastic effect, provides a unique method for manipulating the intrinsic magnetic moments in a material using mechanical energy as opposed to charge motion. This effect occurs by coupling lattice strain to electron orbital distortions which is intrinsically coupled to the electron spin that gives rise to spontaneous magnetization in a material. The effect was first observed by James Joule in 1842 in iron bars. A typical magnetostriction curve, much like the one Joule would have observed, is shown in the left plot of figure 1.3 [3]. A common way of representing the relationship between strain and magnetization is as a line of elliptical particles which are magnetized along their long axis. If the magnetization and long axis directions are rigidly coupled in each individual particle, the transition from a randomly oriented state to a fully saturated state will result in an overall change in length of the total array of particles. This effect is illustrated in the right image of figure 1.3 for a chain of particles under an initial state and a saturated state highlighting the length change (strain) in the particle chain between the two states. Using this model it is easy to see that magnetostriction is the result of 90 degree magnetization reorientation and that 180 degree reorientation will result in zero net strain

from the original configuration. The degree to which this effect occurs is highly dependent on the magnetostrictive materials used and the configuration of the intrinsic magnetic domain structure. In this work several materials are examined which attempt to maximize the coupling efficiency of the applied magnetic field to mechanical deformation. A metric known as the piezomagnetic coefficient q, defined as $d\lambda/dH$, is an effective measure of this efficiency and provides a convenient method to assess how the material will perform in a given system. This metric is examined in depth for actual magnetoelastic materials in later chapters. Magnetostrictive devices find use in several applications ranging from sonar transducers to anti-theft tags although their use in consumer products is not as widespread as their piezoelectric counterparts.

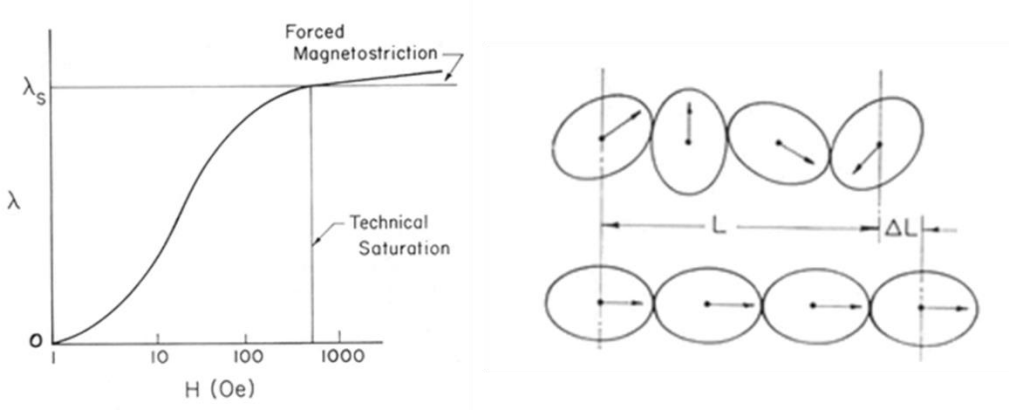

Figure 1.3 – A typical magnetostriction curved showing the characteristic transition points (left). An elliptical particle model demonstrating the intrinsic coupling between strain and magnetization.

An effect analogous to magnetoelasticity, called piezoelectricity, couples the intrinsic polarization of the material and its crystalline lattice deformation. Piezoelectricty was first observed by Pierre and Jacques Curie in 1880 in Rochelle salt and it has been studied extensively

within the last century. Piezoelectricity arises from the motion of the ionic atoms, located at specific lattice points, under applied electric fields resulting in distortions of the piezoelectric unit cell from the un-polarized state. A unit cell of a piezoelectric PZT crystal is shown in figure 1.4 [4] under both zero applied electric field (left) and with an electric field applied to the cell (right) demonstrating the resulting elongation of the crystal structure. The ongoing development of piezoelectric materials with very large coupling coefficients, such as PZT and PMN-PT, has created significant research interest in the use of piezoelectricity for many types of micro and nano scale systems. These materials offer relatively large strains and high electromechanical coupling coefficients which hold potential for applications which require efficient sensor and power transduction characteristics. In addition to the large academic interest in these materials, the piezoelectric effect has found widespread use in consumer technologies ranging from vibration sensors and actuators to energy harvesting applications.

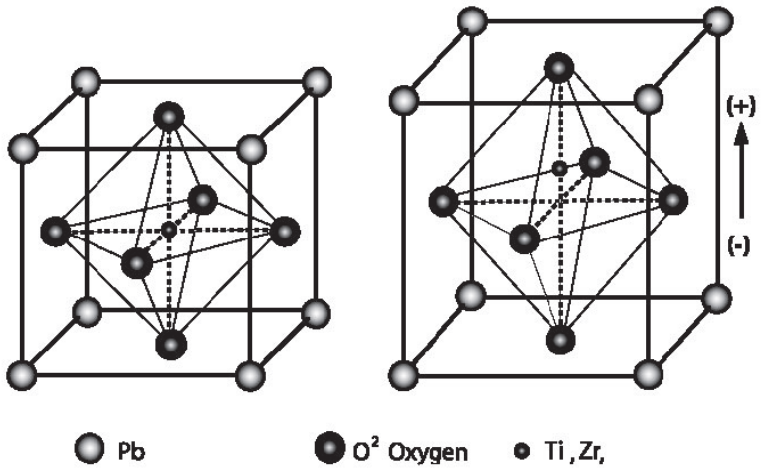

Figure 1.4 – A diagram of a piezoelectric PZT unit cell under no applied electric field (left) and applied electric field (right) illustrating the resulting lattice distortion.

Multiferroic composites use a combination of magnetoelastic and piezoelectric material phases to couple the intrinsic electric polarization and magnetization of the homogeneous material system. Although single phase materials exist which intrinsically possess coupled polarization and magnetization, the efficiency of this coupling is often too small to be useful in practical devices. Strain mediated composites improve on this shortcoming of single phase materials by using the large transduction efficiencies found in piezoelectric and magnetoelastic materials into a mutual mechanical energy domain. Through this indirect approach an efficient coupling is achieved between the polarization in the piezoelectric phase and the magnetization in the magnetoelastic phase of the composite. This effect has been studied extensively for the last two decades in bulk composite structures. The use of multiferroics to manipulate micro and nanoscale systems, however, has experienced rapid expansion only within the last decade with a strong focus on new magnetic memory and spin based logic technology. Despite this increased interest in nano-scale multiferroic composites, few works detail the operation of these material systems at radio frequencies. This uncharted operating regime for strain mediated multiferroics is the focus of the work presented in this dissertation with an emphasis on achieving small size and operating efficiencies in micro and nano scale sensors operating at VHF and UHF frequencies.

In this work multiferroic materials are applied to two types of microscale sensor systems which use the fundamental properties of magnetic ordering to operate. Specifically antennas and magnetometers are examined for an improvement in operating characteristics when using a multiferroic approach over currently available technologies. A new type of antenna is proposed based on the coupling between electromagnetic waves and the magnetoelastic phase of a multiferroic composite. Analysis for such a system is presented and steps are taken to experimentally demonstrate the performance of such a device. Additionally, a magnetometer

system based on surface acoustic wave transduction in multiferroic composites is analyzed, fabricated and tested to demonstrate the high sensitivities achievable in multiferroic based systems. Lastly, a multiferroic magnetometer based on quartz crystal microbalance technology is fabricated and tested using a passive and wireless measurement technique to demonstrate that such systems can be applied across a wide variety of applications while maintaining excellent performance characteristics.

Chapter 2: Multiferroic Antennas

I. Introduction

Communications systems have become ubiquitous in modern life and the impact they have had on the current world culture is extensive. This broad class of devices seeks to unify people over any distance and to make a wealth of information easily accessible to the user anywhere. An outstanding example of this technology is the cellular telephone, a device which has experienced enormous technological advancements in recent decades. These portable communications devices have forever changed the way humans connect and interact with one another, making this modern age one defined by extraordinary connectivity. At the heart of each one of these wireless electronic products is an antenna. This critical component allows for the reception and transmission of information through space by encoding data into electromagnetic waves. The modern day antenna was discovered by Heinrich Hertz in 1887 [5] after analyzing James Clerk Maxwell's equations describing electromagnetic waves which were published in 1865 [6]. Many of the currently operational antenna designs, such as the wire loop or dipole, closely resemble the very first test devices made by Hertz for his experimental work performed over 120 years ago. In fact the operating principles of these devices have not changed significantly since the first observation of wireless transmission. These antennae devices convert electromagnetic waves into electrical power by leveraging the movement of free electrons inside conductive materials when acted on by electric and magnetic fields. The coherent movement of these electrons inside the conductor comprises a dynamic current which is proportional to the power in the impinging wave. In a reciprocal manner, the transmission of electromagnetic waves from an identically shaped antenna can be produced by the application of dynamic current. By modulation of the

current and therefore the corresponding electromagnetic wave at frequencies lower than the wave carrier frequency, information can be passed between a pair of frequency matched antennae over potentially long distances. This simple yet effective transduction method forms the basis for the majority of antennae used in modern day communications.

An example of a simple dipole antenna is shown in figure 2.1.a detailing the two conductive "arms" which carry a radio frequency current of opposite phases. The schematic diagram for such a device is shown in figure 2.1.b. Balanced current is applied to the dipole antenna which creates the current distribution along the length of the conductive wires shown in red. A corresponding electric (orange) and magnetic (blue) field are generated in the space surrounding the wires which radiates outward from the antenna as an electromagnetic wave.

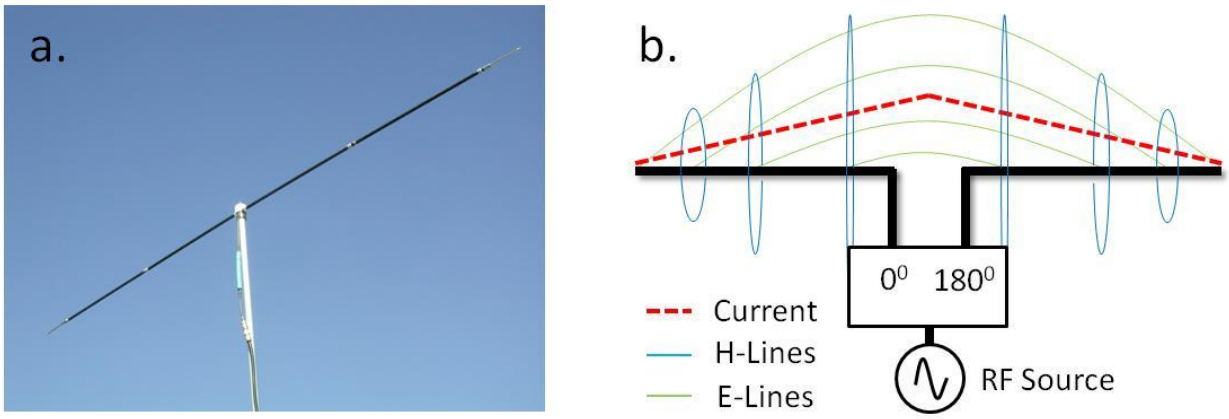

Figure 2.1 – a. An image of a horizontally polarized dipole antenna [Google Images]. b. A schematic view of the currents and fields on a short dipole antenna during operation.

As will be shown in the following section, the radiated power from a simple antenna structure such as the dipole can be solved for using Maxwell's description of electromagnetic waves. For simplicity the result of this analysis for far field power is given for a short dipole antenna as derived by Balanis [7].

$$P_{rad} = Z_0 \frac{\pi}{3} \left| \frac{I_0 L}{\lambda} \right|^2 \qquad [Eq. 2.1]$$

Where Z_0~377ohms, I_0 is the input current amplitude, l is the length of the dipole antenna and λ is the electromagnetic wavelength. It is seen from this analytical description of the infinitesimal dipole that as the length of the antenna decreases, larger current amplitudes are required to achieve the same amount of radiated power. Combining this increase in current with the ohmic losses in the conductive 'arms' of the device, the efficiency of the simple dipole rapidly decreases as its length becomes small with respect to the free space wavelength. Much work has been done attempting to maximize the radiation efficiencies for small footprint antennae by careful manipulation of the antenna geometry [8-16]. Despite these efforts, the sizes of many of the antennae found in modern communications systems are within an order of magnitude of the free space wavelength. This is particularly problematic when attempting to access longer wavelength (lower frequency) communication bands on mobile platforms. For these applications in the VHF and UHF range, antennae can become very large, in some cases exceeding many meters in length. This size/efficiency relationship severely limits the application space where these types of antennae can be used.

In this chapter a new approach to transduction of electromagnetic energy is explored which uses the intrinsic couplings found in multiferroic materials. Because the electromagnetic wave acts on the spontaneous magnetization of the material in a multiferroic system, the ohmic losses associated with free charge motion inside of conductors are significantly reduced. Furthermore, because the multiferroic material converts electromagnetic energy into an intermediate mechanical energy space, the antennae can achieve a resonance condition using much smaller structures. A simple diagram detailing the operation of a simple multiferroic antenna element is shown in figure 2.2. The element consists of magnetoelastic and piezoelectric layers which are

mechanically coupled at an interface shown in step a. Electrodes are placed onto the piezoelectric layer which acts to detect current which will be induced during the transduction process. The magnetization of the magnetoelastic layer is polarized such that the impinging magnetic wave will produce the largest possible moment rotation. When the RF magnetic field illuminates the magnetoelastic layer, as is shown in step b of figure 2.2, the spontaneous magnetic moments are rotated away from their initial configuration toward the h-field direction of the impinging electromagnetic wave. Because the material is magnetoelastic, this moment rotation couples to a proportional mechanical strain illustrated by the orange arrows. This strain is then coupled into the piezoelectric layer at the interface as is shown in step c. Because the spontaneous polarization of the piezoelectric material is intrinsically coupled to the applied strain, an internal electric field, illustrated as blue arrows in figure 2.2.c, develops between the electrodes. This electric field is finally able to drive charge to a connected load circuit, which is not shown in figure 2.2, where the output signal is processed.

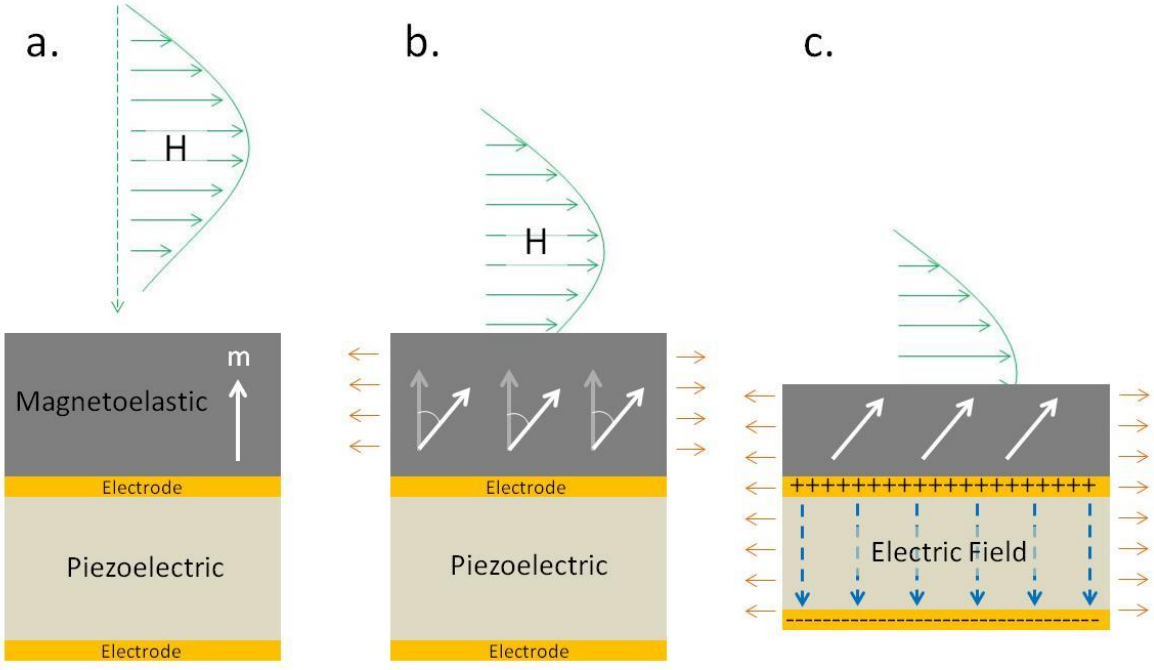

Figure 2.2 – A schematic diagram of the operation of a multiferroic antenna.

One of the advantages offered by this type of transduction mechanism is the significant reduction in the signal wavelength as it transformed from an electromagnetic wave into an acoustic wave. This reduction in wavelength is easily illustrated by examining the ratio of the acoustic wave velocity and the velocity of the electromagnetic wave. This is computed in equation 2.2 using the surface acoustic wave velocity of 3890 m/s for lithium niobate, which is the material chosen for the majority of the devices studied in this chapter.

$$\frac{V_{SAW}}{c} = \frac{3890\ m/s}{3 \times 10^8\ m/s} = 1.3 \times 10^{-5} \qquad [Eq.\ 2.2]$$

This result indicates that the size of a mechanically resonant structure will be five orders of magnitude smaller than an electromagnetically resonant structure operating at the same frequency. In practice, however, there will likely be many resonating structures which comprise the total antenna device to provide the energy density required for the output system. Despite the requirements for this larger phased element array, the final dimensions of a multiferroic antenna will remain many orders smaller than a traditional conductive antenna operating at the same frequency. This characteristic of the multiferroic antenna creates considerable application potential for compact communication devices. Access to longer electromagnetic wavelengths can be achieved efficiently on mobile phone platforms with multiferroic antennae, making all of the advantages these frequency bands accessible in previously inhibited applications.

Similar types of dynamic multiferroic structures have been studied for several decades spurred on by the relatively recent development and accessibility of piezoelectric and magnetoelastic materials with large coupling coefficients. Many of these devices consist of bilayer cantilever type structures and are made to oscillate at their fundamental frequency [17-22] which is typically in the high audio frequency range. Early research in the operation of dynamic multiferroic laminates examines this magnetic/electric coupling in larger plate resonator devices.

Work by Ryu et. al. [23] demonstrates the bias magnetic field dependence of the magnetoelectric coupling coefficient in PZT/Terfenol-D disk shaped plates operating at 1 kHz. An illustration of the three plate resonator types testing in this study is shown in the top of figure 2.3. The corresponding magnetoelastic coupling coefficients are plotted as a function of applied bias field in the bottom graph of figure 2.3 for the three types of plates tested.

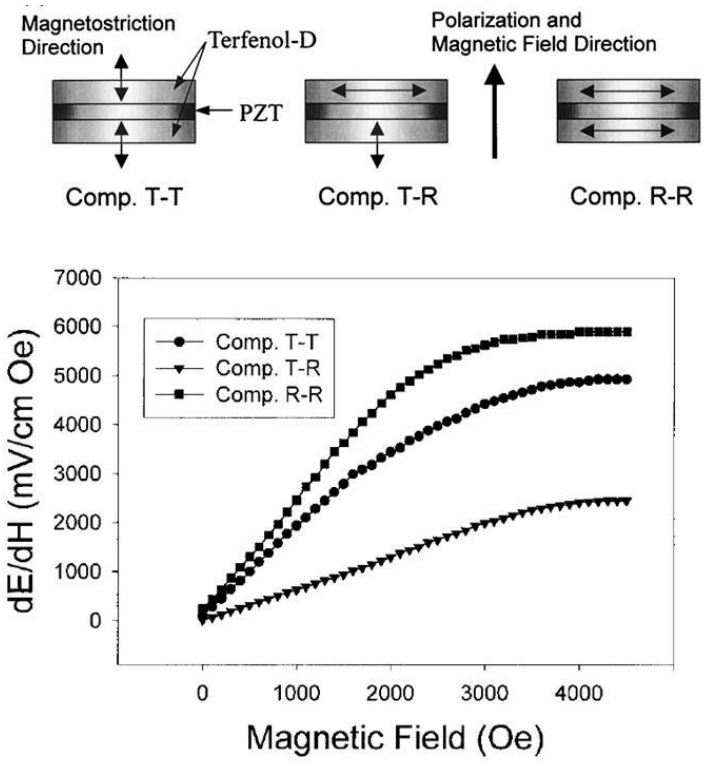

Figure 2.3 – The three types of PZT/Terfenol-D plate resonators tested for coupling (top). The coupling coefficients of the three plates as a function of applied magnetic field (bottom). [23]

Comparison of the device geometry shown in figure 2.3 and those proposed for use as a mulitferroic receiver element in figure 2.2 indicates that these devices are identical in structure. However, because the operating frequency of the previously shown plate resonator device is only around 1 kHz, it is expected that these plates will have much larger dimensions than that of the

proposed antenna resonators which operate at VHF and UHF frequencies. It is apparent from these recent works that the study of the dynamic multiferroic transduction effect has been limited to low frequencies in the audio and ultrasonic range rarely exceeding 100 kHz [24]. This is due to the difficulty of manufacturing these relatively large bimorph type structures with resonant frequencies in the VHF and UHF frequency bands. More frequently these multiferroic type composites are used as a static tuning mechanism for the impedance characteristics of substrates in RF applications. Several of these research efforts demonstrate that homogeneous magnetoelastic composites can alter the electromagnetic propagation characteristics of the composite substrate [25-26]. This field of study demonstrates that the broadband properties of high frequency substrates can be precisely tuned using these ferroelectric and magnetoelastic composite materials. In adjacent research efforts, the study of layered strain mediated structures at radio frequencies often highlights the ability to electrically control the ferromagnetic resonance phenomena in the magnetoelastic layer of the composite [27-34]. This electric field tuning of FMR is demonstrated by J. Lou et. al. [34] using a FeGaB/PZN-PT hetereostructure operating at 9.6 GHz the absorption results of which are shown in figure 2.4 for various electric field values. It is observed from figure 2.4 that relatively small electric fields applied to the piezoelectric layer can induce large changes in the resonance field value. This effect has significant potential in tunable RF devices which leverage the ferromagnetic resonance phenomena for operation such as circulators or filters. Currently these RF components operate by shifting the resonance frequency of the ferromagnet using an applied magnetic field from an electromagnet. Transitioning these types of components to the chip scale requires the use of a tuning mechanism with higher efficiency than can be offered by

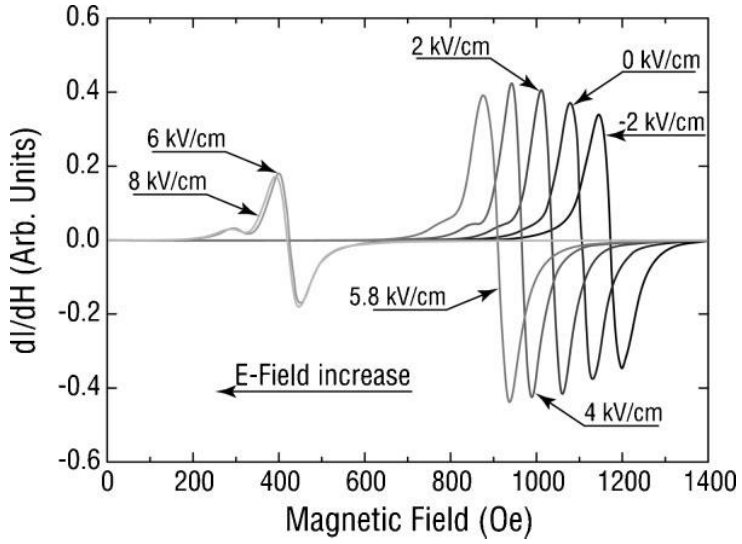

Figure 2.4 – The x-band power absorption of a FeGaB/PZN-PT heterostructure under various electric field values applied to the PZN-PT layer. [34]

scaled conventional electromagnets. The voltage controlled approach found in these multiferroic heterostructures can fill the need for energy efficient frequency tuning in chip scale packaging footprints. In addition to tunable narrow band filter behavior, many of these devices show promise in the detection of static magnetic fields with sensitivities approaching those of currently used magnetometers [35-36]. An excellent review of the field of dynamic magnetoelectric composites is presented by Srinivasin [37]. Despite the extensive work done studying the static tuning properties of these dynamically actuated magnetoelectric composites, these observations do not demonstrate the direct coupling of magnetic and electric fields at radio frequencies.

Recent efforts have shown that this high frequency magnetoelectric coupling is possible by elastically driving the multiferroic structure at ferromagnetic resonance[38-40]. These studies examine the power absorbed in thin magnetoelastic films as they are driven into ferromagnetic resonance using acoustic waves. Labanowski et. al. [38] demonstrates this power absorption

phenomenon using surface acoustic waves (SAW) generated inside a lithium niobate substrate. The experimental setup for this measurement is shown in the top image of figure 2.5. A pair of electrodes is used to propagate and detect a surface acoustic wave through a thin nickel film deposited onto a lithium niobate substrate. A bias field, of various magnitudes and in-plane angles with respect to the nickel film, is applied to the sample and the power absorbed by the film is recorded. This is shown for the various upper harmonic modes of the SAW electrodes as a function of bias angle in figure 2.5.b. The angular dependence of the absorption on the bias magnetic field is shown in figure 2.5.a. These results observe the extremely efficient absorption of acoustic energy by the nickel film as the dispersive relationship between the phonon and magnon modes inside the ferromagnet coincide. These works show that the coupling between elastic waves and magnetic moment rotation is possible in magnetoelastic materials at microwave frequencies. These reports do not include observations of the electromagnetic power radiated from the multiferroic composite but rather take an indirect route to show that energy is being coupling from one domain to another. Additionally these devices are shown to operate at ferromagnetic resonance frequencies where the availability of efficient, conventional and compact antenna systems is widespread. In this chapter the route by which the radiated power from a multiferroic composite operating at VHF and UHF frequencies can be measured is proposed.

In the work presented in this chapter the analysis for the transmission and reception power is presented for the magnetoelastic layer of the proposed multiferroic antenna structure. Several material systems are examined within this analysis for their performance as an antenna device and a set of optimized material parameters are derived. A design for the multiferroic antenna is

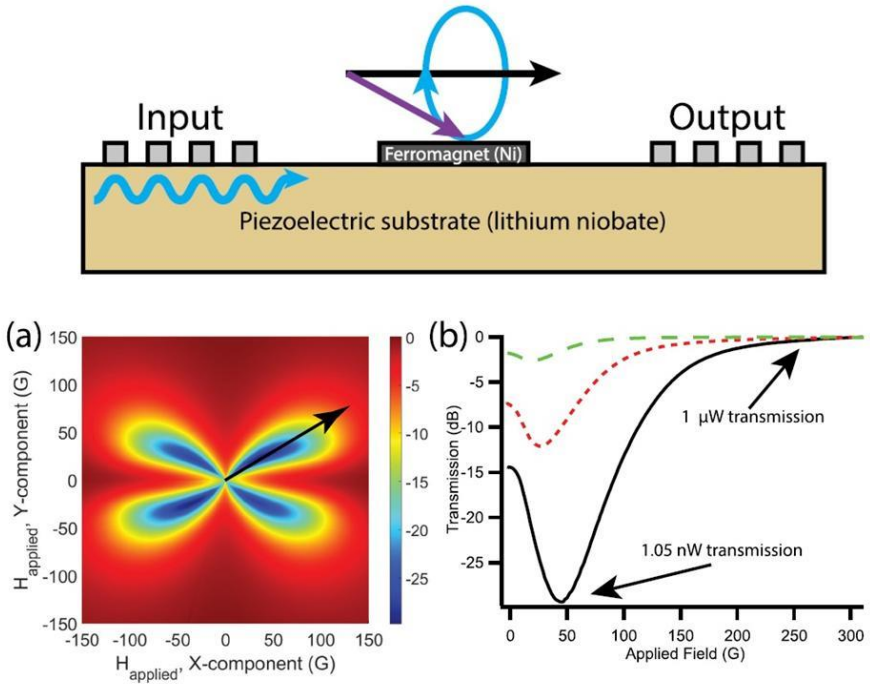

Figure 2.5 – A schematic representation of the FMR absorption experiment using SAWs (top). a. An angular color map plot showing absorption of acoustic energy in the nickel film. b. Transmission measured at the output IDT for various upper harmonic modes as a function of applied bias field

selected based on existing surface acoustic wave filter devices. The geometries and materials for this device are optimized through the use of multiphysics finite element simulations. Using the optimized design geometries and materials, a fabrication process is developed for manufacturing test devices. A measurement system is designed which can detect low power RF signals from the multiferroic receiver antenna while decoupling the magnetoelastic component of the signal from the system noise. Results from these experiments are presented which show small couplings at frequencies of interest which are attributed to potential magnetoelastic phenomena. Optimized materials which can improve the antenna power output are discussed.

II. Analysis

When analyzing the operational characteristics of a proposed multiferroic antenna, carefully selected metrics must be chosen to quantify the benefits of such an approach over what is currently available. This is a common engineering practice in which a new technology is compared against well-established methods which achieve the same end purpose but take significantly different paths to accomplish these tasks. In this case the end purpose is to transform electromagnetic energy into a detectable electrical signal which accurately represents the information contained within the electromagnetic wave. The multiferroic antenna discussed in this work achieves this transformation by first converting the power contained in the electromagnetic wave into mechanical work by way of the magnetoelectric effect found in select ferromagnetic materials. The last step of the process involves converting this mechanical work into an electrical power delivered to a load using the piezoelectric effect.

In contrast to this transduction process, the antennae found in modern day communication systems operate by exploiting the movement of electrons inside conductors when placed in an oscillating magnetic and electric field. The fundamental fields which comprise the electromagnetic wave produce forces on charged particles (or moving charged particles in the case of a magnetic field) which are found unbound in large numbers inside conductive materials. These unbound charges move freely inside the conductive medium when acted on by the impinging electromagnetic wave to produce a dynamic current density. This current is terminated at a load circuit through which the moving charge delivers an electrical power. In this approach careful consideration is given to the geometry and orientation of the conductor with

respect to the wavelength and polarization of the incoming EM wave in order to maximize the efficiency of the transduction process.

In the following analysis the radiation efficiency of a multiferroic cube shaped radiating element is compared to that of a magnetic loop antenna of comparable dimensions. Sources of dissipated power in the multiferroic cube system are the energy conversion losses inherent to magnetoelastic transduction and the geometry driven impedance match of the radiating element to free space. Losses in the loop antenna system include the ohmic loss of the conductor, the effective series resistive loss in the tuning capacitor and the geometry driven impedance match of the loop with free space. It is important to note that the impedance of the driving source is neglected in both cases. This is done to avoid further specifying the methods by which the magnetoelectric block is being mechanically actuated to maintain the generality of the results to many systems. It is important to consider, however, that the impedance match between the antenna and its respective driving source will represent significant transmission losses for both the loop and magnetoelectric antenna in real miniaturized systems.

The following analysis of radiation from an infinitesimally small loop antenna is paraphrased from an original derivation presented by Balanis [7]. To begin, Maxwell's equations [6] are used to describe an electromagnetic wave travelling in an arbitrary medium.

$$\nabla \cdot E = \frac{\rho}{\varepsilon_0} \qquad [Eq.\,2.3]$$

$$\nabla \times E = -\frac{\partial B}{\partial t} \qquad [Eq.\,2.4]$$

$$\nabla \cdot B = 0 \qquad [Eq.\,2.5]$$

$$\nabla \times B = \mu_0 \left(J + \varepsilon_0 \frac{\partial E}{\partial t} \right) \qquad [Eq.\,2.6]$$

It is convenient to define the magnetic field in terms of a vector potential as

$$H_a = \frac{1}{\mu_r \mu_0} \nabla \times A \qquad [Eq.\,2.7]$$

Where H_a is the magnetic field produced by the arbitrarily defined vector potential A. By manipulation of equation 2.7 and substitution into equation 2.4 the electric field can be written in terms of the induced magnetic field.

$$\nabla \times E_a = -j\omega\mu_r\mu_0 H_a \qquad [Eq.\,2.8]$$

From which E_a can now be solved with respect to the magnetic vector potential and the arbitrary electric scalar potential φ_e

$$E_a = -\nabla\varphi_e - j\omega A \qquad [Eq.\,2.9]$$

By substitution of equation 2.7 into equation 2.6 the curl of H_a can be written

$$\nabla \times H_a = J + j\omega\mu_r\mu_0 E_a \qquad [Eq.\,2.10]$$

Further substitution of equation 2.8 into equation 2.7 after taking the curl of both sides yields

$$\mu_r\mu_0 J + j\omega\mu_r\mu_0\varepsilon_r\varepsilon_0 E_a = \nabla(\nabla \cdot A) - \nabla^2 A \qquad [Eq.\,2.11]$$

After substitution into equation 2.9, the magnetic vector potential can be written purely in terms of the source current and the electric scalar potential.

$$\nabla^2 A + k^2 A = -\mu_r\mu_0 J + \nabla(\nabla \cdot A + j\omega\mu_r\mu_0\varepsilon_r\varepsilon_0\varphi_e) \qquad [Eq.\,2.12]$$

Where $k = \omega\sqrt{\mu_r\mu_0\varepsilon_r\varepsilon_0}$. To further reduce 2.12, the divergence of A is defined in terms of the electric scalar potential.

$$\varphi_e = -\frac{1}{j\omega\mu_r\mu_0\varepsilon_r\varepsilon_0}\nabla \cdot A \qquad [Eq.2.13]$$

Substitution of 2.13 into 2.12 results in an expression for the magnetic vector potential in terms of current density J

$$\nabla^2 A + k^2 A = -\mu_r\mu_0 J \qquad [Eq.2.14]$$

By substitution of 2.13 into 2.9 the electric field can also be written purely in terms of the magnetic vector potential

$$E_a = -j\omega A - j\frac{1}{\omega\mu_r\mu_0\varepsilon_r\varepsilon_0}\nabla(\nabla \cdot A) \qquad [Eq.2.15]$$

To obtain solutions to equation 2.14, a spherical coordinate system (φ, θ, r) is considered with current density in the z direction only. When far from the point source (J=0) the differential equation becomes

$$\frac{d^2A_z(r)}{dr^2} + \frac{2}{r}\frac{dA_z(r)}{dr} + k^2A_z(r) = 0 \qquad [Eq.2.16]$$

Where the A_z is purely a function of radial distance r. Solutions of 2.16 have the following form

$$A_{z1} = C_1\frac{e^{-jkr}}{r} \qquad [Eq.2.17]$$

$$A_{z1} = C_1\frac{e^{+jkr}}{r} \qquad [Eq.2.18]$$

For the geometry of a centrally located point source, only the outward flowing wave solution [2.17] is needed. It can be seen that the static solution when k=0 is simply

$$A_z = \frac{C_1}{r} \qquad [Eq. 2.19]$$

By comparing 2.19 and 2.17 it is apparent that to arrive at the time varying solution for A_z the static solution can simply be multiplied by a factor of e^{-jkr}. At the location of the point source and in the static case (J≠0, k=0), 2.14 becomes

$$\nabla^2 A_z = -\mu_r \mu_0 J_z \qquad [Eq. 2.20]$$

Which has a solution of the following form

$$A_z = \frac{\mu_r \mu_0}{4\pi} \iiint \frac{J_z}{r} dv \qquad [Eq. 2.21]$$

Performing the same multiplication procedure for the static case very far from the point source, the time varying solution at the point source now becomes

$$A_z = \frac{\mu_r \mu_0}{4\pi} \iiint J_z \frac{e^{-jkr}}{r} dv \qquad [Eq. 2.22]$$

By solving for the remaining two coordinates as before, the total solution is a superposition of the vector potentials

$$A = \frac{\mu_r \mu_0}{4\pi} \iiint J \frac{e^{-jkr}}{r} dv \qquad [Eq. 2.23]$$

For the purpose of the infinitesimally small loop antenna, 2.23 can be written as a line integral after transforming the source current into cylindrical coordinates (ρ, φ, z).

$$A = \frac{\mu_r \mu_0}{4\pi} \int I_e(\rho, \varphi, z) \frac{e^{-jkR}}{R} dl \qquad [Eq. 2.24]$$

By transforming the observation coordinates into a spherical system and solving 2.24 for a φ moving electric current, the A_φ vector potential becomes

$$A_\varphi \cong \frac{a^2 \mu_r \mu_0 I_0}{4} e^{-ikr} \left(\frac{jk}{r} + \frac{1}{r^2}\right) sin\theta \qquad [Eq. 2.25]$$

Where a is the loop radius and r is the distance from the observer to the loop center. The solutions for the remaining two coordinates become zero. By differentiating A_φ for each coordinate, the resulting magnetic fields become

$$H_r = j \frac{ka^2 I_0 cos\theta}{2r^2} \left[1 + \frac{1}{jkr}\right] e^{-jkr} \qquad [Eq. 2.26]$$

$$H_\theta = -\frac{(ka)^2 I_0 sin\theta}{4r} \left[1 + \frac{1}{jkr} - \frac{1}{(kr)^2}\right] e^{-jkr} \qquad [Eq. 2.27]$$

$$H_\varphi = 0 \qquad [Eq. 2.28]$$

Using equation 2.15 the electric fields can also be solved

$$E_r = E_\theta = 0 \qquad [Eq. 2.29]$$

$$E_\varphi = Z_0 \frac{(ka)^2 I_0 sin\theta}{4r} \left[1 + \frac{1}{jkr}\right] e^{-jkr} \qquad [Eq. 2.30]$$

Where $Z_0 = \sqrt{\frac{\mu_0}{\varepsilon_0}}$, the impedance of free space. To solve for the total radiated power, the Poynting theorem is used to compute wave intensity

$$I = \frac{1}{2} E \times H^* \qquad [Eq. 2.31]$$

Using the radial field components, 2.31 is solved using 2.30 and 2.27 and integrated over a sphere of radius r, which results in a power

$$P_r = Z_0 \left(\frac{\pi}{12}\right)(ka)^4 |I_0|^2 \left[1 + j\frac{1}{(kr)^3}\right] \qquad [Eq. 2.32]$$

When very far from the source, the imaginary terms in 2.32 become zero and the total radiated power is

$$P_r = Z_0 \left(\frac{\pi}{12}\right)(ka)^4 |I_0|^2 \qquad [Eq. 2.33]$$

This is the classical result for radiated far field power from an infinitesimally small loop antenna. For a more rigorous treatment of the preceding derivation please refer to [7]. It is common to contract the coefficients in 2.33 into an effective parameter called the radiation resistance.

$$R_r = Z_0 \left(\frac{\pi}{12}\right)(ka)^4 \qquad [Eq. 2.34]$$

It is apparent from 2.34 that the ability of the loop to radiate power to free space depends strongly on the loop radius and the operating frequency. In order to define the radiation efficiency for the loop system, other losses must be defined. The first of which is the loss of power to Joule heating (ohmic losses) inside the conductor from which the loop is constructed. At frequency, the electrons inside a wire will travel in a very thin layer at the outer surface of the wire called the skin depth. Taking this non-uniform current distribution into account yields the following result for the loop resistance.

$$R_{ohm} = \frac{L\rho}{d}\sqrt{\frac{\pi f \mu_r \mu_0}{\rho}} \qquad [Eq. 2.35]$$

Where L is the diameter of the loop, d is the diameter of the wire, f is the operating frequency and ρ is the resistivity of the wire. It should be noted that 2.35 is only valid for wire diameters sufficiently larger than the skin depth. The final loss mechanism included in the analysis of the small loop antenna is the series resistive losses of an added tuning capacitor. To select a capacitance, the operating frequency and the inductance of the loop must be found. A common approximation for the inductance of a single turn wire loop is

$$M \cong \mu_r \mu_0 \frac{L}{2}\left[\ln\left(\frac{8L}{d}\right) - 2\right] \qquad [Eq.\,2.36]$$

The capacitance required for the loop to operate at a frequency of f is solved by equating the negative and positive reactance

$$C = \frac{1}{(2\pi f)^2 M} \qquad [Eq.\,2.37]$$

The series resistive losses can then be found using the quality factor of the capacitor

$$R_{esr} = \frac{1}{2\pi f C Q} \qquad [Eq.\,2.38]$$

The radiation efficiency for this simple loop system can then be found by taking the ratio of the radiation resistance to the sum of the resistive loss terms.

$$\eta_{loop} = \frac{R_r}{R_{ohm} + R_{esr} + R_r} \qquad [Eq.\,2.39]$$

It should be noted that the loop and loop loss components presented here are chosen for simplicity of comparison with a multiferroic antenna as both are reduced in dimension. In

practical wire loop systems other losses, such as substrate dielectric loss and losses due to the proximity effect, will likely play a key role in reducing the radiation efficiency further.

To solve for the radiation power from a multiferroic antenna, equivalence is drawn between the current and loop area terms in equation 2.33 and the magnetic dipole moment of a magnetoelastic material of volume V. The magnetic dipole moment m_0 of a current I_0 circulating about an area A is defined as

$$m_0 = I_0 A \qquad [Eq. 2.40]$$

By substitution of 2.40 into 2.33 the power radiated to a far field sphere for an oscillating magnetic dipole moment is derived as

$$P_{mf} = \frac{4\pi^3}{3}\frac{Z_0}{\lambda^4} {m_0}^2 \qquad [Eq. 2.41]$$

Where λ is the wavelength of the radiated wave in free space. Considering a magnetoelastic cube of side length N, the magnetic dipole moment can be written in terms of the materials magnetization (m=MV).

$$P_{mf} = \frac{4\pi^3}{3}\frac{Z_0}{\lambda^4} (MV)^2 \qquad [Eq. 2.42]$$

To incorporate the effects of magnetoelastic coupling first the magnetomechanical coupling factor is defined as the ratio of magnetoelastic energy to the geometric mean of purely magnetic and purely elastic energies.

$$k = \frac{U_{me}}{\sqrt{U_e U_m}} \qquad [Eq. 2.43]$$

For a one dimensional problem the piezomagnetic constitutive relationships can be written as

$$S = s^H T + d_{33} H \qquad [Eq. 2.44]$$

$$B = d_{33} T + \mu^T H \qquad [Eq. 2.45]$$

For the one dimensional case, the magnetomechanical coupling coefficient in 2.43 can be used to describe the relationship between the piezomagnetic coefficient d_{33} and the material properties.

$$k^2 = \frac{(d_{33})^2 s_{33}}{\mu_{33}} \qquad [Eq. 2.46]$$

The quantity k^2 is used to describe the overall efficiency of the magnetomechanical transduction process with perfect energy transfer occurring at $k^2=1$. Assuming that there are no applied magnetic fields, the change in magnetic flux is proportional to the applied driving stress in the block.

$$B = d_{33} T \qquad [Eq. 2.47]$$

Which can be written in terms of magnetization as a function of strain

$$M = \frac{d_{33} \varepsilon Y}{\mu_0} \qquad [Eq. 2.48]$$

Where Y is the elastic modulus of the block and ε is the applied strain. It will be useful in this analysis to express the time varying strain as an elastic potential energy.

$$U_e = \frac{1}{2} \varepsilon^2 Y V \qquad [Eq. 2.49]$$

It can be seen that if the driving strain takes the harmonic form $\varepsilon = \varepsilon_0 e^{iwt}$, the rms power amplitude of this strain becomes

$$P_e = \frac{1}{2}\left|\frac{dU_e}{dt}\right| = \pi f(\varepsilon_0)^2 YV \qquad [Eq.\,2.50]$$

Solving 2.50 in terms of strain and substitution into equation 2.48 results in

$$M = \frac{d_{33}Y}{\mu_0}\left(\frac{P_e}{\pi f Y V}\right)^{1/2} \qquad [Eq.\,2.51]$$

Which when substituted into the equation for radiated power 2.42 after writing electromagnetic wavelength in terms of frequency and simplifying terms gives

$$P_r = Z_0 \frac{4\pi^2 Y f^3 {d_{33}}^2 V}{3c^4\mu_0} P_e \qquad [Eq.\,2.53]$$

By dividing the radiated power by the input elastic power, the radiation efficiency of the multiferroic block can be written as

$$\eta_{me} = \frac{P_r}{P_e} = Z_0 \frac{4\pi^2 Y f^3 {d_{33}}^2 V}{3c^4\mu_0} \qquad [Eq.\,2.54]$$

The radiation efficiencies for a magnetoelastic cube of three representative magnetoelastic materials are computed using 2.54 and shown in figure 2.6 compared to the radiation efficiency for a wire loop computed using equation 2.39 for an operating frequency of 200 MHz. The mechanical and magnetoelastic properties for nickel and FeGaB are found in prior works [41] and the properties for this specific ferrite compound (Epcos N87) are measured as described in following sections. The wire loop efficiency is computed using the material properties for copper and a capacitor quality factor of 400. The diameter of the wire is fixed at 10% of the major loop

diameter. The characteristic length is shown for 1 to 100 μm. Figure 2.6 shows that below characteristic lengths of 40 μm a nickel cube becomes a more efficient radiator than a wire loop. Similarly, this crossover point occurs at much smaller sizes for the weak magnetoelastic ferrite shown in black. An optimal material, iron gallium boron (FeGaB), remains the most efficient radiating platform over the range of lengths modeled.

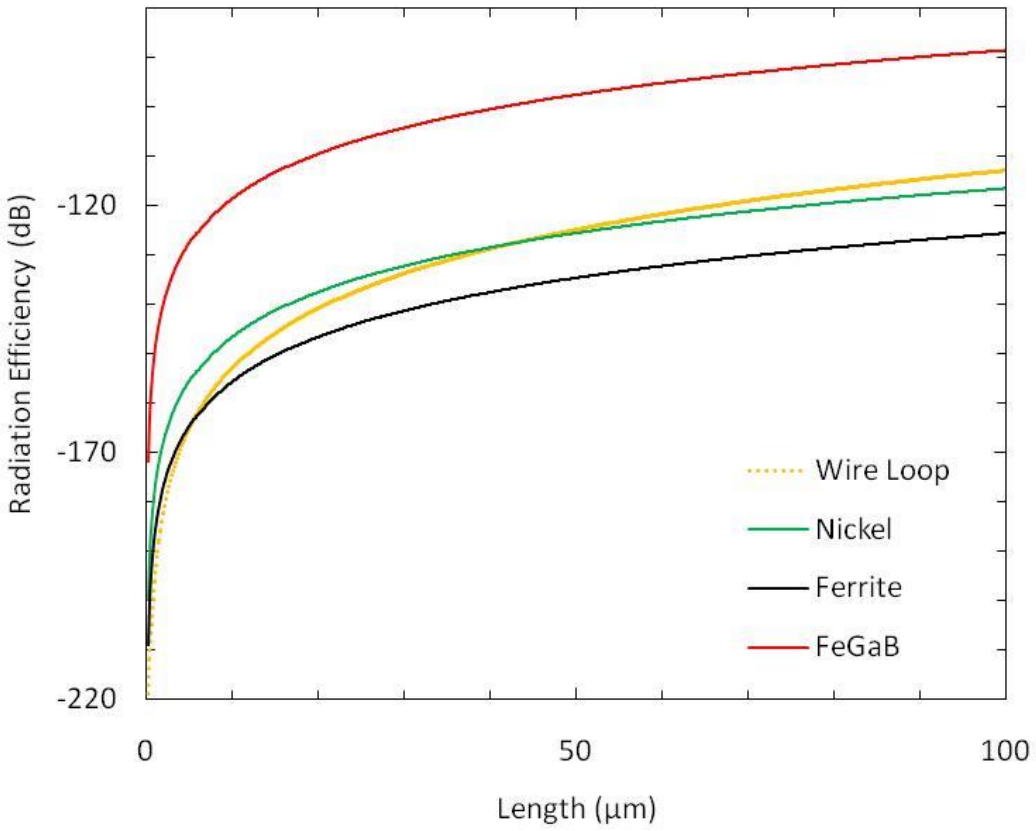

Figure 2.6 – The radiation efficiencies for an electrically small wire loop antenna (yellow) and a strain driven block of three representative magnetoelastic materials as a function of characteristic length operating at 200 MHz. Length is the loop diameter in the case of the wire loop and represents the side length of the magnetoelastic block.

It is obvious from figure 2.6 that even using the most ideal magnetoelastic material, FeGaB, the radiated power from a micron-scale multiferroic antenna to the far field will be very small. Further inspection of equation 2.32, however, shows that within the region close to the source, the imaginary component of power becomes very large. This so called reactive power is radiated from the antenna into the near field. Figure 2.7 shows the imaginary component of radiated power as a function of distance from the source measured in free space wavelengths. It is shown in figure 2.7 that much of the radiated power is stored within the first several wavelengths of media surrounding the antenna.

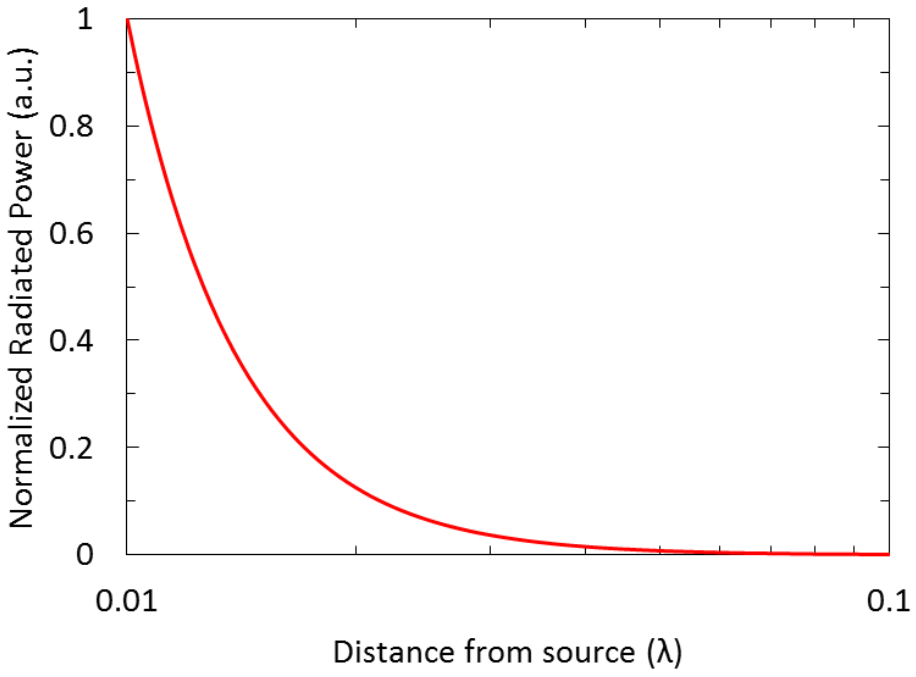

Figure 2.7 – A plot of normalized imaginary radiated power from a wire loop antenna as a function of distance from the source (in wavelengths).

Integrating this result into the previously obtained radiation efficiency becomes simply a matter of adding the imaginary component and taking the total power amplitude as the radius of the enclosing sphere becomes smaller. Figure 2.8 shows the total radiation efficiency for a

multiferroic cube for a side length of 50 μm. The results for three magnetoelastic materials are shown. It can be seen that the efficiency of the simplified multiferroic radiator approaches levels that compare with commercial antennas as the distance of the measurement device from the source becomes small. Practically detectable amounts of radiated power (-50 dB) are achievable from the cube within a 1% wavelength separation in particular for the nickel and FeGaB material systems. This corresponds to a 1.5 cm measurement distance for the operating frequencies of interest which is the near field testing region of focus for the experimental results demonstrated in this work.

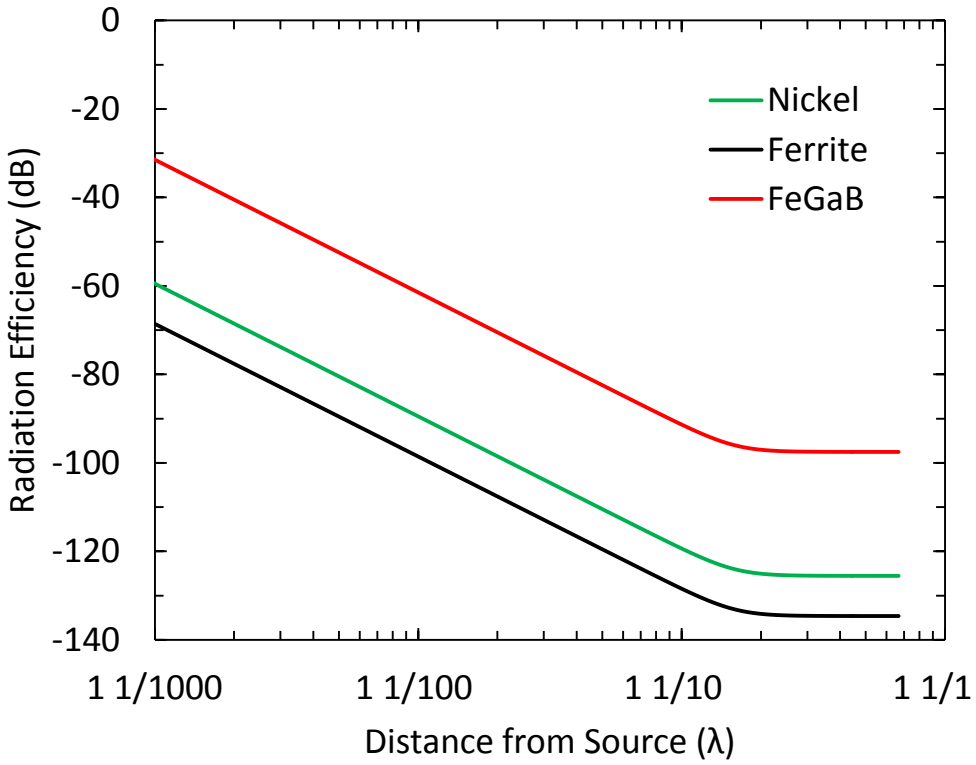

Figure 2.8 – Radiation efficiency as a function of distance from a radiating magnetoelastic cube having 50 μm side lengths for three types of magnetoelastic materials.

With the recent advancements in consumer communication technology, there has been significant interest in communication systems operating solely within this near field region. These systems are typically used in short range wireless data transfer between mobile devices such as cell phones or mobile computers. It is this near field communication (NFC) technology which offers the most promising application space for a long wave, chip-scale multiferroic antenna.

Up to this point analysis has considered only the case of transmission of electromagnetic waves from the multiferroic element to a free space domain. Assumptions about the excitation strain and uniformity of the magnetization inside of the magnetoelectric material have been made in these derivations which limit the applicability of the results to optimum, far field circumstances. In a true conductive medium an incident wave will experience significant reflections from the materials surface. These reflections interfere in a deconstructive manner with the forward travelling wave, reducing the power flow into the system. Furthermore, the transmitted wave induces charge movement inside the conductive film which acts as an additional ohmic power loss mechanism for the travelling wave.

To better represent how these reflections and material losses interact with a continuous magnetoelastic film, a one dimensional plane wave incident onto a conductive surface is modeled using Maxwell's equations to examine the available electromagnetic power transmitted into the film. By using a linear constitutive piezomagnetic model, the strain energy gradient inside of the film due to magnetoelasticity is computed for three representative magnetoelastic materials. The non-linear applied field dependence of the output power on both permeability and the magnetoelastic coupling coefficient is found by fitting the variation of these parameters to experimental data for a representative nickel film. Incorporating these bias field dependent

variables into the strain energy computation and integrating over the thickness of the magnetoelastic film, the total strain power is found and normalized with respect to the incident electromagnetic power for a 500 nm thick nickel film.

Using Maxwell's equations to solve for the curl of the electric and magnetic fields for a plane wave propagating along the z direction inside a linear dielectric medium (P=0, J=0), equations 2.3 and 2.6 become

$$\frac{\partial E}{\partial z} = -\frac{\partial B}{\partial t} \qquad [Eq. 2.55]$$

$$\frac{\partial B}{\partial z} = -\mu_0 \varepsilon_0 \frac{\partial E}{\partial t} \qquad [Eq. 2.56]$$

Taking the partial derivatives of equations 2.55 and 2.56 with respect to both z and t variables and combining results in the following partial differential equations

$$\frac{\partial^2 E}{\partial z^2} = \mu_0 \varepsilon_0 \frac{\partial^2 E}{\partial t^2} \qquad [Eq. 2.57]$$

$$\frac{\partial^2 B}{\partial z^2} = \mu_0 \varepsilon_0 \frac{\partial^2 B}{\partial t^2} \qquad [Eq. 2.58]$$

These take form of the well-known plane wave equation

$$\frac{\partial^2 \varphi}{\partial z^2} = \frac{1}{v^2} \frac{\partial^2 \varphi}{\partial t^2} \qquad [Eq. 2.59]$$

Where the quantity v is the wave velocity. Solutions to this equation take the following form

$$\varphi(z,t) = \varphi_0 e^{i(kz-\omega t)} \qquad [Eq. 2.60]$$

ω is the frequency of the wave and the wave vector k is defined as

$$k = \frac{2\pi}{\lambda} \qquad [Eq.\,2.61]$$

Where λ is the wavelength. Fitting the solution of the wave equation to equations 2.57 and 2.58 results in the classical form for a plane electromagnetic wave travelling in a linear dielectric medium.

$$E(z,t) = E_0 e^{i(kz-\omega t)} \qquad [Eq.\,2.62]$$

$$B(z,t) = B_0 e^{i(kz-\omega t)} \qquad [Eq.\,2.63]$$

It is easy to see that the wave amplitudes E_0 and B_0 are proportional to one another through the wave speed which in a vacuum ($\varepsilon_r=\mu_r=1$) is

$$c = \frac{1}{\sqrt{\mu_0 \varepsilon_0}} \qquad [Eq.\,2.64]$$

For the purpose of this analysis, equations 2.62 and 2.63 will describe a plane electromagnetic wave propagating inside a near field vacuum region before reaching the magnetoelastic film. Because many of the magnetoelastic materials possessing high magnetomechanical coupling factors are metallic, analysis of wave propagation into this layer requires the generalization of the previously derived wave equation to account for a medium with non-zero conductivity. To do so the current density inside the magnetoelastic material is described as

$$J = \sigma E \qquad [Eq.\,2.65]$$

This describes an ohmic conductor with a conductivity σ. Substitution of equation 2.65 into 2.6 and solving as before yields solutions of the same form as equations 2.62 and 2.63. In the case of

a wave propagating in a conductive material, however, the wave vector now becomes complex valued

$$k = \alpha - i\beta \qquad [Eq.2.66]$$

Where the complex constants are derived from the materials electrical properties

$$\alpha = \omega\sqrt{\mu_r\mu_0\varepsilon_r\varepsilon_0}\sqrt{-\frac{1}{2}+\frac{1}{2}\sqrt{1+\frac{\sigma^2}{\omega^2(\varepsilon_r\varepsilon_0)^2}}} \qquad [Eq.2.67]$$

$$\beta = \omega\sqrt{\mu_r\mu_0\varepsilon_r\varepsilon_0}\sqrt{\frac{1}{2}+\frac{1}{2}\sqrt{1+\frac{\sigma^2}{\omega^2(\varepsilon_r\varepsilon_0)^2}}} \qquad [Eq.2.68]$$

It is now apparent that the imaginary component of the wave vector describes an exponentially decreasing field amplitude as the wave propagates into the material giving rise to the concept of a "skin depth" which is defined as the distance the wave travels into the material before the amplitude becomes e^{-1} (or about 37%) of its original value. This occurs at a distance of β^{-1}. It can also be seen that the amplitudes of the electric and magnetic fields are no longer related to one another through the speed of light in vacuum. A factor called the material impedance (Z_{mat}) is now defined to express their new relationship, after using $B=\mu_0\mu_r H$ to write magnetic fields in terms of H.

$$\frac{E_0}{H_0} = Z_{mat} = \sqrt{\frac{j\omega\mu_0\mu_r}{\sigma + j\omega\varepsilon_0\varepsilon_r}} \qquad [Eq.2.69]$$

To derive the reflection and transmission coefficients at the interface of the conductive film the following boundary conditions are defined from continuity.

$$B_i + B_r = B_t \qquad [Eq. 2.70]$$

$$E_i + E_r = E_t \qquad [Eq. 2.71]$$

Where the i, r and t subscripts denote the incident, reflected and transmitted field magnitudes respectively. Using the material impedance from equation 2.69 and the free space impedance $Z_0$to express equation 2.70 in terms of electric fields, the reflection coefficient of the system can be defined.

$$\Gamma = \frac{E_r}{E_i} = -\frac{Z_{mat} - Z_0}{Z_{mat} + Z_0} \qquad [Eq. 2.72]$$

Noting the negative sign which indicates the reflected wave and incident wave have π difference in phase. This leads to a transmission coefficient which is just T=1-Γ

$$T = \frac{2Z_{mat}}{Z_{mat} + Z_0} \qquad [Eq. 2.73]$$

Both the reflected and transmitted components of the electric and magnetic fields can now be written in terms of the incident electric field.

$$E_r(z,t) = \Gamma E_i e^{i(kz-\omega t)} \qquad [Eq. 2.74]$$

$$E_t(z,t) = T E_i e^{i(kz-\omega t)} \qquad [Eq. 2.75]$$

$$H_r(z,t) = \frac{\Gamma E_i}{Z_0} e^{i(kz-\omega t)} \qquad [Eq. 2.76]$$

$$H_t(z,t) = \frac{T E_i}{Z_{mat}} e^{i(kz-\omega t)} \qquad [Eq. 2.77]$$

To compute the ratio of the real time averaged wave intensity now transmitted into the film, the Poynting theorem from equation 2.31 can be used with the result from equations 2.75 and 2.77.

Figure 2.9 shows the electromagnetic power transmitted into a continuous film for three representative magnetoelastic materials: nickel, iron gallium boron (FeGaB) and a commercially available bulk high frequency ferrite (Epcos N87). The power is shown for a depth up to one micron and is normalized to the power applied in the source medium. It is seen from these plots and a comparison of the electrical properties of each of the materials shown, that the reflection and attenuation properties of the film are correlated strongly to the conductivity of the film. This becomes obvious on closer inspection of equation 2.69 where it is shown that the intrinsic material impedance is dominated by the inverse root of conductivity which is, in typical metals, several orders of magnitude larger than the remaining terms. This result demonstrates that to efficiently transmit electromagnetic power into the magnetoelastic layer of a multiferroic antenna, materials with low conductivity such as amorphous metals or ferrites must be used. The strong attenuation as a function of depth seen in the data for nickel indicates that for highly conductive films negligible amounts of power will be harvested beyond the skin depth of the material. This magnetic field gradient in thick films will correspond to non-uniform mechanical strains and the excitation of shear modes inside the film, making the resonant behavior difficult to control.

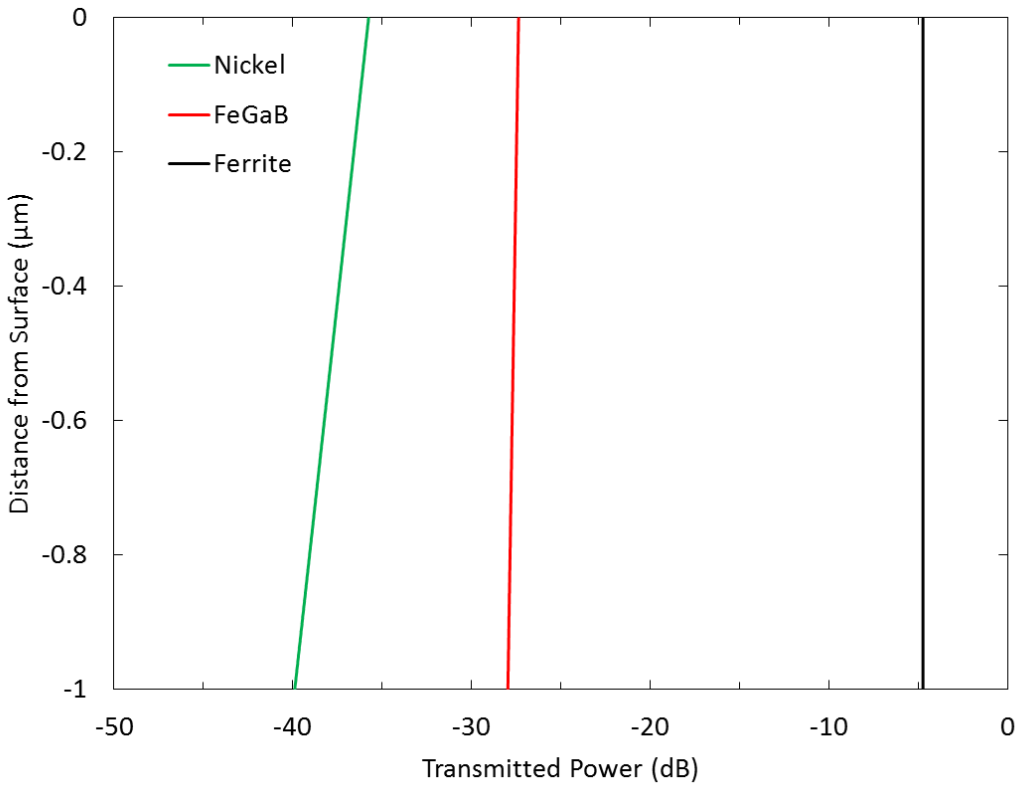

Figure 2.9 – A comparison of the power transmitted into three magnetoelastic films to a depth of 1µm at a frequency of 200 MHz. Output power is normalized to the power applied in the source medium.

It should be noted that many of the multiferroic antennae tested in subsequent experimental sections of this work use non-continuous resonator geometries which will not exactly mirror the results shown here for plane films. The extension of these analytical results to non-planar geometry is involved and better solved for using numerical techniques such as finite elements. Figure 2.10 shows a finite element solution for a 200 MHz electromagnetic TE_{10} wave impinging onto the edge of a nickel 10x10x0.5 µm rectangular prism similar to those discussed in following sections. The color hue and the equipotential lines depict the resulting magnetic field vector norm measured in A/m. It is seen qualitatively from the distribution of fields shown in this figure

that the magnetic field strength is significantly reduced inside of the magnetic element and strong fringing magnetic fields are produced at its edges.

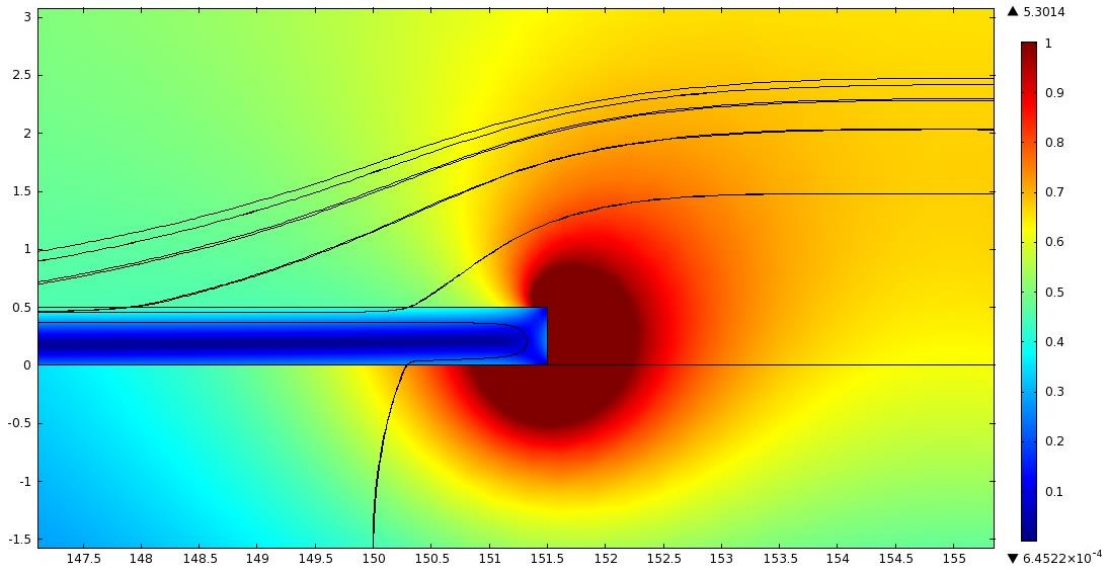

Figure 2.10 – A finite element simulation of a 200 MHz plane wave impinging on a 10x10x0.5μm nickel rectangular prism. Color hue corresponds to magnetic field norm magnitude measured in A/m. Black lines are equipotential magnetic field lines.

This model can be used to examine the effects of reducing the size of the rectangular prism on the reflection coefficients from the nickel/air interface. This test is performed by simulating a 1μm thick nickel square placed at the center a 20x20x100 μm cavity illuminated from the top surface using a TE_{10} wave. The side length of the square shape is swept from 2μm to 20μm and the resulting magnetic and electric fields are computed at the top surface. Using equation 2.31 and normalizing to the intensity computed in air for the same aperture, a transmission coefficient can be extracted as a function of the side length of the nickel square as is shown by the red plot in figure 2.11. When the side of the nickel structure approaches 20 μm, complete occlusion of the cavity occurs and the transmission coefficient becomes approximately the same as that

shown for a continuous nickel film in figure 2.11. As the side length is reduced, the transmission increases by about 12 dB at a side length of 9 μm and reduces again as the side length approaches 2 μm. This reduction in transmission as the size of the element approaches the skin depth, which is 2.2 μm in this case, is due to the large edge fields generated at the sides of the element which are visually depicted in figure 2.10. This analysis does not take into account, however, the reduction in the power transmitted to the nickel element from the scaling of the aperture size. The reduction of aperture size will introduce a loss proportional to the ratio of the source aperture area to the receiving aperture area in the case of an incident plane wave.

$$S = 10\,\mathrm{Log}\left(\frac{L^2}{A^2}\right) \qquad [Eq.\,2.78]$$

The total reduction in transmission gain as a function of element side length is shown as the black line in figure 2.11. It is obvious now that reducing the size of the elements beyond a certain point significantly reduces the available power being transmitted into the system. This effect must be considered when designing the geometry of the resonator array which will be discussed briefly in following sections.

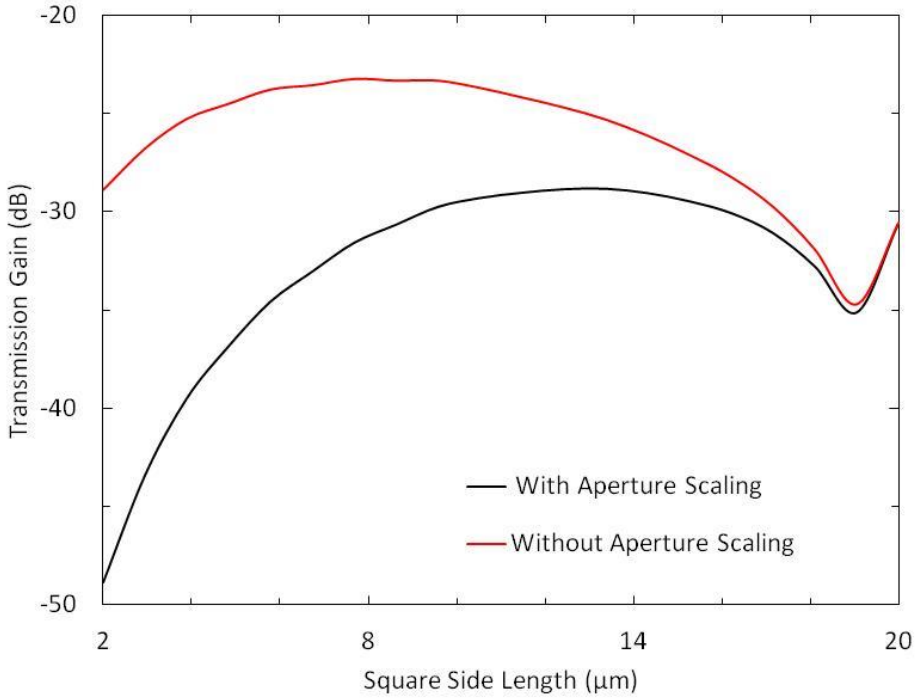

Figure 2.11 – Transmission coefficients for a 1μm thick nickel square illuminated by a TE_{10} wave as a function of square side length. As the side length approaches 20μm the nickel becomes a continuous film.

To express the output of the multiferroic antenna in terms of mechanical power, the linear piezomagnetic coupling equation is found by simplification of the constitutive law 2.44.

$$\varepsilon = qH \qquad [Eq. 2.79]$$

Where ε is the strain in the material, H is the applied magnetic field and q is the piezomagnetic coupling tensor. Comparison of equation 2.79 to the constitutive laws describing linear converse piezoelectricity shows these effects are analogous to one another. To compute the total mechanical work applied to the material, the strain energy is defined for the magnetoelastic as it was for the radiating block system in equation 2.49. By combining equations 2.49 and 2.79 and

assuming the input field H is sinusoidal, the total time averaged power can be computed using the actuation frequency f.

$$P = \frac{\pi}{2} fYV(qH)^2 \qquad [Eq. 2.80]$$

By separating the volume of the film into the area through which the plane wave is impinging and the film thickness, the total intensity as a function of depth into the film can found by writing the magnetic field in terms of its amplitude (the real component of equation 2.77) and solving the definite integral

$$I_{tot} = \frac{\pi}{2} fY(qH_0)^2 \int_0^z ze^{-2\beta z} dz = -\frac{\pi}{8} fY(2\beta z + 1)\left(\frac{qH_0}{\beta}\right)^2 (e^{-2\beta z} - 1) \qquad [Eq. 2.81]$$

Figure 2.12 shows the total intensity as a function of film thickness for three representative magnetoelastic films after being normalized to the power applied in the source medium for a frequency of 200 MHz. Even though the larger conductivity of the FeGaB film introduces increased electromagnetic reflection over that of the non-conductive ferrite film, as is shown in figure 2.9, the large magnetoelastic coupling coefficient of FeGaB makes the harvestable mechanical power output significantly better than either the nickel or ferrite films. Figure 2.12 also shows a strong reduction in the increasing trend in gain past thicknesses much smaller than the skin depth of the material. This indicates that relatively thin magnetoelastic films should produce similar results to that of much thicker films potentially reducing the complexity of device fabrication.

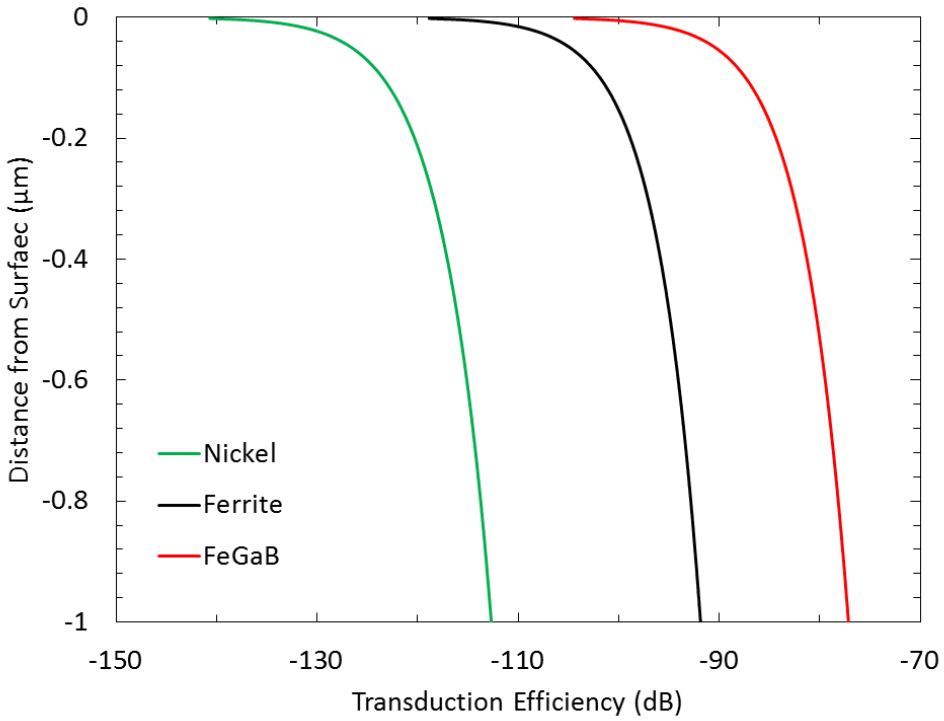

Figure 2.12 – The transduction efficiency computed from the total mechanical power shown as a function of depth for three representative magnetoelastic films. Actuation frequency is 200 MHz.

It will be shown in the measurement section of this work that application of a magnetic bias field to the magnetoelastic material during testing plays a critical role in accurately characterizing the output response of a multiferroic antenna. The previously derived expression for transduction efficiency, equation 2.81, was previously solved using static constants for both the permeability and the isotropic piezomagnetic coupling coefficient for the magnetostrictive layer. To better understand how the output power will vary as a function of bias field, the field dependence for both the relative permeability and the coupling coefficient can be integrated into equation 2.81. First the Langevin function is used to approximate the anyhysteretic magnetization behavior for a representative 500 nm thick nickel film.

$$M(H) = M_s\left(\coth\left(\frac{H}{a}\right) - \frac{a}{H}\right) \qquad [Eq.\,2.82]$$

Where M_s is the saturation magnetization of the film, H is the applied field and a is a fitting parameter. Using a least squares fit to the field averaged characteristic curve, experimentally measured using a MOKE magnetometer system, the fitting coefficient a is extracted as is shown in figure 2.13 for a 500 nm continuous nickel film on a lithium niobate substrate.

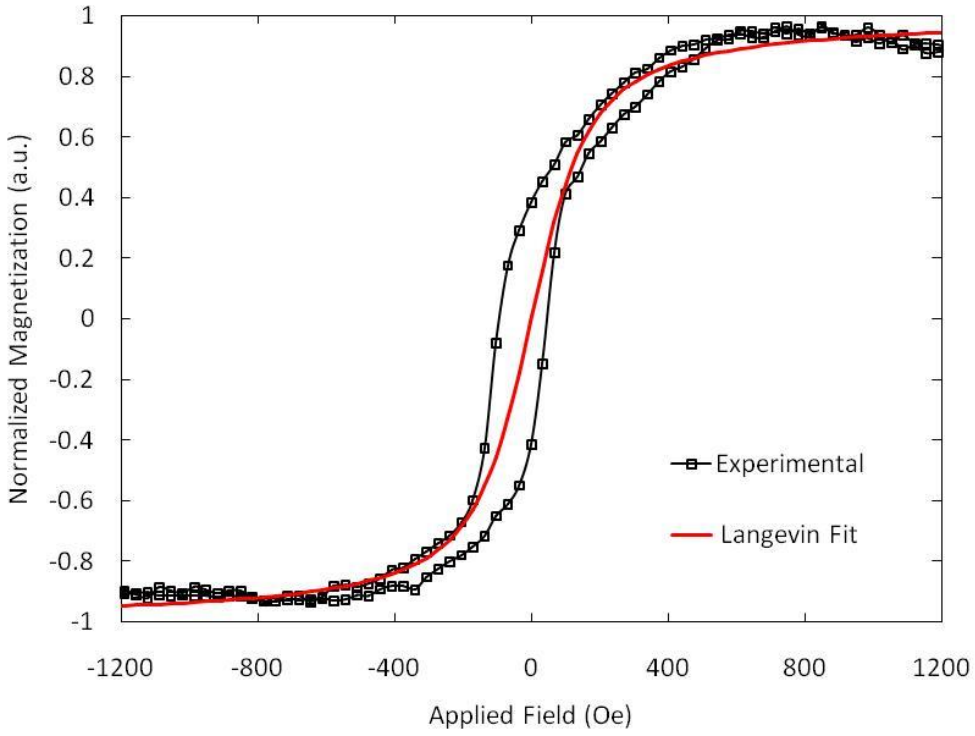

Figure 2.13 – A least squares fit of the Langevin function (red) to experimentally measured MOKE data of a 500 nm thick nickel film on lithium niobate (black).

The anhysteretic susceptibility of the nickel film is then found using the derivative of the resulting Langevin curve.

$$\chi = \frac{dM}{dH} = M_s\left(\frac{1}{a}\sinh\left(\frac{H}{a}\right) + \frac{a}{H^2}\right) \qquad [Eq.\,2.83]$$

The variation of the piezomagnetic coupling coefficient with applied field is found using the quadratic relationship for magnetostrictive strain and the fit Langevin function 2.82 for magnetization.

$$\varepsilon = qH = \frac{3}{2}\lambda_s(\frac{M}{M_s})^2 \qquad [Eq.\,2.84]$$

Where λ_s is the saturation magnetostriction strain for bulk nickel [27]. Figure 2.14 plots both the relative permeability (black) and the piezomagnetic coupling coefficient (red) for the 500 nm nickel film as a function of applied magnetic field.

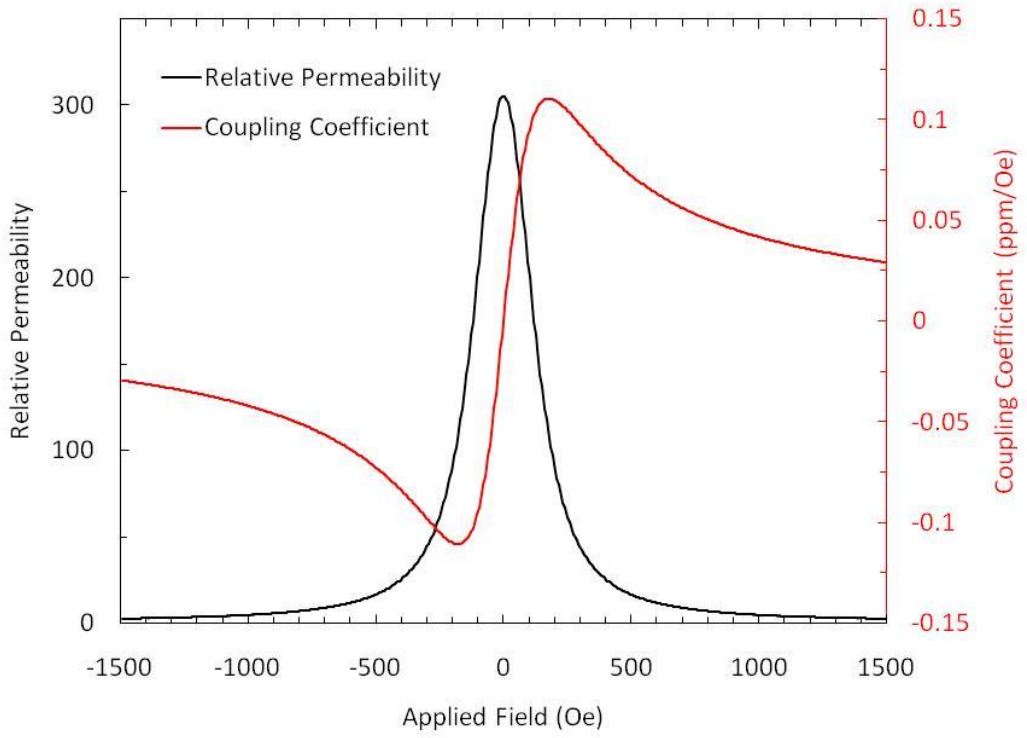

Figure 2.14 – Relative permeability (black) and piezomagnetic coupling coefficient (red) as a function of applied magnetic field for a 500 nm thin film of nickel.

Figure 2.15 depicts total normalized output intensities (black) as a function of magnetic bias field as predicted by equation 2.81 for a 500 nm thick nickel film using the previously derived

magnetic field dependent permeability and piezomagnetic coupling coefficient. To illustrate the effect of the individual field dependent coefficients on the transduction efficiency, the normalized output power is also shown for the case of both constant permeability (red) and constant coupling coefficient of bulk nickel (green).

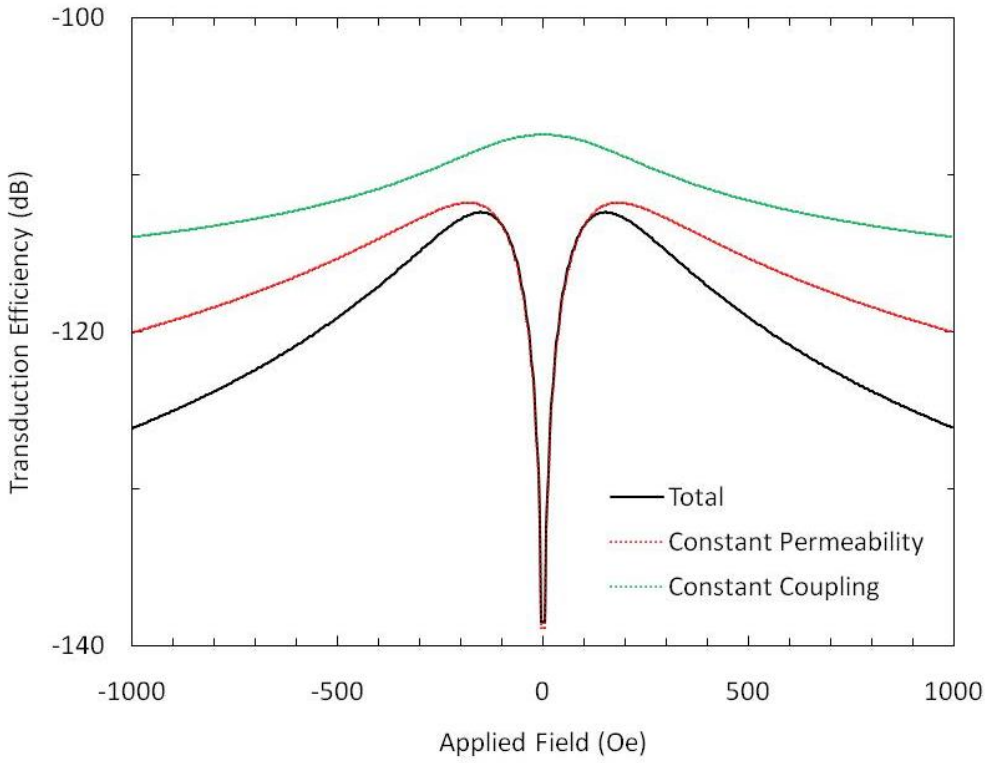

Figure 2.15 – Transduction efficiency (black) for a 500 nm magnetoelastic nickel film excited using a 200 MHz electromagnetic plane wave. Also shown are the effects of constant permeability (red) and constant piezomagnetic coupling coefficient (green) on the output power.

From figure 2.15 it becomes apparent that the output power of a multiferroic antenna is strongly dependent on the magnetic bias field applied during operation. Comparison of the transduction efficiency with the piezomagnetic coefficient, plotted in figure 2.15, shows that the largest increase in output power comes primarily from maximizing the piezomagnetic coupling

coefficient and to a lesser extent the permeability of the material. It is therefore desirable to choose materials which have high resistivity, permeability and magnetoelastic coupling to maximize the achievable power output of a multiferroic antenna. This is a critical result which informs the decisions made in the material selection process of the work presented here. The strong dependence of the output response on bias field not only provides a useful tool for selecting appropriate magnetoelastic materials for the multiferroic antenna but also a method to decouple the actual magnetoelastically produced components of the output signal from measurement system noise as will be shown in the experimental section of this work. Although the output power levels predicted in this analysis are detectable with a carefully designed testing system, even a multiferroic antenna constructed with the most recently discovered optimal materials will likely produce signal levels just above the noise threshold of most radio frequency test equipment when measured in the far field propagation region. For this reason, devices are designed for reception of waves propagating in the near field. As was shown previously the output power expected in this near field region is much higher than from a far field domain. Furthermore the output power is expected to increase significantly with the introduction of a mechanically resonant magnetoelastic layer. With the guidance of the analysis presented in this section, the design of a resonant multiferroic antenna can now be performed with the objective of maximizing the transduction efficiency.

III. Design

Because the proposed mechanism by which the multiferroic antenna operates is primarily that of a mechanically resonant phenomenon, the design of such a device will closely follow that of existing radio frequency acoustic resonators. These devices use the piezoelectric transduction phenomenon to transform electrical energy into resonant mechanical vibration. In performing this transduction, energy can be stored, dissipated or processed in the mechanical energy domain without the need for large valued passive components. Because of the significant decrease in the wavelength when transforming electromagnetic power to mechanical power, resonance can be achieved in the mechanical energy domain using much smaller devices than those operating purely based on electromagnetism. In addition to the reduction in device footprint, these acoustically resonant devices also tend to have high quality factors when low mechanical loss substrates are used making them useful as compact radio frequency oscillators or filters [42-48]. In this work a surface acoustic wave (SAW) type structure is selected for adaptation as a multiferroic antenna.

The basic form of a surface acoustic wave actuator is that of a surface electrode patterned onto a bulk piezoelectric substrate. This electrode is designed such that, when radio frequency energy is applied to it, a periodic electric field distribution is created in the substrate. This periodic electric field couples into the piezoelectric substrate as mechanical energy and an acoustic wave is created. The simplest form of these electrode patterns are long, evenly spaced, parallel, metallic stripes called interdigital electrodes (IDE) or interdigital transducers (IDT), which are designed to generate a plane acoustic wave when excited at the appropriate frequency. This wave, which is typically 1-100 μm in wavelength, is confined to the top surface of the material by the substrate

bulk and the air to substrate interface. This condition causes the free surface to act as a waveguide where the majority of the acoustic wave energy is contained in the first wavelength depth from the substrate surface. This waveguide like confinement allows the surface wave to travel long distances with very little attenuation. This feature has made SAW devices popular where time based control is required for signal processing such as phase shifters or delay lines. These devices are typically many orders of magnitude smaller than those which achieve the same end result through purely electrical means due to the significant reduction in signal wavelength. After travelling some distance, the surface wave can be detected on the substrate using an identical IDT electrode. This simple two port SAW structure is illustrated in figure 2.16.

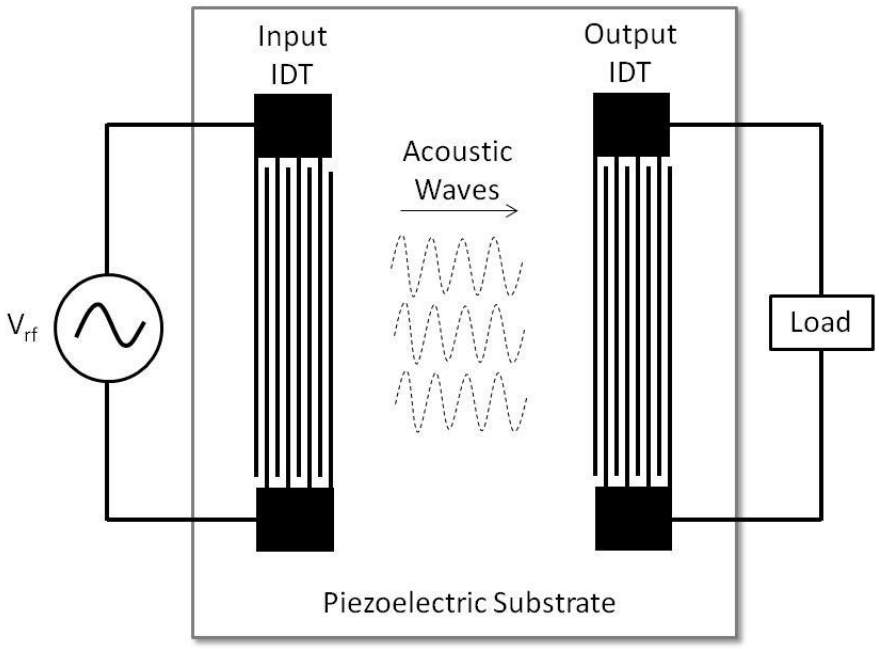

Figure 2.16 - A diagram of the components used to construct a simple two port SAW bandpass filter.

Examining the simplicity of the components of a SAW filter, it becomes obvious that the design of the IDT electrode is the most critical step in defining the filters operating characteristics. The finger pitch, length, width, number, thickness and material are all parameters which will impact the performance of the device to some degree. To understand how these parameters can be optimized for a specific application, finite element simulations of IDT electrodes on piezoelectric materials are constructed in COMSOL multiphysics software. An illustration of the model setup is shown in figure 2.17. This two dimensional model consists of a piezoelectric substrate and two gold IDT electrode patterns. The electrodes are modeled as thin rectangular stripes with a pre-defined in-plane dimension. Connection of the electrodes to the excitation source and the output detection circuit is accomplished through the use of terminals which correspond to nodes in a fully coupled SPICE circuit model. A 50 Ohm voltage source is used to apply excitation voltage to the input IDT and a 50 Ohm termination resistance is used to detect the transmitted power from the output IDT electrode. The alternating polarization of the terminal and ground connections are illustrated in the inset of figure 2.17. To effectively capture the behavior of the electric fields between the electrode patterns, a rectangular domain is defined above the IDT electrodes which is assigned the material properties of air. The bottom interface of the piezoelectric substrate is defined to have a rolling surface condition while the substrate volume is pinned at a corner point. Perfectly matched layer domains are placed at either end of the piezoelectric domain to prevent reflections from the edges of the substrate back into the IDT patterns. These domains are typically defined to be greater than three times the surface acoustic wavelength in order to efficiently suppress these reflected waves. During simulation the steady state solution at each frequency value is computed to assemble the full spectral response of the system.

Results from these two dimensional simulations provides insight into how the input electric fields are distributed in the substrate material and how these fields correlate to acoustic wave propagation at different frequencies. Figure 2.18 shows a frequency domain simulation of 200 nm thickness gold electrodes actuating a 128^0YX cut lithium niobate substrate at 230 MHz. Color corresponds to surface displacement and the black lines represent equipotential electric fields. It is observed from these results that the electric field has both x and y axis components inside the

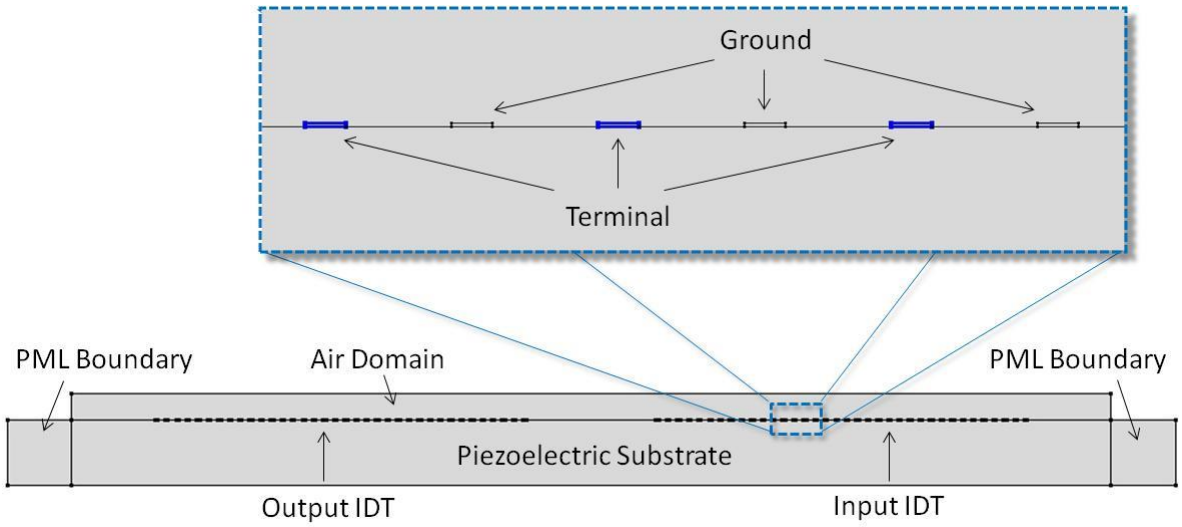

Figure 2.17 – An illustration of the simulation setup used for testing the electrical and mechanical characteristics of a SAW bandpass filter consisting of two IDTs.

substrate material. These field orientations with respect to the substrate crystal axis will create a number of strain components depending on the poling direction of the substrate and the piezoelectric coupling coefficients associated with that state. For the materials used in this work the most substantial coefficients contributing to the generation of surface waves are the d_{33}, d_{31}

and d_{15} coupling terms. These terms will create both longitudinal and shear wave components by which the elliptical surface particle trajectory typical of SAW devices is generated. The combination of these components into a Raleigh type wave yields wave velocities which are neither purely shear or purely compressive but rather have a hybrid SAW wave velocity given a specific substrate and IDT orientation. This combined wave velocity is found experimentally through the use of a simple bandpass filter test which is described in a following section. This value is confirmed with the use of a two port device, simulated using the previously described finite elements construction.

Once the SAW velocity is known, the pitch of the IDT fingers can be defined for a desired operating frequency. The operating frequency and the wavelength of the surface acoustic wave in the substrate can be defined simply by the following

$$\lambda = \frac{V_{SAW}}{f} \qquad [Eq. 2.85]$$

Where V_{saw} is the experimentally measured wave velocity and f is the design center frequency. Because the adjacent IDT fingers will have potentials of opposite signs during operation, a center to center spacing of $\lambda/2$ for adjacent fingers will produce the correct actuation profile for wave propagation.

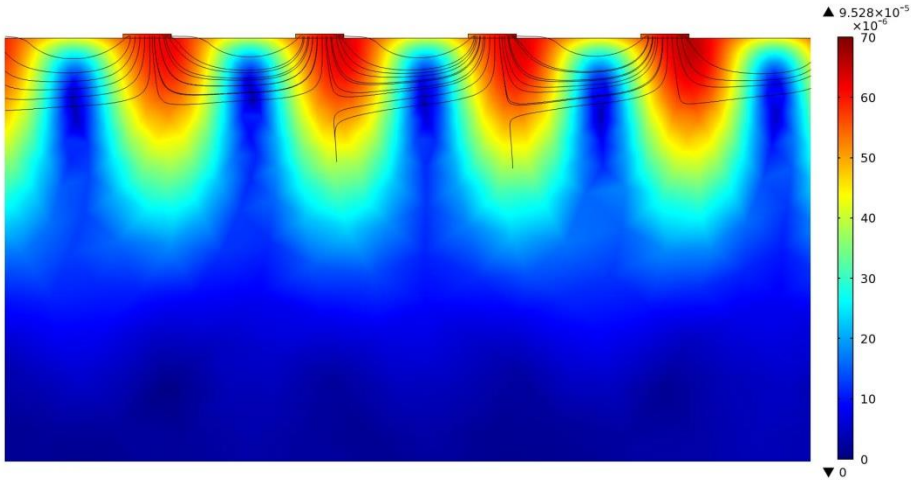

Figure 2.18 – An IDT electrode being actuated on a lithium niobate substrate at 230MHz. Color corresponds to surface displacement in m. Black lines are equipotential electric field lines.

Once the finger pitch for a given operating frequency has been established, the number of fingers must be chosen to reflect the desired operating bandwidth of the IDT. The increase in the number of fingers in the IDT corresponds to a decrease in the bandwidth of the actuator. This is caused by the increase in physical misalignment of the surface wave with the IDT pattern for wavelengths off resonance as the number if IDT finger pairs increases. A lower number of finger pairs can tolerate more of this off resonance wave misalignment while keeping the phase on each finger constant leading to an increase in the bandwidth. This relationship is illustrated in the simulated transmission spectra for a 150 MHz SAW bandpass filter built on a 128^0YX cut lithium niobate substrate as is shown in figure 2.19.a. The finger width is held constant at 5μm and the wave is propagating along the x axis of the substrate in this simulation. It is seen that the bandwidth of the central peak becomes increasingly narrow as the number of fingers in both the input and output IDT pattern is increased from 8 to 32. A marked change also appears in the

transmission magnitude at the IDT center frequency. This is due to the significant change in the IDTs characteristic impedance as the number of fingers is altered. The impedance mismatch between the load and the output IDT will cause energy to be reflected back into the electrode pattern, decreasing the transduction efficiency of the SAW filter. In a similar fashion the transmission spectra can be simulated as the width of each finger is increased. The results from this simulation are shown in figure 2.19.b. It is shown that the width of the IDT fingers has little impact on the overall transmission behavior of the filter. The slight shifts in the IDT center frequency are caused by small changes in the homogenized stiffness and density of the IDT/substrate heterostructure due to the decreased volume of IDT material. The decrease in transmission magnitude in the 1μm case is again due to the relationship between the characteristic impedance of the IDT and its geometry. For the purposes of the SAW antenna a fairly wide bandwidth is desirable to tolerate potential resonant frequency shifts in the magnetic phase of the device. For this reason SAW antenna IDT electrodes are designed with less than 40 finger pairs in order to take advantage of this broadband behavior. The width of the IDT fingers is typically set to one quarter of the SAW wavelength. If the width exceeds the resolution limitations of the lithography process used for fabrication, an acceptable width is chosen which will yield manufacturable devices.

The material used in fabricating the IDT electrode is fixed by the limiting requirements of the measurement system. In this case gold is necessary for its excellent conductivity and ability to produce high quality electrical connections for wire bonding or probed connection techniques. The thickness of the IDT electrode is also specified by measurement requirements to be greater than 150nm in thickness. This relatively thick layer of gold is necessary to ensure wire bonds make sufficient electrical contact with the electrodes and also that the probe pads can withstand

the abrasive forces exerted on them during contacting. For these reasons gold of greater than 150nm thickness is used to fabricate the IDT electrodes for all devices presented in this work.

The last parameter of the IDT geometry to be selected is the length of the fingers. The length of the fingers plays a critical role in determining the impedance of the IDT. Ensuring this impedance is matched to the driving source impedance, in the case of an input IDT or the load impedance in the case of an output IDT, will maximize the power delivered between the SAW device to and from the test system. The relationship between the IDT impedance and finger length becomes complex when also considering the operating frequency, finger width and number of fingers of the electrode. Because of this, the previously established finite elements simulation of a SAW bandpass filter is adapted for finger length parameterization after the other

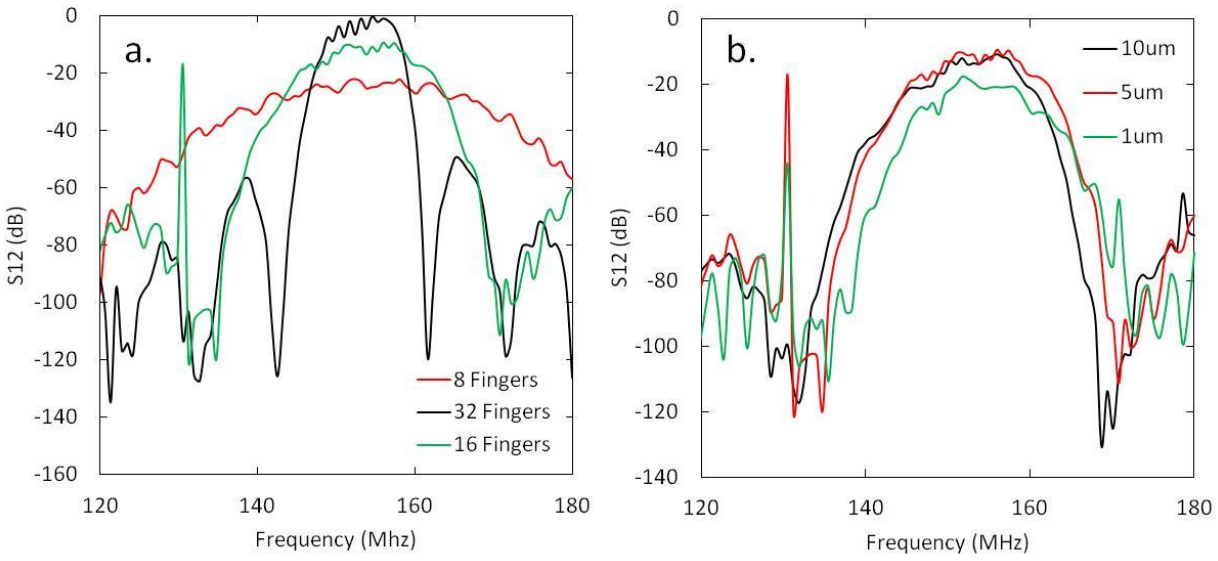

Figure 2.19 – a. The simulated S12 response of a SAW bandpass filter on 128^0YX cut lithium niobate for different numbers of finger pairs in the IDT electrodes. b. The S12 response of the bandpass filter as the width of the finger electrodes is changed.

geometric parameters of the IDT have been selected. To examine this relationship further, the transmission spectra of a bandpass filter is simulated for varying electrode finger lengths. The results for the simulated impedance of a 300 MHz bandpass filter built on 128^0YX cut lithium niobate are shown in figure 2.20 for two extreme cases of finger lengths 13 and 9000 μm. The real impedance, shown in figure 2.20.a, indicates that increasing the length of the IDT finger from 13 to 9000 μm reduces the real impedance by a factor of approximately 300. Similarly the imaginary component of impedance, shown in figure 2.20.b, shows a decrease of about 500 times when the longer fingers are used. This strong dependence of characteristic impedance on the finger length is attributed to the increase in capacitance of the total IDT structure as the effective interaction area between the two oppositely polarized electrodes increases. The decrease in the real impedance indicates that the IDT can source more current due to its increased charge collection area. This effect is akin to placing many voltage sources, having the same potential, in parallel where a proportional decrease in the real source impedance is expect. This also implies that the longer IDT can produce greater power output when the load and source impedances are matched to one another.

To validate the results of these simulations, a bandpass filter matching the dimensions of the simulated devices with 9000 μm finger length is fabricated and tested for frequency response using the techniques describes in later sections. The results of the simulated and experimental impedance are shown in figure 2.21. It is seen that for both the real (a) and imaginary (b) components of impedance that the experimental data follows the same shape as the simulated results but with an impedance offset of about 23 Ohms. In the case the real impedance, shown in figure 2.21.a, this offset originates from the assumptions used for the electrical properties of the IDT material. The finite elements simulation uses a port termination on the outer faces of the

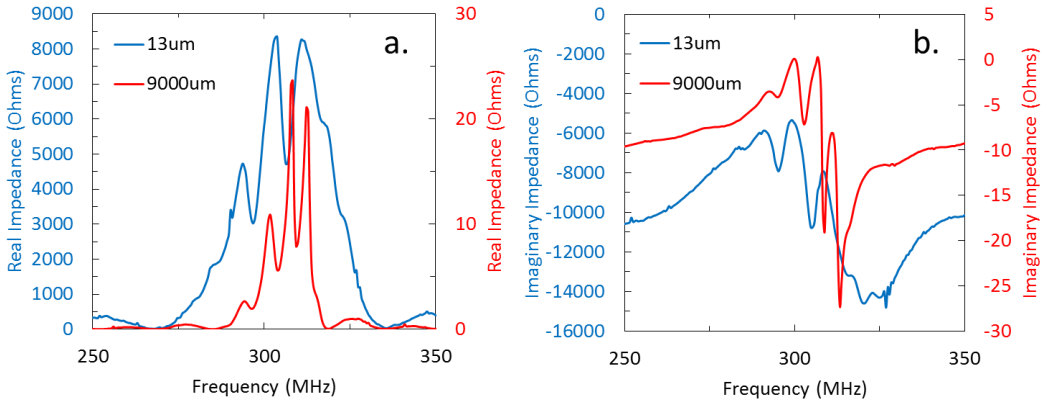

Figure 2.20 – a. The simulated real impedance of a SAW bandpass filter operating at 300 MHz for IDT finger lengths of 13 and 9000 µm. b. The corresponding imaginary impedance for the two test cases.

gold IDT which does not take the real resistivity of the fingers into account. Because the fingers are made very long and are fabricated from thin gold, this finger resistance becomes a significant component of the real impedance as is evidenced by the measured 23 Ohm shift. Similarly the discrepancies observed between the simulated and experimentally measured imaginary impedance originate from the assumptions made while using these types of ports. The simulated ports in this case do not take into consideration the charge motion along the length of the fingers and therefore do not accurately predict the additional inductance of the total device. In the experimental device charge is delivered to the test system through the length of the finger into Ohmic pads patterned at the far ends of the IDT. This charge motion results in energy being stored in the form magnetic field around the finger leading to an increase in the IDT inductance which accounts for the 25 Ohm shift in the imaginary impedance.

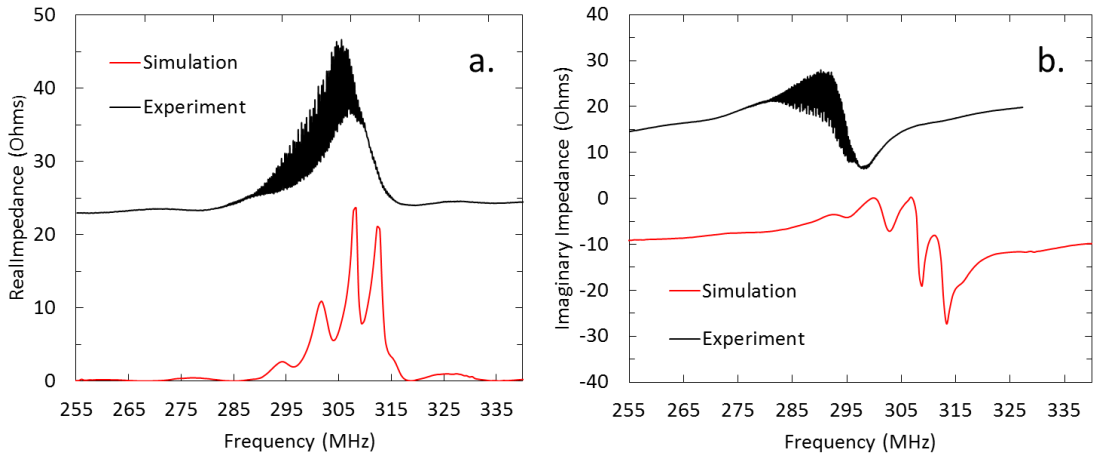

Figure 2.21 – a. The real impedance for a simulated and experimentally measured 300 MHz SAW bandpass filter. b. The corresponding imaginary impedance for the two test cases.

A shift in frequency is also observed in the impedance data shown in figure 2.21. This shift is caused by the slight differences between the properties of the substrate materials used to fabricate test devices and those used for simulation. A periodic rippling behavior is also observed in the experimentally measured impedance data which does not appear in simulated results. This comb filtering characteristic of SAW devices is introduced by phase interference of both time shifted electromagnetic and reflected acoustic waves with the original acoustic wave. These signal components and methods to reduce their impact in measured data are discussed in depth in the measurement section of this work.

Adaptation of the simple SAW based bandpass filter, illustrated in figure 2.16, to function as an antenna involves the replacement of the input IDT, which was previously used to generate the surface wave, with an array of magnetoelastic resonators. An illustration of this adaptation is shown in figure 2.22. The magnetoelastic resonators are designed to create a coherent plane

acoustic wave, in the same manner as the now removed input IDT, when excited by a plane electromagnetic wave whose wave vector is perpendicular to the surface of the piezoelectric substrate. This transformation of energy is accomplished through the coupled magnetic and elastic material parameters inside the magnetoelastic resonators. This wave then travels across the substrate surface where its energy can be harvested by an output IDT which has been optimized for this application using the previously established design methods.

It is immediately apparent that the careful design of these magnetoelastic resonators is necessary for the success of this type of antenna transducer. The array must produce coherent waves with a magnitude sufficient to be detected by the IDT and connected load circuit. Furthermore the complex interactions between the impinging electromagnetic wave and the magnetoelastic resonator must be taken into consideration to capture the behavior of a practical device which

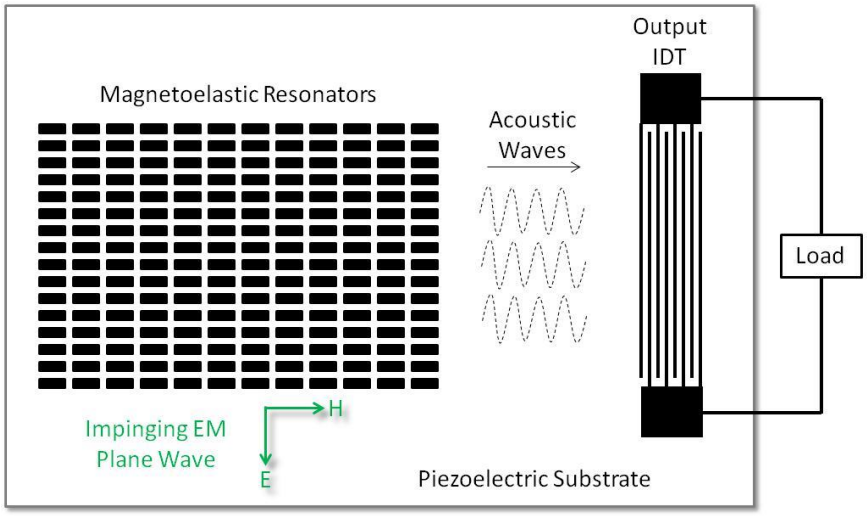

Figure 2.22 – An illustration of a SAW device which has been modified to function as a multiferroic receiver antenna.

would be manufactured for experimentation. For these reasons a multiphysics model is developed to simulate the complete operating characteristics of such a multiferroic SAW based

antenna system. This simulation, built in COMSOL multiphysics software, simulates a magnetoelastic resonator, which has been mechanically attached to the surface of a piezoelectric substrate, as it is illuminated by a plane electromagnetic wave. The simulation uses a linear piezomagnetic coupling relation and the known material properties of the magnetoelastic material to compute the resulting strain developed in the resonator under the given excitation conditions. The strain generated inside the resonator element is mechanically coupled to the substrate at their mutual interface. The strain state in the substrate produced by an infinitely large array of resonators is simulated by applying symmetry boundary conditions to a single unit cell of the resonator system. This quarter symmetry unit cell consists of a magnetoelastic resonator, a piezoelectric substrate and an air domain which acts as the electromagnetic source medium. The unit cell geometry used for simulation of a nickel and lithium niobate based SAW antenna is shown in the left image of figure 2.23. The propagation of the acoustic wave generated by the resonator array is simulated by manually assigning the displacement and voltage profile computed at one face of the simulated unit cell to a boundary on a separate extensional model which contains an IDT electrode. This section of the simulation, the geometry of which is shown in the right image of figure 2.23, contains the source interface, an IDT electrode on the piezoelectric substrate and a PML boundary to prevent acoustic reflections from the boundary behind the IDT electrode. The IDT fingers are assigned to fully coupled SPICE nodes which contain a load circuit through which the output power of the device can be measured and normalized to the input power in the source medium contained in the first section of the model.

The combined simulated allows for the computation of a transmission parameter of the complete transduction process of the receiver antenna. Using this transmission parameter as an objective function, optimization can be performed to maximize the efficiency the antenna by varying the

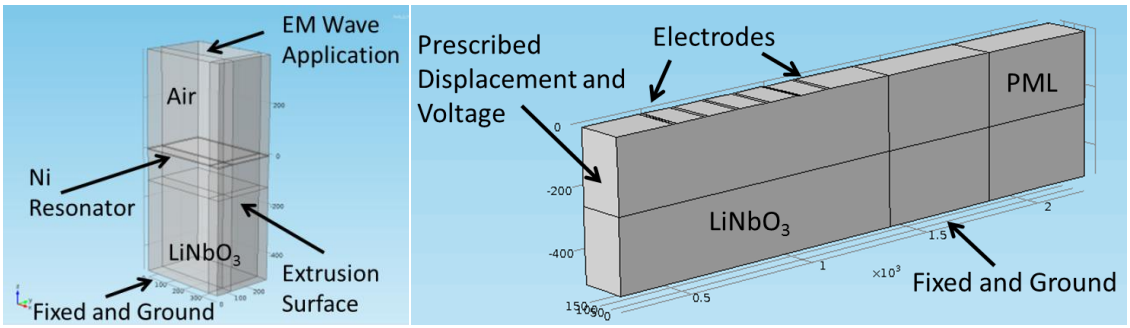

Figure 2.23 – A unit cell of the quarter symmetry geometry used in simulating the interaction of a magnetoelastic resonator and an electromagnetic wave (left). The second section of the simulation which models how the acoustic wave interacts with the IDT output electrodes (right).

characteristics of the resonator. Geometric parameterization is done using the resonator thickness and x and y dimensions and array spacing. A particle swarm optimization is performed using these variables to generate the ideal resonator geometry for a specified frequency. Following generation of the resonator and IDT geometry the full spectral response of the antenna can be assembled in the frequency domain. An effective transmission efficiency is shown for an optimized nickel and lithium niobate based antenna operating at 150 MHz in figure 2.24. The inset image shows a 3D view of the extensional portion of the simulation. This inset image displays an exaggerated displacement profile at the substrate surface from which the clear periodic wave like behavior generated by the resonators can be visualized. A sharp mechanical resonance attributed to the magnetoelastic elements is observed at the design center frequency in the transmission data. Surrounding this resonant peak a central SAW type node is excited in the substrate at very low energy levels (-80 dB) indicating the finite quality factor of the resonator is generating small amplitude broadband waves which cause the spectral behavior of the IDT to appear. The magnitude of the central resonant peak is -16 dB which is sufficient for commercial communications devices. It is noted that this is value is several orders of magnitude larger than

the analytical prediction presented in previous sections of this chapter for a magnetoelastic antenna operating in the near field. This discrepancy is due to the enhancement of the response through the resonance behavior of the element which is accounted for in the full finite elements simulation but not the previously derived estimates. In a realistic system the mechanical and electrical damping of the actual materials will act to further lower the quality factor and resonant magnitude of the output response although it is expected to remain within an acceptable range. The full details of the model setup and the optimization algorithm are presented by K. Wetzlar [49]. Once the ideal materials and geometries for the complete resonator and IDT antenna system have been designed, a manufacturing process is developed for the fabrication of test devices which will provide the experimental results to validate the predictions of these design simulations.

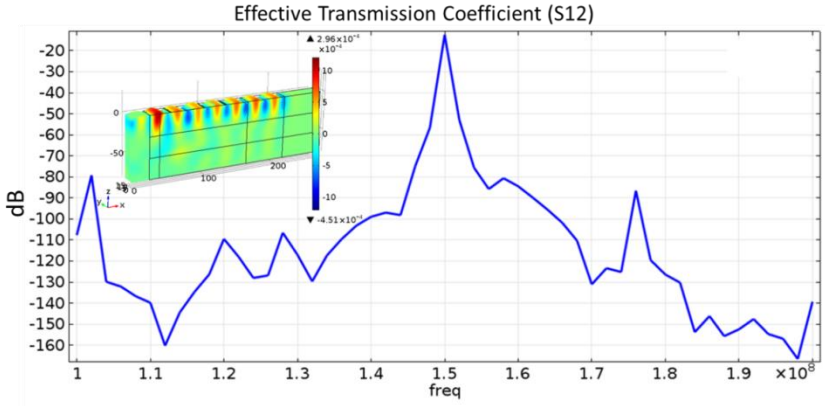

Figure 2.24 – A representative output response of a multifrroic surface acoustic wave antenna built using a nickel lithium niobate material system operating at 150 MHz.

An additional filter type, using bulk mode excitation, is also briefly explored for its potential application as a multiferroic antenna at low frequencies. Presently work is being performed to extend the operation of these bulk acoustic wave (BAW) devices to higher frequencies where

ferromagnetic resonance can be achieved in the magnetoelastic phase of the system [50]. In its simplest form, the bulk acoustic wave resonator is a plate of piezoelectric material with two electrodes on opposite, parallel faces. During operation, an RF electrical signal is placed across the electrodes creating a corresponding dynamic electric field inside the substrate material. Because the plate is piezoelectric, this electric field produces a proportional strain in the substrate material for small amplitude signals. Taking the boundary conditions of the plate into account, this induced strain produces modal resonant behavior whose frequency is dependent on the geometry of the plate and the type of strains being developed. A thickness compression mode BAW resonator, built on 0.5 mm thickness <001> cut PMN-PT, is shown in the right image of figure 2.25. The left plot in figure 2.25 shows the S11 reflection response of the PMN-PT based BAW resonator from DC to 40 MHz before and after poling of the PMN-PT plate. The fundamental BAW mode is seen at the expected 4 MHz point along with three upper harmonic modes. Experiments have been performed to adapt this structure to function as a multiferroic radiator by bonding a thin ferrite plate to the top surface of the BAW. By using the resonance of the PMN-PT plate to couple mechanical vibration into the ferrite plate, the magnetic moments inside the ferrite material can be manipulated through the inherent magnetoelastic coupling. A 2x2x0.5 mm ferrite (Epcos N87) plate is diced from the E section of a commercially purchased EI core using a diamond wafer saw. This plate is then bonded using epoxy (Allied Epoxy Bond 110) to the top of the PMN-PT BAW structure. Transmission testing is performed, using a non-resonant loop antenna, in the measurement system described in the experimental section of this work. No detectable magnetoelastic radiation is measured from the ferrite plate over any of its harmonic modes. This lack of measured radiation is attributed to the low magnetoelastic coupling of the ferrite material and the large dispersive behavior of the materials permeability.

For this reason a BAW based multiferroic antenna is best suited for operation at much higher frequencies where a magnetic resonance condition can be achieved in the magnetoelastic layer. This resonance condition corresponds to a large increase in the permeability of the material which results in an increased radiation efficiency. To achieve high frequency (several gigahertz) actuation of the piezoelectric phase of the BAW structure, thin actuation layers of several hundreds of nanometers must be used. These thin released films can be difficult to achieve without the use of involved processing techniques which are outside the scope of the work performed here. A more detailed investigation of these high frequency BAW antennae structures is presented by S. Tiwari [50]. Actuation of thin surface deposited magnetoelastic resonators is better performed using a SAW approach where resonant mechanical energy can be efficiently delivered over a large area of a substrate. This mechanical resonance condition is achieved using the in-plane geometry as opposed to the out-of-plane geometry used for BAW devices. This eliminates the need for the complex processing required to fabricate thin piezoelectric films and instead leverages the use of well-established lithographic techniques over bulk piezoelectric substrates.

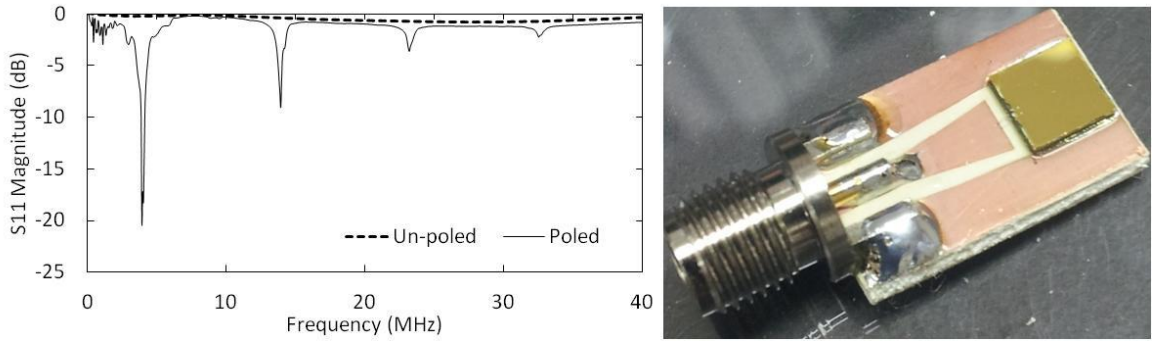

Figure 2.25 – An <001> plate of PMN-PT on a test carrier for use as a thickness mode BAW resonator (right). The plot shown to the left is the S11 reflection from the BAW resonator from DC to 40 MHz shown both before (dotted) and after (solid) poling of the PMN-PT plate.

IV. Materials

Some of the key materials parameters for the magnetoelastic phase of a multiferroic antenna have been discussed in the previous section wherein the radiation efficiency for several representative magnetoelastic materials under different operating conditions was derived. It was shown that materials with large piezomagnetic coupling and permeability and low conductivity will maximize the radiation efficiency of a multiferroic antenna. Table 2.1 assembles these material parameters for a selection of commonly used magnetoelastic materials for comparison.

Material	Coupling Coefficient (ppm/Oe)	Relative DC Permeability	Conductivity (S/m)
Ni	-0.17	300	1.43×10^{7}
FeGaB	7	2000	6.67×10^{5}
Metglas 2605	5.6	1300	8.47×10^{5}
FeGa	3.0	100-300	1.16×10^{6}
TbDyFe	0.3-0.8	4.1	1.67×10^{6}
CFO	-0.19	4.5	3.86×10^{-7}

Table 2.1 – Comparison of the material metrics important in maximizing the response of the multiferroic antenna. [3][41][51-65]

The relatively large conductivities of the materials shown in table 2.1, with the exception of CFO, will produce high electromagnetic reflection coefficients in an antenna application as was shown previously. Magnetic materials typically used in microwave applications are specially tuned ferrite compositions whose low conductivities serve to significantly reduce reflections and ohmic losses. The availability of highly magnetoelastic oxides which also have desirable magnetic and electrical properties is low as is evidenced by the low permeability and coupling coefficient of CFO. To further explore the possibility of using other ferrite compounds as the

magetoelastic layer of a multiferroic antenna, commercially available high frequency NiZn ferrite transformer cores are tested for magnetostriction and coupling coefficient.

In this experiment, commercially purchased EE transformer cores (Epcos NiZn N87) are diced into 20x10x4 mm blocks and a strain gauge is applied to the top surface. The ferrite block is glued to a teflon rod with a thick layer of compliant epoxy (E6000) which is then mounted between the poles of an electromagnet (Varian). A compliant epoxy is used to prevent clamping at the bottom surface of the ferrite while testing. The strain gauge is aligned such that the strain measurement direction aligns with the field produced by the electromagnet. The rod and block assembly is secured between the magnet poles using foam pads to prevent movement of the block during testing. Figure 2.26.a shows the ferrite block mounted to the teflon rod for testing. Measurement wires are soldered to the strain gauge pads and connected to an analog strain gauge amplifier (Vishay MM) whose output is read using a USB connected data acquisition system (National Instruments 6009). The electromagnet current is swept using a GPIB controlled Agilent system power supply model 6680A and the magnetic field strength is monitored at each current value using an FW Bell gauss meter (6010).

Figure 2.26.b shows the resulting magnetostriction curve for the ferrite block. Because the block is initialized to a remnant state opposite to the field direction applied during data collection, the material does not exhibit the expected magnetostriction behavior until a coercive field of about 190 Oe is applied. From this coercive point to the saturation field, the ferrite shows a saturation magnetostriction value of 3ppm. The instantaneous slope at a bias field of 230 Oe is computed as 0.056 ppm/Oe. Despite the excellent magnetic and electrical properties of this ferrite compound, comparison of the experimentally measured coupling coefficient to those listed in table 2.1 show that these high frequency ferrites have very poor magnetoelastic coupling. Furthermore, the

previously derived transduction efficiencies using these measured parameters demonstrate that these ferrites are not suitable for use in a multiferroic antenna.

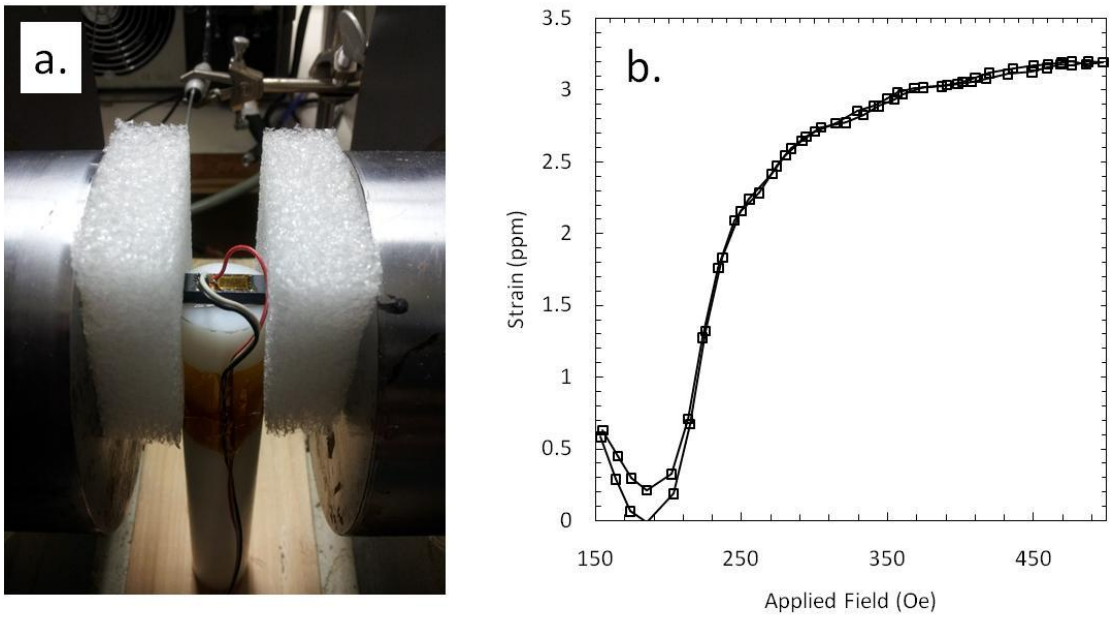

Figure 2.26 – a. A ferrite block mounted to teflon sample holder between the poles of an electromagnet during magnetostriction testing. b. The resulting magnetostriction curve for the ferrite block.

Confirming this lack of commonly available highly magnetoelastic microwave ferrite materials, the most desirable candidates remain the amorphous iron alloys shown in table 2.1. These amorphous magnetic compounds exhibit large dc permeabilities and relatively low conductivities due to their lack of crystallinity. The specific compounds of interest (Metglas and FeGaB) also possess large magnetoelastic coupling coefficients making them an attractive option for use in multiferroic transducers. In this work, nickel and FeGaB films are studied for use in surface acoustic wave based multiferroic antennae.

Nickel is chosen for the majority of the devices studied in this work because of its widespread use and well characterized deposition properties in standard micro-manufacturing processes. Thin film deposition and patterning of elemental metals, such as nickel, is typically a more robust process when compared to complex alloys. This is in large part due to the differences in partial vapor pressures of the individual elements when depositing complex materials. Often times these alloys require co-deposition, layering and post annealing or finely tuned processing parameters to achieve the correct composition in the sample film. Additionally, when compared to other commonly available elemental magnetoelastic materials such as cobalt or iron, nickel presents with relatively large piezomagnetic coupling and magnetic permeability. The magnetic and structural properties of nickel deposited by PVD are studied to evaluate its potential function in the multiferroic antenna. The structural properties of nickel are studied using scanning electron microscopy. This technique allows for the visualization of the surface of both continuous and patterned films. Ideally the films will present with low surface roughness and fine polycrystalline domains throughout the film thickness. Figure 2.27.a shows an SEM micrograph of a corner of patterned nickel film which has been sputter deposited to 480nm film thickness. It is seen that the film consists of fine granular domains which are smaller than 20nm in diameter. This morphology is consistent throughout the thickness of the film and similar regardless of the PVD technique used. Large crystalline regions are undesirable in this magnetic layer as they can increase resistance to domain wall motion which increases the energy required to magnetically actuate the film. The additional roughness which would be presented by these large grains can also introduce loss into the mechanical behavior of the system leading to a decrease in resonator quality factor. The magnetic and magnetomechanical properties of nickel are studied using a laser MOKE magnetometer system. This type of measurement allows for the

observation of the magnetization versus applied field behavior of various types of magnetic samples. A four point bending fixture can also be used to apply uniform strains to the film while measurements are taken. This allows for the correlation of the known applied elastic strain to the observed shift of magnetic anisotropy energy in the film. An example of a strained and unstrained MH response of a representative nickel film on a silicon substrate is shown in figure 2.27.b. A marked shift in the coercive and anisotropy field with the application of strain is evident in the measured data. By numerically solving for the energy difference between curves at different strain values, a rough estimate for the saturation magnetostrictive strain can be calculated. For the case shown in figure 2.27.b the calculated value is 30 ppm which agrees closely with the reported bulk values for nickel [51].

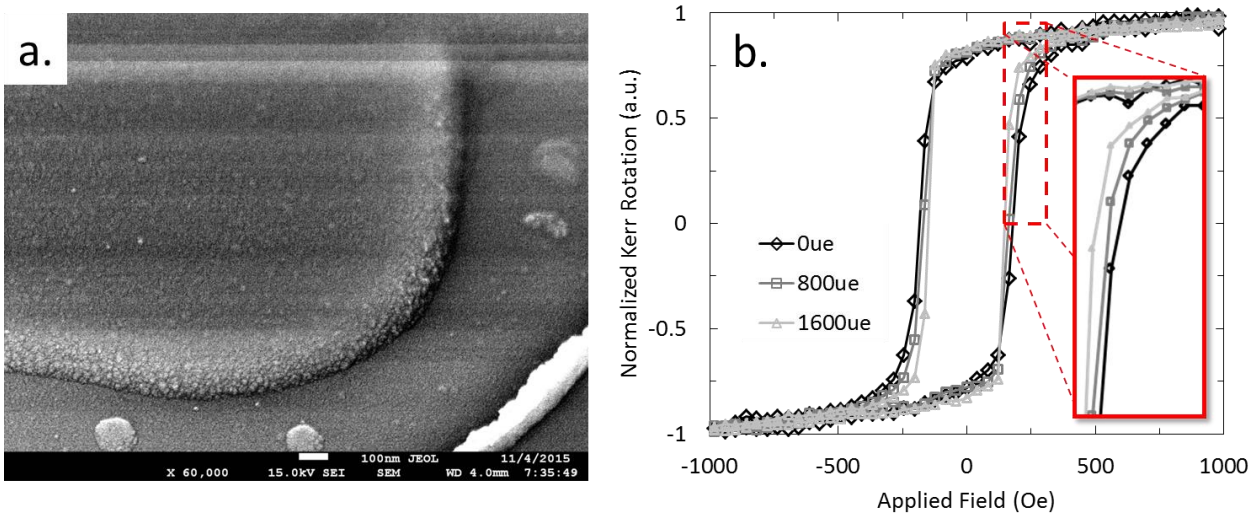

Figure 2.27 – a. An SEM image of the corner of a sputtered nickel film of 480 nm thickness. b. The MH response of a nickel film on a silicon substrate as measured in a MOKE bending system for three compressive strain values.

Iron gallium boron films are also studied in this work for use as the magnetoelastic layer in the SAW based multiferroic antenna. This amorphous soft magnetic alloy presents with extremely large magnetoelastic coupling for boron concentrations below 12%, as is shown in table 2.1. A thorough discussion of the magnetic and compositional properties of this alloy is presented by Lou et. al. [41]. Films of FeGaB are deposited using a single target sputtering system and characterized as before for their morphology and magnetic characteristics. An SEM surface image of a 330 nm FeGaB film on a lithium niobate substrate is shown in figure 2.28.a. A nanocrystalline grain structure is observed with grain diameters below 20 nm. These grain dimensions are confirmed with atomic force microscopy measurements. These grains represent tall columnar structures extending through the entire thickness of the film which are visually observed through SEM cross section analysis of the film. The grain structure of the film is fine enough that crystal planes are not observable in x-ray powder diffraction analysis of the films. Bending tests are performed on FeGaB films in a MOKE magnetometer system, the results of which are shown in figure 2.28.b, with no observed shift in the magnetic properties with applied strain. This lack of observed magnetic change with strain is due to the lack of sufficient resolution in the MOKE system to small magnetic perturbations. The shifts expected for FeGaB films are less than 14% of those observed in figure 2.27.b for nickel. This decrease in the strain modulated magnetization is due to the significantly lower elastic modulus and higher saturation magnetization of the FeGaB films. For this reason the magnetoelastic properties of the films are found by referring to the work performed by Lou et al. [63]. It is also implied from the MH behavior shown in figure 2.28.b that the films are very soft magnetically when compared to the previously studied nickel films. This is evidenced by a coercive field value of roughly 5 Oe for these samples. This soft magnetic behavior is also confirmed using SQUID magnetometry.

Because the FeGaB films present with very soft magnetic behavior, the film is susceptible to stray magnetic fields which are applied to the film during deposition. This applied field can

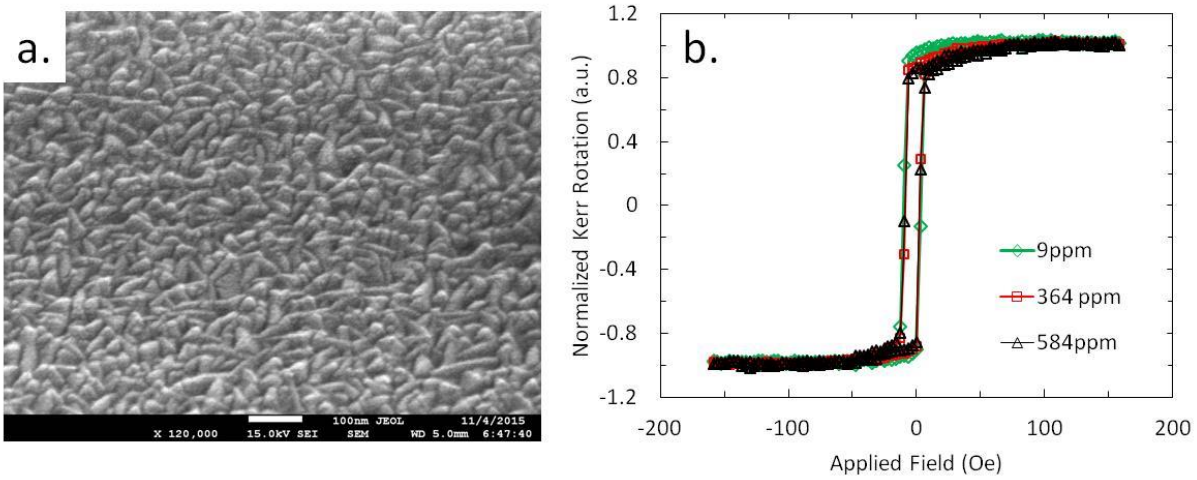

Figure 2.28 – a. An SEM image of the surface of a 330 nm thick FeGaB film deposited on a lithium niobate substrate by sputtering. b. MH loops of the FeGaB film at various applied bending strains measured using MOKE magnetometry.

introduce a preferential in-plane orientation for the magnetization in the film through magnetic manipulation of the epitaxial growth behavior. This presents in the film as an easy magnetic axis in the film plane. For other types of magnetic materials such as nickel, the degree to which this induced internal anisotropy will impact the resulting films magnetic behavior is small when compared to the summation of other isotropic energies contributing to the overall magnetic behavior of the material. This anisotropy is characterized for the entire film volume using a broadband measurement of the films ferromagnetic resonance over a variety of applied magnetic fields. This measurement is accomplished by placing the FeGaB sample over a shorted coplanar

waveguide transmission line and measuring the reflected energy from the stripline as a function of frequency and applied magnetic bias field. When the magnetic resonance condition is achieved in the film by applying the correct bias field and excitation frequency, a change in the amount of electrical energy delivered to the line is observable. This is visually shown as the blue absorption dip in the color map plot shown in figure 2.29.a. The color represents the normalized return loss of the CPW in decibels. The expected resonant frequency characteristic curve, shown as the overlaid black dashed line in figure 2.29.a, is computed using the Kittel relation describing dynamic magnetization precession in thin ferromagnetic films. It is seen in figure 2.29.a that the analytical prediction and the measured data for the resonant frequency of this film are in close agreement with a small offset in the applied magnetic field direction. This offset represents the internal magnetic anisotropy in the FeGaB film which can be determined as a function of sample rotation angle using the same FMR measurement technique. The sample is affixed to a rotating stage which can be precisely rotated in increments of 10 degrees. The FMR spectra, such as the one shown in figure 2.29.a, are collected at every 10 degree increment for a full 180^0 of sample rotation. For each dataset corresponding to a single angle, a Lorentzian line shape is fit to every frequency/reflection pair at each applied field. The fit is performed using a least squares algorithm from which the center frequency of the peak is extracted from the dataset as a function of applied field. This relationship is fit to the Kittel equation [66] for magnetic precession in thin ferromagnetic films using the saturation magnetization value measured for the same film by SQUID magnetometery. This fitting procedure is also performed using a least squares method and the anisotropy field is extracted from the dataset for each angle of sample rotation. A polar plot of the effective anisotropy field versus rotation angle for a 500 nm FeGaB film deposited on silicon is shown in figure 2.29.b. A strong uniaxial anisotropy is observed in the film with a

maximum magnitude of about 25 Oe. The presence of this anisotropy field is confirmed with SQUID magnetometry. The appearance of this internal anisotropy indicates that a magnetic stray field is present in the deposition chamber while the film is being deposited. This field most likely comes from the very strong magnet which is placed behind the target electrode to increase the plasma density at the target surface. Even though the target material is highly permeable, weak magnetic flux can extend outwards from the target onto the sample. It is expected that the presence of this internal field will impact the quality factor of the complete resonator array given the previously derived dependence of the resonators output response on the effective applied field. This effect will become more prominent if the array extends over a large area of the wafer which experiences non-uniform field stray fields giving rise to many different localized anisotropies across a single array. For this reason the resonator array is limited to a 1 cm^2 area.

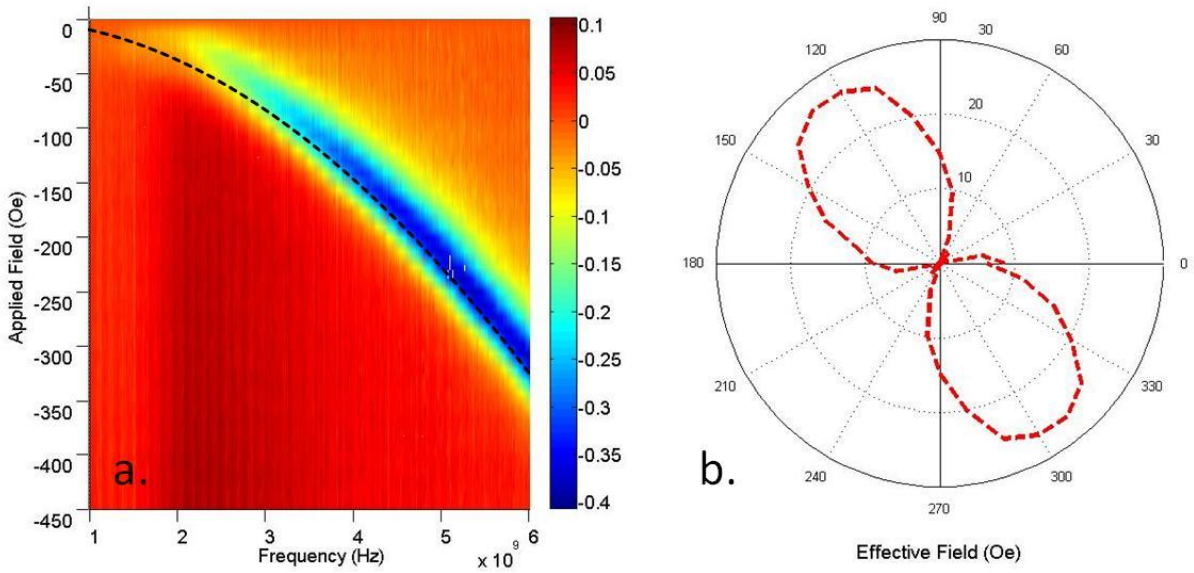

Figure 2.29 – a. The S11 reflection coefficient of a CPW transmission line loaded with a FeGaB film as a function of bias field and frequency. b. The effective anisotropy field computed from experimental FMR data for the FeGaB film

The second critical material phase of the multiferroic antenna device is the piezoelectric substrate. The surface acoustic wave operation mechanism of the piezoelectric substrate was described in the previous section emphasizing the importance of the piezoelectric coupling matrix in the creation of these types of waves. The mechanical energy generated by the magnetoelastic material is coupled into the piezoelectric substrate at their mutual interface. It is the piezoelectric substrate which then carries this mechanical energy to the output electrode structure in the form of an electroacoustic wave. Selection of a piezoelectric substrate which will maximize the output signal involves predicting the dynamic mechanical behavior of this electroacoustic wave. In this work a Raleigh type acoustic wave is studied for its ability to communicate energy over long distances with relatively low insertion loss. These types of devices have been studied in literature for many years and find application in radio frequency filters and MEMS sensors [42-48]. Much work has been done characterizing the Raleigh wave propagation characteristics of many types of piezoelectric substrates [45][48][67]. A comparison of several common piezoelectric substrates used for SAW applications and their associated wave speed is shown in figure 2.30.

Despite the low insertion loss characteristics for the materials listed in figure 2.30, the piezoelectric coupling coefficients for these materials are quite low typically ranging from 1-10 pC/N for the transverse shear d_{15} coefficient [68]. This results in acoustic waves which travel with low mechanical and electrical damping but also low strain amplitudes. The recent availability of certain piezoceramic single crystals with very large coupling factors has introduced the possibility of devices which can produce large amplitude acoustic waves at radio frequencies. A material with these large coupling properties could provide the strain magnitudes needed to drive magnetic moment reorientation in multiferroic transmitting antennae. One such

Wave type	Material and cut	Velocity (m/s)
Rayleigh	Quartz-ST	3158
SAW	YZ-$LiNbO_3$	3488
	YX-128° $LiNbO_3$	3992
Leaky	LST-Quartz	3948
SAW	64°YX $LiNbO_3$	4478
	36°YX $LiTaO_3$	4112
Surface	Y-cut ST quartz	4990
transverse	36°YX $LiTaO_3$	4211
wave (STW)	35.5°(AT)Y-cut Quartz	5100

Figure 2.30 – A chart comparing several common SAW substrates and their associated wave types and velocities.[69]

substrate material studied in this work, which does not find common use in SAW applications, is single crystal lead manganese niobate lead titanate (PMN-PT) cut in the <111> crystal orientation. Several studies have examined the SAW propagation characteristics of the <001> and <011> cut of PMN-PT with limited results [70-71]. Although wave propagation is shown to be possible on these materials, the electrical and mechanical loss characteristics of these substrates are quite high and the transmission gain is therefore low. Nevertheless, the strain magnitudes expected from SAW devices built on PMN-PT is much larger than that of lithium niobate providing a possible path to better detection of the small vibration energy produced by the magnetoelastic resonators. This increase in strain comes from the extremely large d_{15} shear coefficients found in <111> oriented PMN-PT crystals (>2000 pC/N [72] compared to ~7 pC/N

for $LiNbO_3$ [73]). This crystal orientation also presents with relatively low longitudinal actuation coefficients when compared to the other commonly used PMN-PT orientations which are speculated to create bulk waves modes. These bulk waves travel through the substrate thickness rather than on its surface leading to lossy and highly uncontrollable wave propagation characteristics. The potential suppression of these coefficients through selection of the appropriately rotated crystal will allow energy to efficiently transfer into shear surface waves rather than the bulk longitudinal modes.

To study the SAW propagation characteristics of the <111> oriented PMN-PT crystal, an experiment is designed to allow for the measurement of the transmission spectra through this material using IDT electrode pairs to create and detect surface acoustic energy. IDT patterns which are incrementally rotated every 10 degrees for a total range of 0 to 90 degrees allows for the characterization of wave propagation as the wave vector is rotated away from the in-plane <011> axis. The in-plane crystalline directions are measured using x-ray diffraction analysis of the sample edges which serve to align the IDTs to the proper crystal axis. These IDTs are contacted using GSG style microwave probes to coplanar contact pads patterned into each IDT. To begin fabrication a 10x10 mm plate of <111> oriented PMN-PT is prepared by depositing a 150nm gold film on the top surface of the substrate. A thin 10nm layer of titanium metal is deposited prior to the gold film which acts as an adhesive layer between the gold electrodes and the substrate surface. These films are both deposited under high vacuum using electron beam evaporation (CHA Solution). Following the deposition of this gold electrode layer, a 50nm thick titanium layer is deposited onto the backside of the plate using evaporation. This continuous titanium film serves as the counter electrode for poling of the ferroelectric crystal. Using contact lithography, an IDT pattern is printed into positive tone AZ5214E photoresist over the gold film.

The mask is aligned to the <011> in plane edge of the plate using alignment markers contained in the photomask. Once the lithography step is complete, the PMN-PT plate is poled through its thickness using a 0.8 MV/m electric field applied across the top gold and bottom titanium electrodes taking care that the topside electrical contacts do not damage the photoresist patterns. The sample is then immersed in a 1:4 dilute mixture of deionzed water and commercial potassium iodide based gold etchant (TFA) for 50 seconds at room temperature. The sample is removed from the etchant to be cleaned in deionized water and dried with dry nitrogen. The sample is then immersed in a dilute 1% solution of hydrofluoric acid at room temperature for 60 seconds to remove the remaining titanium adhesion layer after which it is cleaned with water and dried. Following etching, the photoresist is stripped in room temperature acetone for 60 seconds to yield the remaining finalized gold IDT patterns. An etching technique is chosen over lift-off patterning to define the IDT patterns in this process due to the low depolarization temperature of the substrate material. The relatively high photoresist baking temperatures experienced by the plate during lithography can cause thermal depolarization of the substrate if it is poled prior to processing. Because of these low temperature requirements, special care is taken throughout sample fabrication to ensure the PMN-PT plate does not exceed 50^0C. A completed 10x10 mm test sample is shown in figure 2.31.a. A magnified view of the IDT pair rotated 30 degrees to the <011> crystal axis is shown in figure 2.31.b.

To perform testing, the sample is mounted into a Cascade Microtech Summit 9000 microwave probestation. GSG style probes (Cascade I50-A-GSG-100) are mounted to micromanipulators and are connected to both test ports of an Agilent PNA E8361A. The system is calibrated to the probe tips for a two port measurement using a Cascade impedance standard substrate (101-190).

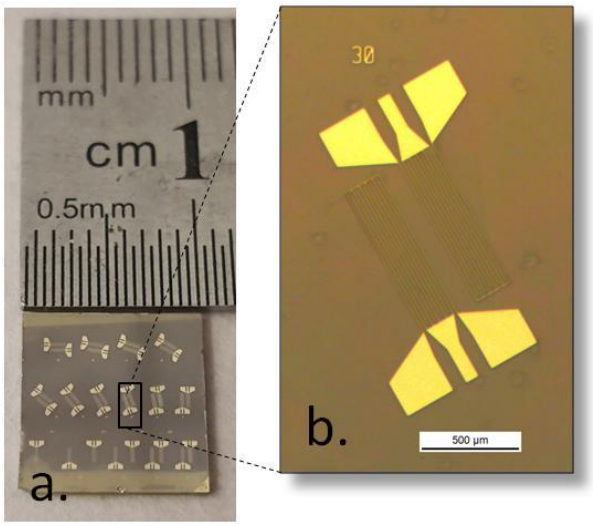

Figure 2.31 – a. A <111> cut PMN-PT substrate that has been patterned with 10 IDTs rotated every 10 degrees in the sample plane. b. A magnified view of one of the IDT patterns used in SAW transmission testing.

The PMN-PT sample is then placed onto the probstation stage and the probes are aligned and contacted to the IDT patterns in a two port IDT to IDT transmission configuration. The S12 parameter is recorded for 9 total IDT pairs which are oriented at every 10 degree increments to the <011> crystal axis for a frequency range of 40-80 MHz. The input power to the IDT electrodes is fixed to -10 dBm. The S12 transmission data is shown for angles of 10, 30, 50, 70 and 90 degrees from the <011> axis in figure 2.32.a. It is seen that the central pass band of the IDT frequency response is centered around 60 MHz for the measured data. The shifting of this center band frequency with respect to IDT rotation angle shows the dependence of the surface acoustic wave speed on the propagation direction about the <111> axis. A reduction in transmission magnitude is also observed in the data corresponding to the inherent anisotropy in the material coefficients. The center frequency is extracted from the transmission data using a fit

Lorentzian frequency distribution. This center frequency along with the known pitch of the IDT fingers (20 µm) can be used to estimate the surface acoustic wave velocity. The wave speed extracted from the experimental data is shown in figure 2.32.b (red) with a smooth polynomial fit to the results. A simple 2D FEM simulation is used to extract the expected wave speed from a two port SAW measurement using the material parameter for the field stabilized <111> cut [72]. The experimental data is plotted in black in figure 2.32.b. The extracted experimental wave speed is within 6% of the simulated values. The angular dependence of the wave velocity exhibits the expected trigonal characteristic inherent in the 3m crystal class to which the <111> cut of PMN-PT belongs.

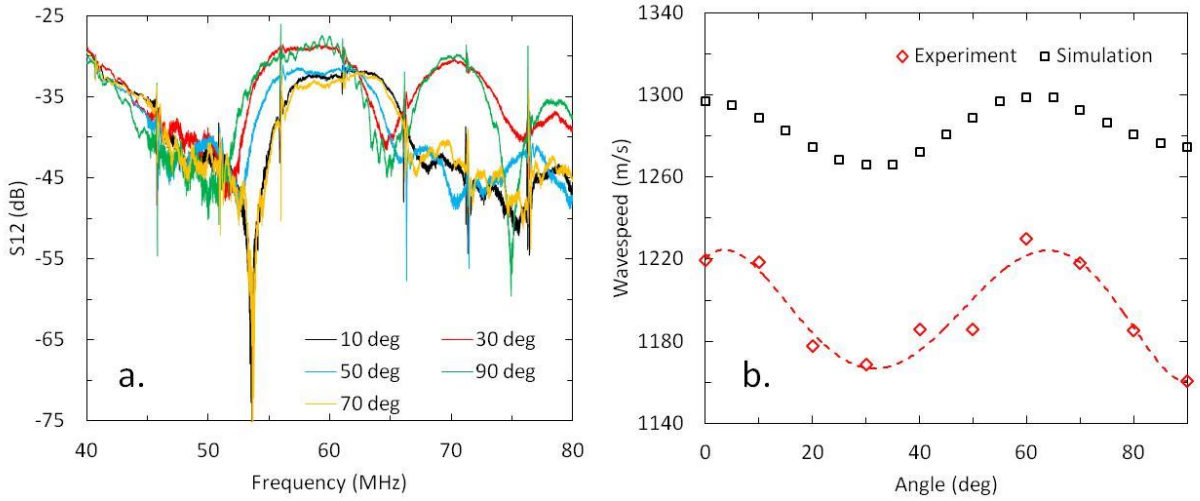

Figure 2.32 – a. The S12 transmission response of the IDTs for various measured propagation angles measured from the <011> crystal axis. b. The experimentally extracted wave speed (red) as a function of angle from the <011> axis compared to the simulated wave speed (black) using a 2D finite elements IDT to IDT transmission simulation.

The reported literature values for this cut of PMN-PT crystal indicate that shear strains of approximately 60 ppm can be achieved using an impedance matched IDT structure and typical VNA power levels (0 dBm) [72]. Through the use of an RF amplifier potentially much larger strain magnitudes could be developed within the operating parameters of the IDT structure. Despite this, the high insertion loss of the IDT test shown in the measured data indicates that this transduction process is not an efficient mechanism for detection of surface waves. This is potentially due to the high dielectric and mechanical losses incurred by the wave as it travels across the substrate. Additionally the generation of bulk modes, while suppressed in this cut, remains large when compared to other common choices for SAW propagation such as lithium niobate or quartz. For this reason the antenna devices tested in this work are focused on those which use the well-established 128^0YX cut of lithium niobate.

The 128^0YX cut of lithium niobate is selected for the substrate material in the multiferroic antenna because of its low loss characteristics, relatively large shear coupling terms and very high electromechanical coupling coefficient [68][73]. This substrate corresponds to a crystal orientation where the c-axis of the hexagonal unit structure of the lithium niobate crystal, called the z axis, is rotated toward the in-plane x axis by 128^0. The surface acoustic waves are then propagated along the in-plane y axis direction which is typically indicated macroscopically by a flat ground into the wafer. This rotation produces the ideal loss and piezoelectric coupling characteristics to support coherent Raleigh wave propagation which can be detected with simple surface electrode geometries. A thorough numerical investigation of the wave propagation characteristics on several lithium niobate substrates with a focus on multiferroic antenna applications is presented by K. Wetzlar [49].

To validate the surface acoustic wave speed of the 128^0YX lithium niobate reported in figure 2.30, a simple SAW bandpass filter is constructed on commercially available substrates of the same crystal orientation. These substrates are provided by Atom Optics and are available in 50 and 100mm wafer diameters which have had both sides optically polished. In order to experimentally measure the acoustic wave speed, a pair of IDT electrodes is fabricated on the substrate surface using evaporated gold and a liftoff patterning technique. These electrodes are designed with 15 finger pairs having 9.5 μm pitch which corresponds to a full wavelength of 19μm. The IDT patterns also contain a CPW pad layout for connection by a GSG probe to the test port of a network analyzer. A representative IDT pair is shown in figure 2.33.a. The IDT pairs are connected to an Agilent E8361A test system through calibrated 100 μm GSG microwave probes (Cascade I50-A-GSG-100) in a two port test arrangement. The excitation power of the PNA is set to -10 dBm. Full two port transmission data is collected between the two IDT pairs. The transmission response of the IDT system is shown in figure 2.33.b. A large central peak is observed in the frequency response which corresponds to the center frequency of the IDT electrode patterns. Using the known pitch of the IDT fingers and the experimentally measured transmission data, the surface wave speed can be calculated as ~3890 m/s. Comparison of the experimentally measured wave speed with that reported in figure 2.x for this crystal show that the measured value is within 3% of the reported value [74]. The slight decrease in the measured wave speed is due to small orientation tolerances incurred during crystal growth which was also observed in the previous section through the use of finite element simulation. The relatively large insertion loss (-15 dB) of the transmitted signal is due to the poor impedance match between the IDT pattern, which is measured to be 230 Ohms at resonance, and the 50 Ohm test system. The appearance of closely spaced comb filtering at the central peak is due to

phase mixing of the transmitted SAW signal and the electromagnetic radiation transmitted from one IDT to another. This effect is discussed in the experimental section of this chapter. Taking these sources of measurement noise into consideration, the SAW transmission observed in these tests indicates that the 128^0YX cut lithium niobate substrate is suitable for use in the design of a multiferroic surface acoustic wave receive mode antenna. In this receive only operation, the small strain amplitudes generated by the magnetoelastic resonators are detected through the sample substrate. For this purpose, the low electrical and mechanical losses found in this substrate material are necessary in maximizing the transduction efficiency of the complete antenna device.

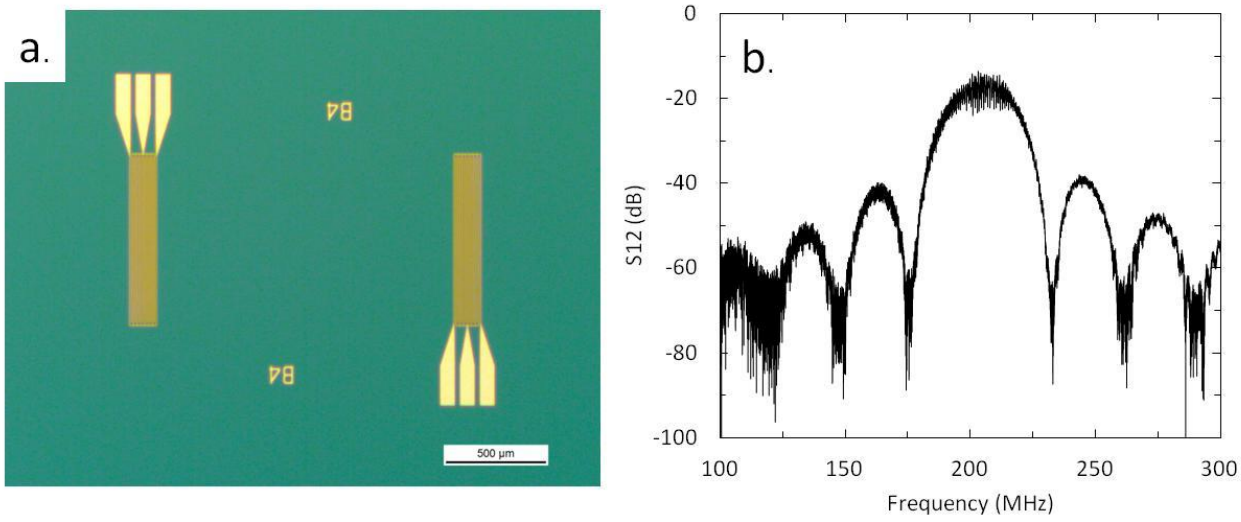

Figure 2.33 – a. An dual IDT test pattern printed on 128^0YX cut lithium niobate for wave speed testing. The x propagation axis is perpendicular to the long axis of the IDTs. b. The transmission response from one IDT to another in dB.

Upon selection of the appropriate material system for use in the surface acoustic wave antenna, the parameters for these materials are used in the design simulations discussed previously from which the optimum IDT and magnetoelastic resonator geometry is found given a design frequency. These parameters must then be translated into a manufacturing process from which test samples can be fabricated for measurement.

V. Device Fabrication

Fabrication of the multiferroic antenna involves a series of standard CMOS and MEMS processing techniques to create electrodes, resonators and other structures necessary for device operation. These micro-fabrication processes follow strictly designed and sequentially performed layer by layer operations to form a complete device. The operations performed during each layer step can consist of adding material (deposition) usually as thin films, removal of material (etching) and intermediate patterning steps (lithography). Well established methods for performing each these steps have been developed for building planar layers on silicon substrates following the development of the CMOS transistor. In recent decades, however, the interest in miniaturizing electromechanical devices has standardized many non-conventional techniques for building three dimensional structures across a variety of substrates.

For the purpose of the multiferroic antenna, features smaller than 2 μm are typically not required as the acoustic wavelengths in lithium niobate and PMN-PT are within the range of 13-30 μm for frequencies studied in this work. This means the smallest feature sizes will be found in the IDT fingers. For this reason a contact lithography method is used for patterning as it can resolve features as small as 2 μm and is easily adaptable to many substrate sizes and materials. Contact

lithography begins by applying a photo sensitive polymer to the surface of the substrate to be patterned. This polymer, called photo resist, is a mixture of thinning solvents and photoactive resin (novolac) or epoxy. The photoresists used in this work are i-line resists indicating that they are sensitive to the 365 nm wavelength UVA radiation emitted from medium pressure mercury vapor lamps. Prior to spinning of the photoresist, an adhesion promoter can be used to improve the adhesion of the resist film to the surface of the substrate. Typically a commercial promoter using hexamethyldisilazane (HMDS) is applied to the surface using spin coating or vapor coating. This process creates reactive silylate OH groups on the surface which readily bond to the following resist layer. The resist is applied to the substrate by a process called spin coated whereby resist is applied in a liquid pool onto the substrate surface which is then rotated at high speed to spread and even the resist to a thin layer. The speed of sample rotation during spinning of the resist will determine the final thickness of the photo resist film which remains on the surface of the substrate. Spin curves, such as the one shown in figure 2.34 for the common negative tone resist series nLOF 2000 [75], are provided by the resist manufacturer for choosing a spin speed appropriate for the application. It is important, in the case of the multiferroic antenna, to consider the uniformity of the photoresist over the surface of the substrate. During spinning, the surface tension experienced by the resist at the substrate edges will create a small region with a parabolic thickness profile called the edge bead. This non-uniformity in resist thickness toward the substrate edges can create large variations in the way the patterns are resolved in these regions. Although this region is typically small when compared to full 100mm wafers, it can significantly reduce the acceptable patterning region when using very small substrates such as PMN-PT.

After spinning of the resist, the substrate and resist layer are heated to a specific temperature called the soft bake temperature for a set period of time. This heating step causes the diffusion and evaporation of solvents from the photoresist film. This serves to prepare the film for exposure by solidifying the resist and improving the resist to substrate adhesion. The soft bake also degrades photoactive compounds with higher temperatures and long bake times leading to a slowing of the resist solution rate during later development steps. The rate of solvent reduction follows an exponential decay with respect to time with bake temperature playing an important role in the decay rate of the solvent concentration. The times and temperatures for soft baking are typically specified by the manufacturer for silicon substrates but can be readily modified to suit different substrate materials.

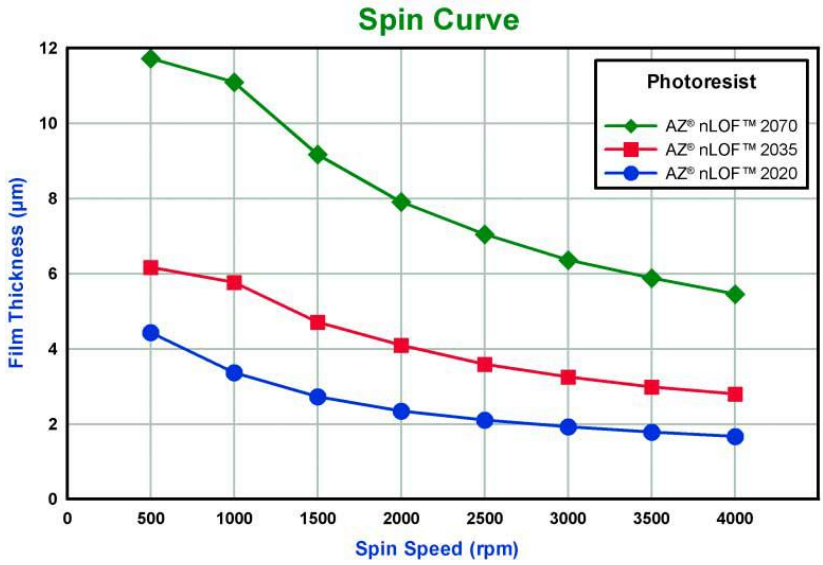

Figure 2.34 – Spin speed vs thickness curves for nLOF 2000 series of negative tone photoresists. [75]

Following soft bake, the substrate and resist are ready for exposure. The substrate is mounted into an alignment tool which allows for the precise alignment of a photomask to previous layer

patterns on the sample using a two axis micrometer stage and microscope. To perform alignment and exposure first the sample is mounted to a vacuum chuck and placed below the photomask. To prevent misalignment of the mask plane to the sample surface plane, the stage rotates on a gimble which is locked while pressing the sample into the mask. The sample and mask are separated by a small offset (typically 50-100 μm) and the sample is oriented to the mask manually using a microscope. Often times, orienting complex patterns with respect to one another will require the use of alignment markers. Vernier style alignment markers shown in figure 2.35 are used on the outside edge of the antenna wafers for fast alignment and quantifying layer to layer translation or rotation after fabrication is complete. Figure 2.35.a shows a perfectly aligned Vernier pattern for a dual layer process involving nickel and gold films. Figure 2.35.b demonstrates a pattern with a 1μm lateral misalignment between the nickel and gold patterns as can be seen in the Vernier gauge. This allows for the evaluation of certain manufacturing tolerances and their impact on the operation of the device. Typically small misalignments, such as that shown in figure 2.35.b are well tolerated by the robust design of the SAW antenna.

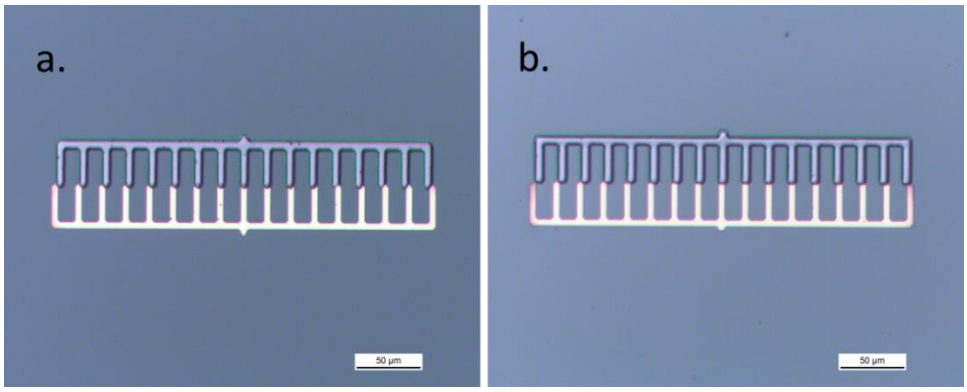

Figure 2.35 – a. An aligned Vernier style alignment marker in gold and nickel materials following two layer liftoff deposition. b. a Vernier which indicates a 1 μm lateral misalignment between the two layers.

Following alignment, the sample is pressed into the photomask with a set amount of pressure and exposed with a mercury light source for a specified amount of time. The exposure time is critical to the success of the lithography process and is determined based on the resist contrast curves. Poor control of exposure time can lead to resist features which do not represent the original mask patterns well. The resist manufacturer specifies the exposure energy density required to achieve optimal results. In practice, however, these times are typically optimized through parametric studies specific to the substrate and any layers underneath the resist. This time and the contrast properties of the resist also control the profile of the resist sidewalls, making the resist more or less useful for certain layer operations.

Photomasks for contact lithography are fabricated on soda-lime glass plates which have been patterned with a material opaque to UV radiation (in this case thick chrome) to represent the patterns to be transferred to the substrate. Masks are designed in a computer aided design (CAD) program specific to MEMS micro-fabrication called L-Edit. Completed CAD file are then sent to the UCLA nanoelectronics research facility (NRF) mask shop to be printed. Figure 2.36 shows an example antenna mask ready for use on a 10x10 mm plate of PMN-PT. The chrome layer appears as a metallic brown layer over the glass plate.

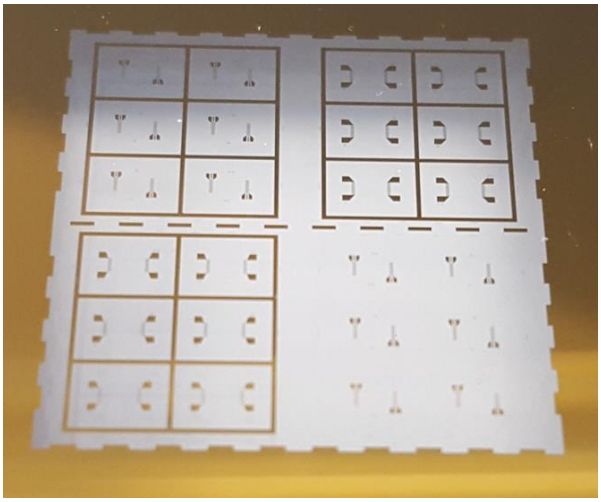

Figure 2.36 – A photomask printed onto a glass plate for performing contact lithography on a 10x10 mm PMN-PT substrate. The metallic brown layer is a thin film of chrome.

Depending on the tone of the resist and the layer operation to be performed, masks can be manufactured with the structure to be printed opaque to the exposing UV energy or transparent with the surrounding area serving to block incident light.

Following exposure, certain types of resists, primarily negative tone resists, will need an additional baking step which crosslinks the exposed areas of film making them insoluble in the development solution. The time and temperature used in this step are specified by the manufacturer. Many positive tone resists do not require this step and are ready for development upon being exposed. Development is performed on samples by immersing them in a developer solution which removes the photoresist areas specified by the exposure step. Typically these basic solutions are used at room temperature with mild agitation to provide fresh reactive compounds to the resist surface. The development time is critical in resolving the desired features accurately. The resist surrounding the exposed features are generally not completely

insoluble in the developing solution meaning long immersion times will result in geometric distortion of the pattern. When the desired development time has been reached, the sample is quickly immersed in deionized water to stop the reaction between the developer and the resist. Depending on the resist and the layer process to be performed, the resist may be baked following development to further remove remaining solvents.

Because the design of the surface acoustic wave multiferroic antenna consists primarily of planar metallic patterns, a common and simple technique called lift-off patterning is used to define these structures. In this technique, schematically shown in figure 2.37, a negative tone resist is first deposited and exposed over the substrate (a). A negative tone photoresist is used to take advantage of the inherent sloping sidewalls that it produces during lithography. This sidewall profile occurs due to the bulk effect whereby the intensity of light penetrating into the resist exponentially decays as it travels through the resist thickness. This attenuation occurs due to the reaction process of the UV energy with the resist and the dielectric and scattering losses associated with the resist. The inverted sloping sidewalls are useful in preventing the deposited materials from adhering to and building up on the sides of the resist features. Without the inverted resist sidewalls, the desired material adhered to the substrate can attach itself to these sidewall deposits leaving severe artifacts on the finalized patterns. Often times it is necessary to remove residual photoresist left at feature sites to ensure the following deposited material is making direct contact with the substrate surface. This resist cleaning step is performed in an oxygen plasma which physically ablates any organic layers on the sample surface. Following lithography and plasma cleaning, physical vapor deposition (PVD) is performed on the sample as is shown in figure 2.37.b. It is seen in figure 2.37.b that the deposited material makes contact with the substrate surface only at the desired openings patterned into the photoresist. At all other

locations on the sample, the deposited film falls incident onto the top of the photoresist layer. In this work two main types of PVD are used with lift-off patterning; sputtering and electron beam evaporation. In electron beam evaporation the angle of incidence of the deposited material to the sample surface plane normal (called the deposition yield angle) is very shallow. This results in highly directional deposition which is well suited to lift off patterning and accurately reproduces the geometry defined by the resist. Sputter deposition produces much wider yield angles which will result in rounding of the top of the final features and broadening of the feature dimensions at the base. This restricts the use lift off patterning with sputter deposition to thin deposits and low aspect ratio resists in order to prevent sidewall build up and artifacts in the final features. Finally the sample is immersed in a photoresist stripping solution which removes the resist and delaminates the undesired deposited material as shown in figure 2.37.c. The undesired material is washed into the stripping solution which typically contains a surfactant to prevent the re-deposition of this material to the sample surface. In some cases it is necessary to aggressively remove the photoresist and undesired deposits from the sample using ultrasonic cleaning. This method is especially useful when the features have minor, weakly attached sidewall artifacts (called wings) that need to be removed. Once the undesired deposits and the photoresist have been removed, the sample is cleaned of the stripping solution and the process is complete. This patterning technique is applicable across a wide range of feature sizes extending from micron to nanometer dimensions and is used in the fabrication if the multiferroic antenna to create the IDT electrodes and the magnetoelastic resonators.

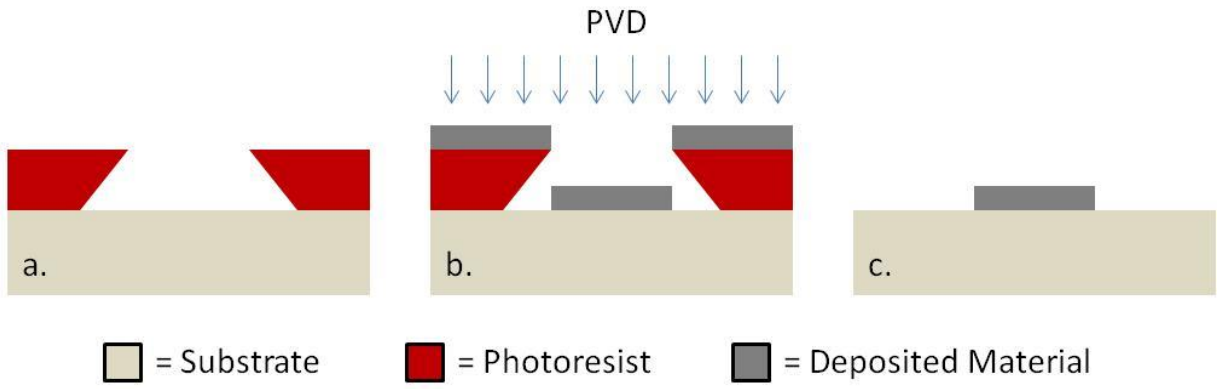

Figure 2.37 – Three step schematic diagram of lift off patterning used in making micron to nanometer size features using physical vapor deposition.

Deposition of the metallic electrodes and the magnetoelastic resonators for the multiferroic antenna is accomplished using two forms of physical vapor deposition as was previously discussed; sputtering and evaporation. These are standard industry techniques which allow for the deposition of materials in layers of highly controlled thickness and composition. Electron beam evaporation is a technique by which a bulk piece of the material to be deposited is heated with a source of focused electrons to its vapor temperature. Typically these electrons are magnetically focused into a water cooled crucible which holds the target material. The electron beam is swept in a circular or diamond pattern using control plates to prevent the beam from burning through the target material to the bottom of the crucible. Samples are placed opposite the crucible in a hemispherical carousel which rotates during deposition to improve film uniformity. The shape of the carousel is designed such that the deposited material falls incident perpendicular to the plane of the sample surface. This is critical for processes involving liftoff or high cross wafer thickness uniformity. Once the vapor temperature of the material is reached, a

shutter is rotated away from the crucible and the evaporated material is allowed to reach the sample carousel. The deposition rate and thickness of the film are monitored using a quartz crystal microbalance (QCM) which serves as the feedback element for the electron source power controller. This entire process must be performed under high vacuum (typically around 1 μTorr) to prevent scattering of both the source electrons and the evaporated target material with atmospheric gasses. A simplified illustration of electron beam evaporation is shown in figure 2.38. Electron beam evaporation is excellent for depositing thin elemental metals and dielectrics where directional deposition and extremely fine control of film thickness is needed. Depositing complex alloys becomes complicated by the differences in partial pressures of the alloy elements and the lack of control parameters in the electron beam system. This lack of control over deposition parameters also makes the intrinsic film stress difficult to control which can lead to problems with delaminating or cracking in very thick deposits. For films which require precise control over alloy composition or film stress often times sputter deposition is a better option.

Sputter deposition is a process by which a target material is ablated from a disk shaped electrode using an argon plasma. These ablated atoms are ejected away from the target and fall incident onto a sample which is placed in proximity to the target surface. In this technique the sample and target are placed a fixed distance apart in a vacuum chamber. Once a pressure set point has been reached, argon is allowed to flow into the chamber at a controlled rate. The plasma is struck with the use of a strong ionizing electric field which can be calculated using the Paschen law given the argon pressure and the anode to cathode separation of the sputter system. Once the plasma is struck, the sputtering power can be modulated to alter the kinetic energy of the ionized argon gas which in turn allows for control over deposition rate and some of the final film properties. Often times the sputtering system uses a strong ring shaped magnet placed behind the target material to

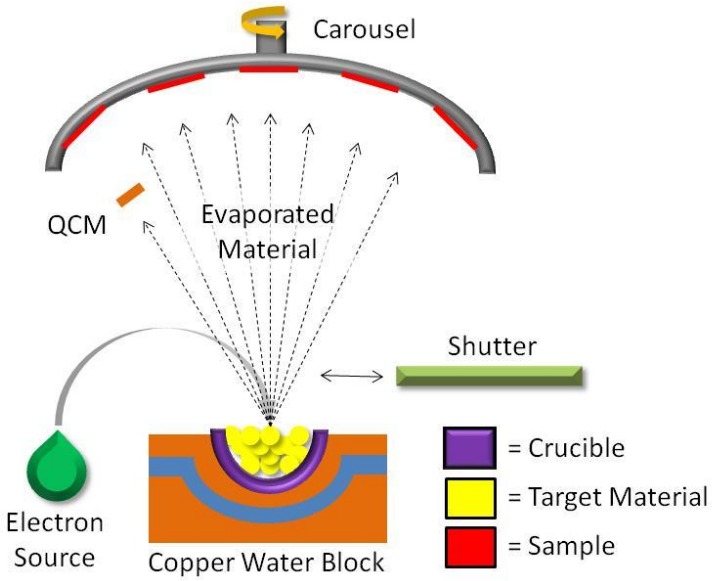

Figure 2.38 – Simplified diagram of an electron beam evaporation system. The entire system is contained inside of a high vacuum chamber (not shown).

increase the density of the plasma near the target surface. This increased plasma density at the target can significantly increase the deposition rate of the system but also introduces stray magnetic fields inside the deposition chamber and causes uneven wear on the target electrode. Additionally, some sputtering systems use radio frequency modulation of the ionizing electric field to prevent charge buildup when using dielectric target materials. Figure 2.39 shows a simplified illustration of a DC magnetron sputtering system. Sputter deposition produces high quality films with decent control over the final film thickness and stress. Because most sputtering systems are open loop, the control over film thickness and rate must be determined from prior calibration depositions using the same system parameters. By controlling the sample to target separation, the argon pressure and the sputtering power, many of the compositional, morphological and mechanical characteristics of the deposited film can be tightly controlled.

This is especially useful when depositing complex alloys which require precise stoichiometry or low film stresses in application.

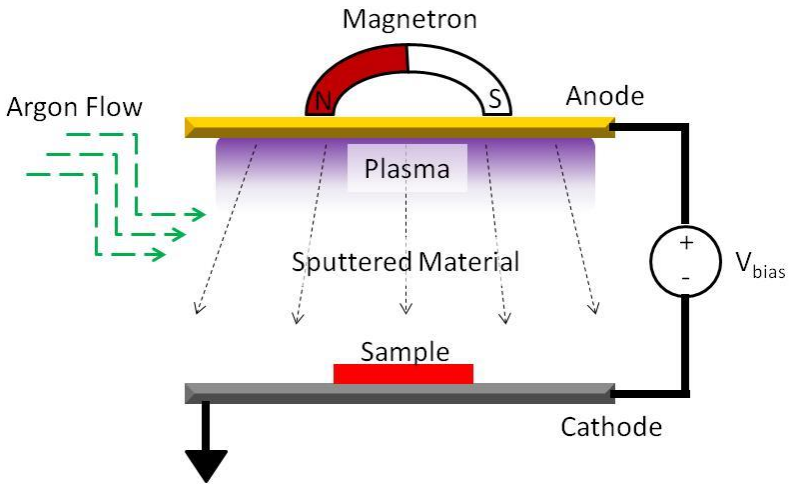

Figure 2.39 – Simplified schematic drawing of a DC magnetron sputtering system. The entire system is contained inside of a vacuum chamber (not shown).

Multiferroic antenna devices are fabricated on two types of piezoelectric substrates; PMN-PT and Lithium Niobate. Because the basic antenna components between the two material systems remains identical, the processing steps taken for both of these devices are similar. Devices begin with bare substrates of standard 0.5 mm thickness. In the case of lithium niobate, substrates are single crystal 50 mm diameter double sided polished wafers with a flat cut perpendicular to the SAW propagation axis (x-axis) of the crystal. PMN-PT substrates are 10x20 mm plates which have been polished on both faces. Both of these substrate types are provided by Atom Optics located in Shanghai. Wafers are cleaned in a solvent solution of acetone, methanol and isopropyl alcohol followed by rinsing in deionized water and drying with dry nitrogen. This step is performed to remove any polishing compound left on the substrate surface by the manufacturer.

The substrates are baked for 5 minutes on a 100^{o}C hotplate to evaporate any remaining moisture. Following this initial substrate cleaning, resist spinning and lithography are performed to define the IDT electrode patterns.

Cleaned substrates are mounted into a Headway Systems Inc. PWM32 controlled photoresist spinner. HMDS is applied with a plastic dropper to cover the surface and then spun onto the substrate using the three step procedure outline in table 2.2. Following this step, resist is applied to the substrate using a dropper until surface coverage is achieved and spun using the same procedure in table 2.2. Processing for lithium niobate uses nLOF2020 negative tone photoresist which will have a final resist thickness of 2µm. Lithography for PMN-PT substrates is performed using AZ5214-IR resist in a negative mode which will result in a 1.6 µm final resist thickness.

Step #	Description	Ramp Rate (rpm/s)	Speed (rpm)	Step Time (sec)
1	Ramp up to distribute resist	500	500	6
2	Hold to achieve final thickness	500	3000	50
3	Ramp down to stop	500	0	0

Table 2.2 – Spinning recipe for PMN-PT and Lithium Niobate lithography processes.

Following spinning, the substrates are placed onto a hotplate for 60 seconds to perform a softbake. The hotplate temperatures for the lithium niobate and PMN-PT processes are 110^{o}C and 90^{o}C respectively. Substrates are removed from the hotplate and allowed to cool to room temperature before exposure. Samples are then mounted onto the vacuum chuck of a Karl Suss MA6 alignment tool. A photomask containing the IDT patterns to be printed is mounted into the MA6. The tool orients the sample and mask to one another for alignment. IDT masks contain

markers which are designed to align the photomask patterns to the lithium niobate wafer flat or the PMN-PT substrate edges. This ensures the IDTs are oriented along the proper axis for SAW propagation. Upon proper alignment the tool exposes the resist with a 66 mJ/cm^2 UV dose. The lamp power for the MA6 is typically in the range of 8-12 Watts. Exposed samples are then post exposure baked on a hotplate. Lithium niobate samples are baked for 60 seconds at 110^oC while PMN-PT samples are baked for 45 seconds at 115^oC. Following this step lithium niobate samples are ready for development. The lithium niobate wafers are immersed in an AZ300MIF development solution for 60 seconds after which they are quickly rinsed with deionized water and dried with dry nitrogen. After the post exposure bake of PMN-PT samples, an additional exposure step is required to make the previously unexposed AZ5214-IR resist soluble in the development solution. This process is called image reversal. The PMN-PT samples are mounted into the Karl Suss MA6 aligner which has had the photomask removed. A flood exposure of 250 mJ/cm^2 is applied to the entire surface of the substrate. Samples are removed from the tool and immersed in a 1:4 solution of AZ400K developer to deionized water for 50 seconds. After 50 seconds the samples are removed from the development solution and rinsed with deionized water and dried with dry nitrogen. At this point both the lithium niobate and PMN-PT samples are ready for oxygen plasma cleaning. A hard bake is not performed on the final samples as it was found to make the resist removal step following deposition more difficult. This is likely due to the lower solvent concentration in the hard baked resist. Figure 2.40 shows a set of IDT patterns in nLOF2020 on a lithium niobate wafer (right) and AZ5214-IR on a PMN-PT substrate (left) after the successful completion of the lithography process.

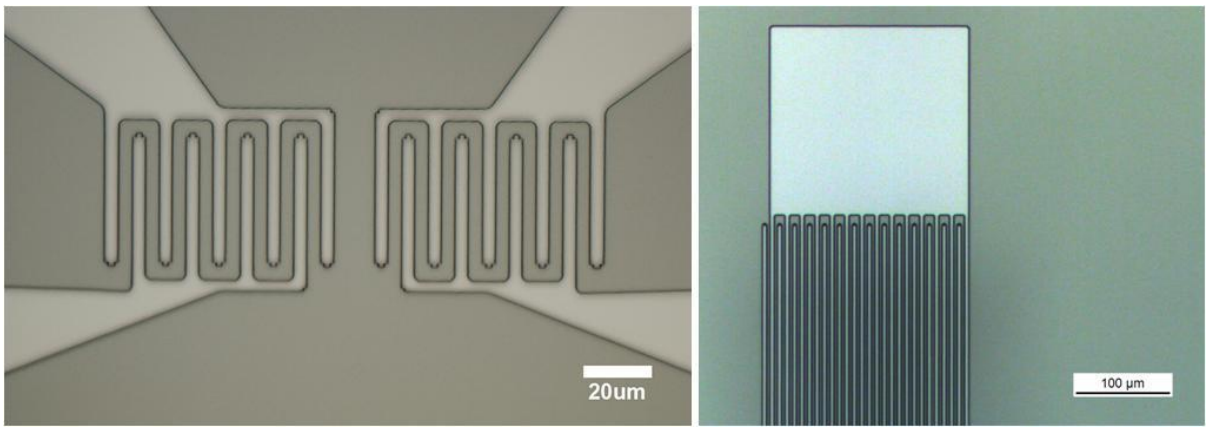

Figure 2.40 – Exposed and developed resist with IDT electrode patterns ready for deposition of gold. AZ5214-IR on PMN-PT is shown in the left figure and nLOF2020 on lithum niobate is shown to the right.

After lithography is performed successfully, samples are cleaned in an oxygen plasma. Samples are placed into a Tegal Plasmaline 115 and etched for 120 seconds. During this time the samples are heated to 80^{o}C and a plasma power of 200 Watts is applied to facilitate etching of the resist. Samples are removed and are now ready for evaporation of the electrode material. Samples are mounted to 4 inch aluminum carriers using Kapton tape placed around the outer edges of the substrate. The carriers are mounted into the carousel of a CHA Solution electron beam evaporation system. Titanium and gold are placed into appropriate crucibles inside the system. The chamber is sealed and pumped to a vacuum pressure of 1 µTorr. Upon reaching the pressure set point, the titanium target material is heated using the electron source and evaporated onto the samples at a rate of 1 Å/s. This titanium layer serves to adhere the non-reactive gold to the lithium niobate substrate. Chrome and nickel can also be used as reactive adhesive layers but are, because of their magnetic ordering, not desirable for this application. The thickness for the

adhesion layer is designed to be 10 nm to allow for a sufficient volume of reactive material to be present. Upon completion of titanium deposition, the gold crucible is now heated with the electron source to its vapor temperature. Gold is evaporated onto the samples at a rate of 2.5 Å/s to a final thickness of 150 nm. This layer is designed to be relatively thick to withstand the wire bonding process used in making electrical contact to the IDTs. If the gold film is insufficiently thick, the pads can delaminate or the wire will not properly adhere to the gold layer. Following deposition, the samples are removed from the evaporation chamber and immersed in a stripping solution. This stripping solution is a commercial mixture of n-methylpyrrolidone (NMP) and tetramethylammonium hydroxide (TMAH), trade named AZ300T. The solution is heated on a hotplate to 80^{o}C inside a fume hood and the samples are submerged for several hours with occasional agitation of the solution. The exact time necessary for stripping depends strongly on the density of patterned to non-patterned areas on the samples. Typically, sparsely patterned samples will require longer stripping times as the area of resist exposed to the stripping solution is small. This process can take anywhere from 30 minutes to 12 hours to complete. Upon completion of resist stripping, the samples are rinsed with deionized water and dried with dry nitrogen. At this point in the process, the samples are ready for fabrication of the magnetoelastic layer.

Lithography of the magnetoelastic layer of the multiferroic antenna proceeds identically to the first layer in which the IDT was patterned into a photoresist film. The alignment of the photomask patterns used in this step is performed relative to the previously deposited gold patterns which are now visible on the sample surface. Deposition of the magnetoelastic layer is performed using a number of PVD techniques based on the film thickness requirements and the material to be deposited. Nickel films below 400nm in thickness are deposited using electron

beam evaporation. The rate used for this deposition is 2 Å/s. Nickel resonators which require larger thicknesses up to 1μm are deposited using sputter deposition in an Ulvac JSP 8000 sputtering system. The sputtering power used for nickel deposition is 350watts which results in a deposition rate of 1.75 Å/s at an argon pressure of 15mtorr. Films of FeGaB are also studied in this work which are deposited using a sputtering process described by Lou et al. [41] at Northeastern University. All films use a thin adhesion layer of titanium which is in the range of 10-40nm in thickness. Following deposition of the magnetoelastic material, liftoff is performed on the samples using the technique described for the IDT layer. It is useful to place a small, powerful magnet inside the stripping solution while performing liftoff of the magnetoelastic layer to attract fine particles of magnetic film away from the sample surface. When liftoff is complete, the samples are rinsed with deionized water and dried with dry nitrogen. Figure 2.41 shows a multiferroic antenna pattern on lithium niobate upon completion of the magnetoelastic layer process using sputter deposition. The nickel structures are 450nm thick.

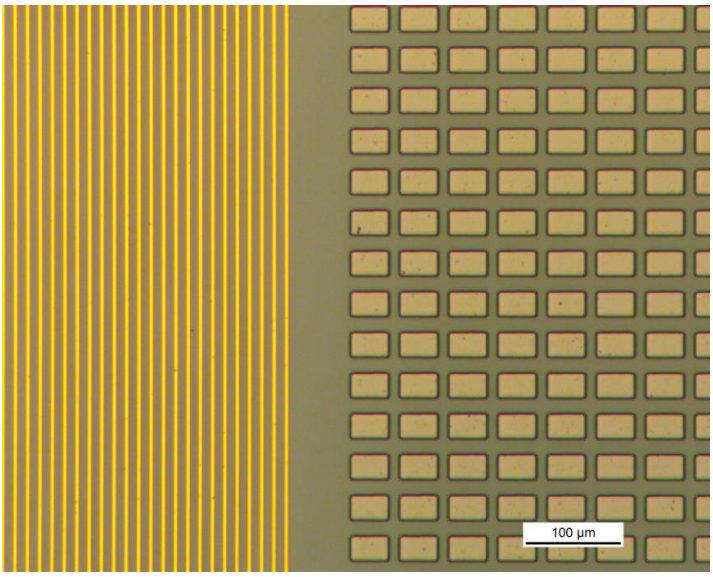

Figure 2.41 – Optical image of completed gold IDT electrodes and nickel resonators on the surface of a lithium niobate wafer.

Several supporting processes have been developed during the course of this work for the fabrication of certain design features which were ultimately omitted from final antenna devices. These processes include the electrodeposition of thick nickel films, the electrodeposition of thick copper films and the etching of single crystal PMN-PT substrates. Etching of single crystal PMN-PT substrates was developed to make deep trench patterns on SAW antenna devices to precisely control the locations of reflecting boundaries. These boundaries serve to reflect the acoustic waves generated by the magnetoelastic resonators or the IDT electrodes to create destructive or constructively interfering waves. Early simulations show that being able to control the location at which these reflections occur with respect to the wave generation source can significantly increase the output signal magnitude. The trenches should be several microns in depth to efficiently reflect the energy in the surface acoustic wave. A process was developed which uses reactive plasma etching to selectively remove material from the substrate surface. In this process a PMN-PT wafer is patterned using the previously described lithography process for AZ5214-IR photoresist. A 1μm thick nickel film is sputtered onto the sample using a Denton Discovery 550 sputtering system and liftoff is performed to produce the final nickel patterns. The sample is mounted onto a 100mm diameter silicon wafer using Cool Grease and mounted into a Surface Technology Systems (STS) AOE etching tool. The tool places the wafer inside a vacuum chamber where a number of reactive and inert gas species are allowed to flow. The argon gas flow rate is set to 45 sccm while C_4F_8 gas is set to 7 sccm. The platten power is set to 300 Watts while the inductively coupled coil power is set to 1500 Watts. These parameters result in an etch rate of 220 nm/min of the PMN-PT substrate with a 1:3 selectivity to the nickel hard mask. This low selectivity indicates a major component of the etch process comes from physical ablation of

the material with argon ions. The process produces uniform pits with angled sidewalls as can be seen in a cross section SEM micrograph shown in figure 2.42. Although this process was successful, models predict that reflections from the steeply angled sidewalls, produced during the etching process, are difficult to control precisely. This eventually led to the use of absorbing polymers at the SAW die boundaries to prevent reflections from occurring as will be discussed in later sections.

The electrodeposition of thick copper film was also studied on PMN-PT substrates for its effects on surface acoustic wave reflections. Copper layers can be deposited many microns in thickness using electroplating making it useful for producing large acoustic impedance boundaries on the substrate surface. This deposition process uses the electrically driven reduction of metal ions in a plating solution onto the sample which serves as the cathode of the plating cell. To begin this process, a conductive seed layer is deposited onto the PMN-PT substrate using evaporation and

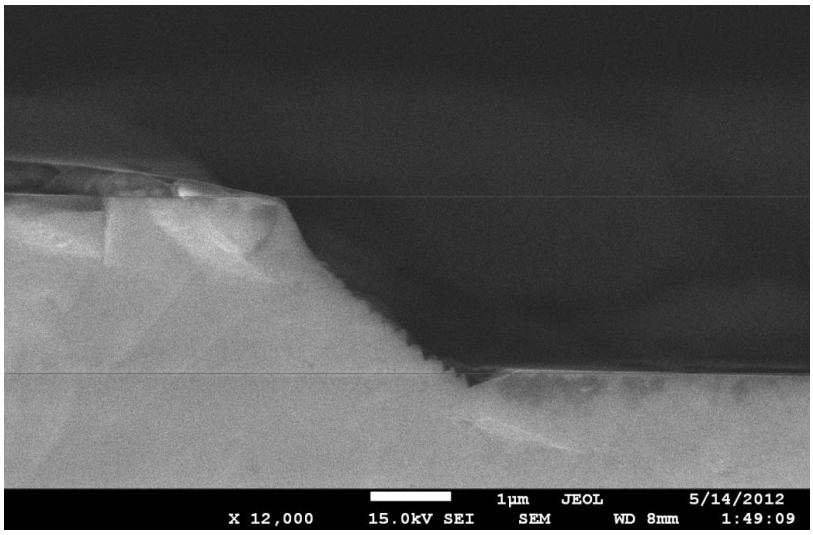

Figure 2.42 – An SEM cross section micrograph of a PMN-PT trench after a 10 minute etch in a reactive plasma.

liftoff. The seed layer consists of a titanium adhesion layer and a 100 nm thick copper film. Following deposition and liftoff of the seed layer, an identical lithography step is performed over the seed layer using AZ5214-IR to control the sidewalls of the copper deposits and to protect the existing layers from being damaged by the highly acidic plating solution. The seed pattern is designed with a large contact patch to which an electrical connection is made using a brass spring clip. This contact serves to connect the seed layer metal to the negative terminal of a laboratory dc power supply (BK Precision 1611) through a current limiting potentiometer and resistor network. A large anode is formed from a pure copper sheet which is connected to the positive terminal of the DC supply. This copper anode is oxidized during the reaction, replenishing the solution with copper cations. Both the copper anode and the sample are placed into a commercial copper sulphate based plating solution (MG Chemicals 41670) in a glass beaker. The sample and anode planes are oriented parallel to one another and spaced apart by 40mm. The DC power supply is turned on in constant voltage mode and held at 10 Volts. A resistor is connected on the anode side of the cell in series and its voltage drop is monitored with a voltmeter. A potentiometer, also in series with the anode side of the cell and the sensing resistor, is tuned to achieve the proper loop current in the series network. This current is converted to current density with the known area of the seed electrode exposed to the plating solution. A current density of 84 A/m^2 is used which results in a deposition rate of 126 nm/m. Typical film thicknesses used are around 30 μm. Figure 2.43 shows a multiferroic antenna sample on a PMN-PT substrate after electroplating a 30 μm thick copper boundary around each die. The image is shown prior to the removal of the protective photoresist layer which is covering the gold IDT electrodes and the nickel resonators. It should be noted that because electrodeposition is a highly isotropic process, once the copper reaches the top of the photoresist,

the deposit begins to “mushroom” whereby the material being deposited is no longer laterally confined. This is inconsequential in the operation of the acoustic reflecting boundary as the reflection of the wave will occur at the point where copper contacts the PMN-PT substrate.

The electrodeposition of nickel has been studied for the fabrication of thick magnetoelastic structures. Electrodeposition can produce much thicker films than standard PVD techniques making it a valuable tool for fabricating thick magnetic structures. Electrodeposited nickel is an industry standard coating used in the electronics industry as well as a hard barrier coating found on many consumer products. This process begins by depositing a continuous seed layer of titanium, copper and a capping layer of titanium onto the sample using evaporation. The film thicknesses used are 20 nm, 100 nm and 20 nm respectively. The top capping layer prevents oxidation or other contamination of the copper layer which would prevent proper nickel

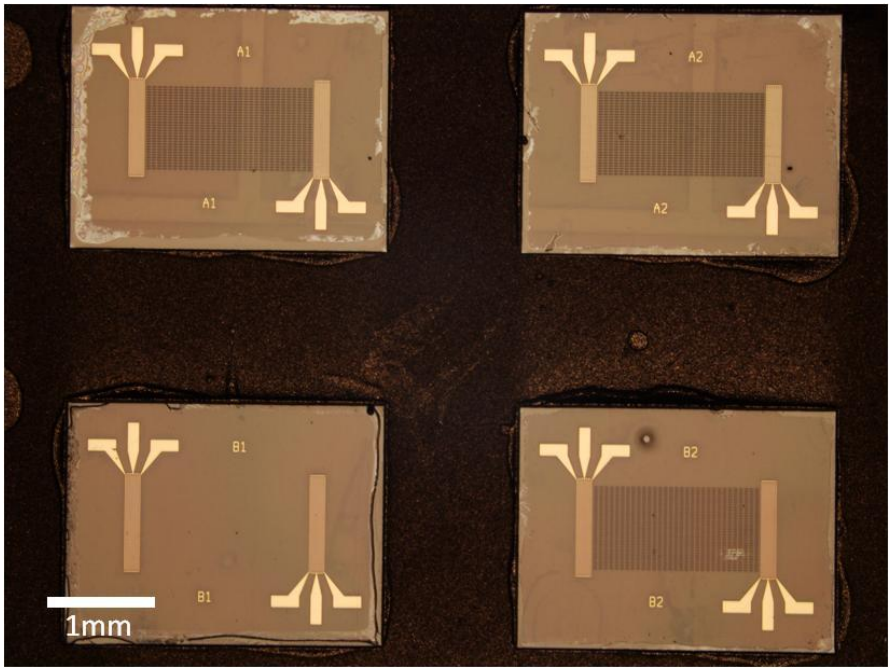

Figure 2.43 – A multiferroic SAW antenna after deposition of a 30 μm copper boundary around each antenna die.

deposition during plating. This layer is omitted when the sample does not experience significant handling or washing between deposition of the seed layer and plating. Lithography is performed on the sample using AZ5214-IR as described previously or KMPR 1005 for high aspect ratio structures. KMPR 1005 is an epoxy based, negative tone photoresist that produces thick resist films which are ideal for plating tall structures. The final resist thickness used in the KMPR process is 7μm. Following lithography the sample is immersed in a 1% hydrofluoric (HF) acid solution to remove the titanium capping layer after which the sample is thoroughly washed and dried. The etching time is typically around 30 seconds but periodic visual inspection of the layer is performed to ensure the titanium is completely etched. This is confirmed by a clearly visible color change in the film at the mask openings when the copper is fully exposed. The seed layer is then electrically contacted with a brass spring clip or copper tape and connected to the sink terminal of a laboratory DC current source. The sample is immersed in a commercially available nickel plating solution (Technics HT-2) of the standard Watt's composition. The solution is heated to 55^{o}C using a hotplate to improve concentration uniformity during plating. The sample is mounted in the bath parallel to an opposing pure nickel cathode which is connected to the source terminal of the current supply. The current density is digitally controlled with the current source and set to 50 A/m^2 which results in a nickel deposition rate of 100nm/min. Once the desired film thickness has been reached, the sample is removed from the plating cell and cleaned. The photoresist is stripped from the sample surface in an 80^{o}C heated bath of AZ300T for 30 minutes. The excess seed electrode surrounding the nickel deposit is then etched. The top titanium layer is etched in a 1% HF solution for approximately 30 seconds. The copper seed film is etched using a commercial copper etchant (APS 100) for approximately 30 seconds or until a

visible color change takes place indicating the copper is completely removed. Finally the titanium adhesion layer is etched again in a 1% HF solution after which the sample is rinsed and dried. Figure 2.44.a is an SEM cross section micrograph of a 2 µm plated nickel resonator patterned on PMN-PT using AZ5214-IR photoresist. The steep negative sidewall profile of the photoresist can be clearly seen in the shape of the nickel structure. The effect of mushrooming is also visible in figure 2.44.a at the point where the deposit reaches the top of the photo resist which is only 1.6 µm in thickness. Figure 2.44.b is an optical image of 4 µm thickness nickel resonators patterned onto lithium niobate using KMPR 1005 photo resist.

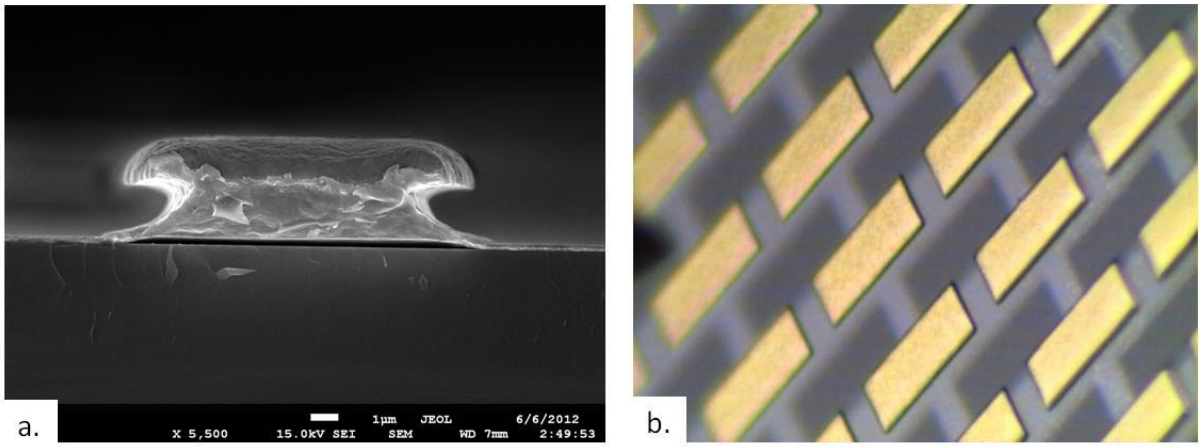

Figure 2.44 – a. An SEM cross section micrograph of a 2 µm thick nickel resonator on a PMN-PT substrate. b. Optical image of an array of 4 µm thick plated nickel resonators on a lithium niobate substrate.

VI. Experimental Setup

Upon completion of sample microfabrication, sample substrates are diced into individual die. Each of these die contain a single antenna structure with a magnetoelastic resonator bed and one

or two IDT electrodes. Dicing is performed with a digitally controlled Disco DAD321 wafer saw provided by the UCLA Center for High Frequency Electronics (CHFE). Depending on the design of the antenna device, the individual die can be several millimeters to centimeters square. Depending on the device size, substrate size and the yield of the fabrication process, the number of usable devices per wafer varies significantly between design generations. Once the substrates are diced, the individual die are optically inspected using a microscope for major defects introduced during microfabrication and sorted accordingly. Major defects include shorts or breaks in the IDT fingers, delaminating of the magnetoelastic material and significant redeposition of material onto the die surface. Additionally, any test patterns which are patterned onto the wafer are removed for characterization. Once devices have been sorted they are ready for assembly onto testing boards or for characterization in the case of probed samples.

Two methods of electrically contacting the output IDT patterns are used in this work; wire bonding and high frequency probing. High frequency probes use a coplanar waveguide transmission line up to the probe tips. If properly design contact pads are used to interface with the test device, the entire measurement is electrically shielded and impedance matched up to the device under test. This provides an extremely clean method of probing devices where very accurate measurements are needed or external noise in the test environment is problematic. Because this technique uses a mechanical method of contacting the device, the sample and probes must be mounted onto a vibration isolated probestation. This probestation typically has a vacuum stage which holds the sample secure during the measurement. Probes are attached to three axis micro-manipulators which can position the probes with high accuracy. The positioning of the probes is done manually while observing with a long focal length microscope. A Cascade Micromanipulator 6000 probestation is used to test antenna samples which use the HF probing

technique. To interface the output of the antenna to the testing system, high frequency probing requires the use of special IDT contact pads for measurement. The contact pads to the IDT are fabricated for a specific probe pitch of the GSG probe type. The pitch of the probes is defined as the lateral spacing between the ground and signal contact elements. These probes require a matching GSG pad layout for contact to the test device. An image of an IDT sample with 150 µm pitch GSG probe pads is shown in figure 2.45.a. Because the sample must be secured to the probestation stage when using the HF probing technique and the HF probes are highly susceptible to breaking, the ability to apply external testing stimuli during measurement is limited. In the case these external stimuli are necessary for testing, such as the application of magnetic fields or RF excitation, a wire bonding connection method is used to connect the IDT to the test system. In this technique a 20 µm diameter aluminum wire is bonded using ultrasonic energy to a gold contact pad patterned into the IDT structure. Gold bond pads are typically larger than 200 µm square and 150 nm in film thickness. The other end of the wire is attached to copper traces on a Rogers high frequency substrate. These copper traces typically form the contact pads for additional electronics or transmission lines which will eventual interface with an SMA connector through which the device is connected to the testing system. Because this method does not require the use of a sample stage or contact probes to make electrical connections, the device under test can be used in a wide variety of test environments. This allows for significantly increased flexibility when designing experiments at the cost of increased noise and the inductive reactance introduced by the bond wires. A SAW filter device fabricated with wire bonding pads is shown in figure 2.45.b.

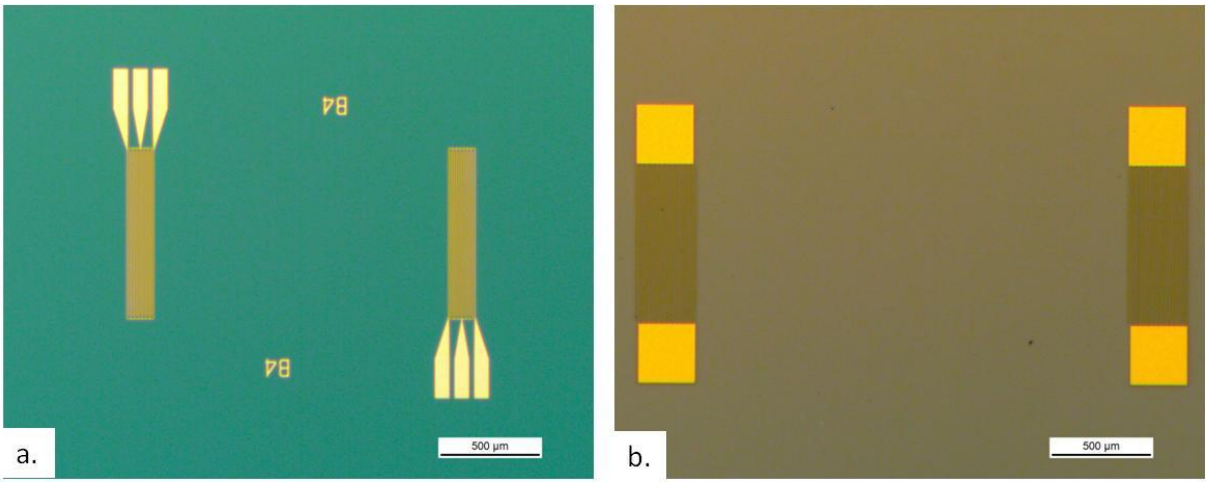

Figure 2.45 – a. A SAW filter device with GSG probe contacts for measurement. b. A SAW filter device with wire bonding pads for measurement.

Samples which use the wire bonding connection method must also have a carrier board to which the electrical connections from the IDT are made. These carrier boards are fabricated from many substrate types but are most often Rogers high frequency substrates of the RO4360G laminate type and the RT5880 duroid type. The precisely controlled loss and electrical properties of these substrates allows for the design of proper transmission line patterns to and from high frequency components on the carrier which minimize environmental noise and impedance mismatch. Substrates used in this work are either 0.72 or 1.54 millimeters in thickness and have full ounce (32 µm) double sided copper cladding. Patterning on the board is performed using i-line lithography and etching. To begin this process a mask design is built in AutoCAD design software. This mask design is translated into a tool path and used by a Heerbrugg Wild AvioTAB TA30 rubylith cutter to cut the design pattern into a rubylith film which is then manually exfoliated to produce a complete photomask. A clean substrate is cut to size and the protective film is removed. The substrate is mounted into a Headway PMW32 controlled photoresist spinner. AZ5214-E photoresist is applied to the substrate surface with a glass dropper

until complete surface coverage is achieved. The substrate is spun at 2000 rpm for 40 seconds. The substrate is then soft baked in a Transite convection oven for 120 seconds at 110^{o}C. Following baking and cooling of the substrate, the mask is aligned to the substrate and the assembly is mounted resist side down in a UV light box (Millington Machine Co. VF-MMDP). The light box exposes the substrate with UV energy for 180 seconds. The substrate is then transferred to a development solution of 1:4 AZ400K developer to water and developed for 90 seconds with constant agitation. The substrate is rinsed in water and dried with compressed air before hard baking for 300 seconds at 110^{o}C in a BlueM transite convection oven. Following lithography, the substrate is then transferred into a 1:1 water to ferric chloride ($FeCl_3$) copper etching solution. If the backside copper is to remain un-etched or saved for double sided patterns, the back of the substrate is protected with cellophane tape before etching. The substrate is mounted into a Nalgene holder which suspends the substrate in the etching solution to prevent contact with the stirring rod. The solution is heated to 55^{o}C on a hotplate and stirred at 400 rpm with a 25mm stirring rod. Etching takes approximately 30 minutes to complete but is checked constantly to ensure over etching does not occur. The sample is then rinsed and dried. The backside covering, if used, is removed and the photo resist is stripped in acetone. If a double layer board is being fabricated, the substrate is drilled with alignment holes and the front side patterns are protected with cellophane tape. Lithography and etching is performed on the second layer using the same procedure as was previously described for the first layer with the addition of a mask alignment step prior to UV exposure. Figure 2.46 shows a completed rubylith mask after cutting and exfoliating and a single sided carrier board fabricated on RO4360G substrate using the same mask.

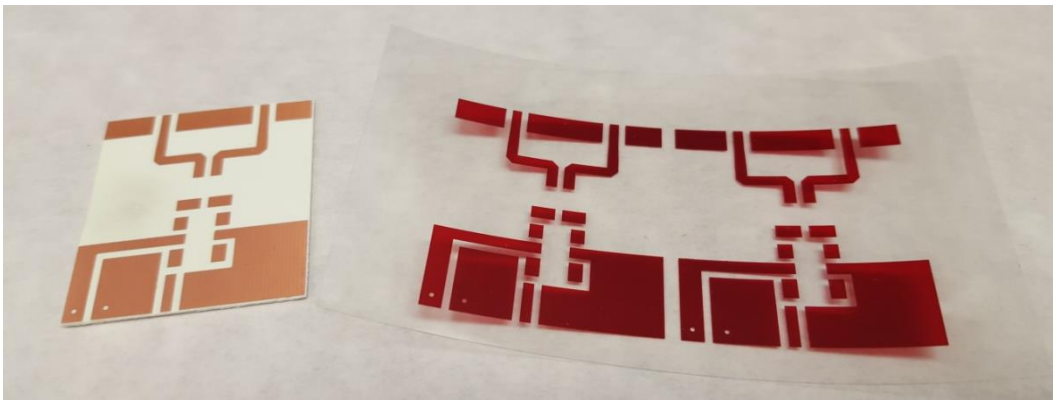

Figure 2.46 – A rubylith mask (right) and an RO4630G substrate after lithography and etching is performed (left).

A wide variety of board configurations are used for measurement of the multiferroic antenna. The two main classifications of carriers used in this work are those containing a board mounted low noise amplifier and those without any active electronics. Boards without active electronics are used for direct testing of the IDT impedance as well as the transmission response of the antenna. These boards can also be used in test setups where space or the presence of DC power wires are an issue such as the resonant cavity tests discussed in following sections. Boards without electronics have a simple coplanar waveguide transmission line which the IDT is directly bonded to in a single ended arrangement. The geometry of the CPW is designed along with the known electrical properties of the substrate to match the 50 Ohm source impedance of the network analyzer used for measurement. The opposing end of the transmission line is connected to an SMA connector which is of the end launch or surface mount termination style. A carrier board with a completed antenna die and no amplifier electronics is shown in figure 2.47.

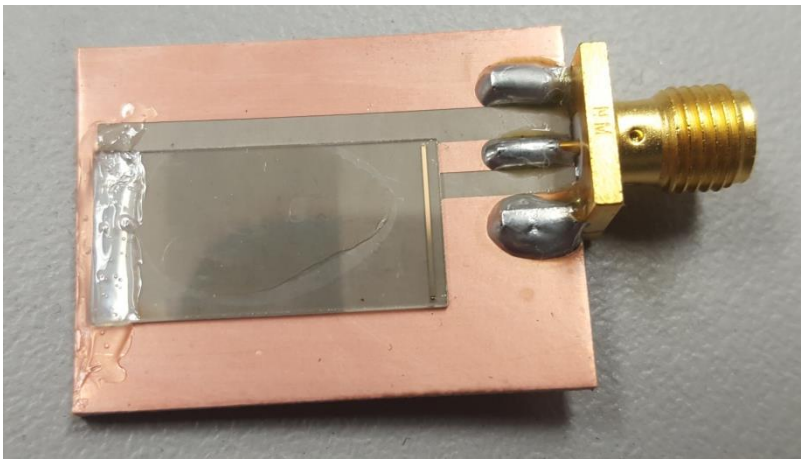

Figure 2.47 – A SAW antenna test device on a carrier board fabricated on RT5880 with no active test electronics.

Before transmission testing is performed, several operating characteristics of the IDT are obtained through the use of a simple SAW bandpass filter test. In this test two IDT patterns, identical in geometry to the antenna device, are used to send and receive surface acoustic waves. Often times these tests can be performed on an actual antenna sample if the second wave generation IDT is patterned onto the die. The resulting transmission data allows for the observation of the characteristic frequency response of the IDT electrodes. Reflection data can be used to obtain the characteristic impedance of the electrodes which can then be correlated to simulation impedance data, as was shown previously, to validate the IDT portion of the simulation. To perform this test, a sample is physically attached to a carrier board, patterned with two CPW transmission lines, using cyanoacrylate based adhesive (Loctite 401). The input and output IDT are wire bonded in a single ended arrangement to two isolated CPW transmission lines which are terminated at SMA connectors of the edge launch type. The left image in figure 2.48 shows a 230 MHz SAW filter die attached to a RO4360G carrier which has been prepared for two port IDT characterization tests. The input and output SMA lines are connected to a

calibrated HP 8720ES vector network analyzer using ports one and two respectively. Both S12 transmission data and S11 impedance data is recorded using the VNA. An example transmission plot is shown for a 230 MHz antenna die in figure 2.48.a for devices with and without the nickel resonator elements. It is seen that the presence of the nickel elements significantly decreases the transmission magnitude by 10 dB indicating the acoustic wave experiences a large amount of scattering from the now highly periodic interfacial condition at the substrate surface. It is also important to note from this plot the bandwidth of the main peak and the locations of the sideband peaks and nulls for following transmission tests. Figure 2.48.a also gives the insertion loss into the system (-5 dB) which characterizes how efficiently the SAW travels in the material and how well matched the output IDT is to the 50 Ohm VNA test port. Figure 2.48.b shows the real and imaginary impedances for the 230 MHz IDT. From the vector magnitude of these two resulting curves the IDT impedance is found, in this case, to very closely match the 50 Ohm test port of the VNA. This data set is useful in characterizing the potential system losses due to reflections and how a matching circuit can be designed, if needed, to reduce these mismatch losses.

Often times it is desirable, when dealing with small signal amplitudes, to amplify the output signal from a receiving antenna as close to the source as possible to reduce the effect of environmental noise or transmission line loss. For this reason many multiferroic antenna carrier boards are constructed with a built in low noise amplifier (LNA) which is placed at the same location as the die. A commercially available design is chosen based around the Analog Devices

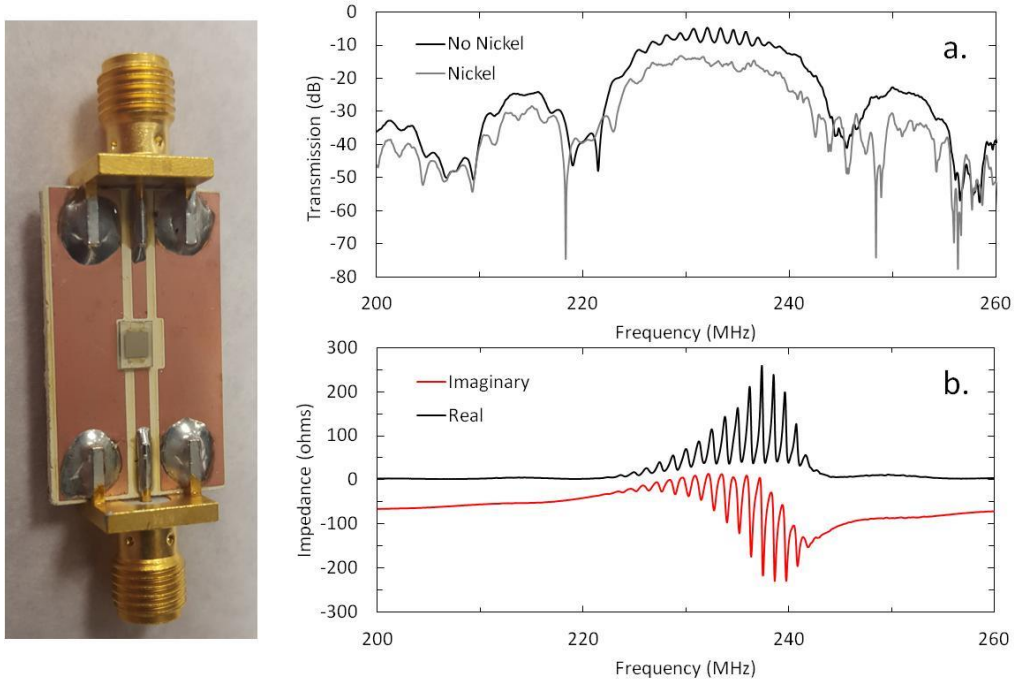

Figure 2.48 – A 230 MHz SAW die bonded to an RO4360G carrier with non-magnetic SMA connectors (left). a. The S12 transmission response of 230 MHz filters with and without nickel resonators between the IDT electrodes. b. The real and imaginary components of the S11 impedance from the 230 MHz IDT.

AD8350-15 RF amplifier. This device is a differential amplifier which produces 15 dB of gain with a -3 dB bandwidth of 1 GHz. The impedance at the differential inputs and outputs of the amplifier is 200 Ohms. The amplifier is powered from a single polarity 5-10 Volt supply and has a current consumption of 28 mA. For the purposes of the multiferroic antenna, the amplifier is configured for differential input and single ended output. This provides optimal connection to the measurement system while maintaining the common mode noise rejection characteristics offered by differential connection at the low signal IDT input side of the circuit. The amplifier is configured according to the circuit diagram shown in figure 2.49.

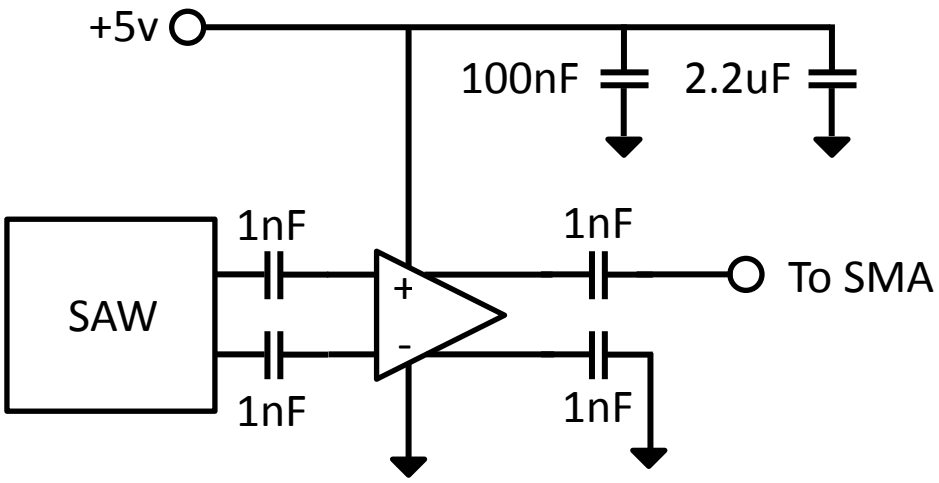

Figure 2.49 – Schematic diagram of the amplifier circuit used to amplify the signal coming from the IDT of a multiferroic antenna. The amplifier in the schematic is the Analog Devices AD8350-15.

To characterize the operation of this amplifier circuit for use in SAW applications, the amplifier is tested for both gain and threshold input power. SAW bandpass filters are fabricated on a lithium niobate substrate and diced into 4x4mm samples. The filters consist of two identical IDT electrodes spaced 0.8 mm apart. The IDTs have a finger pitch of 8.5 μm resulting in a filter center frequency of 230 MHz. A sample is mounted on a carrier board which allows for the single ended connection of both IDTs to a two port HP 8720ES vector network analyzer testing system without the use of amplifying circuitry as was previously shown. An additional sample is mounted to a carrier board with the amplifier circuit shown in figure 2.50 electrically connected to the output IDT of the filter. The amplifier output is connected to one test port of the VNA. The input IDT of this board is driven directly with the other test port of the VNA. The results for both the amplified and unamplified transmission scatter parameter are shown in figure 2.50.a. It is

seen from these plots that the shape of the frequency response curve remains the same with only the magnitude of the amplified signal increasing by roughly 10 dB when the amplifier is used. The small variations in the frequency response between the two samples are attributed to tolerances in the fabrication of the sample die and the addition of dispersive reactive components in the amplifier circuit. To study the threshold input power for the AD8350-15 amplifier, the test sample and board with the amplifier circuit is measured at various input power levels. In this test the source port power is set to incrementally decreasing values of 0, -20, -40 and -70 dBm at the directly connected SAW generation IDT. At each power level, the output transmission response of the filter is measured through the attached amplifier circuit. The results are shown in figure 2.50.b. It is seen from these plots that the amplifier remains sensitive to very low levels of power on its input. The side lobes of the filter remain visible even at an input power level of less than

-90 dBm.

Following sample preparation onto the appropriate style of carrier board and basic characterization of the IDT electrode, the sample is now ready for transmission testing. As was derived previously, the most optimistic radiation efficiencies from a multiferroic antenna to a

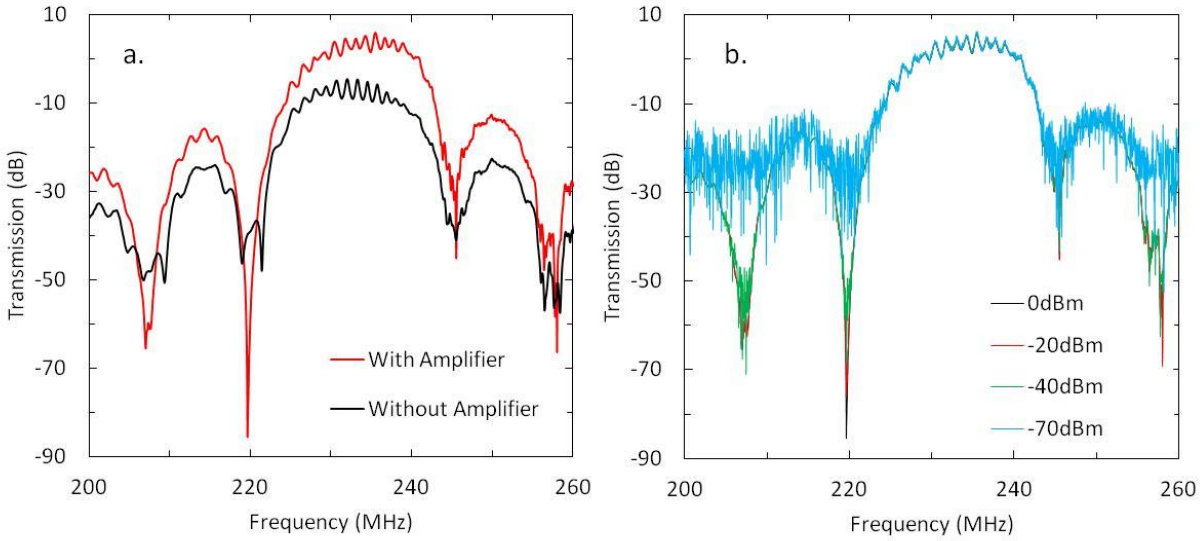

Figure 2.50 – a. The transmission spectra of a SAW bandpass filter with and without the use of an AD8350-15 RF amplifier. b. The transmission response of a SAW bandpass filter, measured using an AD8350-15 amplifier, for various excitation powers.

receiving or transmitting source are achieved in the near field within a distance of λ/100. The test systems used in this work correspond to source/antenna separations within this region. It was also shown previously that the precise application of a magnetic bias field is required to maximize the response of the multiferroic antenna. This field also serves as a decoupling variable to remove non-magnetoelastic transmission noise components from measured data. This field is accomplished with the use of a computer controlled electromagnet or less frequently permanent magnets. Permanent magnets are used where the testing fixture cannot physically be placed inside the pole gap of the magnet. Such is the case with large resonant cavities and tests requiring microwave probe connection to the sample.

A schematic diagram of a basic two port multiferroic antenna test system for wire bonded samples using an electromagnet for DC magnetic biasing is shown in figure 2.51. Antenna samples and the associated carrier board are mounted between the poles of a water cooled Varian electromagnet. This magnet can accommodate test fixtures up to 120 mm in width and can apply over 1T fields depending on the pole spacing and the current applied. The sample is typically mounted to a stage which allows for the rotation of the sample with respect to the applied magnetic bias field. An electromagnetic radiator is oriented near the sample such that the polarization of the radiated wave matches that specified by simulation. The radiators used in this work take several forms as will be discussed in following sections. Both the radiator and the multiferroic antenna sample are connected to individual test ports of an HP 8720ES network analyzer which performs a full two port analysis of the scattering parameters of the system. This data is collected using a GPIB connection to a computer through a National Instruments GPIB-USB-HS. This GPIB connection is also used to control the bias field by controlling the winding current of the electromagnet from an Agilent 6684A system power supply. The current passes through a DPDT relay which switches the current direction through the electromagnet windings for bipolar magnetic field application. The relay coil is controlled by using a National Instruments 6009 control voltage output which switches an MJE340 based coil driver. The coil switching voltage and current are 25 V and 48 mA respectively. The magnetic field magnitude is monitored using an FW Bell 5080 gauss probe whose analog signal output is read into the computer from the USB connected National Instruments 6009.

During testing the magnetic field can be incrementally swept from high field to low field then to high field again to obtain full hysteretic data. More commonly, however, the system is initialized using a large saturating negative field after which data is taken as the field is swept from zero to

a positive saturating value. This one way measurement reduces the data set and measurement time while collecting only the response in a single desired operating region. At each field step the current and magnetic field values are recorded as well as the full two port frequency domain response for the system. This data is typically normalized to a low or zero bias field value to emphasize signal variations with respect to magnetic field rather than frequency. The data is represented as a two dimensional color-map plot where frequency and magnetic field represent the x and y axis respectively and color variation corresponds to changes in the transmission or reflection parameters. In other testing fixtures the procedure is identical with the exception that

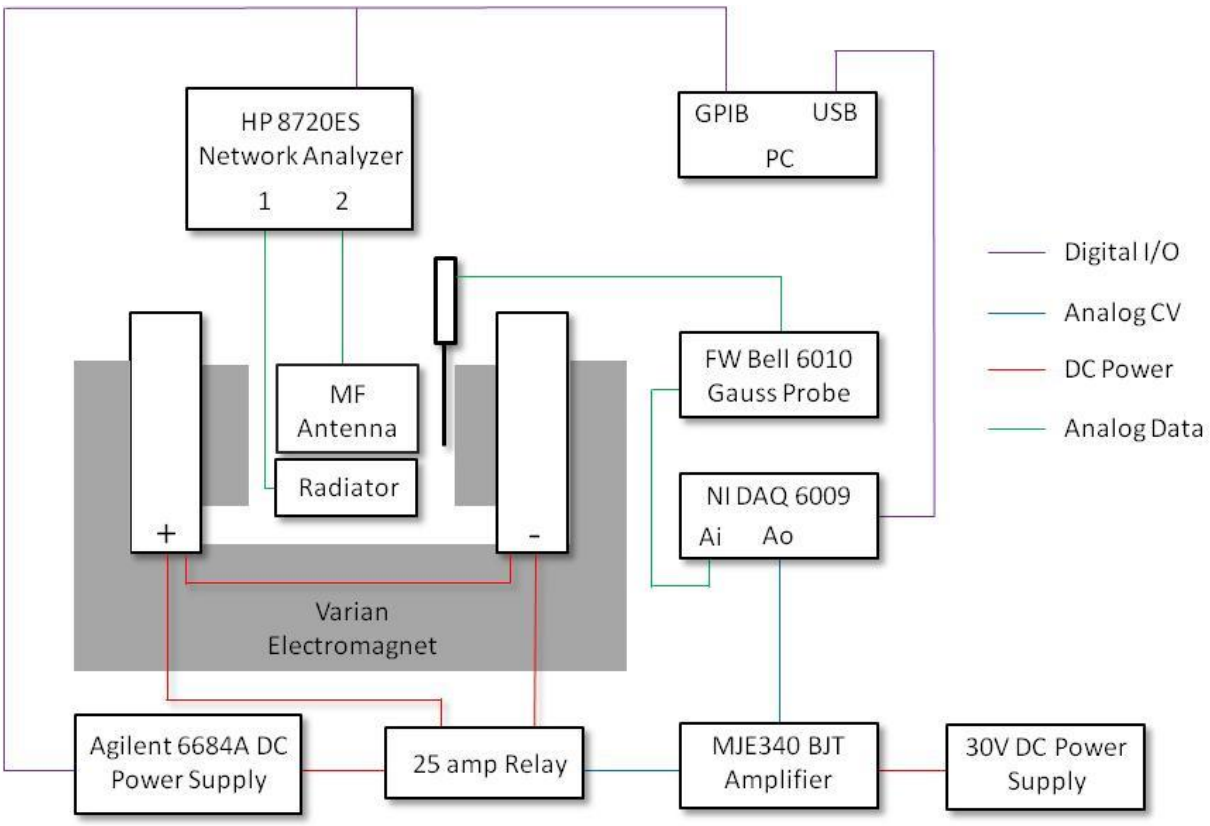

Figure 2.51 – A schematic diagram of the test system used for transmission testing of a wire bonded multiferroic antenna device.

the magnetic field is applied using a manually controlled permanent magnet. This magnet is attached to the test system using a spacer or holder which precisely controls the separation between the magnet and the test sample. This type of test requires characterizing the fields as a function of distance from the magnet prior to testing using a gauss probe. Because this field/separation relationship is highly non-linear, the magnitude and directions of the bias fields from a permanent magnet are very difficult to control using this method and it is reserved for cases where the use of an electromagnet is not an option.

Several types of radiating transmitters are used to deliver radio frequency magnetic fields to the magnetoelastic resonator array on the sample. These devices must be well characterized such that the radiated field magnitudes and polarizations correspond to those which are expected to mechanically actuate the magnetoelastic elements. These devices must also be designed to minimize the reflection of energy back into the electrical driving source caused by impedance mismatch. The need for such precise operating conditions makes simulation of these radiating devices critical to achieve optimal behavior. The electromagnetic waves module in the COMSOL Multiphysics software package is used to simulate these devices under appropriate test conditions. Three types of radiating devices are used in this work; the cavity resonator, the transmission line and the loop antenna. The most basic form of the loop antenna is that of a conducting wire loop carrying a time varying current. For the purpose of this work, the loop antenna is considered very small with respect to the free space wavelength and the current distribution throughout the loop circumference is therefore considered uniform. A dynamic magnetic moment is induced perpendicular to the loop plane and the associated electromagnetic wave radiates outward from the device. The geometry of the loop and the conductivity of the wire are critical factors in determining how efficiently the loop current is transformed into

electromagnetic energy as was derived in previous sections. For this reason the size of the loop is typically made much larger than that of the multiferroic antenna making the field uniformity over the magnetoelastic array better than would result with the use of a smaller loop antenna. A loop antenna can be made to resonate with the series addition of a capacitor. In conjunction with the inherent loop inductance this capacitance acts as the electric field storage component of an LC oscillator circuit. Because the geometry of the loop is usually fixed by the patterning process, the capacitor chosen is a variable type which allows tuning of the loop resonant frequency to the desired value. This resonant frequency value is chosen to coincide with the expected resonant frequency of the multiferroic antenna during measurement to maximize transmission efficiency. Tuning capacitors are of the film type (Sprague) or the air variable type (E.F. Johnson). Air variables are chosen for excellent stability and high quality factors where film capacitors are used when small footprint and larger tuning ratios are required. Figure 2.52.a shows a variety of radiating loops used for transmission testing of multiferroic antennae. The same basic shorted wire geometry can be seen in each device. Figure 2.52.b shows a side view of a resonant 20mm loop antenna simulated using finite elements. The loop is driven with 0dBm input power at 250MHz from a 50 ohm source. To ensure there are no reflected components in this simulation, a 2λ sphere surrounds the loop which acts as a perfectly matched boundary layer to absorb the outward travelling wave components. The z component magnetic field strength is represented by color hue and the red lines show equipotential fields. It is computed that the magnetic component of the radiated field through the loop center is about 0.05 A/m for the prescribed driving conditions. It is also demonstrated in these simulations that the fields are fairly uniform at a sample located just in front of the loop plane. Identical models for other loop geometries

demonstrate similar levels of field uniformity and magnitudes which range from 0.01 to 0.5 A/m when excited with 0 dBm input power to coincide with the experimental test system power.

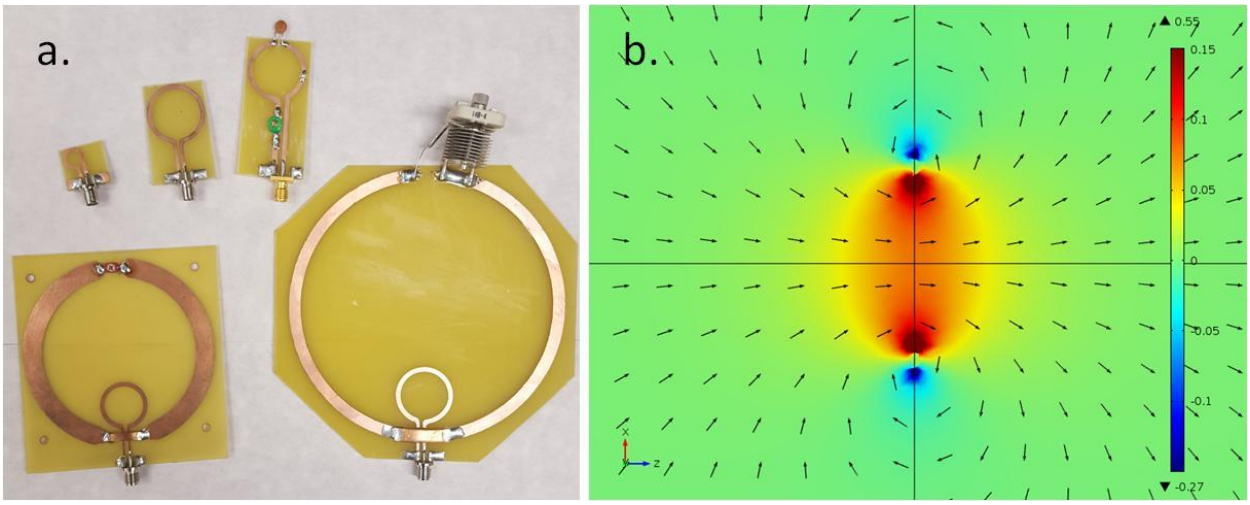

Figure 2.52 – a. A collection of resonant and non-resonant loop antennae used as radiators in transmission testing. b. Side view of the simulated magnetic fields radiated from a resonant 20 mm diameter loop antenna at 250 MHz for 0 dBm input power. The black arrows indicate magnetic field direction. Color contrast corresponds to field magnitude measured in A/m.

During testing the loop radiator is fixed with respect to the multiferroic antenna. The direction of the AC magnetic field is directed outward perpendicular from the loop plane as shown in figure 2.52.b. The sample is placed just in front of the loop center to maximize the field strength at the resonator location and to avoid the large field gradients further away from the loop. The loop is connected to the VNA test port and excited with 0 dBm of input power. The reflection response from the loop allows for the observation of how efficiently energy is being delivered from the loop to the surrounding environment. In the case of a non-resonant loop, the reflection is expected to be a low value, typically -3 to -10 dB, across the entire frequency band. Because

energy is distributed evenly across all frequencies for the non-resonant loop, this type of radiator is useful in characterizing the resonance characteristics of the mulftiferroic antenna without superimposing the dispersive frequency response of the source. In the case of the resonant loop antenna, energy is available only at a narrow range of frequencies but at significantly larger magnitudes than the non-resonant case. This appears as a dip or inverted peak in the reflection response which indicates the resonant frequency of the loop/capacitor circuit. The capacitor can then be tuned such that the resonance of the loop matches that of the IDT and magnetoelastic element resonance by overlapping the S11 and S22 dips.

Another common radiating device used in transmission measurements is the transmission line. A typical RF transmission line consists of a conductive trace on a dielectric substrate and often uses precisely placed ground planes or ground traces to control the impedance of the line. In this work the coplanar waveguide (CPW) style of transmission line is used as a radiating device. The CPW line consists of a central signal trace and two parallel, closely spaced ground traces patterned in the same plane as the signal trace. These types of transmission lines are intended for the transport of electrical signals from one physical location to another with minimal reflections or loss per unit length. For use as a radiating pattern, the CPW is shorted on one end to achieve the maximum current condition through the signal trace. The antenna sample under test is placed directly on the top of the signal trace which is designed to accommodate the width of the magnetoelastic resonator array. This arrangement allows for the application of relatively large magnitude, uniform magnetic fields to the resonator array on the antenna sample. The transmission line, if designed properly, has no resonant frequency behavior up to the first standing mode of the line. This makes the CPW line an ideal radiator for testing other resonance phenomena. Stripline measurements are common in ferromagnetic resonance experiments where

the absorption of energy from the radiating transmission line by a ferromagnetic sample is observed as a function of applied magnetic field. This experimental technique was demonstrated in previous sections as a tool for characterizing the magnetic properties of the magnetoelastic material, FeGaB. The CPW radiators used in this work are patterned onto RT5880 substrates and are designed to have a right angle mitered bend in the transmission line. This 90^o signal trace orientation allows for the ideal perpendicular orientation of the AC magnetic field radiated from the CPW to the DC magnetic bias field applied by the electromagnet while maintaining an outward SMA connector orientation. A secondary CPW line is patterned perpendicular to the main radiating trace which functions as the transmission line that serves to connect the test system to the IDT electrode on the sample die. This short IDT CPW is oriented 90^o to the radiating CPW to avoid excessive cross coupling between the lines. A CPW radiator and sample transmission line board is shown in left image of figure 2.53 before the mounting of a sample die. The results of a finite elements simulation of this type of radiating transmission line excited with 0 dBm at 250 MHz are shown in figure 2.53.a and 2.53.b. Figure 2.53.a shows a top view of the circuit board with the y axis magnetic field magnitude represented by color hue. It can be shown that the field strength is highly uniform over the width of the central CPW trace. The magnetic field strength at the location of a sample 0.5mm from the board surface is 0.3A/m. Figure 2.53.b shows a cross section view of the transmission line with y-axis magnetic field magnitudes represented by color hue and field direction represented by the red arrows. It is seen that the field quickly decreases in magnitude and becomes non-uniform moving away from the top of the radiating trace. Frequency characterization of these CPW patterns shows a very wideband response up to the first standing wave mode which appears at roughly 2 GHz for the device shown in the left image of figure 2.53. During testing, the sample die is bonded to the

CPW radiator signal trace using adhesive (Loctite 401) and wire bonds electrically connect the sample IDT to the short sample CPW. SMA connectors interface the radiating CPW line and the sample CPW line to the measurement system. The board is placed between the poles of the magnet with the bias field parallel to the radiating trace. Transmission data is recorded at a variety of bias field values.

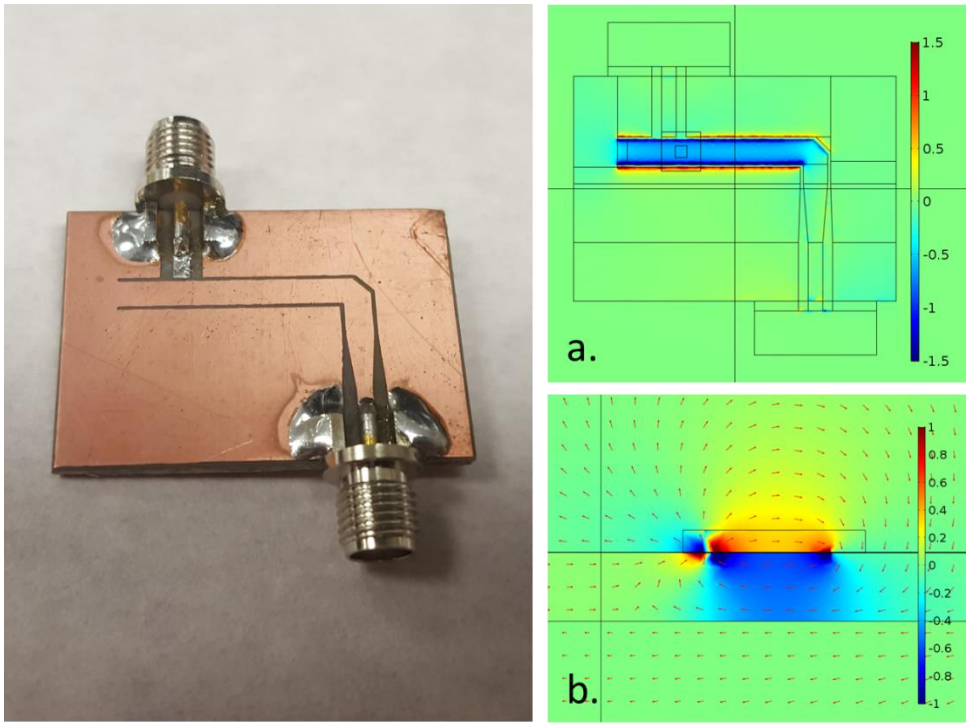

Figure 2.53 – An image of a right angle CPW transmission line radiator used for RF testing (left) built on a RT5880 substrate. a. A simulated top view of the y axis magnetic fields (A/m) CPW pattern when excited by 0 dBm of power at 250 MHz. b. The simulated cross section view of the bus at the location of the sample. Red arrows indicate magnetic field direction.

The last type of radiating device used for transmission testing of the multiferroic antenna is the resonant cavity. This structure is identical to an electromagnetic waveguide which serves to

transmit energy from one location to another. The cavity, however, is designed not to transmit electromagnetic energy but rather to store it at very narrow frequency bands. This is done by creating an electromagnetic standing wave confined in a conductive walled enclosure. The dimensions of this enclosure are designed to support one or a number of transverse Hermite-Gaussian modes for a specific operating frequency. Because of this frequency/dimension relationship, the geometry of the cavity can become large when lower frequencies are involved. For these tests a 520 mm long cylindrical cavity with roughly 133 mm diameter is used to sustain a TM_{010} resonant mode at frequencies from 130 to 170 MHz. This cavity length corresponds to a quarter of the electromagnetic wavelength in air. The frequency is tuned using a telescoping conductive post which is oriented concentric to the center of the cavity. The length of this post is adjusted using a threaded brass rod which has a tuning handle outside the cavity. The cavity is excited using a pure copper loop antenna which extends 50 mm from the top surface of the cavity. This loop is rotated about its mounting axis parallel to the long axis of the cavity to maximize the quality factor of the cavity mode it generates. The left image in figure 2.x shows the cavity used in testing of 150 MHz multiferroic SAW antennae. The tuning post and plastic tuning handle are shown extending from the top of the cavity. The loop and sample holder connectors are seen also extending off center from the top of the cavity. The center image in figure 2.54 is a finite element result for the magnetic field norm inside the cavity as viewed from the side at an excitation power of 0dBm and frequency of 150 MHz. This distribution of magnetic field correlates with the expected quarter wavelength behavior the cavity is designed for. The field strength at the sample location is calculated to be about 0.3 A/m and the uniformity over the expected sample region is excellent. The right image in figure 2.54 is a simulated top view of the cavity with the color hue representing the norm magnetic field strength in A/m. The

black arrows indicate the field directions at different points in the cavity. It is seen that the TM_{010} mode corresponds to a magnetic field distribution which circulates around the central post in the cavity. It is expected that the largest electric field amplitudes will be at the bottom of the cavity furthest from the excitation loop antenna which is confirmed using this simulation (results not shown).

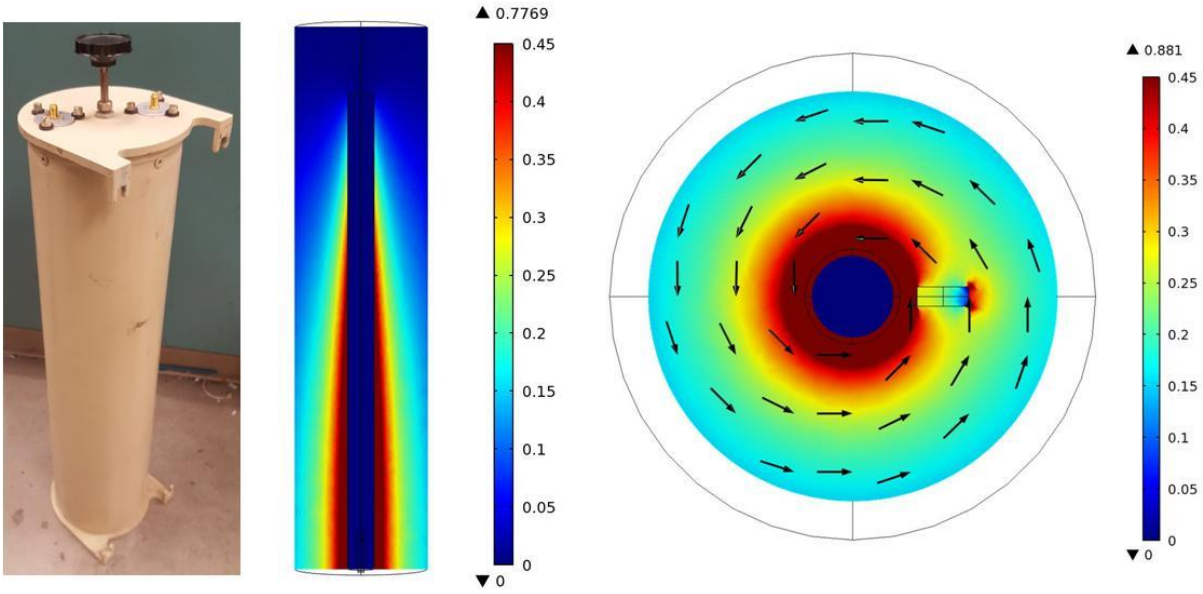

Figure 2.54 – A 520 mm long quarter wave cylindrical resonator cavity used for transmission testing (left). Side view of the simulated magnetic field magnitude inside of the cavity at 0dBm input power and 150 MHz (middle). Top view of the simulated cavity showing magnetic field uniformity and direction (right). All field values are shown in A/m.

During testing, the sample is placed inside the cavity through a hole in the top plate of the cavity. This hole is covered by an aluminum disk which has been machined to accept a panel mounted SMA connector through which the network analyzer can interface with the sample. Other

configurations are also used where the sample is inserted into a small rectangular opening machined into the side of the cavity nearest the top such that the sample is located inside the magnetic field node of the cavity. The network analyzer interfaces with the sample through a printed transmission line on the carrier board. Because the diameter of the cavity is larger than the pole gap of many commercially available electromagnets, the sample must be biased using strong permanent magnets placed on the outside of the cavity. The bias field strength is characterized before testing by placing a gauss probe inside the cavity at the sample location and applying the bias magnet. The narrowband frequency behavior of the resonator cavity makes it useful for the application of large magnetic fields with precise uniformity and control over reflections. This narrow band response also tends to superimpose itself onto the output response of the multiferroic antenna, which is a collection of broad and narrow band components making decoupling system noise from the desired response difficult when using the cavity radiator.

Two additional radiating devices were developed during the course of this work but their use in actually transmission testing was limited in favor of the previously described radiators. These are the gapped ferrite ring and the near field probe. The near field probe is functionally identical to the transmission line radiator in that a current carrying conductor is used to generate strong dynamic magnetic fields very close to its surface. During testing this current carrying conductor is placed over the sample to actuate the magnetoelastic resonators and transmission is measured between the conductive radiator and the sample. In this work, the probe tip consists of glass substrate which has been patterned with a conductive patch. This patch is fabricated using 200 nm gold deposited using electron beam evaporation and patterned using liftoff. The gold patch is a 3 mm square region composed of thin horizontal stripes with current feed points located on opposite sides of the square. An image of the probe tip is shown if figure 2.55.a. During

operation, the current feed lines are connected to a source which drives RF current across the patch which, in turn, creates a dynamic magnetic field distribution at the surface of the probe tip. A simulated y axis field distribution at the surface of the probe tip is shown in figure 2.55.b for an input power of 0 dBm at 250 MHz. Color hue corresponds to the magnetic field magnitude in A/m and the black arrows indicate the magnetic field direction. The field magnitude near the tip is about 0.7 A/m with good uniformity over a small 1 mm^2 area directly above the center of the patch. The addition of stripes is to allow for ease of visual alignment of the patch over the resonator array of a SAW antenna using a long focal length microscope. It is shown in simulation that these stripes do not affect the uniformity of the field at the location of the sample during measurement.

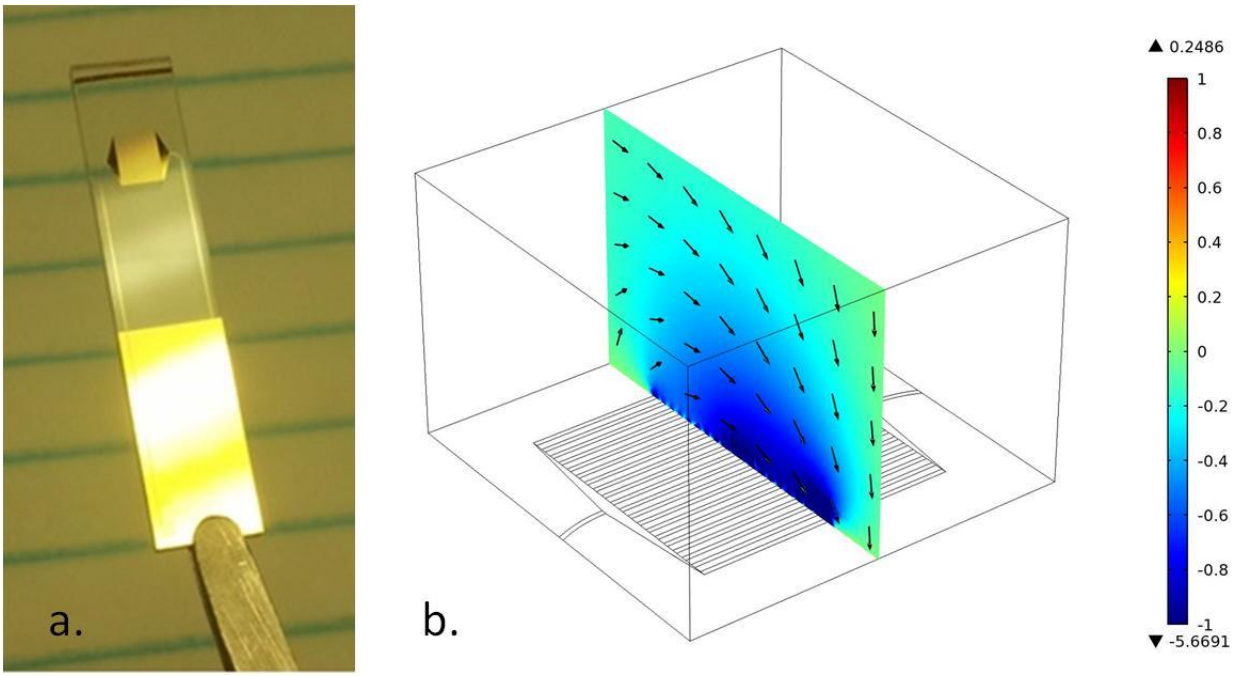

Figure 2.55 – a. A probe tip used in the transmission testing of a multiferroic antenna. b. The simulated magnetic field distribution at the surface of the probe tip. Color hue corresponds to magnetic field magnitude in A/m and black arrow show the field direction.

During testing the probe tip is bonded physically and electrically to an FR4 carrier board which contains a transmission line and SMA connector through which the probe interfaces with the network analyzer. The carrier and tip are mounted to a three axis micro-positioner which is then rigidly mounted to an aluminum stage. The antenna sample is placed into the middle of an electromagnet and the probe is positioned over the sample. The micro-positioner is used to visually align the probe tip with the magnetoelastic array with the aid of a microscope. The probe tip is lowered toward the sample taking precautions not to disturb the sample wire bonds. The probe is typically located within 1 mm of the sample surface during measurement. While simulation of the near field probe predicts desirable radiation characteristics, the resistivity of the gold traces used for actual device fabrication were not considered in these models. Because of this, the relatively high resistance of the long and thin gold transmission lines in actual fabricated devices produced large impedance mismatches with the 50 Ohm driving source that were not present in simulated results. This prevented the probe tip design from efficiently generating magnetic fields at the test end of the patterns. Ultimately these devices were not used for measurements in favor of the transmission line radiator which was significantly easier to fabricate and produced similar magnitude magnetic fields.

Another radiating device investigated for use in transmission testing of multiferroic antennae is the gapped ferrite ring. This structure is adapted from the writing systems used in many of the early magnetic tape based memories where strong, highly localized magnetic fields were required to magnetize hard magnetic films. In this type of radiating device a ferrite toroid (Epcos N87), which is commercially available for use in the construction of high frequency transformers, is used to amplify radio frequency magnetic fields in a very small region outside of the face of the toroidal core. This fringing field region is created by cutting a 0.2 mm gap

through the core using a diamond saw. The face of the toroid is polished flat so that the resonator array on the antenna die can be placed close to this gapped area. In commercial tape memory write heads, this gap is often filled with a diamagnetic material to "push" the magnetic flux away from the highly permeable core. In this work the gap is left unfilled. The discontinuity introduced by the gap in the ferrite core causes the magnetic field to expand outward from the core a very short distance from the polished face with much larger magnitudes than could be created using a coreless coil alone. This field amplification leverages the large permeability of the ferrite material to increase the field strength by several orders of magnitude. Figure 2.56.a shows a 20 mm diameter Epcos N87 ferrite toroidal core which has been gapped and polished for transmission testing.

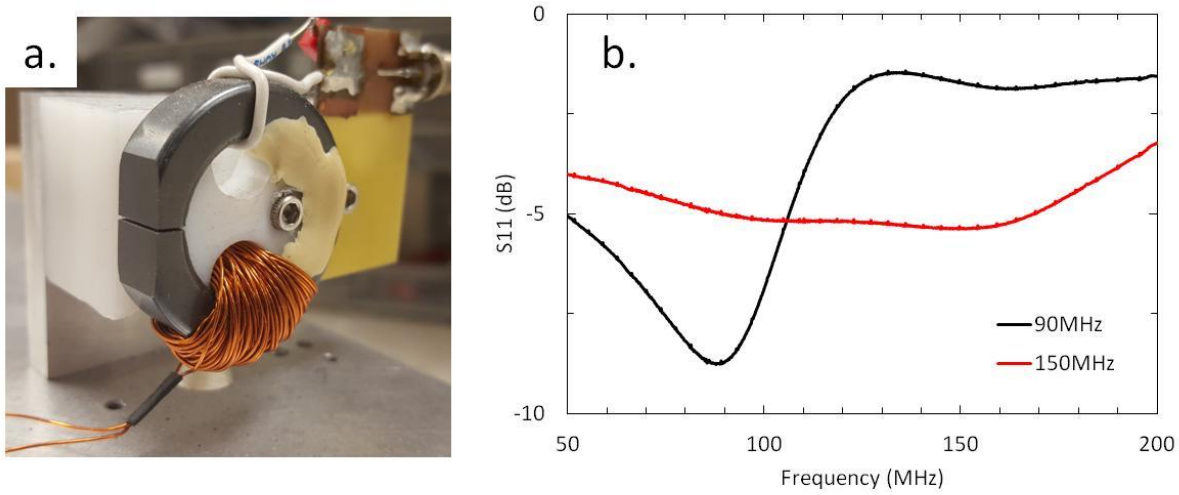

Figure 2.56 – a. A gapped ferrite toroid which has been prepared as a transmitter antenna for measurement of a multiferroic antenna. b. The return loss for the ferrite core as the resonant frequency is tuned from 90 to 150 MHz.

During testing with the ferrite core, a jacketed wire loop is wrapped around the toroid as is shown in figure 2.56.a. This loop can have a single turn or have many turns depending on the

loop inductance required to operate the connected oscillator circuit. A variable film capacitor (Sprague) is placed in series with the wire loop and the driving source to form a tunable resonant LC circuit. A DC bias coil is constructed using many turns of enamel coated transformer wire opposite to the wire excitation loop which can also be seen in figure 2.56.a. This bias coil is connected to a laboratory current source and serves to deliver a controlled bias field to the resonator array during measurement. Unfortunately this coil arrangement fixes the AC and DC magnetic field directions to be parallel with one another reducing the versatility of this type of test fixture. The coil is rigidly mounted to an aluminum stage and the sample is aligned to the gap in the core using a three axis micro-positioner and a long focal length microscope. Upon sample to core alignment, the capacitor is tuned such that the resonance of the ferrite core matches that of the SAW device by overlapping their reflection parameters. Further investigation into the properties of the ferrite materials used to build this device at the desired test frequencies shows that the cumulative magnetic losses inside the core material become quite significant above 100 MHz. To characterize these losses, the reflection coefficient from the excitation loop is measured as the core resonance is tuned to frequencies above 100 MHz as is shown in figure 2.56.b for frequencies of 90 and 150 MHz. It is seen that when the core frequency is set to 150 MHz the pronounced resonant dip observed at 90 MHz is no longer visible. Instead the quality factor of the resonating system becomes very low at frequencies above 100 MHz indicating the increase in magnetic loss in the core material. This loss can be attributed to a number of factors but is mainly interpreted as the dynamic hysteretic motion of magnetic domains in the ferrite core. This leads to a rapid decrease in the real component of the ferrites relative permeability at high frequencies which correlates closely with the published values for this material. Due to these significant inefficiencies introduced by the ferrite core material, air core loop antennae are

chosen to replace ferrite systems as no ferromagnetic material is present in their construction. For this reason the loop antenna discussed previously can fill the need for small footprint, high Q radiators at the frequencies required in this work.

Because surface acoustic wave devices can communicate vibration energy across relatively long distances with low attenuation, wave reflections from the substrate edges or surface structures can create significant interference in the output response of the device. These reflections create identical frequency content which is phase shifted with respect to the original signal depending on the distance the wave has travelled before arriving at the output electrode. This time shifted interference appears in the output signal as a series of evenly spaced constructive and destructive frequency nodes, very much resembling a comb filter, superimposed onto the original non-reflected signal. Figure 2.57.a shows the transmission spectra of a SAW bandpass filter centered at 290 MHz. The strong comb like behavior shown in figure 2.57.a indicates the presence of many large acoustic reflection components in the output signal. The frequency envelope of these closely spaced comb filter nodes follows the expected bandpass response for this SAW filter. To confirm presence of these reflected signal components, the complex valued signal can be viewed in time domain using a Fourier transformation. Figure 2.57.b shows the Fourier transformation of the SAW bandpass output signal. A strong initial pulse is seen at t=0 which indicates the presence of electromagnetic coupling between the two IDT electrodes. The first non-reflected SAW signal is seen at t=2 μs which corresponds to the time the acoustic wave takes to travel from the input IDT to the output IDT. Following this incident pulse are a series of reflected waves arriving at the output IDT at evenly spaced intervals in time. These periodic signal components correspond to the acoustic wave reflections from the boundaries of the sample die as well as the input IDT electrodes. It is seen in this time domain response that the reflections decay

exponentially with time indicating the attenuation of wave energy as it is reflected from these boundaries. This attenuation occurs due to the conversion of mechanical energy to electrical work at the VNA output test port and any scattering or damping of the wave incurred during its travel time. While these reflected waves are not completely detrimental to the performance of the multiferroic SAW antenna, it is desirable to reduce the signal components to only the incident non-reflected wave to remove any uncertainty in the measurement.

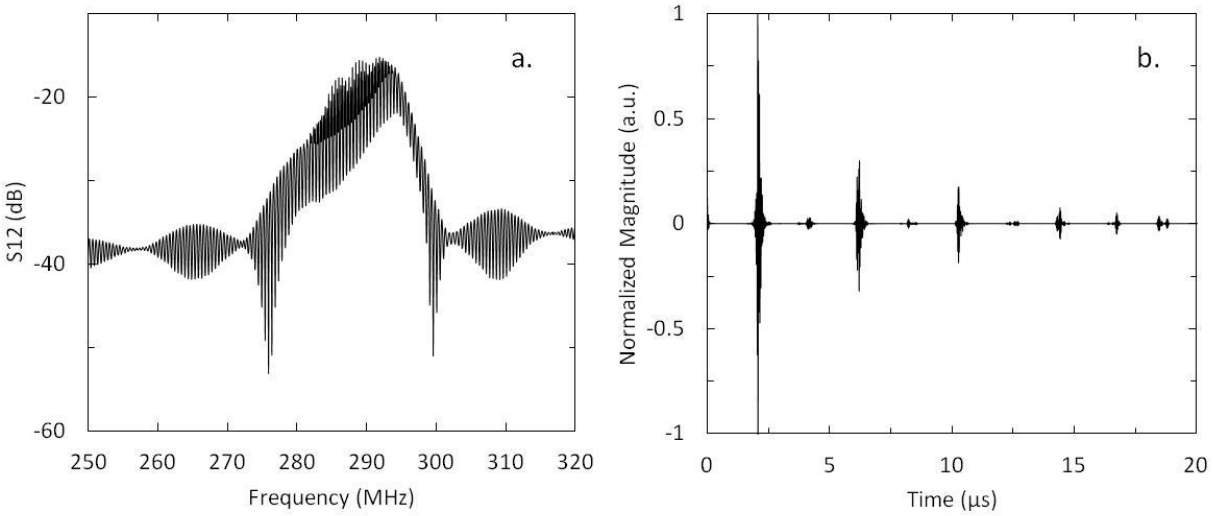

Figure 2.57 – a. The transmission spectra of a SAW bandpass filter centered at 290MHz. b. The corresponding time domain response of the bandpass filter obtained using Fourier transformation.

Removing the reflected acoustic components from the output signal of the SAW antenna can be accomplished in a number of ways. In this work we examine post processed removal of reflected signal components using time domain transformation and mechanically damping the reflected wave. Mechanical damping of the reflected wave involves extending the SAW die boundaries

outward such that a thick, lossy material can be applied to the surface of the sample. This layer acts to absorb and attenuate the incident acoustic wave before it can reflect from the diced sample edge. Typically this technique is reserved for larger devices where the increase in die size will not significantly affect the measurement footprint of the total packaged device. In this method a 5mm un-patterned region is allocated on the saw die near the edge of the resonator array opposing the output IDT electrode. A commercial single part epoxy (E6000) is applied onto the surface of the die and spread evenly over a 3-4 mm region extending outward from the edge of the die. The epoxy is allowed to cure overnight at room temperature after which a 0.5-1 mm thick compliant absorbing layer is formed. Figure 2.58 shows a prepared SAW die with a cured epoxy damping layer on the edge of the device opposing the output IDT. To examine the efficacy of this damping epoxy layer, a simple bandpass experiment is performed. In this test a SAW bandpass filter is constructed on a 10x10 mm lithium niobate substrate and the characteristic reflection and transmission response of the filter is recorded using an Agilent E8720ES VNA. This is shown in the grey plots in figure 2.58. The expected comb filter frequency response produced by the reflected signal components is observed in both the reflection (2.58.a) and the transmission (2.58.b) response of the filter. Following this characterization, E6000 epoxy is applied to the center of the SAW die and spread evenly into a 4x10mm rectangular region whose long axis is parallel to the long axis of the IDT electrodes. The epoxy is allowed to cure overnight at room temperature into a 0.5-1 mm thickness film. The reflection and transmission spectra of the filter are then measured following the same procedure as before. These now modified responses are shown as the black plots in figure 2.58. It is immediately apparent from figure 2.58.a that the epoxy damping layer absorbs virtually all of the acoustic energy which previously took the form of a reflected acoustic wave. This leaves the

expected electrical reflection response characteristic of test port to input IDT impedance mismatch. Also obvious from the transmission spectra, shown in figure 2.58.b, is the significant attenuation of the surface wave by the epoxy layer. The central peak of the bandpass filter response is attenuated by roughly -35dB when the epoxy layer is added with only a small remaining portion of the acoustic wave visible at 300MHz. This indicates that the epoxy damping layer will serve to effectively reduce acoustic wave reflections in the multiferroic SAW antenna.

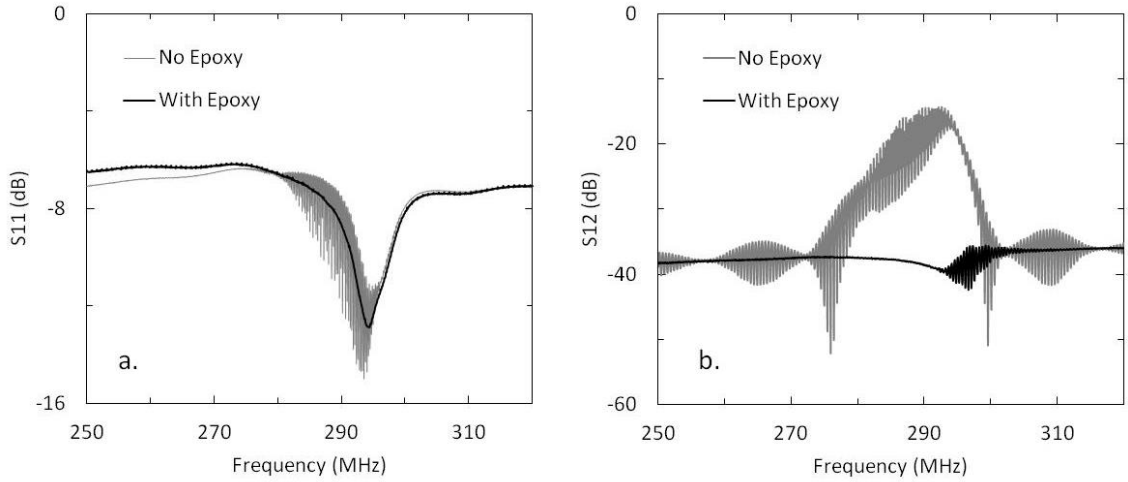

Figure 2.58 – a. The reflection response of a SAW bandpass filter centered at 290MHz with and without epoxy in the acoustic gap. b. The transmission response of the SAW bandpass filter with and without a damping epoxy layer.

Reducing the effect of reflection noise in the output response of a mulitferroic antenna is also accomplished using software based time windowing. This technique is applied when the SAW die is too small to apply an epoxy damping boundary without effecting the antenna operation of the device. This process is performed after the measurement data has been collected. The

frequency domain data is transformed into time domain using an inverse fast Fourier transformation (iFFT) method. The results of such a transformation were shown previously in figure 2.57.b where the time domain of a SAW bandpass filter was computed. Specific time ranges can be selected from this time domain data which correspond to the desired signal components. In the case of the bandpass filter transmission data shown in figure 2.57.b, the desired part of the signal is the initial acoustic pulse which occurs at about 2μs. To isolate this signal component, only the time range between 1.75 and 5.96 μs is selected for transformation into the frequency domain. This is a process called time windowing or gating where narrow windows of time are used to isolate certain spectral components. The data inside this time window is then transformed back into the frequency domain using a fast Fourier transformation (FFT). The transformed data for the SAW filter is shown in the black plot of figure 2.59. It is seen that the effect of acoustic reflection is reduced in the transformed data which yields a clean bandpass response. Few comb-like filter nodes still appear in the transformed data which correspond to short acoustic reflections which arrive at the output IDT in the same time window as the initial acoustic signal. These reflections are most likely generated at the die boundary closest to the source IDT. Because of their overlapping arrival times, these short reflection components and the desired acoustic pulse cannot be separated using time windowing, somewhat limiting the usefulness of the technique.

Software based time windowing is also used to reduce the electromagnetic components of the output signal. These signal components originate from the nature of electromagnetic coupling between the output IDT and other IDT electrodes or, in the case of antenna transmission measurement, the transmitting antenna. Direct coupling into the IDT electrode occurs due to the motion of charges in the conductive fingers by the impinging electromagnetic wave. These

charges are terminated at the load impedance, in this case the VNA test port, and appear as received power. The ability for the IDT to detect these stray impinging fields depends on the polarization of the incoming wave with respect to the IDT and the geometry of the IDT electrode

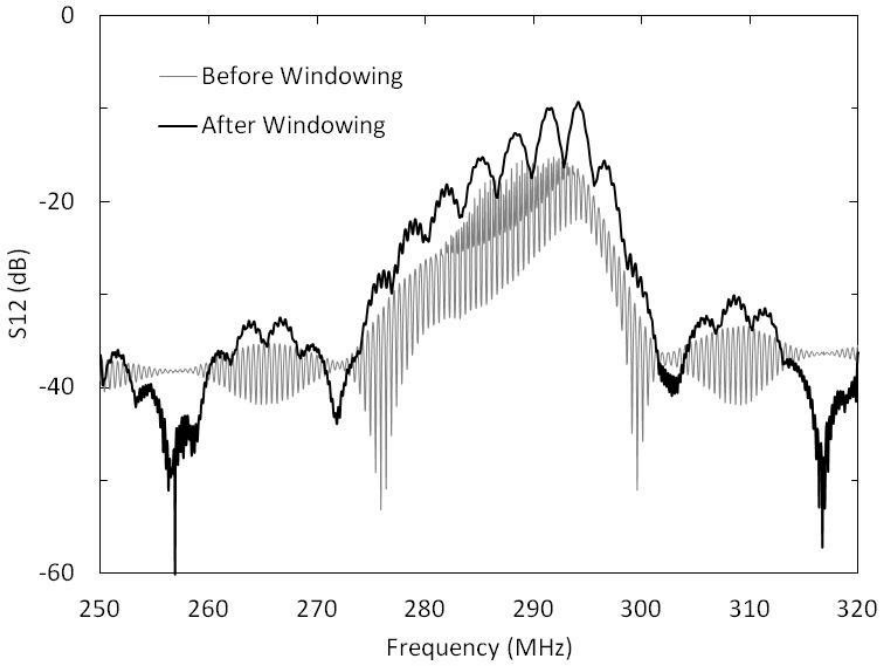

Figure 2.59 – The bandpass response of a SAW filter before and after time windowing the initial acoustic signal. The time window is applied from 1.75 to 5.96 μs.

Typically the IDT is small with respect to the electromagnetic wavelength making it a highly inefficient receiver antenna. Although the received power from this inefficient IDT antenna is small, it is comparable in magnitude to the expected output signal power from the vibration of the magnetoelastic material making it a significant source of measurement noise. The effect of this direct coupling was shown previously in figure 2.58.b where the acoustic coupling components, both direct and reflected, had been significantly attenuated by the epoxy applied

onto the substrate surface yet the S12 signal level remained constant across the frequency span at a value of about -38 dB. This indicates that there are broadband signal components which are responsible for low but non-negligible amounts of power being transmitted between the input and output IDTs. Using the iFFT method, described previously and whose results were shown in figure 2.57.b for a SAW bandpass filter, it is seen that at t=0 a small magnitude signal is present in the time domain data corresponding to this direct EM coupling. By time windowing this EM component out of the signal, as was shown in figure 2.59, the frequency response of the filter can be computed without this contribution. The noise floor of the windowed measurement reduces to the expected low level of a filter without this broadband electromagnetic coupling between the input and output IDT as can be seen in the filter nulls.

In the previous example the transmitted electromagnetic power between the input and output IDTs is small because these surface patterns both represent inefficient antennas. During RF transmission measurement, however, this is typically not the case. In this case a strong radiating electromagnetic antenna is placed in the near field of the SAW device and the coupling between the two is recorded. For this measurement method the nature of coupling between a strong radiator and the weak IDT receiver must be characterized to examine its contribution to the overall signal magnitude. To perform this characterization two samples are constructed with identical IDT electrode patterns on two different substrates. One substrate material is lithium niobate while the other is high resistivity silicon with a 500 nm surface layer of silicon dioxide deposited using PECVD. The gold electrodes have a pitch which corresponds to a SAW center frequency of 150MHz on the lithium niobate substrate. Samples are diced and bonded physically and electrically to a short carrier built on Roger RT5880 substrate with no electronics and a simple single ended SMA termination. The sample is connected to an Agilent E8720ES VNA

and placed into the H-node of a 20.5 inch long cylindrical TM_{010} notch filter cavity. The source test port of the VNA is connected to the excitation loop antenna in the cavity and the sample is rotated so that the magnetic field lines are oriented parallel to the IDT fingers as they would be during actual device testing. The cavity resonance is varied by actuating a screw driven conductive post which extends or contracts in length through the cavity center. The cavity reflection (dotted) and the loop to IDT transmission (solid) are shown in figure 2.60.a for the sample built on lithium niobate at several cavity resonances. It is shown that the resonant mode of the cavity couples strongly into the IDT patterns with little energy being delivered outside the fundamental frequency. It can also be seen in the transmission response of figure 2.60.a that the corresponding resonance of the IDT serves as a loss mechanism by transforming electrical energy into mechanical energy. This is made apparent from the additional nulls, which extend below the -50 dB off resonance baseline, corresponding to the reflection behavior of the IDT. Similar coupling behavior is observed in the sample built on a silicon substrate whose cavity reflection and loop to IDT transmission response is shown in figure 2.60.b. The strong transmission coupling between the loop and IDT follows that of the cavity resonance mode with a signal magnitude identical to that of the sample built on lithium niobate. The absence of the additional nulls further confirms the correlation of the nulls seen in the lithium niobate transmission response and the piezoelectric generation of acoustic waves.

Time windowing is an effective tool in removing these early arriving signal components to reduce the effect of direct coupling between the transmission antenna in the measurement system and the output IDT electrode. A slightly more difficult source of noise in the test system to eliminate is that of acoustic wave generation by unused IDT patterns on the substrate surface due to this direct electromagnetic coupling. Matching IDT electrode patterns are fabricated onto

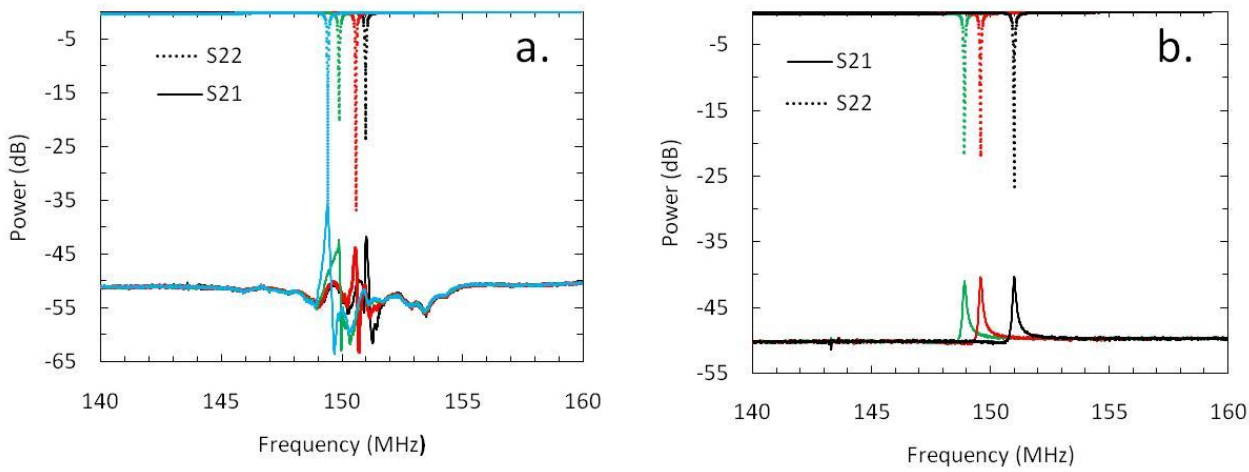

Figure 2.60 – a. The cavity reflection (dotted) and transmission (solid) between the cavity and sample for an IDT built on a lithium niobate substrate inside a cylindrical TM_{010} cavity. b. The reflection and transmission for an IDT built on 500 nm SiO_2 on high resistivity silicon in the same cavity.

samples in order to test the characteristic IDT frequency response and impedance prior to transmission testing. These IDT patterns are typically placed on either side of the magnetoelastic resonator array. During transmission testing of the multiferroic antenna a single IDT is used to measure the signal output from the device while the other IDT remains un-terminated. While filtering of electromagnetic signal components originating from antenna to output IDT coupling is possible using time windowing, the removal of EM generated acoustic signals created by the opposing IDT is not. This is due to the very closely spaced arrival times of the wave expected from the magnetoelastic resonator array and the surface wave generated at the opposing IDT. To confirm the presence of this phenomenon, an experiment is performed to examine the output of a SAW IDT electrode when it is excited by a nearby radiating transmission line. The sample has

an identical IDT which is spaced approximately 0.8 mm from the output IDT. A SAW bandpass filter with center frequency of 238 MHz is bonded to the top of a shorted CPW transmission line with a 90 degree mitered bend built onto Rogers RT5880 substrate. The sample is oriented over the wide signal trace of the main CPW such that connection to another CPW transmission line, oriented 90 degrees to the main CPW, can be performed using wire bonding to the IDT pads. The width of the main CPW line is designed such that both IDTs are located above the copper trace. The shorted main CPW line and the IDT connection line are terminated at SMA connectors. The test sample and carrier board are shown in the left image of figure 2.61. The transmission response between the shorted CPW transmission line and the output IDT of the SAW sample is measured for different termination conditions on the unused IDT electrode. Three conditions are tested; open, short and removed. For open termination the unused IDT electrode is left electrically unconnected. For the short termination, a wire bond is applied between the two sides of the IDT electrode. Removal of the unused IDT is performed by gently scraping the gold pattern from the die surface using a sharp hobby razor. The time domain response for each of these terminating conditions is shown in figure 2.61.b. It is seen from these plots that the removal of the unused IDT electrode virtually eliminates the slow arriving acoustic components of the output signal. Small amplitude acoustic reflections are observed in the response in the removed case which corresponds to wave reflections originating from the source IDT to the closest edge of the sample die. These results confirm that the unused IDT electrode is producing surface acoustic waves through wireless electrically excitation by an impinging electromagnetic wave. It can also be shown that the arrival time of these acoustic signal components correspond to those expected for magnetoelastically driven vibrations. For this reason, the unused IDT electrode pattern is omitted from devices which are to be tested as

receiver antennas. It is also obvious from the results shown in figure 2.61.b that the incident electromagnetic wave couples significantly more power to the output electrode than the induced acoustic response. It is shown that the acoustic components in the time domain signal are at least an order of magnitude smaller than the incident electromagnetic wave arriving at t=0s. This effect also appears in the frequency domain response as comb filter nodes in the case of open and shorted terminations where the acoustic noise is strongest.

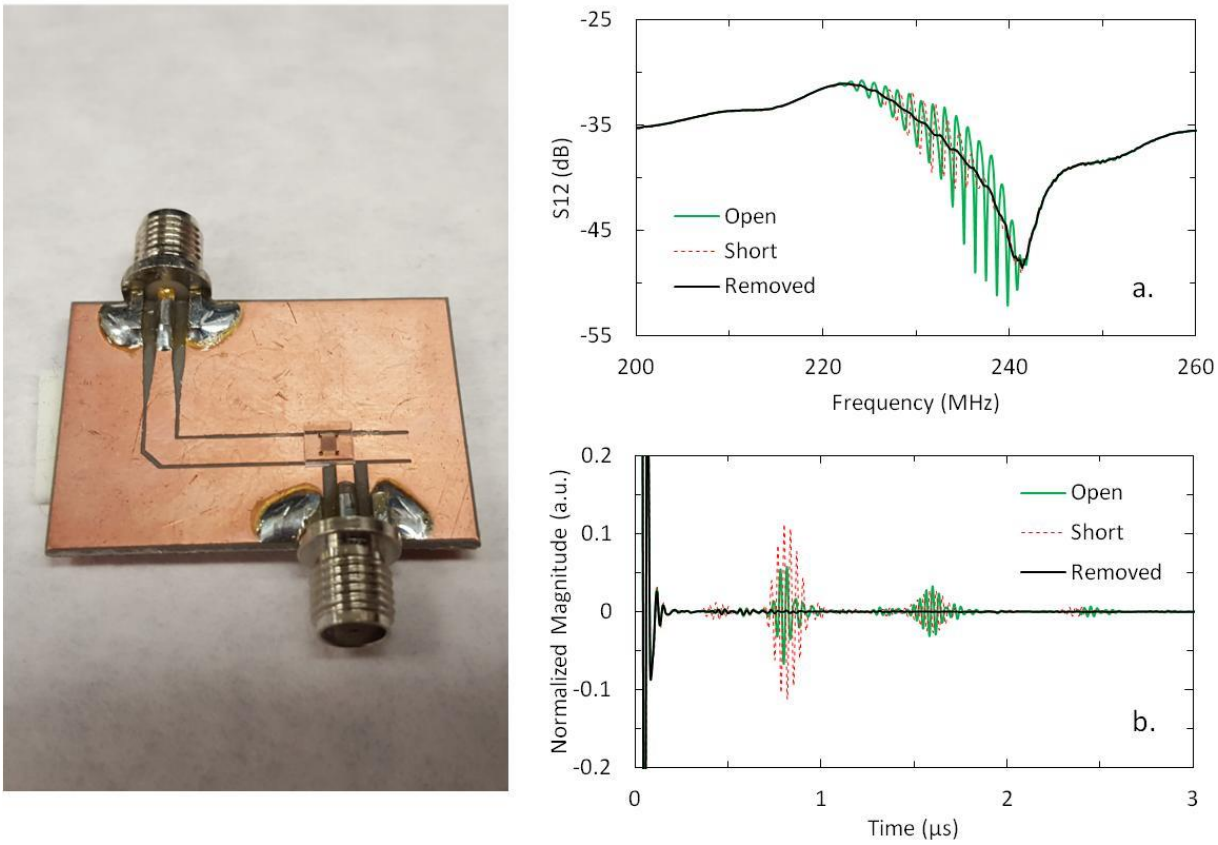

Figure 2.61 – Left image shows a shorted coplanar waveguide with a SAW bandpass filter bonded to the top of the signal line. a. Frequency domain plot of the transmission response from the CPW to the SAW output IDT for three terminating conditions on the unused IDT electrode. B. Time domain response of the transmission response of the filter for three terminating conditions.

The last source of noise investigated in the test system is that of ferromagnetic resonance in specific test system components. Because transmission testing involves near field radiating antennae and resonant excitation of IDT electrodes, the materials which compose the test system components also experience non-negligible amounts of electromagnetic energy from these sources. This electromagnetic energy for the frequencies of interest in this work is applied in the near field region of the radiating source. Because of this, materials placed near the devices under test can significantly change the operating characteristics of the IDT electrodes or the radiating transmitter. If the electrical properties of these components is altered during testing, as would be the case with materials under ferromagnetic resonance conditions, this can appear as signal variations in the measured data. Modulation of the nearby materials electrical properties with applied magnetic field in particular can introduce signal variations which will produce results similar to the expected magnetoelastic behavior. In order to systematically identify the components of the test system which will produce these unwanted signal variations, an experiment is designed to probe the near field region where an actual test sample would be located using a resonant electromagnetic radiator which resembles the transmission lines used to couple the IDT electrodes to the network analyzer. A 50 mm long CPW transmission line is fabricated on a RO4630G substrate and shorted at one end using a pure copper sheet. The other end of the CPW is terminated with a standard edge mounted SMA connector (Linx Technologies CONSMA003.031) through which the reflection coefficient of the CPW is measured using a network analyzer. The shorted CPW transmission line creates multiple standing waves in the waveguide when excited, resulting in high magnetic field magnitudes being generated at several narrow frequency bands. The fundamental mode of the shorted CPW in this case is about 2.4 GHz. During testing the CPW is placed inside the electromagnet of the test system shown in

figure 2.62. The CPW is oriented so that the ground plane is coplanar with the face of one of the magnet poles and separated by 2 mm. The normalized S11 reflection from the CPW is recorded as the magnetic bias field is swept up to 5000 Oe. The reflection data is shown in figure 2.62.b for a test frequency range from 2 to 10 GHz. The fundamental mode at 2.4 GHz and several of the higher order standing modes of the CPW are clearly visible as constant frequency color nodes. The 3.8 GHz harmonic appearing after the primary mode exhibits a strong decrease followed by an increase in the reflection response as the magnetic bias field is increased. This behavior is plotted as a function of the applied field for the 3.8 GHz mode in figure 2.62.a. It is seen that this behavior is symmetric about zero applied magnetic field and has clear hysteretic behavior indicating it is ferromagnetic in origin. Similar behavior is observed at the higher order standing modes appearing at 7.3, 8.4 and to a lesser extent 6.2 GHz. These curves follow a similar shape to those shown in figure 2.62.a but the magnetic bias field at which the lowest reflection magnitude occurs is now dependent on the frequency of the mode. This is represented as the blue colored, constant frequency regions in figure 2.62.b.

The relationship between the magnetic bias field at which the minima in the reflection response, shown in figure 2.62.b, occur and their mode frequency can be accurately described by the resonance equation for a thin ferromagnetic film described by Kittel [29].

$$\omega = \gamma\sqrt{B(B + \mu_0 M_s} \qquad [Eq. 2.86]$$

Where γ is the gyromagnetic ratio for an electron, B is the applied field and M_s is the saturation magnetization of the film. The coincidence of this relation with the experimentally measured results gives strong indication that the CPW is inducing ferromagnetic resonance in nearby components. The two most likely sources of this type of noise in the test system are the

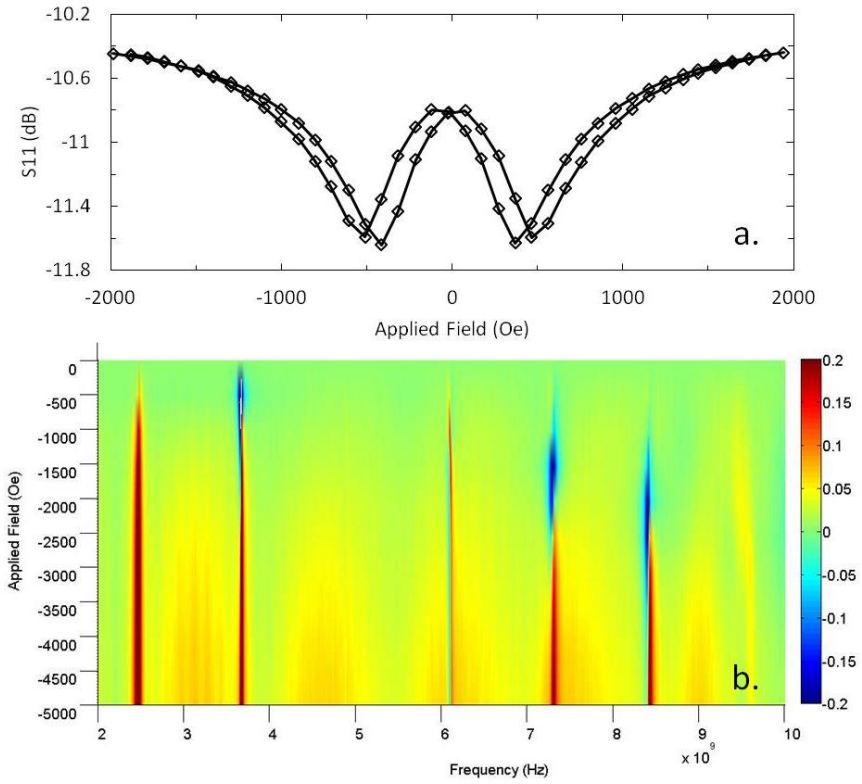

Figure 2.62 – a. The reflection coefficient versus applied magnetic field for a 50 mm shorted CPW inside an electromagnet. b. A colormap plot of the reflection coefficient versus field and frequency for the same experiment.

ferromagnetic poles and associated protective coating of the electromagnet and the RF connectors used to interface the test devices with the measurement electronics. The coating materials used in the main RF connectors used for measurement are not reported by the manufacturer but will typically have a thick nickel base layer for corrosion resistance. By using these connectors in proximity to the antenna device under test and under strong magnetic biasing conditions, ferromagnetic resonance can be excited in this outer nickel coating. To confirm the presence of the nickel base layer, two common connectors are tested in a laser based MOKE

magnetometer system. A right angle SMA adapter (Amphenol 132172) and an edge mount SMA connector (CONSMA003.031) are tested for the magnetization of their surface coatings. These connectors are chosen as they are common choices for many of the experiments performed in this work and they represent two very common types of coating types. The right angle adapter has a gold colored coating while the edge launch connector has a silver colored coating. An image of these two connectors is shown in figure 2.63.a. The outer coatings are polished with metal polishing compound to increase the reflectivity of the surface for testing. The normalized M-H behavior for the connectors is shown in figure 2.63.b. It is apparent from the resulting data that the coatings on both connector types exhibit strong ferromagnetic behavior consistent with that of pure nickel thin films. The "silver" coating type presents with slightly harder magnetization behavior possibly due to the variations in thickness between the two coating types.

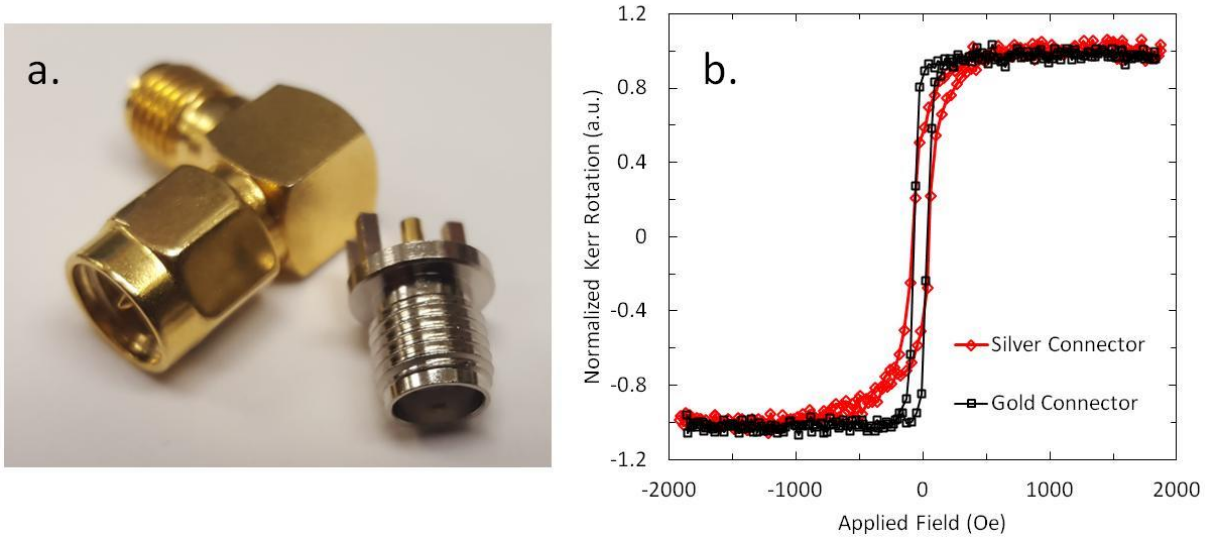

Figure 2.63 – a. Two representative SMA connectors used in antenna transmission experiments being tested for ferromagnetic coatings. b. MH behavior for the two types of coatings found on common SMA connectors measured using MOKE magnetometery.

Once the magnetic nature of the connectors had been characterized, the impact of using these types of components in transmission testing was examined. The previously used 50mm long shorted CPW transmission line is adapted for these experiments by removing the existing edge launch connector and replacing it with a new non-magnetic edge launch connector (Johnson Solutions 142-9701-801). The CPW is fitted into the test system and the reflection is recorded as a function of field using the same procedure as before. A color map plot of the resulting reflection coefficient from 1-10 GHz and bias fields up to 3500 Oe is shown in figure 2.64. When compared to the previous case, the strong absorption peaks appear to be concentrated at higher frequencies for the data shown in figure 2.64 but still exhibit clear FMR behavior. This change in the FMR characteristic indicates that there is still a component within the near field of the CPW transmission line acting to absorb energy through excitation of FMR. The next major ferromagnetic components of the test system which are investigated in this work are the pole pieces of the electromagnet used in biasing the antenna during testing.

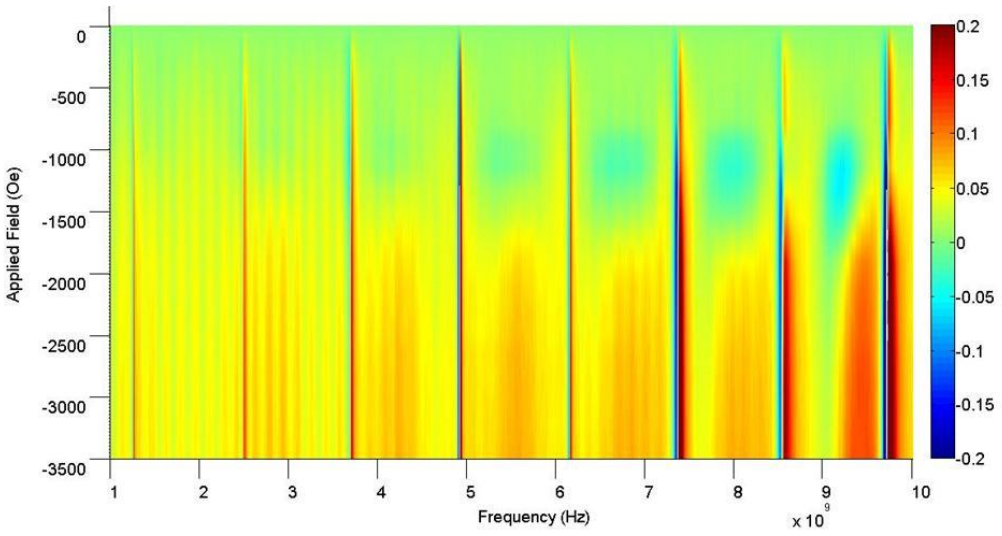

Figure 2.64 – The normalized reflection coefficient as a function of both frequency and bias field for a shorted CPW test using a non-magnetic SMA connector.

To examine the effect of the electromagnet poles on the measurement data the poles are covered with a thick foil of pure alloy 110 copper. This copper shielding layer has a thickness much greater than the skin depth of the impinging electromagnetic at the test frequencies of interest. Because of this, the incident electromagnetic wave incurs complete attenuation or reflection before ever reaching the underlying ferromagnetic pole material. Because the bias field is applied statically for these measurements, the copper shield has little to no influence on its magnitude or uniformity during testing. The effectiveness of this copper shield is tested by performing the same CPW reflection test as before with the copper shields attached for both the case of non-magnetic connectors and the connectors which have a ferromagnetic coating. In the latter case the full absorption spectra reveals similar behavior as that shown in figure 2.65.b for the case where no copper shield is present. The reflection magnitude for the 3.8GHz mode for this test case is shown in figure 2.65.a as a function of applied magnetic field. The magnitude follows similar behavior as was shown in figure 2.65.a with the minima occurring at a slightly higher bias field (712 compared to 414 Oe). The appearance of this behavior in both the case of shielded and non-shielded pole pieces as well as the results shown in figure 2.65 for non-shielded poles and non-magnetic connectors indicates that both of these components are responsible for the FMR absorption measured from the CPW line. To demonstrate this conclusion, a test is performed using both shielded poles and non-magnetic connectors in the same manner as before. The measured reflection results for this test are shown in figure 2.65.b. It can be seen that no FMR absorption behavior is present in the measured reflection data for this test case. The absence of the absorption minima is attributed to the now shielded electromagnet poles and the non-magnetic SMA connector. Use of these noise reduction measures is critical in achieving

magnetic noise isolation for transmission and reflection tests involving very small signal variations and resonant samples.

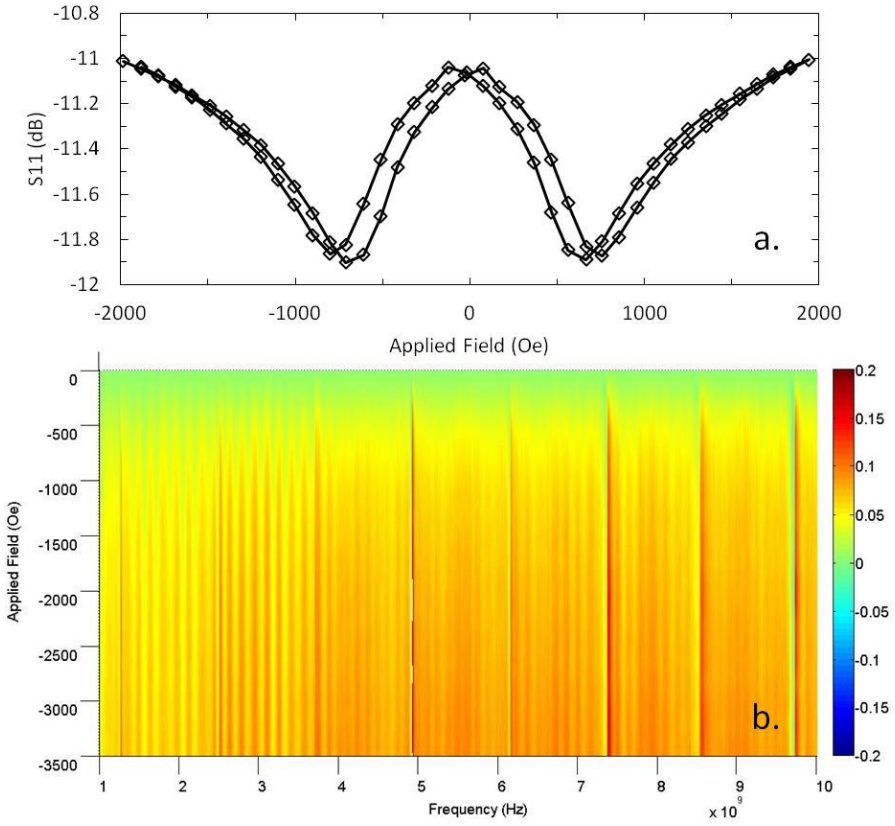

Figure 2.65 – a. The S11 reflection as a function of bias field for the test case of connectors with ferromagnetic coatings and shielded pole pieces. b. The reflection coefficient as a function of bias field and frequency for the case of both non-magnetic connectors and shielded pole pieces.

VII. Results

Figure 2.66.a shows a 170 MHz SAW antenna die on top of a shorted patch which has been printed on rogers RT5880. During the test the die is placed over the patch to excite the sample

with a uniform RF magnetic field and the sample is contacted with the RF probe (shown to the right of the image). Figure 2.66.b shows the S12 transmission response measured between the shorted patch and the SAW device for samples both with and without the nickel resonator elements. A distinct deviation from the reference sample is observed at the center frequency of the sample with magnetoelastic resonators. This deviation shows a 3 dB increase in the transmission response followed by a sharp drop to about -5 dB with respect to the reference. This indicates the presence of narrow band coupling in the response between the two at the frequency the IDT's and the resonators are designed to operate. It is difficult to extract a true transmission gain from this sample as the test setup is limited in its configurations; specifically in the ability to apply precise external magnetic fields to the sample which would allow for the modulation of the magnetoelastic coupling properties of the resonator elements.

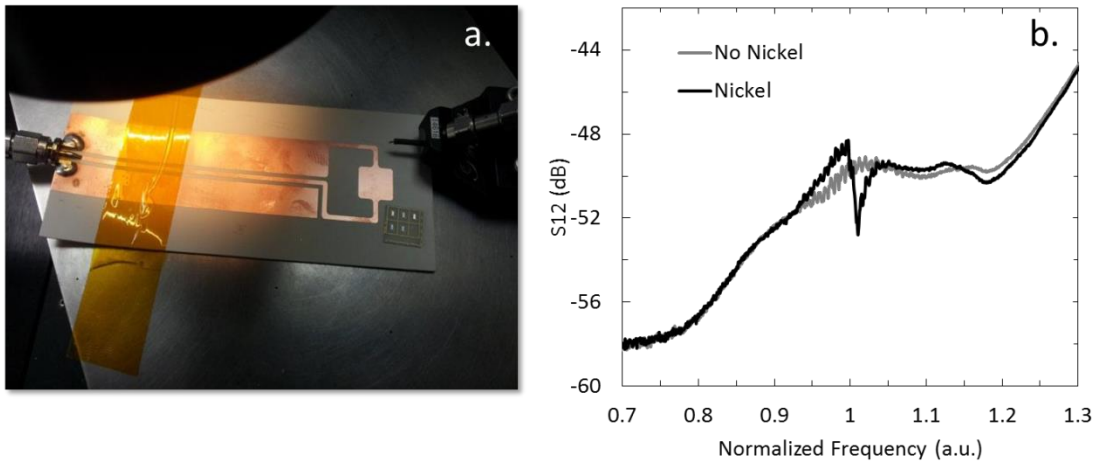

Figure 2.66 – a. A shorted patch like transmission line used to excite the SAW antenna sample shown placed near the patch. b. The transmission response for a 170 MHz SAW antenna for samples with and without magnetoelastic material.

Figure 2.67 plots the transmission response of a 150 MHz SAW antenna excited using a quarter wavelength cylindrical resonant cavity. The sample is placed into the magnetic field node of the resulting standing wave with the field direction aligned to the resonator excitation axis designed in the finite elements analysis. The transmission response shows a clear peak at the cavity center frequency and lower amplitude side band peaks which are believed to correspond to the SAW sidebands. The large central peak is known to be caused by the strong coupling from the cavity to the IDT patterns directly. When a saturating field is applied to the samples using a strong permanent magnet placed on the outside of the cavity wall, a 5 dB increase in the transmission signal magnitude is observed across the entire frequency band. This correlates with analytical predictions which show that above a saturating field the transmitted peak strength should be stronger than at the remnant state where the coupling coefficient is very low. This excitation technique, however, does not allow for the application of precise magnetic fields to the sample which would be necessary to observe the full field dependent behavior of magnetoelastic transmission.

Figure 2.68 shows the color map transmission surface for a 150 MHz SAW antenna which uses long stripe resonators instead of rectangles as it is being excited using a CPW transmission line. The signal trace of the line is placed below the substrate surface (0.5mm away from the resonator bed). The CPW in this case is shorted at the far end and has a broadband response up to 1 GHz. A clear increasing trend is observed in the case of both positive (b) and negative (a) applied field directions. This symmetric behavior indicates that the signal variations at the design frequency are due to ferromagnetic coupling. The stripe type discretization of the elements in this case, however, makes the reflection and Ohmic loss properties of the wave highly dependent on the electrical properties of the nickel material. This could result in the frequency shifting behavior

seen in the data as the permeability of the nickel resonator is decreasing with increased bias field application. The signal magnitude is extremely low (about 0.2 dB change).

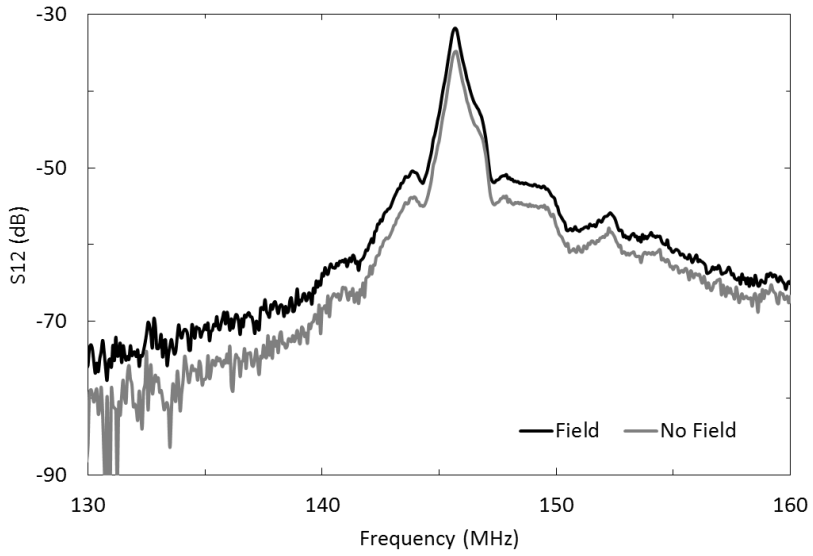

Figure 2.67 – The transmission response of a 150 MHz SAW antenna based on nickel/lithium niobate while excited by a ¼ wavelength resonant cavity. The applied field is above the saturating field .

Figure 2.70 plots the transmission response of a 150MHz SAW antenna using rectangular shaped resonator elements being excited by a shorted CPW transmission line. The response is shown for positive (b) and negative (a) applied magnetic fields. No field dependent transmitted response is observed for either applied field direction. Despite the sample being placed very close to the transmission line, a mechanical excitation of the elements through the magnetoelastic effect is not observed as would be evidenced by a red, constant frequency streak in the color map. This lack of output response is due to the low coupling found between nickel and the electromagnetic

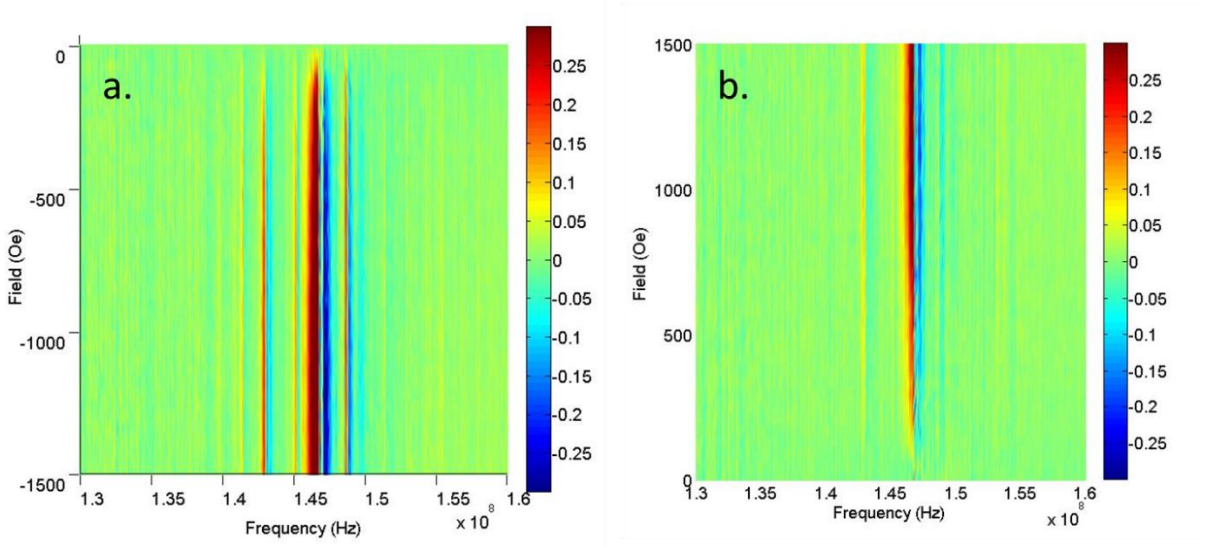

Figure 2.68 – a. The transmission response for a 150 MHz SAW antenna as a function of frequency and applied field for positive field values. b. The same sample response for fields applied in the negative direction.

wave as predicted by the analysis. The use of a small resonant loop antenna placed in the near field of the sample could potentially couple energy more efficiently to the sample than the shorted transmission used for this test. Figure 2.70 shows the same SAW sample being excited with a small loop antenna. The loop is 11mm in diameter and is placed roughly 1cm from the test sample. The transmission response is shown for both positive (b) and negative (a) applied fields. Similar to the test using a shorted transmission line as a radiator, the transmission from the loop also results in a lack of field dependent transmission at the design frequency (150 MHz).This indicates that the higher magnetic field magnitudes produced using a resonating loop are not large enough to excite a significant amount of mechanical power inside the nickel elements. The use of both a resonant loop antenna and a differential LNA on the output of the IDT may

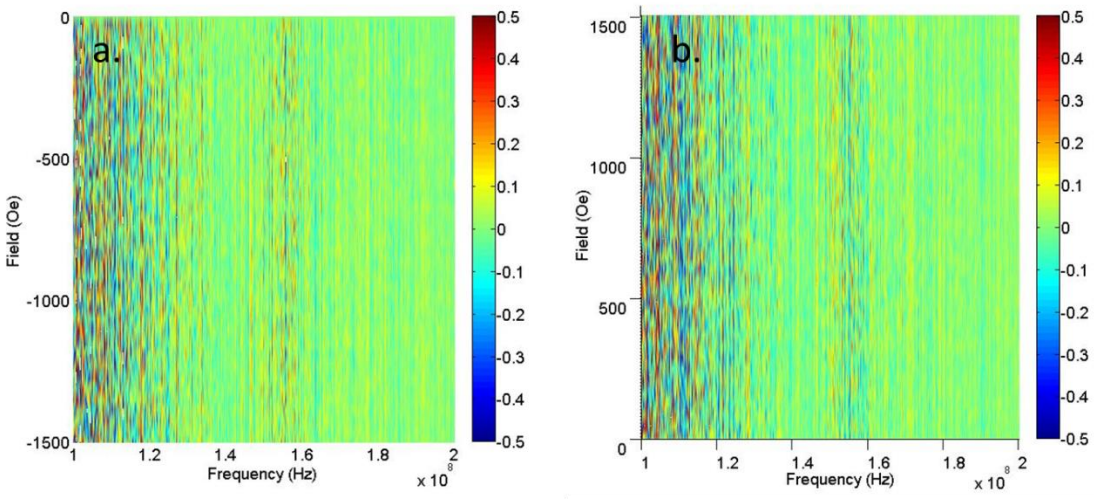

Figure 2.69 – a. The transmission response of a SAW antenna designed to operate at 150 MHz excited by a shorted CPW transmission line. b. The same plot except for negative applied fields.

improve the signal response from this sample to the point where the magnetoelastic resonance of the nickel rectangles may be observed. Additionally, increasing the operating frequency of the SAW device can act to improve the signal to noise ratio of the measurement.

Figure 2.71.a shows the reflection response of a resonant loop antenna (black) and SAW antenna device (grey). The response of the loop antenna is tuned to coincide with the resonance of the IDTs. The antenna test sample operates at 300 MHz in an effort to improve the noise figure for transmission measurements. The resonator array is designed to be 100 times larger (1 cm^2 versus 1 mm^2) than previous designs. This is increase in resonator area and material volume should provide significantly improved power generation in the array. Additionally, a differential LNA is used to interface the output IDT to the VNA test system which provides roughly 15 dB of gain. The IDT for the 300 MHz sample is shielded using a 110 copper alloy shield soldered over the

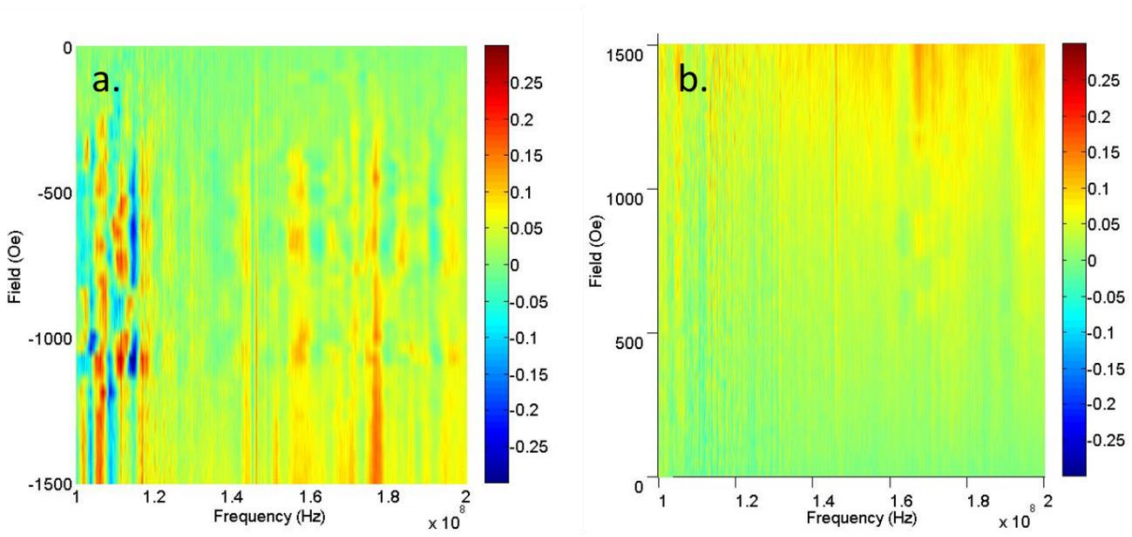

Figure 2.70 – a. The transmission response of a SAW antenna designed to operate at 150 MHz while excited by a resonant loop antenna. b. The same transmission plot but for negative applied fields.

IDT area. It is seen in the unbiased transmission response between the loop and SAW antenna shown in figure 2.71.b that the noise reduction efforts have reduced the direct electromagnetic coupling from the loop antenna to the sample electrode significantly. This is indicated by the 1 dB variation in the transmission response over the measurement range despite the resonant behavior of the excitation loop demonstrating that the additions of the IDT shield and the differential amplifier have reduced such unwanted couplings. Figure 2.71 shows the color map transmission surfaces for the 300 MHz sample being excited by the resonant loop antenna for three bias angles. The bias angle is defined as the angle between the static and RF fields while the RF field orientation to the sample is fixed. The expected field dependence of transmission is not observed for these test cases. This lack of signal reinforces the previously presented analysis

for a nickel based multiferroic antenna system which showed that the transduction efficiency for such a device would be near the noise floor of current measurement capabilities.

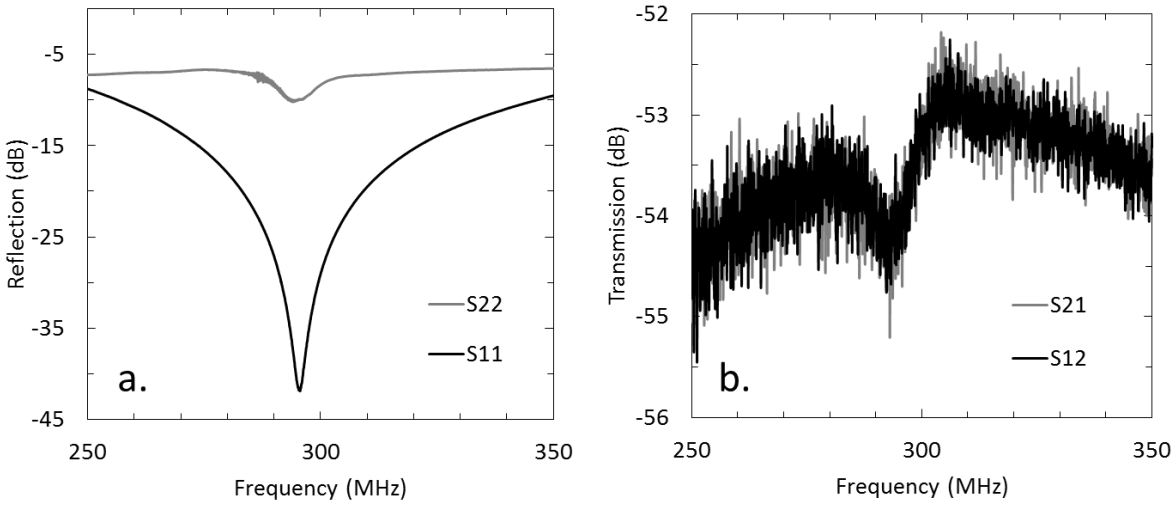

Figure 2.71 – a. The reflection response for a resonant loop (S11) and SAW antenna (S22) designed to operate at 300 MHz. b. The transmission response of the antenna when excited by the loop at zero applied field.

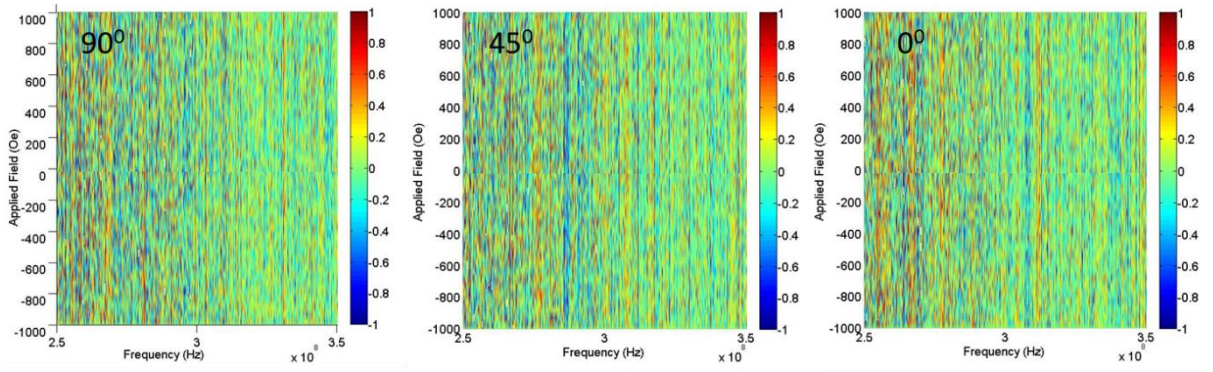

Figure 2.72 – The transmission response of the 300 MHz SAW antenna for three applied bias field angles defined with respect to the RF field direction.

VIII. Conclusion

In this chapter the operation of new type of resonant receiving antenna was proposed. This type of antenna leverages the small length scales of acoustic resonators operating at radio frequencies to reduce the size of the receiving structure by many orders of magnitude over the currently used methods. Through an intrinsic coupling phenomenon called strain mediated multiferroic transduction found in laminated magnetoelastic and piezoelectric layers, electromagnetic energy can be transformed into a detectable electrical output. A simple analytic framework was developed, based on Maxwell's equations describing electromagnetic waves which predicted the transduction efficiency of such a device. The effects of scale on this efficiency were also examined and compared to that of a standard resonant loop antenna. This analysis showed that the radiation efficiency for multiferroic antennae at the micron scale exceeds that of the simple loop system for certain material systems. The effect of measurement distance from the source was also studied and it was found that a multiferroic antenna performs best in the near field region of operation. The relationship between transduction efficiency and the magnetic bias field applied to the magnetoelastic material is derived to predict the operating characteristics of the antenna system. The results of this study showed a clear dependence on the applied magnetic field and provided valuable insight into measurement techniques and material systems selection. In light of these positive analytical results, a multiferroic antenna was designed by adapting existing surface acoustic wave technology with magnetoelastic resonator elements whose purpose is to transduce electromagnetic energy into a coherent surface acoustic wave. Materials which would optimize performance of these types of devices were selected based on their coupling coefficients and loss characteristics. Nickel and FeGaB films were selected to function as the magnetoelastic layer while 128^0YX cut lithium niobate was chosen as the piezoelectric

substrate. The actual materials used for device manufacturing were characterized both for their mechanical and electrical properties. These parameters were used in a multiphysics finite elements simulation to optimize both the geometry of the output electrode and the magnetoelastic resonators for maximum transduction efficiency. These simulations predict the output characteristics of the complete device when it is excited by an electromagnetic plane wave and show reasonable efficiencies which agree with analytical prediction. Once the optimized geometry was generated by simulation for the given material system, a fabrication process was developed. The development of this process involved optimizing the use of contact lithography and various thin film deposition techniques to create the final IDT electrode and magnetoelastic resonator array. Test devices were then prepared and a test system was designed which would allow for measurement of both the reflection and transmission properties of the multiferroic antennae. Several radiating devices were designed which would efficiently illuminate the test samples with large magnitude and well controlled electromagnetic waves while allowing for the simultaneous application of magnetic bias fields. Several sources of noise were indentified in the test system and solutions for the reduction of these signal components were applied. The results of the radiation efficiency from various source antennae to the multiferroic receiver were measured. Several tests showed small signal perturbations at the design frequency which were attributed to magnetoelastic coupling. Field dependence corresponding with the expected behavior for magnetoelastic coupling was not observed in the measured signal for any of the test samples. The implementation of noise reduction techniques showed a significant improvement in the signal to noise ratio of the measurement system.

The work presented in this chapter provides insight into the both the fundamental physics of high frequency dynamic magnetoelastic coupling and also device level design of how to utilize this

coupling in a practical setting. Although definitive electromagnetic coupling was not observed, the analytic framework for predicting the output response for various material systems demonstrates that this type of near field antenna structure will be possible with the correct materials and geometric design. Furthermore the methods by which such a device would be measured and characterized were thoroughly developed and their ability to detect low signal levels with high accuracy was proven. The establishment of these powerful design/measurement tools and optimal materials, such as those studied in this work, promises to significantly improve the transmission efficiency of future multiferroic antenna devices.

Chapter 3: Multiferroic Magnetometers

With the constant reduction in size of modern computational systems, a large demand for similarly miniaturized sensing capabilities has been created in the current electronic technology landscape. This demand for smaller sensors is driven largely by the concept of a self-contained unified system on chip. Such a concept incorporates computation and environmental sensing technology in small packages to enable smart devices which collect information about their surroundings and conveys it to the consumer or larger scale control system. This concept leverages the ability to create small and easily accessible sensors with high sensitivity and inexpensive manufacturing techniques. One such sensing device is the magnetometer which allows the user to detect the direction and magnitude of an impinging magnetic field which is typically applied statically or at low frequencies. These devices find application across many fields including biomedical imaging, magnetic anomaly detection and geomagnetic survey. The miniaturization of magnetometers is an actively studied topic which is driven by the need to take such magnetic field measurements in previously inaccessible environments such as inside the human body or under the surface of the ocean.

Traditional macroscale magnetometers take many forms. Hall sensors, search coils, Superconducting Josephson junctions and fluxgate devices have been studied over the past century for their high sensitivity. In particular SQUID type magnetometers can provide detection of magnetic fields beyond the pico-Tesla (10^{-12}) limit. These devices use the voltage differential measured at adjacent Josephson junctions on a superconducting loop through which the field to be measured is incident. This technique is valuable in the characterization of magnetic test samples, fundamental constants and electrical activity in the human brain. Figure 3.1 shows a

seven channel SQUID magnetometer used for mapping electrical activity in biological organisms [76]. Although the size of the superconducting loops used in SQUID magnetometers can be made extremely small [77-81], the cooling system and electronic measurement system are typically very large inhibiting the use of such devices in truly mobile applications. An excellent overview of the operation of SQUID magnetometers is presented by Ryhanen et. al. [76].

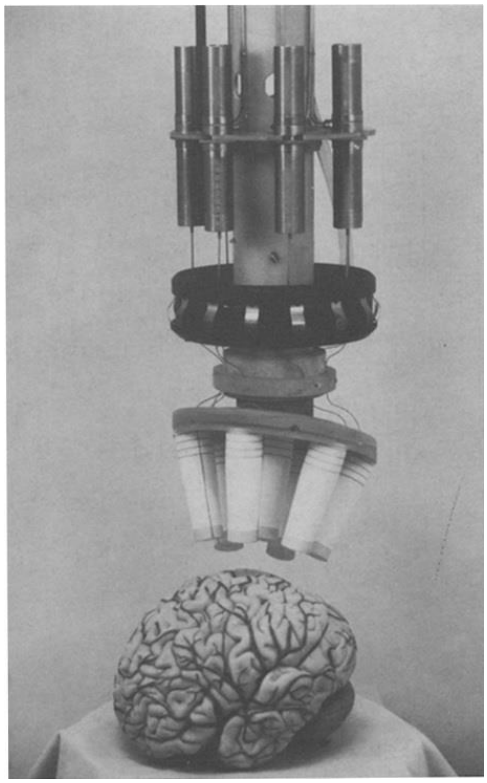

Figure 3.1 – A seven element SQUID magnetometer used for mapping spatially varying magnetic signals in the human brain [76].

A design which is more frequently employed on mobile platforms is the fluxgate magnetometer. This device uses the change in flux through a balanced arrangement of highly permeable ferromagnetic core or cores to detect externally applied magnetic fields. The detection of the flux

change through the cores is performed with a conducting wire coil. These devices can achieve extremely high sensitivities to the pico-Tesla magnitude range although stable devices are often used only in the nano-Tesla regime. Often times the core is arranged to provide a flux change through the detection coil only when an external field is applied to improve sensitivity of the device. To detect such flux changes, a time varying field must be constantly applied to the ferromagnetic core to induce a measureable output variation in the detection circuit. A racetrack fluxgate arrangement is illustrated in figure 3.2 [82]. Overviews of the fluxgate type magnetometer are presented by Ripka [82] and Primdahl [83]. Fluxgate magnetometers require relatively large powers to drive the excitation current necessary for operation reducing the efficiency of such a system. Although efforts have been made to miniaturize these devices [82], the scaling of the coil and core components critical to the operation of the magnetometer face the same issues with ohmic and core losses as many other micro scale magnetic field control applications. These scaling problems ultimately limit the use of the fluxgate magnetometer concept to macroscale devices.

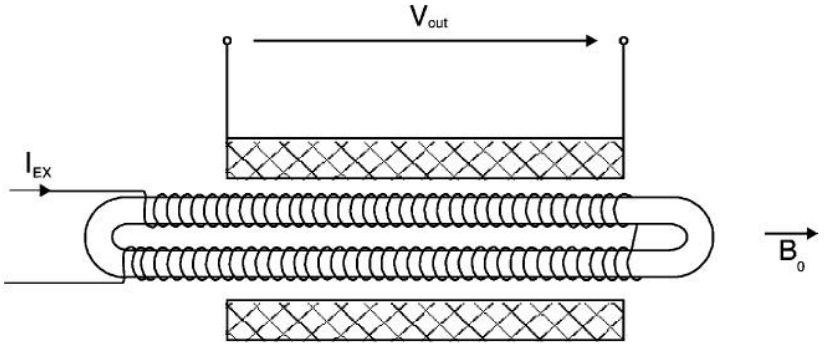

Figure 3.2 – A fluxgate magnetometer with a racetrack core arrangement. The excitation coil is wrapped directly onto the core and the detection coil surrounds the entire core.

Recently the magnetoresistive phenomenon has been examined for its potential use in magnetometer systems [84-87]. These types of devices use the resistance change in magnetized magnetic materials to infer the magnitude of the external magnetic field applied to the device. This resistance change phenomenon known as magnetoresistance (MR) arises from the quantum torque interaction between the polarized spin of the electrons in the ferromagnetic material and the incoherent spin polarization of the measurement current being passed through the material [51]. This change in resistance can result in external field sensitivities on the nano-Tesla field level in micron scale device packages for devices using the anisotropic magnetoresistance mechanism (AMR). Furthermore these devices are extremely simple consisting of usually only a two or four wire electrical connection to a thin film of magnetic material. This simplicity makes the AMR magnetometer an ideal candidate for chip scale sensing devices. The AMR magnetometer finds widespread use in many applications such as digital compasses for navigation and automobile detection for traffic control systems. A digital compass test device based on a three axis AMR magnetometer is shown in figure 3.3 [87]. Despite finding widespread consumer use, these devices are highly susceptible to environmental noise such as temperature or low frequency electrical radiation. Furthermore the relatively high probe currents required to detect the resistance changes in the ferromagnetic layer can create high ohmic dissipation in the film or sensing traces.

In this section we study the application of two types of thin film magnetometer systems which overcome the efficiency scaling problems found in traditional magnetometer techniques. By using the intrinsic coupling to magnetization found in multiferroic composites, losses associated with ohmic dissipation can be minimized. In the first section of this chapter the use of surface acoustic waves to probe the elasticity changes in a magnetoelastic film under different

magnetizing condition is explored. Simulations inform the design of such devices which are then fabricated using CMOS processing methods. The devices are testing and their performance aligns closely with the expected simulated results and reported literature values. In the second section of this chapter a micro-machined quartz crystal micro balance (QCM) is used in a layered arrangement with a Metglas thin film to study the effect of an externally applied magnetic field on the mechanical properties of the composite system. The device is tested using a unique wireless radio frequency detection method based on the coupled reflection characteristics of a nearby resonant detector antenna. The magnetometer characteristics for the QCM/Metglas laminate structure are examined for both the case of wired and wireless detection and the sensitivity for both connection methods is analyzed. The two methods are in close agreement and demonstrate the potential for these devices in applications where remote detection of localized magnetic field is required.

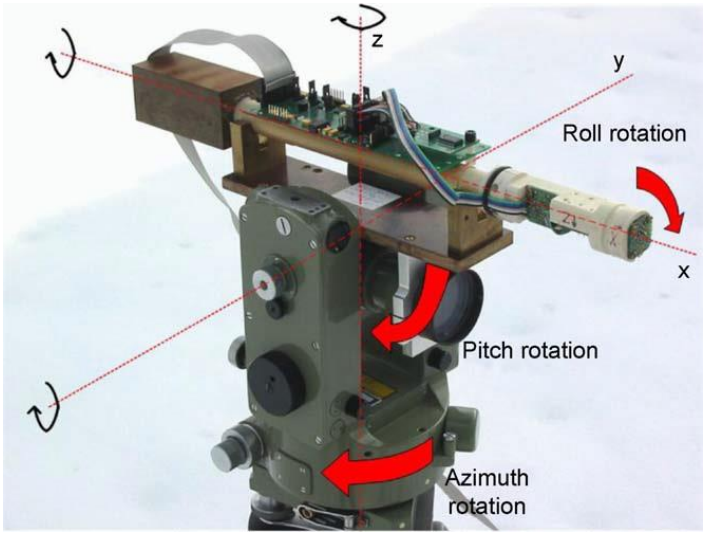

Figure 3.3 – A three axis magnetometer used for detecting earth's geomagnetic field based on AMR thin film sensors [87].

3-1: Multiferroic Surface Acoustic Wave Magnetometers

I. Introduction

The detection mechanism of the magnetometer device proposed in this section is constructed around a two port band pass filter using commercial SAW filter technology. These types of filters use interdigital electrodes (IDE or IDT) to actuate the surface layer of a bulk piezoelectric substrate. The electrodes consist of long parallel stripe conductive patterns with alternating RF potentials whose pitch sets the half wavelength of the acoustic wave to be created in the substrate. When the IDT excitation frequency intersects with the dispersion relationship for the desired wave mode and the wavelength set by the electrode geometry, a narrow band acoustic wave is generated and allowed to propagate outward from the IDT. For an in depth design procedure for IDTs and the operating characteristics of SAW filters the reader is referred to the design section of chapter 2. The multiferroic SAW magnetometer uses two identical IDT patterns to create and receive acoustic waves on a bulk piezoelectric substrate. The transmit and receive IDTs are separated by some distance and a continuous magnetoelastic film is deposited between them such that the generated surface wave is allowed to propagate through the magnetic film before reaching the output IDT. With this configuration the acoustic properties of the magnetic film will impact the propagation characteristics of the travelling wave before it reaches the output electrode. By correlating the output properties of magnitude and frequency of the output signal with the input wave certain properties can be inferred about the elastic properties of the magnetoelastic film. A schematic diagram showing the basic device components is illustrated in figure 3.1.1. In this case the magnetoelastic film is shown to be nickel while the piezoelectric substrate is single crystal lithium niobate.

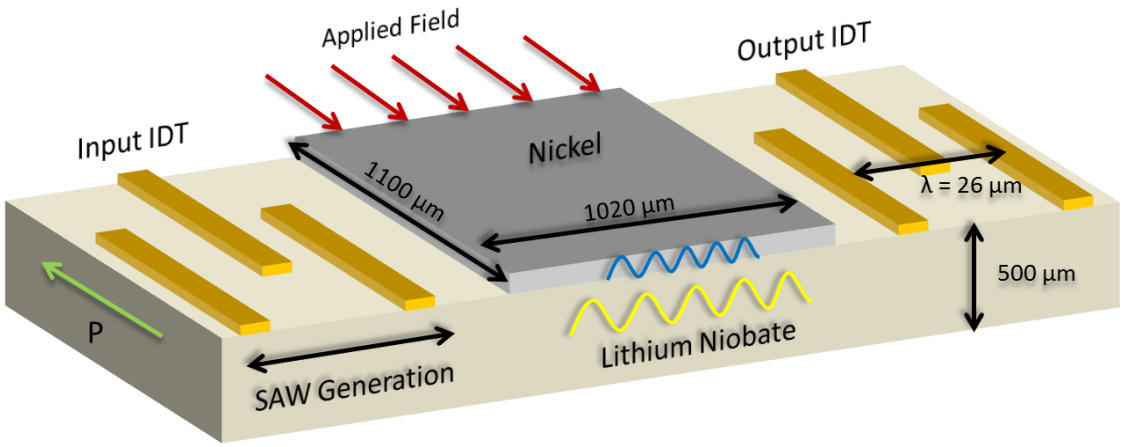

Figure 3.1.1 – A simplified diagram of the device components used to construct a multiferroic SAW magnetometer.

Because of the small acoustic wavelengths found in SAW filter devices (in this work 26 µm at 150 MHz), small changes in the mechanical properties of the magnetoelastic film can induce large changes in the output response of the magnetometer device. In particular many magnetoelastic materials exhibit coupling between magnetization and elasticity in a phenomenon known as the delta-E effect. This magnetic field dependent change in the elasticity of the film is directly related to the magnetomechanical coupling coefficient of the material [51][88].

$$k^2 = \frac{\Delta E}{E} \qquad [Eq.\,3.1.1]$$

This relationship provides a powerful tool in characterizing the transduction efficiency of new magnetoelastic materials and together with the resonance-antiresonance technique [89-92] form the two major methodologies for measuring this parameter. Additionally this change, measured as phase or frequency shifts in the output signal, can be directly correlated to an externally

applied magnetic field, forming the basis for the operation of this device configuration as a magnetometer. Because these types of acoustic wave devices are widely used in existing commercial products and the fabrication is relatively simple, the multiferroic SAW magnetometer is an ideal candidate for use in chip scale applications which require high sensitivity and smaller packaging footprints over the fluxgate type magnetometers currently in use [82-83].

The concept of magnetostrictive delay lines for use as a magnetometer device has been studied in bulk samples using traditional measurement approaches [93]. In this technique large magnetoelastic samples which are typically in the form of wires are used to detect the magnetic field in the surrounding environment. Although highly sensitive to applied fields, this technique involves large measurement systems which suffer from the same Ohmic loss scaling found in traditional search coil type magnetometers. The use of surface acoustic waves to probe the elastic properties of a magnetoelastic film, which can overcome many of the scaling issues found in traditional magnetometers, are also reported [94-97]. Some of the earliest devices use nickel and lithium niobate heterostructures similar to the ones proposed in this work [96]. In this report, the phase response of a SAW propagating across an 850nm thick nickel film is measured as a function of applied bias field. The phase response for the film is shown in figure 3.1.2 for bias fields applied up to 1 T along the three primary axis of the film. Prominent shifts in the output phase are observed with a clearly anisotropic behavior in the signal. This phase shifting effect is described in this report as the increasing disparity between the magnetic precession frequency and the excitation frequency of the surface acoustic wave with applied field. Although this explanation is reasonable for higher frequencies where magnetic resonance is achievable (and in fact this effect is observed in later studies [38-40]), the shifting is better described as the change

in wave velocity due the delta E effect. This account also considers films which are small in thickness compared with the fundamental SAW wavelength such that the mechanical influence of the nickel film on the wave properties is small.

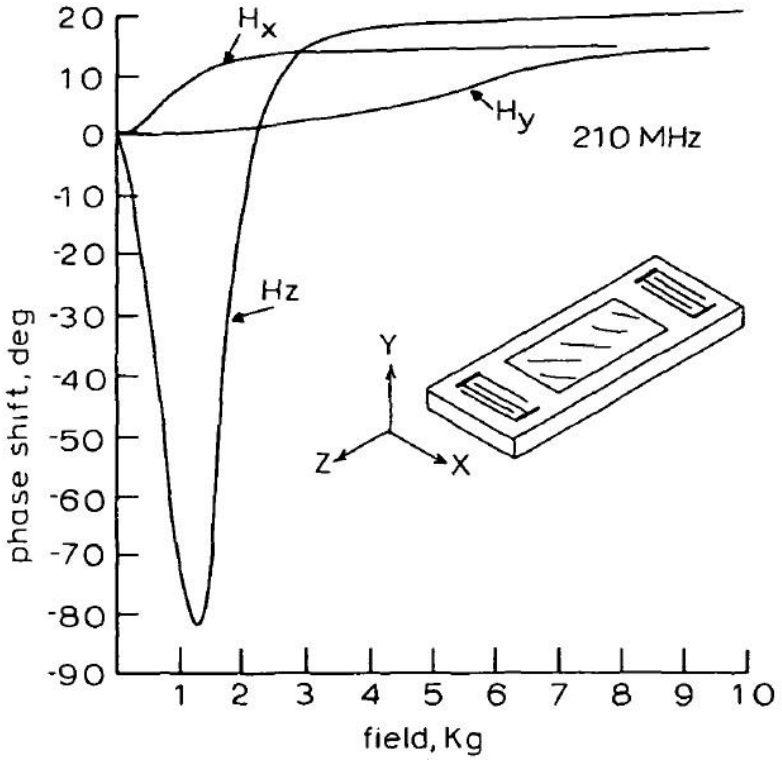

Figure 3.1.2 – A SAW phase shifter based on the delta E properties of an 850nm thick evaporated nickel film for fields applied along the primary axis of the sample [96].

More recent reports demonstrate relatively large velocity changes in a surface acoustic wave device built using FeCoSiB and ZnO films [98]. In this study a surface acoustic wave generator is constructed on the highly magnetoelastic and low anisotropy film FeCoSiB as is illustrated in the top image of figure 3.1.3. The admittance amplitude of the resonator system is monitored for applied magnetic fields and the center frequency shift is extracted at each field as is shown for

field applied along the sample hard axis in the bottom image of figure 3.1.3. For this type of material system very large tuning ranges are achieved on the order of 0.6%. Although this represents the largest reported shifting range available in SAW devices, these experiments require the use of bulk magnetoelastic foils and the complex deposition of piezoelectric films which would severely limit the applicability of such devices in micro scale applications.

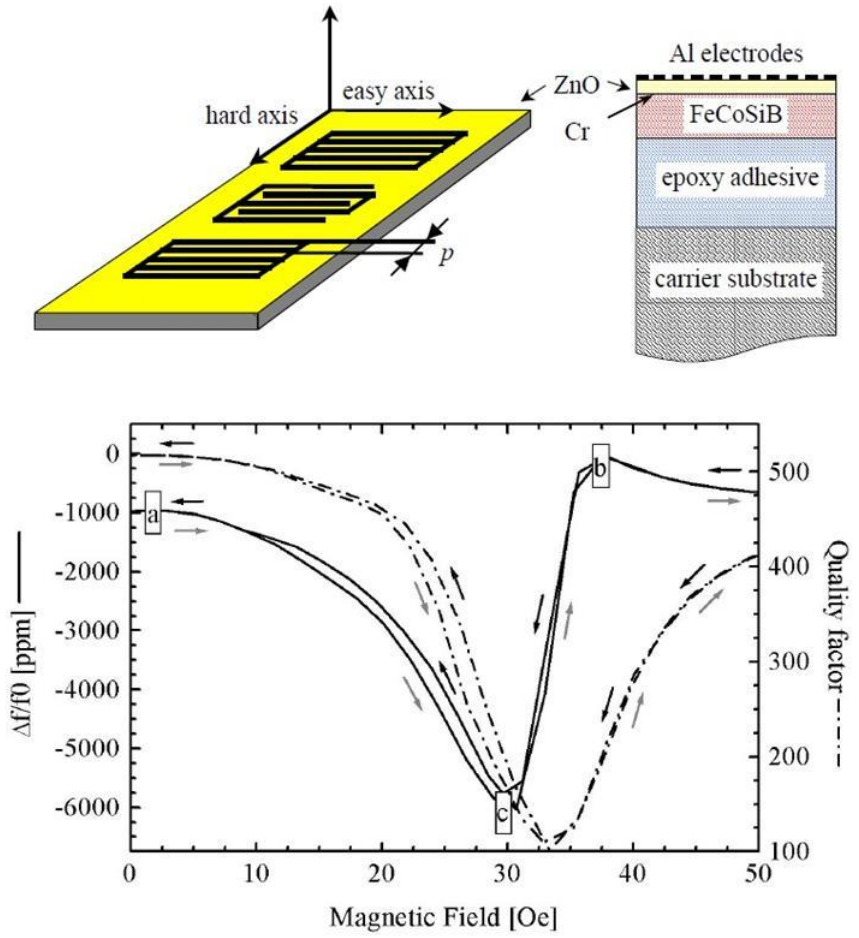

Figure 3.1.3 – A single port surface acoustic wave frequency shifting magnetometer built on ZnO/FeCoSiB layers (top). The center frequency extracted from the admittance amplitude (a) of the SAW resonator as a function of applied magnetic field along the sample hard axis (bottom) [98].

In this section a SAW based frequency shifting magnetometer is proposed based on thick, electroplated nickel films and lithium niobate substrates. Materials and processing techniques are chosen which significantly simplify device construction making the SAW magnetometer easily translatable to industry standard chip-scale fabrication. Simulations are performed which show the linear frequency shifting versus elastic modulus behavior of a two port SAW system. Samples are fabricated for three thicknesses of nickel films using standard CMOS processing techniques. A measurement system is designed to record the frequency spectra of the fabricated samples as a function of applied magnetic field from which the frequency and wave velocity relationship can be extracted. A very large ~0.7% change in wave velocity is observed for a device with a 4 μm electroplated film. The anisotropy behavior of the frequency shifting action is observed. The frequency changes measured experimentally correlate with an approximate 5.3% change in the elastic modulus using the simulated system results which correlate closely with the bulk reported values.

II. 2D Finite Elements Simulation

To study the operating characteristics of the SAW and magnetoelastic system, the dynamic mechanical characteristics of the layered device must first be understood. This relationship between the elastic state of the magnetic film and the transmitted acoustic signal is highly complex and depends strongly on the thickness and acoustic impedance of the film being used. In this work nickel is used as the magnetoelastic layer because of its relatively large delta-E coefficient (typically reported around 3-6% [99-101]) and its excellent acoustic impedance match with the piezoelectric lithium niobate substrate. Additionally nickel is widely used in the

microelectronics industry as an electronic and mechanical coating. A 128^{o}YX cut of lithium niobate is chosen as the piezoelectric substrate material for its very large shear electromechanical efficiency and low electrical loss characteristics. This material has been well characterized for it SAW propagation characteristics in literature [68][73-74] and is readily available from commercial crystal manufacturers. To study the correlation between the properties of the magetoelastic nickel film and the wave propagation characteristics of this system, a finite element model is constructed to reflect the geometry and materials used in an actual test device. This model is built in COMSOL Mutliphysics software using the piezoelectric constitutive law. A two port bandpass filter is constructed using 200 nm thick gold IDTs with 32 fingers in each pattern as is illustrated in figure 3.1.4. The pitch of the fingers is 13μm corresponding to a full wavelength of 26 μm. Using the known surface acoustic wave speed, shown measured experimentally in chapter 2, of the substrate material, this finger pitch corresponds to a center frequency of 150 MHz. The IDT electrodes are coupled to SPICE circuit nodes with 50 Ohm characteristic impedance. This SPICE simulation provides the electrical connections which simulate the measurement source and load components to and from the IDTs. A 1020 μm continuous nickel film is placed between the input and output IDT electrodes which serves as the magnetoelastic layer for the device. The elastic and electrical properties are simulated in this domain although conductivity of this layer is found to have negligible impact on device performance both numerically and experimentally. The nickel film and IDT electrode are modeled on a piezoelectric lithium niobate substrate which has PML boundaries on all sides except for the top surface. These PML boundaries absorb impinging acoustic energy to eliminate the effect of wave reflection back into the electrodes. The substrate is fixed at its two bottom corner points to constrain the system from translation or rotation. A dielectric air domain is

defined above the free surface of the substrate to realistically capture the electrical properties of the IDTs.

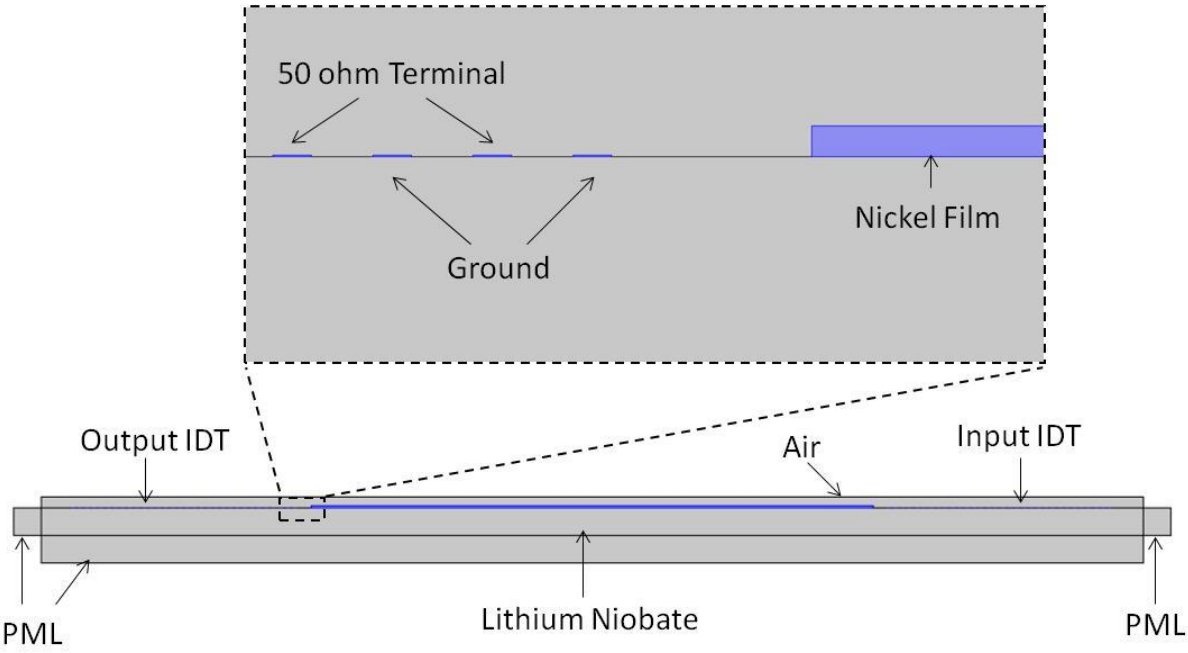

Figure 3.1.4 - A finite elements simulation used to predict the output characteristics of a multiferroic SAW magnetometer.

Using this model setup, the impact of increasing the nickel film thickness is examined. The S12 parameters are recorded for films ranging from 200 nm to 6 μm over a frequency range of 100 to 200 MHz as is shown in figure 3.1.5.a. The typical band pass frequency behavior is apparent for all thicknesses shown. It is observed, however, that as the thickness of the nickel film increases the magnitude of the transmitted wave significantly decreases. This decrease in magnitude is plotted at the center frequency of 150 MHz as a function of increasing film thickness in figure 3.1.5.b. It is seen that as the film approaches 4 μm, the S12 magnitude drops by roughly 30 dB. For films with thicknesses greater than 4μm the amount of attenuation remains about the same.

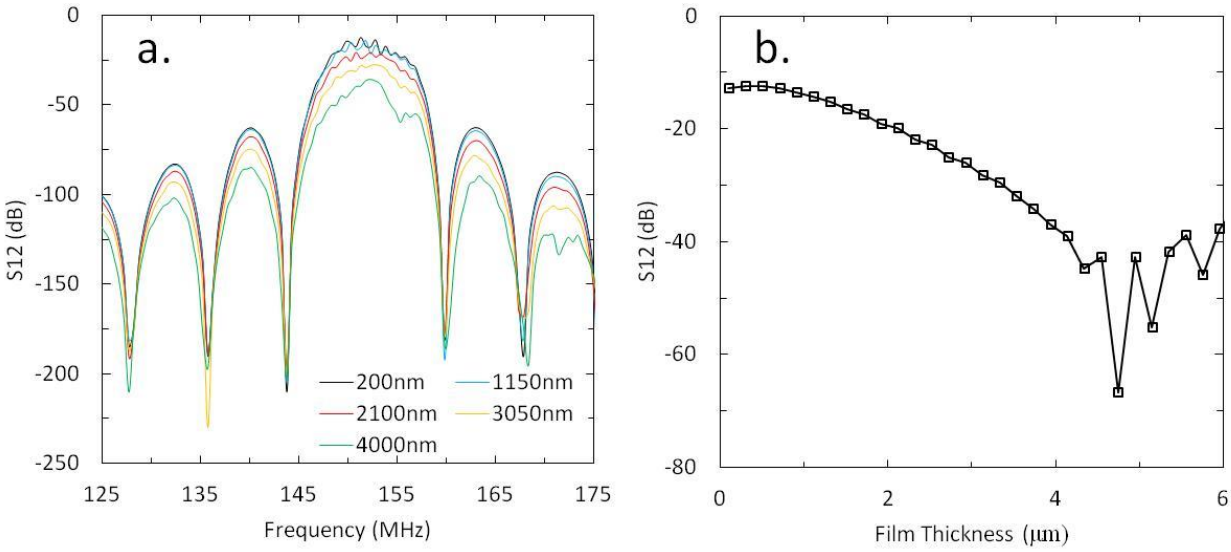

Figure 3.1.5 – a. The transmission response of a SAW magnetometer for a selection of nickel film thicknesses. b. The S12 transmission at 150 MHz as a function of nickel film thickness.

This attenuation characteristic of the thicker nickel films is attributed to waveguiding behavior inside the nickel layer. As the film thickness becomes a more significant fraction of the acoustic wavelength, an increasing amount of mechanical energy is stored and reflected within the nickel film. This effect can be observed by plotting the volumetric displacement profile for two representative films at 150 MHz as is shown in figure 3.1.6. In the case of a 600 nm thick nickel film shown in figure 3.1.6.a, the majority of the acoustic wave is contained within the upper surface of the lithium niobate substrate. In sharp contrast, a 4 μm thick nickel film, shown in figure 3.1.x.b, will cause the majority of the travelling wave to be contained within the nickel film. An additional loss mechanism is observed in figure 3.1.6.b where a large fraction of the acoustic wave impinging on the nickel film edge is scattered at an angle into the bulk of the substrate. These two loss mechanisms, additional scattering and the waveguide like behavior of

the nickel film, when combined result in the large observed amplitude attenuation as the wave propagates from the input to the output electrodes.

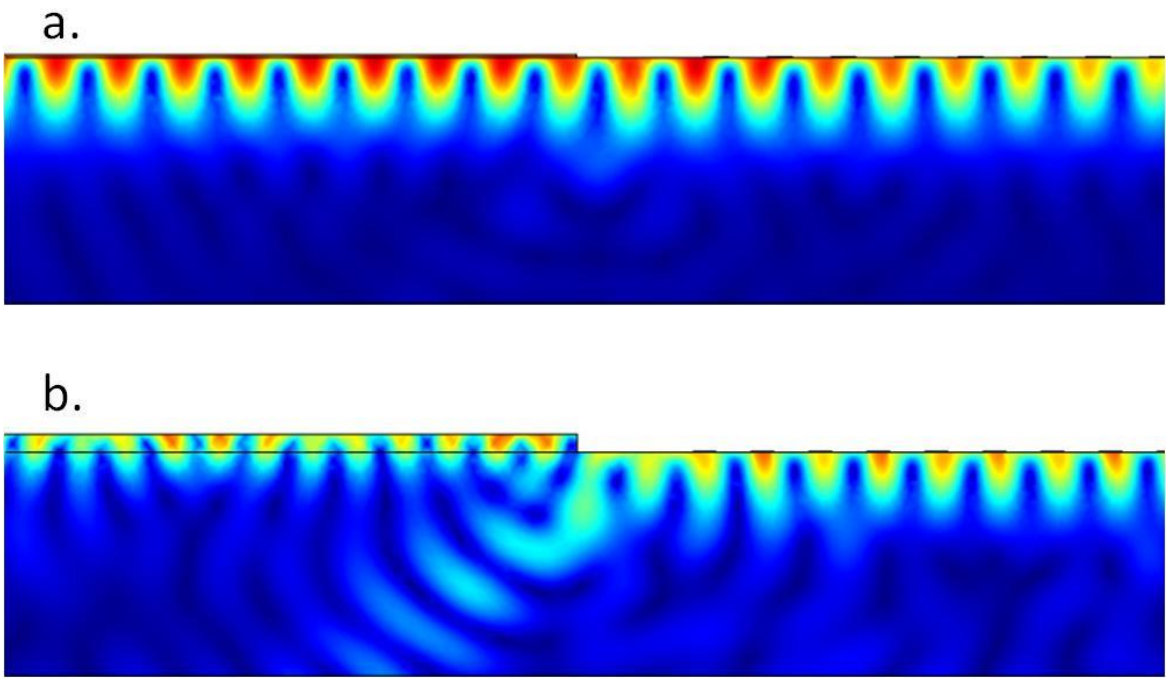

Figure 3.1.6 – a. A 150 MHz SAW wave travelling into a 600 nm thin nickel film. b. A 150 MHz SAW wave travelling into a 4 μm thick nickel film. Color corresponds to volume displacement.

Using the same model setup the effect on the propagation properties of the device due to modification of the isotropic elastic coefficient of the nickel film can be simulated. This is modification of the elastic modulus is assumed identical to those which will occur due to the magnetoelastically induced delta-E effect in the nickel during device operation. In this study the spectral transmission response, normalized to the input power, can be plotted for a range of values of Young's modulus defined inside the nickel domain. The spectral transmission response

is shown for a 4 μm nickel film in linear units in figure 3.1.7.a for a number of elastic moduli around the known bulk modulus for nickel. Clear shifting of the central SAW peak is observed as the modulus is changed. This shifting is quantified in figure 3.1.7.b for three nickel film thicknesses by fitting a Lorentzian frequency distribution to the spectral data such that a center frequency can be extracted. The relationship between the isotropic modulus and the frequency shift follows a monotonic trend in this shifting range with the slope highly dependent on film thickness. The slopes for the 200 nm, 600 nm and 4 μm films are 10, 56 and 224 kHz/% respectively.

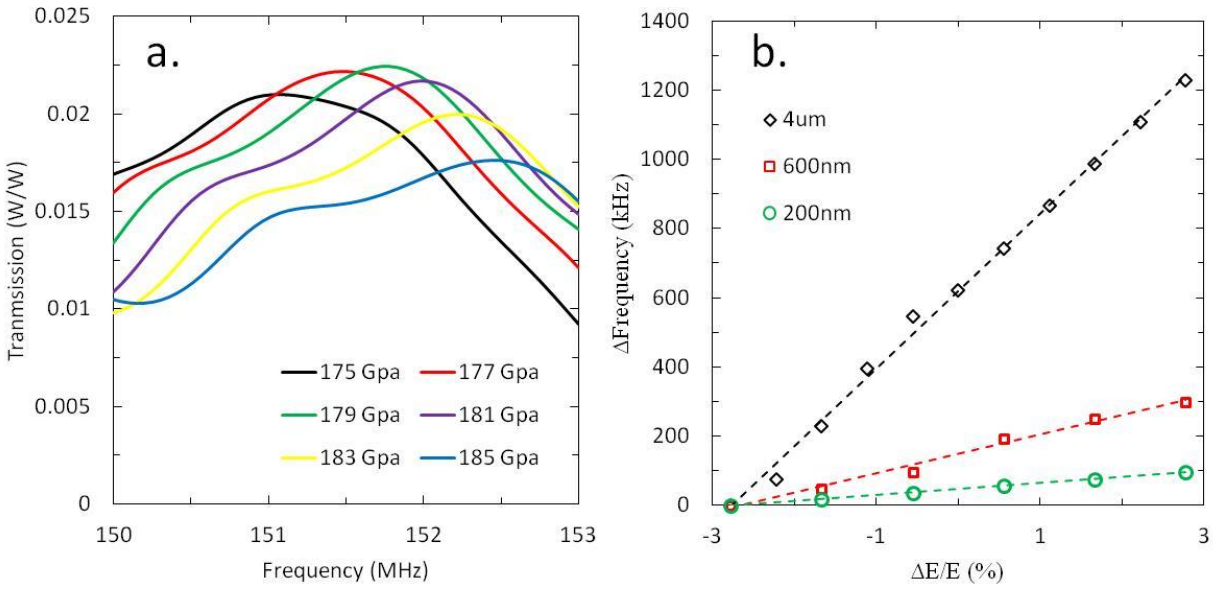

Figure 3.1.7 – a. The linear transmission spectra of the simulated SAW magnetometer device for varying values of elastic modulus applied to a 4 μm thick nickel film. b. The relationship between center frequency shift and elastic modulus for three film thicknesses.

III. Device Fabrication

Following the design of a SAW magnetometer based on nickel and lithium niobate multiferroic material system, samples are manufacturing to validate the behavior predicted by simulations. Test samples are fabricated on 50 mm diameter 128^{o}YX cut lithium niobate wafers (Atom Optics) which have been polished on both faces. Samples are first prepared by solvent cleaning to remove any residual compound left on the wafers by the manufacturer during the polishing process. A negative tone photoresist, nLOF2020, is spun onto the wafer at 3000 RPM using a PWM32 controlled Headway Research spinner to yield a final resist thickness of 2μm. Samples are soft baked at 110^{o}C for 60 seconds using a hotplate. A Karl Suss MA6 alignment system is used to perform contact lithography on the wafers. Photomasks for lithography are designed using L-Edit CAD software and printed into a chrome thin film on a 5" square soda lime glass plate by the UCLA Nanoelectronics Research Facility mask shop. The mask patterns are aligned to the wafer flat such that the wave propagation direction of the IDT is oriented along the x-axis of the wafer. The wafers are exposed using a mercury vapor lamp with an exposure intensity of 66mJ/cm^{2}. Following exposure, wafers are baked at 110^{o}C for 60 seconds on a hotplate to cross link the UV activated compounds. The wafers are then immersed in a room temperature AZ300MIF developer solution for 60 seconds after which they are cleaned with de-ionized water. Following lithography, the patterned wafers are descummed using a 200W oxygen plasma (Tegal Plasmaline 512) for 120 seconds. The wafers are then placed into a CHA Solution electron beam evaporation system where a titanium then gold film is deposited onto the surface of the patterned samples. The thicknesses of the titanium and gold layers are 20 and 150 nm respectively. The thin titanium layer acts as a reactive adhesion layer between the gold film and the substrate surface. Once deposition is complete the wafers are immersed in an 80^{o}C solution

of AZ300T stripper for several hours. This solution chemically removes the nLOF2020 resist from the wafer surface and the gold which is not in direct contact with the substrate. Once stripping of the resist and excess gold is complete, the completed IDT electrode patterns are left on the wafer. At this step of the fabrication process the wafer is ready for the patterning and deposition of the magnetoelastic layer.

Two deposition techniques are used for fabrication of the nickel magnetoelastic layer, liftoff patterning using PVD and through mask plating using electrodeposition. For samples with 4 μm thickness magnetoelastic films, electrodeposition is chosen for its ability to quickly deposit thick films with relatively low stress. This process begins with the patterning and deposition of a seed electrode onto which the nickel will be grown. This layer is patterned and deposited using the same liftoff and deposition technique described previously for the gold IDT electrodes. This layer is aligned with respect to the previously patterned gold layer rather than the wafer flat. This layer to layer alignment is performed using Vernier style alignment markers which are included in both mask layers. Titanium and copper films are used to form the seed electrodes which are 10 and 100 nm in thickness respectively. Following the deposition and liftoff of the seed electrode, an electroplating mask is fabricated over the seed electrode to guide the growth of the nickel layer during electrodeposition. This plating resist is first created by spinning the negative tone resist KMPR1005 onto the wafer at 3000 RPM which yields a final resist thickness of 7 μm. The wafers are then exposed using an exposure intensity of 400mJ/cm^2. The solution is developed in SU-8 developer for 120 seconds. Once patterning is completed the sample is descummed in a 200 W oxygen plasma for 120 seconds. The samples are mounted onto an FR4 substrate which is patterned with a contact electrode to which the seed layer on the samples are electrically wire bonded. This sample assembly, which forms the cathode of the plating cell, is placed into a room

temperature bath of commercial electroplating solution (Technics HT2) of the Watt's composition. A pure nickel electrode acts as the anode of the plating cell and is placed opposite the sample at a separation distance of 70 mm. The sample and nickel electrode are connected to a laboratory DC power supply held at 10 Volts. A current limiting/sensing resistor and tuning potentiometer are placed in series with the cathode of the cell to control the current density at the sample surface. The current through the cell is monitored through the resistor with a digital voltmeter and is tuned to 50 ASM using the potentiometer. This current density yields a deposition rate of 100 nm/min which for a total deposition time of 40 minutes leaves a 4 μm nickel film. Following electrodeposition the sample is removed from the FR4 holder and immersed in an 80^{o}C solution of AZ300T commercial photoresist stripper for several hours to remove the KMPR1005 layer. The final thickness of the nickel is confirmed using profilometry. An image of a 10 μm thickness nickel film deposited using this technique is shown in figure 3.1.8. It is seen that the roughness and uniformity are excellent over the surface of the film.

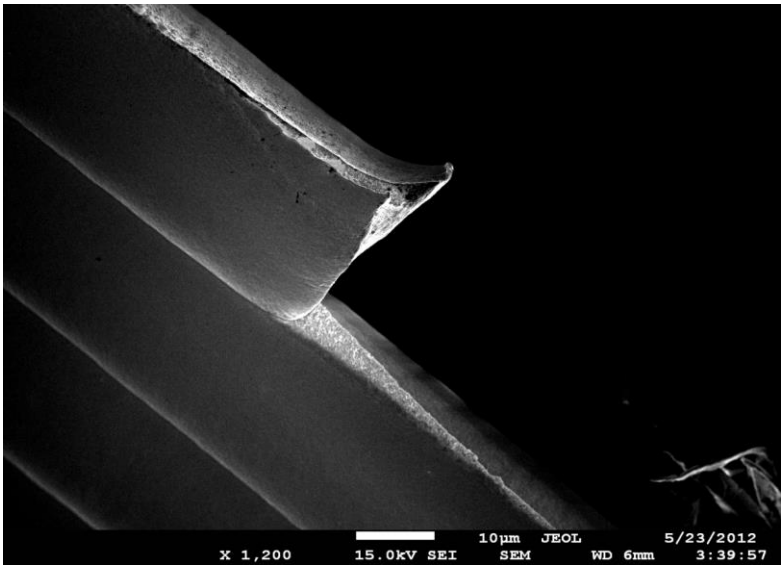

Figure 3.1.8 – An SEM micrograph detailing the top surface and sidewall profile of a 10μm thickness electroplated nickel film.

Samples are also fabricated with nickel films of 200 and 600 nm thicknesses. These nickel films are deposited using electron beam evaporation. Lithography is performed using nLOF2020 photoresist as was described previously for the fabrication of the gold IDT electrodes. Following lithography and descumming of the photoresist, titanium and nickel films are successively deposited onto the wafer using electron beam evaporation. Nickel films of both 200 and 600 nm thicknesses are fabricated. The titanium adhesion layer is fixed at 20 nm for both thicknesses of nickel. Once the evaporation of the films is complete, the solution based liftoff of the photoresist and excess nickel is performed as was described previously. Figure 3.1.9.a shows an optical image of a complete device with a 600 nm nickel film. Figure 3.1.9.b is a detailed view of the IDT fingers and the nickel film.

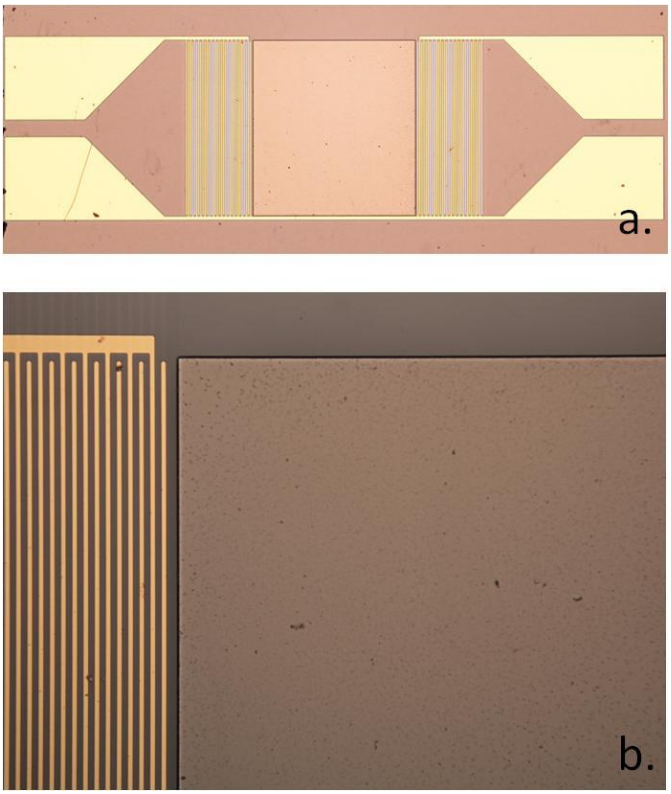

Figure 3.1.9 – a. An optical image of a completed test die fabricated with a 600 nm nickel film. b. A higher magnification image of the same die detailing the IDT fingers and the nickel film.

Completed devices are separated from the wafers using a Disco DA321 wafer saw into 3x2 mm dies. These die are prepared for testing by bonding them onto a Rogers Corp. RO4360G substrate which has been patterned with two coplanar waveguide transmission lines using cyanoacrylate based adhesive (Loctite 401). These CPW transmission lines act to connect the SAW input and output IDTs to the test system. Each CPW is terminated with a non-magnetic edge launch SMA connector (Johnson Solutions 142-9701-801). The transmission lines are designed for a 50 Ohm impedance match at 150 MHz. The transmission lines are connected in a single ended arrangement to the SAW IDT's using wire bonds. An image of a completed device mounted to a test substrate is shown in figure 3.1.10.

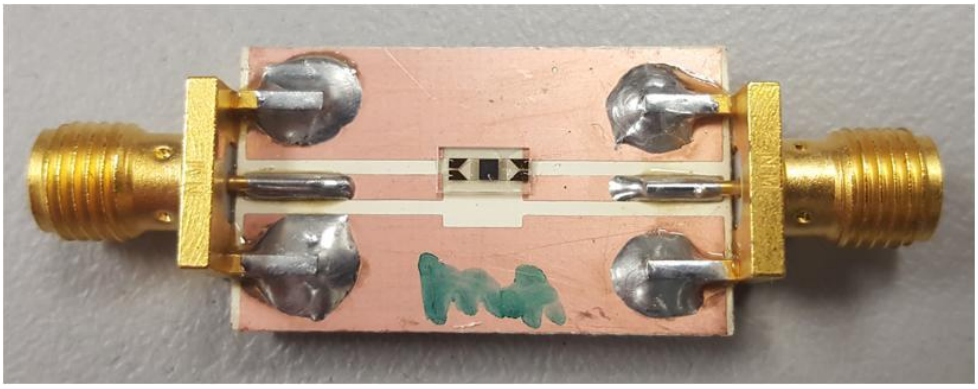

Figure 3.1.10 – A complete sample with a 4 µm electroplated nickel film which has been prepared for testing on a patterned RO4360G circuit board.

IV. Characterization

Prior to testing for magnetic field sensitivity, the samples are characterized for both the magnetic field independent transmission and the magnetic properties of the nickel film. The magnetic properties of each thickness of nickel film are measured for both the in plane and out of plane

directions using a laser magneto-optical Kerr measurement system. This measurement is performed in situ on the PCB mounted test die. The in-plane hysteretic behavior for the three nickel film thicknesses tested are shown in figure 3.1.11.a. The out of plane M-H behavior is shown for the three films in figure 3.1.11.b. Hard axis characteristics are observed in the 200 and 600 nm thin films for both the in and out of plane directions. This hard axis behavior is due to the intrinsic tensile stresses introduced during the deposition process. Previous work demonstrates that for nickel films deposited using identical processing methods [102-103] the intrinsic film stress can be very large (as high as 1 GPa) when the substrate is held at room temperature and tends to be tensile in nature. Because of the magnetoelastic character of the nickel, this tensile stress corresponds to significant anisotropy which is large enough to counteract the demagnetizing effect of the thin film geometry. This out of plane stress induced anisotropy leads to the hard in-plane behavior observed in the experimental data. The 4 μm film exhibits an easy in-plane axis and a hard out of plane axis. This behavior is attributed to the intrinsic compressive film stress (-40 MPa) measured for identical deposits using wafer curvature. This small valued compressive stress and the demagnetizing anisotropy act together to create a preferential in-plane orientation for the magnetization of the nickel film. By comparison of the MH behavior for the 200 and 600 nm films and the 4 μm film it is apparent that the tensile stresses in the evaporated nickel deposits comprise an effective out of plane energy equivalent to an applied field of about 1500 Oe. This significant anisotropy energy is expected to have a large effect on the operation of devices built using these types of films. For all films the coercive field is about 60 Oe.

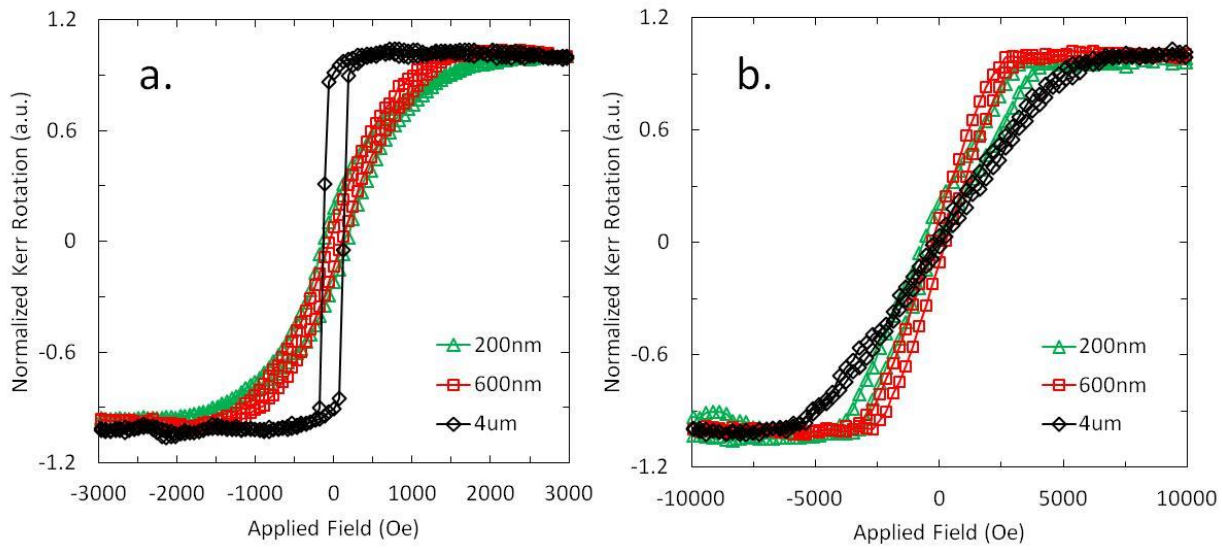

Figure 3.1.11 – a. The in-plane M-H characteristics for test samples of three different film thicknesses. b. The out of plane M-H behavior for the same three samples.

S12 transmission data for the samples is also collected prior to magnetic field testing. Full two port scatter parameters are recorded using an Agilent 8720ES network analyzer connected to the sample in a simple band pass arrangement. The S12 transmission is shown in figure 3.1.12. It is observed that the samples with thin nickel films of 200 and 600 nm thicknesses have significantly larger power transmission within the pass band frequencies of the IDTs than the 4 µm film sample. The sample with the 4 µm electroplated nickel film shows a 30 dB reduction in transmission gain with respect to the 200 and 600 nm films. This confirms the simulated trend shown in figure 3.1.5 where it was observed that the transmission gain drops significantly for films having thicknesses greater than 1 µm. This gain reduction in the thickest nickel film is attributed to the waveguide and scattering losses observed in the simulation results. A significant amount of broadband noise is also observed in the measured transmission response evidenced by

the constant -40 dB signal components off of the SAW resonance peaks. This is due to the electromagnetic transmission from the input IDT to the output IDT electrodes. This effect in SAW devices and techniques to mitigate its impact on measured results are discussed in the measurement section of chapter 2. For the purposes of the experimental work collected in this chapter, hardware based time gating is applied during measurement to capture only the initial acoustic signal components.

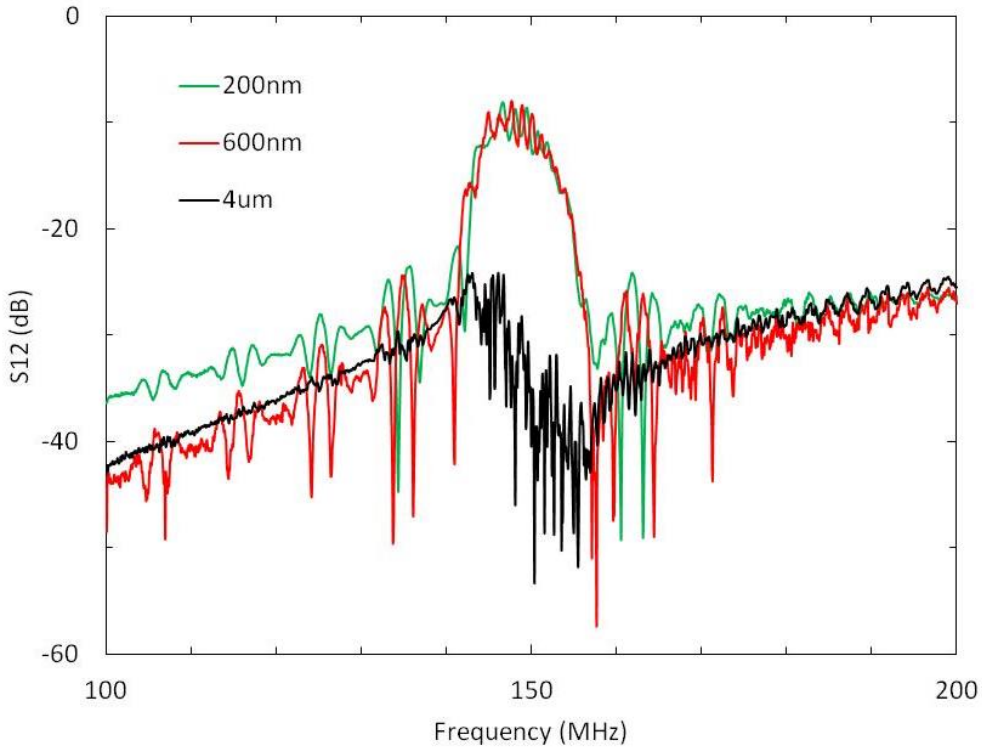

Figure 3.1.12 – The S12 transmission parameter for three multiferroic SAW magnetometer devices with various nickel film thicknesses.

V. Experimental Setup

During magnetic field testing the devices are placed onto a rotating stage between a Varian electromagnet. The poles of the electromagnet are covered with 110 alloy copper sheet metal to shield the device under test from nearby ferromagnetic materials. The input and output connectors are attached to the test ports of an Agilent 8720ES vector network analyzer. The analyzer is interfaced with a PC through GPIB connection. An Agilent 6684A system power supply is used to deliver a controlled current to the electromagnet through a relay which allows the direction of the supply current to be reversed using a digital controller. The current source is controlled and monitored from the PC using GPIB connection. An F.W. Bell 5080 Gauss Meter is placed between the magnet poles to monitor the strength of the magnetic bias field. The field values are read from the gauss meter into the PC using an analog signal output into a National Instruments 6009 DAQ. A simplified schematic diagram detailing the test system connections is shown in figure 3.1.13.

During testing, a controlled current through the electromagnet is specified by the PC to the power supply. This creates a uniform DC magnetic field at the location of the sample. For each bias field value the network analyzer records the S12 transmission spectra over a 100-200 MHz frequency span using a test port power of 0dBm. Frequency domain data is only collected for a time window specified from 70-800 ns using the internal time gating feature in the network analyzer. At each current value the magnitude of the magnetic field at the sample location is recorded with the gauss probe. This test is performed for a full hysteretic sweep of magnetic field values up to the saturating field of the sample and its given orientation. For the in-plane orientation, the sample is rotated through three angles; 0, 45 and 90 degrees. This angle is

defined as the angle of the externally applied bias field to the propagation direction of the acoustic wave. The sample is also measured with the bias field applied in the out of plane orientation. This test is performed for devices with the 200 nm, 600 nm and 4 μm thin films.

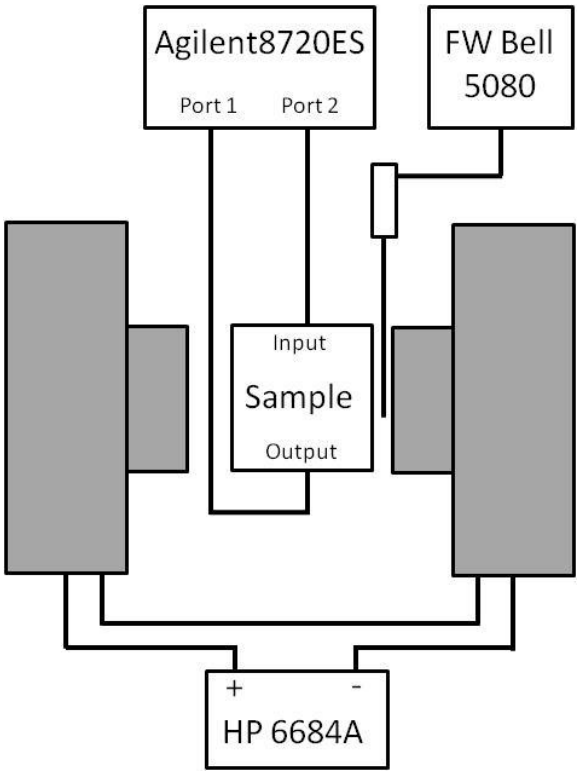

Figure 3.1.13 – A schematic diagram of the test setup used to collect bias field dependent transmission data for the SAW magnetometer device. The electromagnet is shown in grey.

VI. Results

Transmission testing of SAW magnetometer devices using the 200 and 600 nm evaporated nickel films produced no observable frequency shifting over a wide range of magnetic field conditions. This lack of wave speed shifting is attributed to the large out of plane anisotropy

introduced by the intrinsic tensile film stresses during the deposition process. This large stress magnitude significantly reduces the magnetoelastic coupling and the appearance of the delta E effect in the thin nickel films. This reduction of the magnetoelastic coupling in materials with high intrinsic stress is well documented in bulk samples [104-105]. Shifting is observed, however, in transmission data for the device with the 4 μm nickel film deposited using electroplating.

Figure 3.1.14.a shows a normalized color map of the applied field and frequency dependence of the transmission magnitude (shown in normalized linear units) for a magnetic bias field applied 90 degrees to the axis of the SAW propagation in the plane of the nickel film. The adjacent blue and red streaks indicate the presence of a strong frequency shifted peak at the center frequency of the SAW device. Figure 3.1.14.b shows the frequency spectra of the 4μm film for a selection of field values. The central SAW peak is seen to shift in frequency and amplitude as a magnetic field is applied to the sample. The shape and frequency shifting behavior of this plot can be compared with the simulated data shown in figure 3.1.14.b to show that the experimental data is in close agreement with the numerical model.

To extract the shifting of the central SAW transmission peak, a Lorentzian frequency distribution is fit to the experimental data using a least squares method. Figure 3.1.15.a plots the extracted frequency shift (kHz) versus the applied magnetic field for three in-plane orientations. The angles shown in figure 3.1.15 are defined as the angle, in the plane of the nickel film, between the applied magnetic field and the propagation axis of the SAW. The alternate axis shown to the right of figure 3.1.15.a is the percentage that the surface acoustic wave velocity shifts. This total percentage shift (about 0.7%) is larger than values reported for other material systems which use exotic material systems or complex device configurations. This increase in wave velocity change

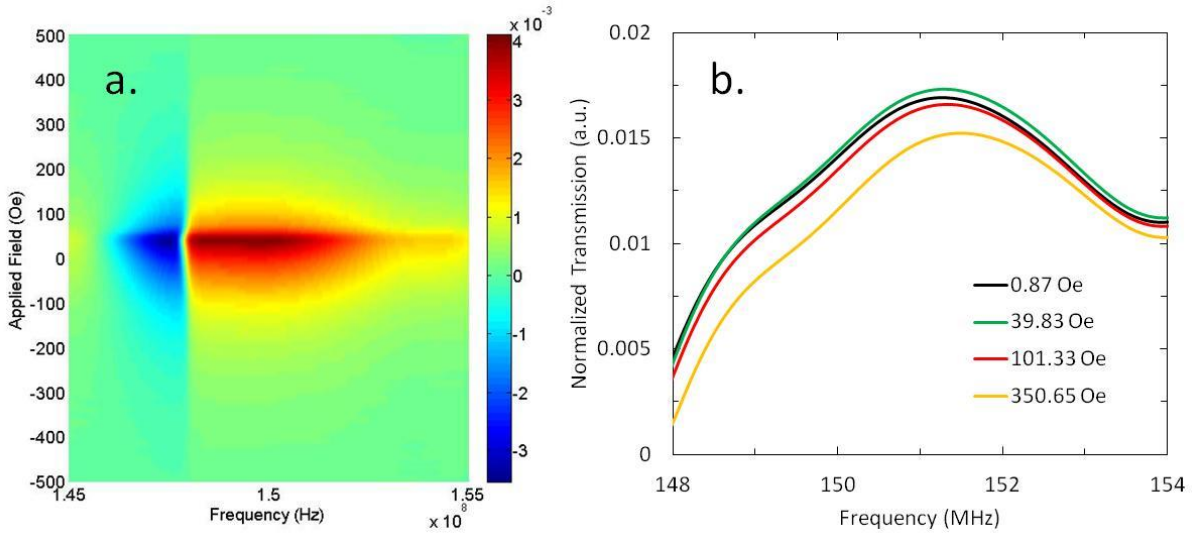

Figure 3.1.14 – a. A color map showing frequency shifting behavior in the transmission response (S12) for a 4 μm SAW magnetometer as a function of frequency and field around 150 MHz. b. A selection of transmission spectra for the magnetometer at various applied magnetic fields.

is attributed to the large fraction of the surface acoustic wave which propagates inside the magnetoelastic layer for the case of magnetoelastic films which have substantial thicknesses relative to the surface acoustic wavelength. The total percent shift in elastic modulus in the 90 degree case is computed using the linear frequency shift versus modulus change slope of the simulated results to be about 5.3% which correlates closely with values measured for bulk nickel samples [99]. The anisotropic behavior of the frequency shifting response as a function of bias angle is caused by the inherent anisotropy of the magnetomechanical coupling coefficients for a biased system. Figure 3.1.15.a can also be illustrated as the directional k coupling coefficients with the 0 and 90 degree data corresponding to the k_{33} and k_{13} coefficients respectively. It is seen

that the k_{13} direction shows the largest remnant response and the most rapid approach to saturation. All of the films show a symmetric minima at about 50 Oe which correlates closely with the coercive field of the film. Figure 3.1.15.b shows the in-plane MH behavior of the 4 μm nickel film as measured using MOKE magnetometry for applied field orientations 0, 45 and 90 degrees to the SAW propagation axis. The film is observed to be magnetically isotropic in plane. This confirms that the anisotropy measured in the transmission data is in fact due to the relationship between the direction of the small stresses in the nickel film introduced by the SAW and the orientation of the applied magnetic field.

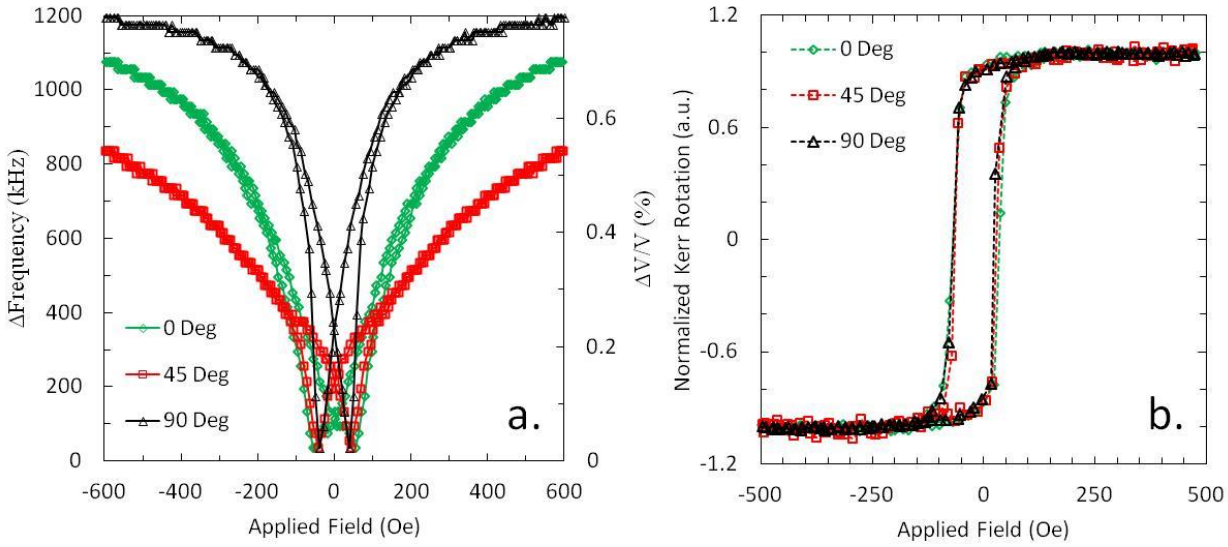

Figure 3.1.15 – a. The extracted frequency shift and wave speed change measured at the output IDT for a SAW magnetometer device with a 4 μm thin film for three in plane bias angles. b. The in-plane MH behavior for the same nickel film.

Similarly the frequency shift is extracted from the transmission response of the 4 μm sample for a bias field applied orthogonal to the plane of the film which is shown in figure 3.1.16 as a function of bias field magnitude. Although the frequency shifting magnitude is similar to the in-plane biasing cases, the bias field required to achieve this shift is much larger. This result reflects the out of plane MH characteristics of the film which show hard axis behavior from the in-plane compression and strong demagnetizing anisotropy which act to drive the magnetization into the film plane.

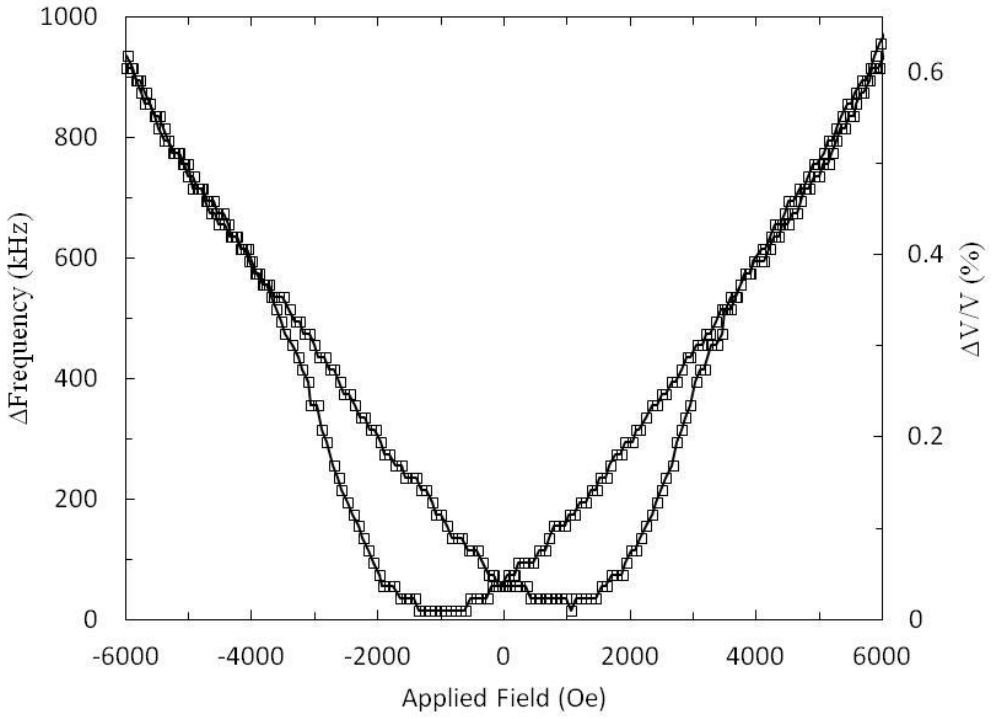

Figure 3.1.16 – The extracted frequency shift and simulation correlated Young's modulus change for a SAW magnetometer with a 4 μm thick nickel film for bias fields applied out of the film plane.

VII. Conclusion

In this section the use of thick nickel films in a SAW based magnetometer were explored. A finite element simulation of the proposed SAW device was created using the linear constitutive laws for piezoelectricity and electrostatics. Results were obtained which showed clearly observable frequency shifting for a variety of nickel film thicknesses as the isotropic elastic modulus of the film was changed. The relationship between the elastic modulus and the shift in center frequency was found to be linear inside of a small 5% region around the bulk value. Three test samples were fabricated with different nickel film thicknesses and a measurement system was constructed to record the transmission characteristics of the SAW across the film. Devices with 200 and 600 nm thin nickel films deposited by evaporation show no measurable frequency shifting which is attributed to the highly tensile nature of the intrinsic stress of the films. The effect of this stress is also clearly observed in the magnetic character of the film. The device with the 4 μm electroplated film shows frequency shifting which corresponds to behavior consistent with reported delta E changes in the nickel film. The extracted value for the delta E change correlates closely with the values found in literature. The experimentally extracted wave speed demonstrates a maximum 0.7% shift which is very large with respect to other reported values for similar devices. The anisotropy of the shifting is also clearly observed by measuring the response of the film at various applied bias field orientations with respect to the SAW propagation axis. By examining the slope of the shifting data shown in figure 3.1.x.a in the linear regime around the magnetic remnant point, a linear frequency sensitivity of about 8.2 kHz/Oe is extracted. This high sensitivity and the large wave speed shifting capabilities of the SAW magnetometer indicate that a device with sufficiently high quality factor and a measurement system with single Hertz resolution could potentially resolve magnetic fields with nano-tesla magnitudes. Furthermore the

significant anisotropy of the response and the asymmetry at the remnant state can act to provide vector capabilities in a single device. The small packaging footprint and CMOS friendly materials and fabrication processes associated with this concept mean that this type of magnetometer system can significantly contribute to fill the need for smaller chip-scale environmental sensors.

3-2: Wireless Detection of a Force Frequency Magnetometer

I. Introduction

In this section the wireless detection of a magnetoflexoelastic based magnetometer is studied. This new type of magnetometer has recently been proposed and characterized because of its small footprint and excellent sensitivity to applied magnetic fields [106-108]. The fundamental operation of the magnetoflexoelastic magnetometer leverages the high quality factors and temperature stability found in acoustically resonant quartz crystal microbalances (QCM) to detect environmentally produced shifts in the resonant frequency. This frequency shift $\Delta f/f$ can then be correlated to the external parameters of interest to provide sensor information to the user. This resonance condition in such devices is highly sensitive to many different kinds of external stimuli making it a valuable tool for analysis across a wide range of applications. Mass loading of the QCM resonance is one of the most prominently used mechanisms by which the device is able to sense environmental changes. This type of sensing is particularly useful in characterizing the physical properties of both liquid and gaseous media. Quartz plate sensors are widely used as gas concentration sensors with high sensitivity and specificity [109] and biological detection applications [110-111]. Often time these devices consist of an electroded bulk or micromachined AT cut quartz plate that has been functionalized with materials designed to absorb specific molecules of interest from the surrounding environment. This increase in the mass of the functionalized film loads the resonance of the QCM. The resonant frequency is highly sensitive to these mass changes in the vibrating structure and the small but detectable frequency shifts can be correlated to the environmental concentration of the molecule in question. Figure 3.2.1 shows resonant frequency shift versus time for a QCM with an 8 MHz center frequency that has been

functionalized with cryptophane-A, which is designed to absorb CH_4 gas molecules, as the sensor is exposed to different concentrations of CH_4 (methane) gas [109]. Large and clear shifts of up to 200 Hz are clearly observed at the QCM output which correspond directly the CH_4 concentrations in the environment.

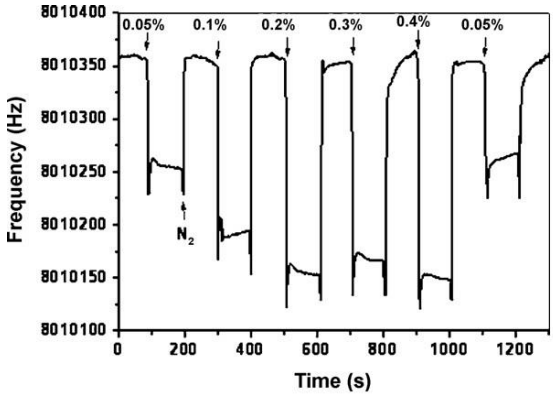

Figure 3.2.1 – The time versus center frequency response of an 8 MHz QCM functionalized with cryptophane-A surface to varying concentrations of CH_4 (Methane) gas [109].

Recent efforts adapt a similar operational mode of the QCM concept to detect magnetic fields [112]. This work shows that the magnetic field dependent viscoelastic properties of ferrofluids can cause surface loading of the QCM resulting in measureable conductance shifts in the device corresponding to nano-Tesla applied field magnitudes. Similar work demonstrates that such magnetic field sensing operation can be also achieved by using a surface deposited magnetoelastic film (Metglas) in place of the ferrofluid [106-108]. This surface loading of the QCM is achieved in this type of system through a coupling between the in-plane shear forces at the QCM surface induced by applied flexure force and the resonant frequency. This so called force-frequency effect was originally studied to describe the effect of intrinsic film stresses on the performance of QCM resonators and is well documented in previous works [113-117]. By correlating this shift in resonant frequency due to the magnetostrictive stress of the Metglas film

and the force-frequency effect, externally applied magnetic fields can be determined. The right image of figure 3.2.2 shows the device geometry for a QCM magnetometer operating using the force frequency principle. The device consists of thin etched AT cut quartz plate with a surface deposited Metglas thin film. To maximize the force frequency effect, the QCM has been released into a beam structure using focused ion beam milling to allow the QCM to bend. The left image of figure shows the conductance versus time response at the QCM center frequency (~193 MHz) for low frequency applied magnetic fields of various amplitudes. The sensor is found to be capable of resolving magnetic fields as low as 79 nT. [107]

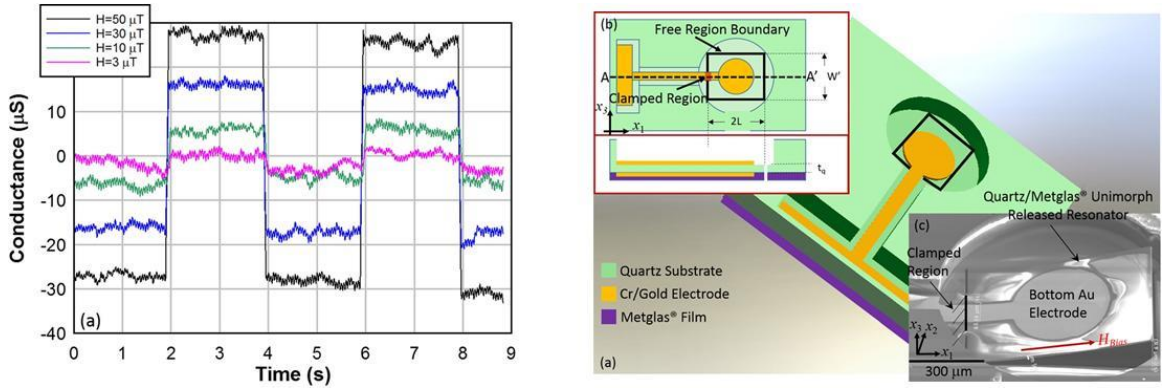

Figure 3.2.2 – The structure of a QCM magnetometer based on the force-frequency effect in thing vibrating plates under flexure (right). The response of a 193 MHz QCM magnetometer to externally applied magnetic fields of various amplitudes (left). [107]

These novel types of magnetic field sensors can be applied across a wide variety of environments and because of their small physical size and CMOS based manufacturing process, many devices can be constructed onto a single wafer. The use of such magnetometers in harsh or inaccessible environments such as the human body is limited only by the ability to connect the device to the measurement system. This disadvantage of the QCM based sensing platform has been addressed in numerous studies which demonstrate that the resonance of a functionalized device can be

detected remotely using electromagnetic waves [118-121]. These devices use conductive wire antennae to excite and detect the resonance of a functionalized quartz plate in a noncontact arrangement. The left diagram in figure 3.2.3 shows a measurement system used to wirelessly detect the resonance of a QCM sensitive to human immunoglobulin G (IgG) concentrations. The right plot of figure 3.2.3 shows the frequency dependence on the ratio of the IgG absorption layer and the resonator mass for wire excitation and detection antennae place 3 mm away from the QCM. [120]

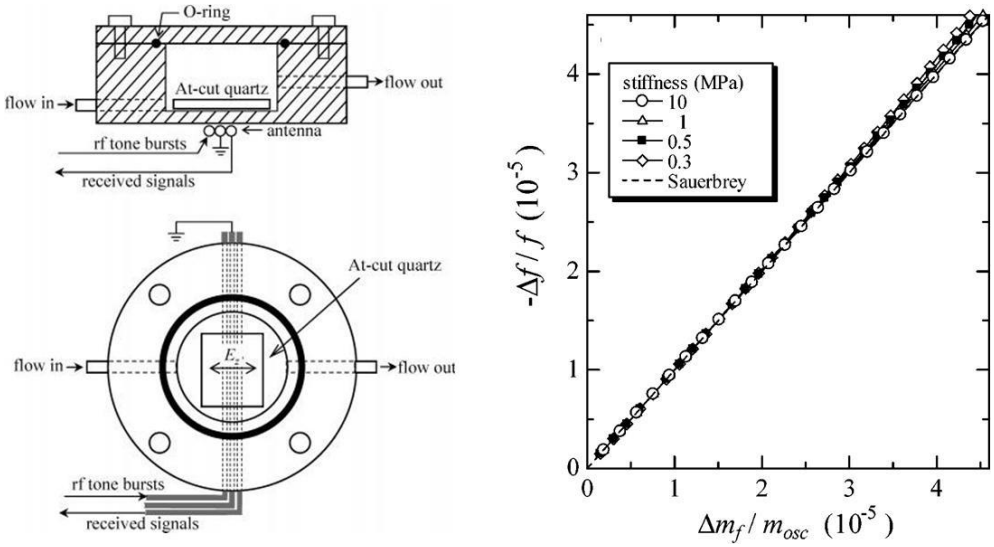

Figure 3.2.3 – An illustration of a testing apparatus used in the wireless detection of a QCM functionalized to detect human IgG concentrations (left). The frequency shifting action of the QCM as the mass ratio of the absorption layer to the oscillator is increased by the IgG. [120]

In this section we propose a QCM magnetometer operating using the force-frequency effect which can be detected remotely and passively using a series of wire antennas. A shear mode bulk acoustic wave resonator with a fundamental resonance frequency of 86 MHz is fabricated using micromachined AT cut quartz substrates and thin Metglas films. The device is packaged and attached to a test system which allows for the wireless measurement of the acoustic resonance

using a pair of coupled loop antennae. The properties of the coupled system are measured for a variety of applied static and low frequency magnetic fields. The wireless characteristics of the magnetometer are found to follow the behavior of the wired device closely demonstrating that true remote and passive operation of the device are achievable. The shift in acoustic resonance is detected at the test antenna up to 45mm away from the magnetometer. The extracted frequency sensitivity is found to be 49.1 Hz/Oe and the limit of detection using a 0.5 Hz square wave input is found to be 7 μT. The demonstration of this type of wireless detection mechanism has broad implications in the use of QCM devices not just for the field of magnetometery but also for the numerous sensing technologies which are based on these acoustic resonators. Additionally the high quality factors found in QCM resonators enables the detection of large arrays of sensors with addressed resonant frequencies. This capability along with the small physical dimensions of the resonators provides a mechanism for general purpose and highly dense sensor arrays with high spatial resolutions which can be detected remotely and in parallel. The small overall footprint, passive and wireless characteristics make the sensors deployable in environments not accessible with standard RF measurement connectors.

II. QCM Magnetometers and Wireless Detection

The fundamental operation of the magnetoflexoelastic magnetometer is built around the well-established physics governing the quartz crystal microbalance or QCM. These devices belong to a broad class of acoustic resonators called bulk acoustic wave or BAW oscillators. The most basic form of the BAW oscillator is that of a thin piezoelectric substrate with metallic electrodes placed on adjacent faces of the plate. When an RF potential difference is placed onto the electrodes an electric field is created in the piezoelectric material. Due to the intrinsic coupling

between polarization and strain inside the piezoelectric material, this induced RF electric field causes the plate to vibrate. Many different oscillating modes can be created in the plate depending on its geometry and the piezoelectric coupling coefficients of the substrate material. In the case of the QCM, which is designed specifically for sensing the mechanical characteristics of the surrounding media, AT cut quartz is typically used. This cut of quartz is used for its excellent temperature stability, low losses and high quality shear vibration mode [122]. The detection mechanism by which the proposed QCM structure is sensitive to externally applied magnetic field is called the force-frequency effect. This phenomenon appears in oscillating structures, such as a vibrating quartz plate, which are allowed to freely bend either from stresses applied in a bilayer arrangement or an external force applied to the end of the free vibrating plate [113-117]. As the plate is bent the equivalent bending force applied at the plate end causes the frequency of the oscillating beam to shift. Hatipoglu et. al. derive the fractional frequency shift in a rectangular quartz plate due to transverse bending as [106]

$$\frac{\Delta f}{f} = \frac{1}{2C_{66}}\left(2{E_1}^{(0)} + C_{662}{E_1}^{(0)} + C_{662}{E_1}^{(0)} + C_{662}{E_1}^{(0)} + C_{662}{E_1}^{(0)}\right) - \left(\frac{t^2}{\sqrt{3}\pi C_{66}}\left(C_{165}\frac{\partial {E_5}^{(1)}}{\partial x_1} + C_{165}\frac{\partial {E_5}^{(1)}}{\partial x_1} + C_{165}\frac{\partial {E_5}^{(1)}}{\partial x_1}\right)\right) \quad [Eq.\,3.2.1]$$

Where C_{ij} and C_{klm} are the second and third order stiffness and E_i are the zero and first order strains. The variable t is the thickness of the resonator and x_{ij} are the in plane Cartesian coordinates. In the proposed magnetometer, a thin magnetostrictive film is applied to the top surface of the QCM which provides the transverse strains that shift the resonant frequency of the device. These transverse strains (and corresponding frequency changes) in the magnetostrictive layer can be correlated to the magnetization state of the material through the strain-field relation

typical of the Joule magnetostriction found in many ferromagnets. By solving the linear constitutive relationship for the magnetoelastic layer, the magnetostrictive strains E_i can be derived for a magnetic field applied to a generalized magnetoelastic material. These strains can be used in equation 3.2.1 to arrive at the relationship between fractional frequency shift and applied field for a QCM force-frequency magnetometer.

Wireless detection of the QCM magnetometer is achieved be measuring the power absorption spectra of the QCM through the use of a remotely located resonant antenna. A large resonant loop antenna is used to broadcast electromagnetic waves at frequencies corresponding to the acoustic resonant frequency of the QCM. A small non-resonant coupling loop is attached across the QCM electrodes into which the near field electromagnetic energy generates an RF current. This RF current excites the QCM resonance and energy is converted from the electromagnetic wave to mechanical energy stored in the quartz oscillator. Because this energy is taken out of the electrical space at the QCM resonance, these frequencies should appear in either the reflected response of a single broadcast antenna or the transmission response of a pair of catch and receive antennae. For simplicity the reflection response of a single resonant loop antenna is examined in this work although it is expected that the transmission measurement using a pair of matched antennas will produce significantly better sensing distances. In the case of reflection the QCM resonance will produce an increase in the reflected energy measured at the broadcast antenna. This effect can be described in terms of impedance ratios in a series of elements inductively coupled to one another. The larger resonant loop antenna reflects the least amount of energy when the impedance of the driving source matches that of the losses in the loop (ohmic, dielectric, etc) and the radiation resistance of the loop to the surrounding environment. Because the QCM and associated coupling loop are placed in the reactive near field of the broadcast

antenna, the impedance of the coupling loop and QCM network are reflected into the radiation resistance of the broadcast antenna. Figure 3.2.4.a shows the real, imaginary and total impedances for a QCM with an 86MHz fundamental frequency. At resonance, a decrease in the total impedance is observed. At this frequency the impedance becomes ~78 Ohms and the QCM is best matched to the test port of the measurement system (50 Ohms) indicating that more power is being transferred into the piezoelectric. In the case of the coupled loop system, the QCM impedance is superimposed in parallel onto the load impedance seen at the detector antenna. Because the coupling loop connected to the QCM is small and the broadcasting loop has relatively low directionality, the radiation resistance of the detector loop to the surrounding environment remains the dominant load through which power is delivered. The impedances for a coupled detector antenna and QCM system are shown in figure 3.2.4.b. In the absence of the QCM, the antenna is very well matched to the 50ohm RF source as is evident by the real (lossy) component of the antenna impedance at the center frequency indicating the efficient transfer of power from the source to the surrounding environment. When the QCM and associated coupling loop are added to the system, as is shown in figure 3.2.4.b, a fraction of the QCM and loop impedance are added in parallel to the impedance seen through the detector antenna. This addition of the QCM impedance acts to reduce the effective radiation resistance (in this case away from the ideal 50 Ohm value) of the detector antenna and the QCM resonant frequency is visible in the reflection as an increase in reflected power. This QCM contribution is clearly visible in the impedance plots shown in figure 3.2.4.b as a narrow band peak around 86MHz. The fraction of the QCM impedance which is seen by the detector antenna is a strong function of the separation distance between the detector and the coupling loop, the size and orientation of the coupling loop and the directionality of the detector antenna. This impedance ratio change at the

QCM resonant frequency forms the basis for the wireless measurements of the force-frequency magnetometer presented in this section.

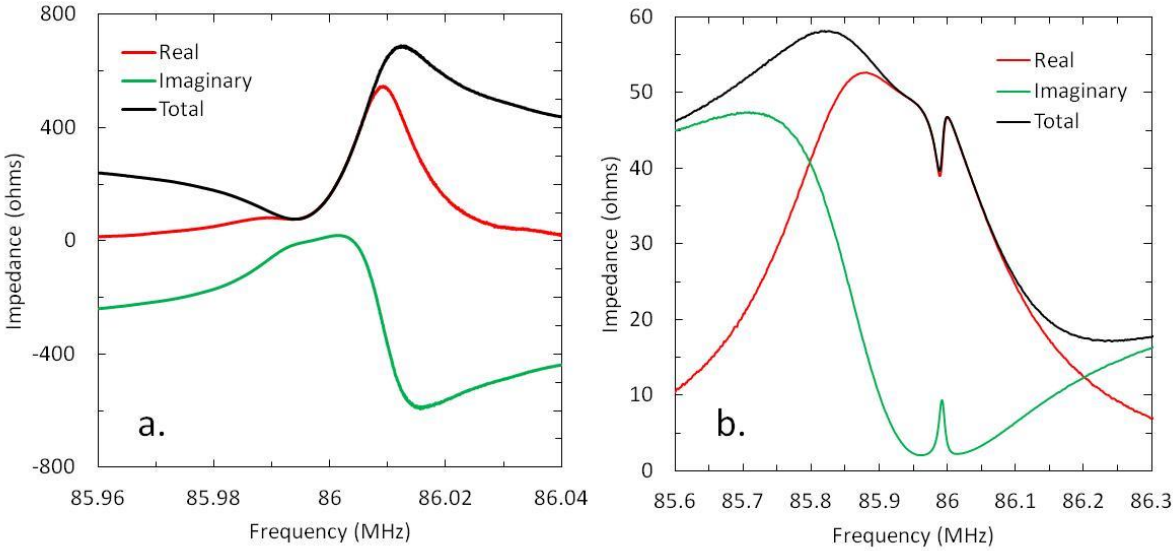

Figure 3.2.4 – The real, imaginary and total impedance of a QCM operating at a fundamental frequency of 86 MHz.

III. Device Fabrication

Because the availability of highly magnetoelastic thin films by PVD is typically limited to thicknesses of only a few microns, the largest bending deformations in the QCM/magnetoelastic bilayer structure will be achieved with quartz plates of comparable thicknesses. This is a particularly challenging problem in that quartz oscillators are normally built onto bulk (100-500 μm) substrates which can be prepared using traditional methods. To construct thin quartz oscillators, a 100 μm thickness AT cut quartz substrate is selectively thinned using reactive ion etching (RIE). Eight 500 μm diameter QCMs and the associated electrical traces are etching into the quartz substrate using an Ar/Sf_6 plasma leaving a final quartz thickness of 19 μm. A 10-12

μm nickel mask is electrodeposited using through mask plating which acts as the hard mask during the etching process. The nickel hard mask is removed upon completion of the etch step from the quartz surface using aqua regia. A detailed description of the fabrication process is given by P. Kao et. al. [123]. Following etching, a patterned 10/100 nm thick Cr/Au electrode is deposited onto the etched surface of the quartz which acts as the isolated signal electrodes through which each QCM is addressed. Traces and wire bonding pads are also patterned in this step which allow for the electrical connection to the QCM signal electrodes using wire bonding. Figure 3.2.5.b illustrates the layout of etched QCM devices and their associated electrodes for a 10x10 mm AT cut quartz plate. A 20/100/20/300/20/20 nm thick Cr/Au/Ti/($Fe_{85}B_5Si_{10}$)/Ti/Au layer is then deposited as a continuous film on the un-patterned side of the quartz substrate. This multilayer film stack is deposited using sputter deposition. The bottom gold layer acts as a high conductivity path for the QCM ground electrode. The $Fe_{85}B_5Si_{10}$ (Metglas) is an amorphous magnetic alloy with very large piezomagnetic coupling properties [52] making it an ideal film for field sensing applications. A gold capping layer is deposited onto the top surface of the material stack to prevent oxidation of the Metglas layer under atmospheric conditions. The intermediate chromium and titanium films act as reactive adhesion layers to increase the strength of the mechanical interface between relatively non-reactive materials such as gold. To improve the response of the magnetic field sensor, a static magnetic field is applied to the sample during deposition using permanent magnets. By applying this field during the growth of the magnetic layer, a preferential magnetic orientation can be created in the film by orienting the grain structure of the deposit. Upon completion of the backside metal layer, the QCM is released using a focused ion beam to allow the resonator to freely bend. Figure 3.2.5.a shows QCM after the

release of the quartz diaphragm to form the freely bending beam geometry. Fabrication of test samples is performed at The Pennsylvania State University.

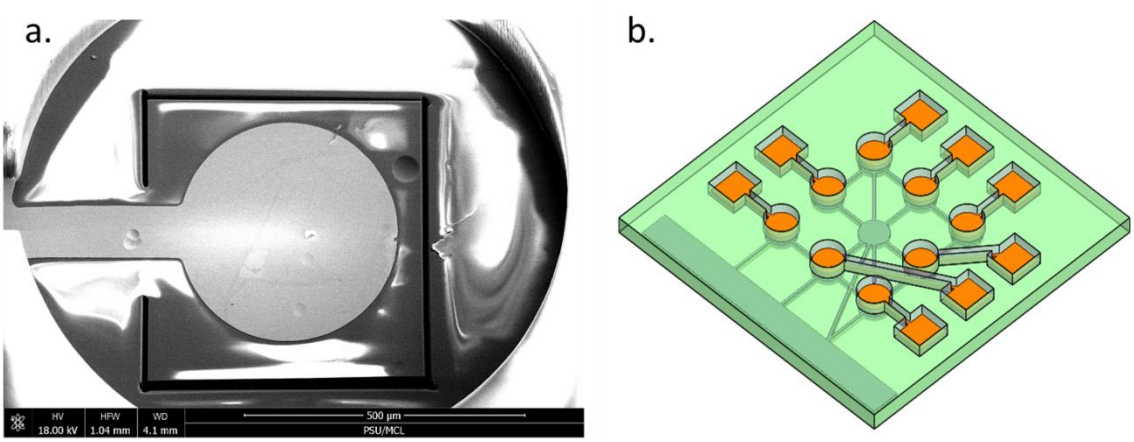

Figure 3.2.5 – a. A complete QCM magnetometer that has been released from the quartz diaphragm using focused ion beam milling. b. An outline of a 10x10 mm quartz substrate which has been etched and metalized with 8 QCM devices. (Penn State University)

Upon completion of device fabrication, the 10x10 mm substrates are mounted into a ceramic chip carrier (Kyocera CSB02491). To prevent mechanical clamping at the bottom surface of the QCM devices, the material below the QCM area is removed from the ceramic carrier as is shown in figure 3.2.6.b. The QCM die is bonded into the carrier using silicone based adhesive. The bottom side ground electrode is connected to the packaging ground plane trace using silver epoxy. The top side electrodes are electrically connected to the packaging leads using wire bonding. Figure 3.2.6.a shows a competed die mounted into a chip carrier ready for wire bonding to the chip carrier leads. A class cover slip is taped to the top of the ceramic carrier to prevent accidental damage of the wire bonds or the QCM devices during handling and testing. The completed carriers are then mounted and soldered onto a patterned PCB built on Rogers Corp.

RO4360G substrates. Each of the signal electrodes is connected to an edge mounted SMA connector using a 50 Ohm transmission line in a single ended arrangement.

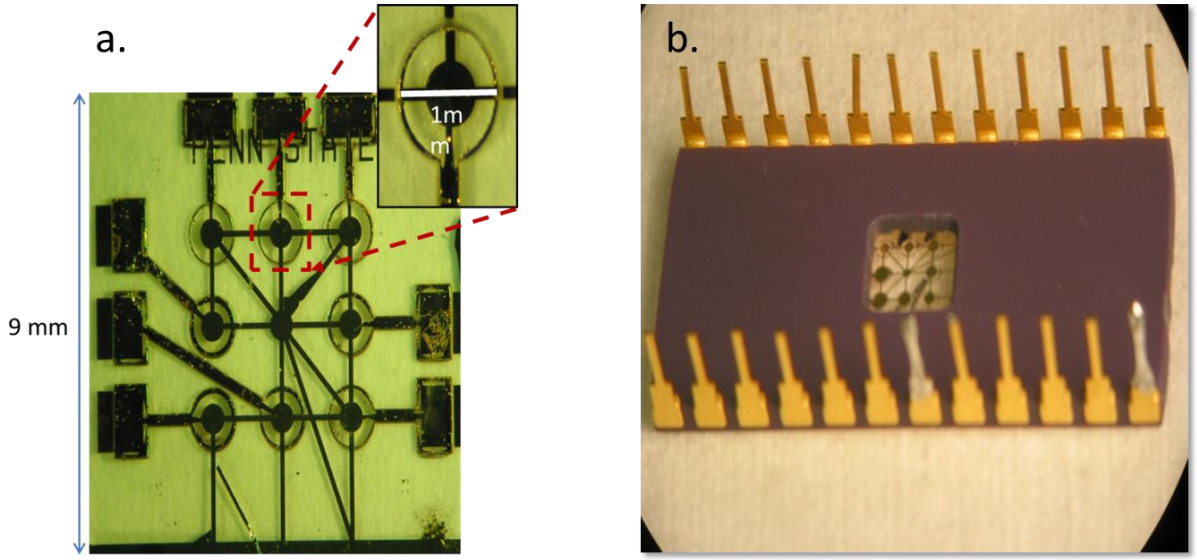

Figure 3.2.6 – a. A completed 10x10mm quartz substrate with 8 test devices ready for wire bonding to the carrier package. b. A device bonded into a ceramic chip carrier ready for mounting onto the circuit board carrier. (Penn State University)

The wireless components of the measurement system are fabricated on patterned FR4 substrates. The detector antenna pattern consists of a 110 mm diameter loop with a series air-dielectric variable capacitor (E.F Johnson 148-4 3.2-50 pF) which acts as the tuning element for the resonant frequency of the antenna. A smaller 22mm driving loop is patterned inside the larger oscillating loop which acts to match the 50 Ohm test port impedance of the measurement electronics to free space. This driving loop is connected to the test system using an edge mounted SMA connector. The coupling loop consists of a single 22 mm diameter loop which is connected

to the QCM using an edge mounted SMA connector. The wireless test system components are shown in figure 3.2.7 attached to the QCM and oriented as they would be placed during testing.

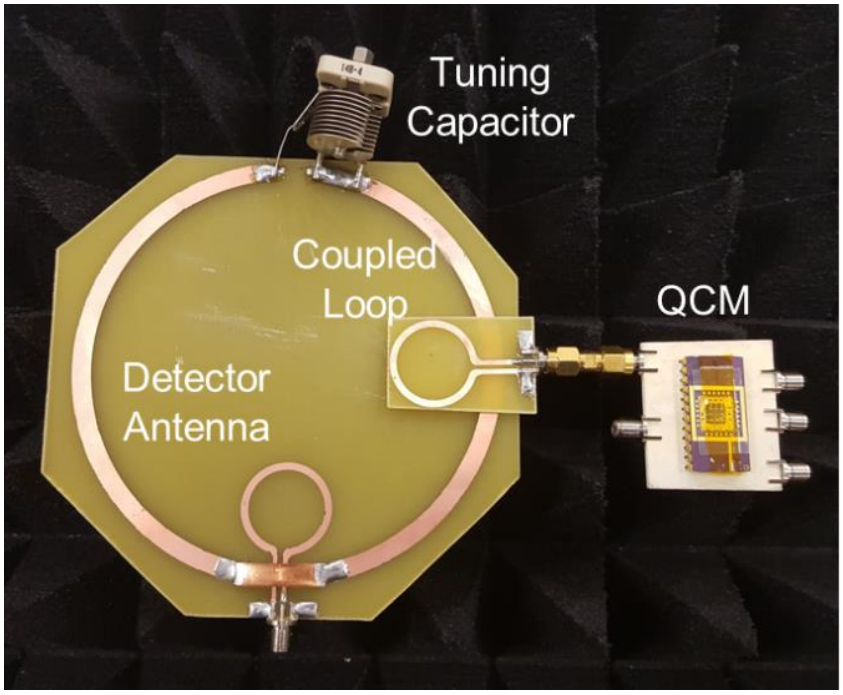

Figure 3.2.7 - The wireless test system components used in the remote sensing of a force-frequency QCM magnetometer. The QCM is shown connected and the components are arranged to represent the position of the components during RF testing.

IV. Experimental Setup

During testing the QCM sample and attached coupling loop is placed onto a plexiglass stage at the center of a Lakeshore MH-12 Helmholtz coil. This Helmholtz coil serves to apply highly controlled and uniform magnetic fields to the QCM sample either statically or at low frequencies. The coil is driven using a GPIB controlled Agilent E3632A power supply. The sample is oriented such that the internal anisotropy direction in the Metglas films is

perpendicular to the direction of the applied field. The detector antenna is attached to a holder parallel to and directly over the coupling loop. The holder allows the detector antenna to move vertically while maintaining its parallel orientation. The reflection scatter parameters of the detector antenna are recorded using a GPIB connected Agilent 8720ES vector network analyzer. A diagram of the test system components and their orientations during measurement is shown in figure 3.2.8. The separation distance d is the vertical distance between the parallel planes of the detector and coupling loop. Prior to RF testing, the QCM and detector antenna are connected to the network analyzer in a two port arrangement. The variable capacitor on the detector loop is visually tuned to match the resonant frequency of the QCM. The entire testing system is measured inside the Near Field Systems Incorporated (NSI) anechoic chamber at the Center for High Frequency Electronics (CHFE) housed at UCLA. Because the near field region of the detector antenna is relatively large (~14 meters) at the design frequencies, the shielded room acts to prevent the introduction of electrical noise from the surrounding environment.

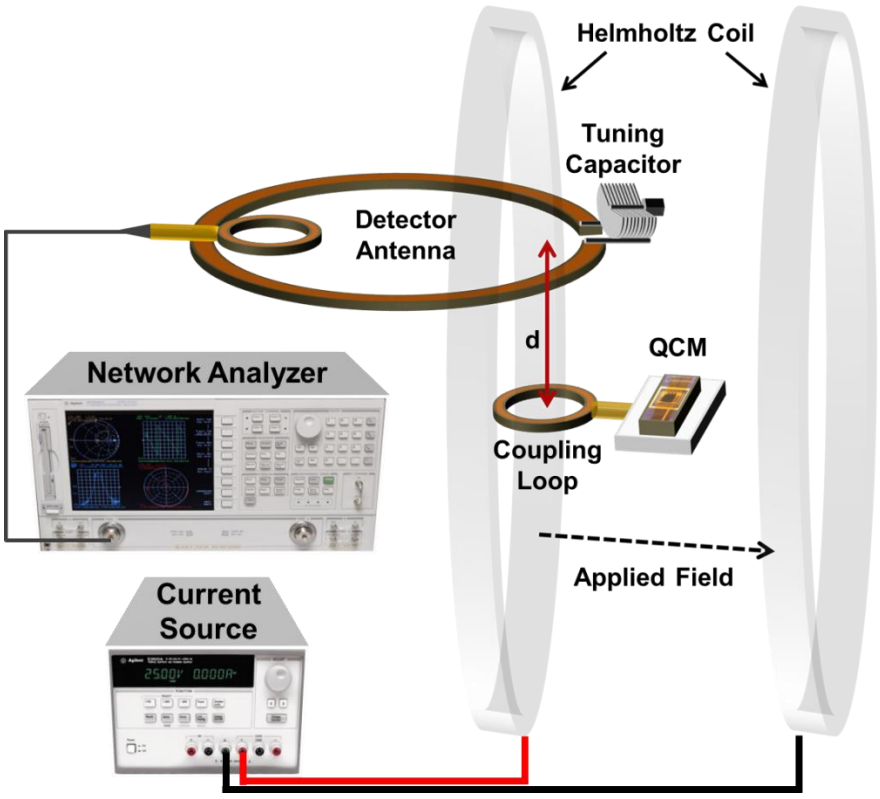

Figure 3.2.8 – A schematic diagram of the test system components used to characterize a QCM force frequency magnetometer. This setup is used inside an anechoic chamber during actual testing.

V. Results

The magnitude and phase of the reflection spectra for the coupled detector antenna and QCM system are shown in figure 3.2.9 for a separation distance d=0 mm. The larger downward peak represents the reflection response of the tuned detector antenna. This has a reflection magnitude of about -16 dB at the center frequency indicating a good match from the driving source to the surrounding environment. At 86 MHz the resonance of the QCM appears as an increase in the reflected power by approximately 8 dB. This indicates that the impedance mismatch produced by

the parallel detector and QCM network is significant and provides a large magnitude signal from which the shifting frequency of the QCM can be extracted.

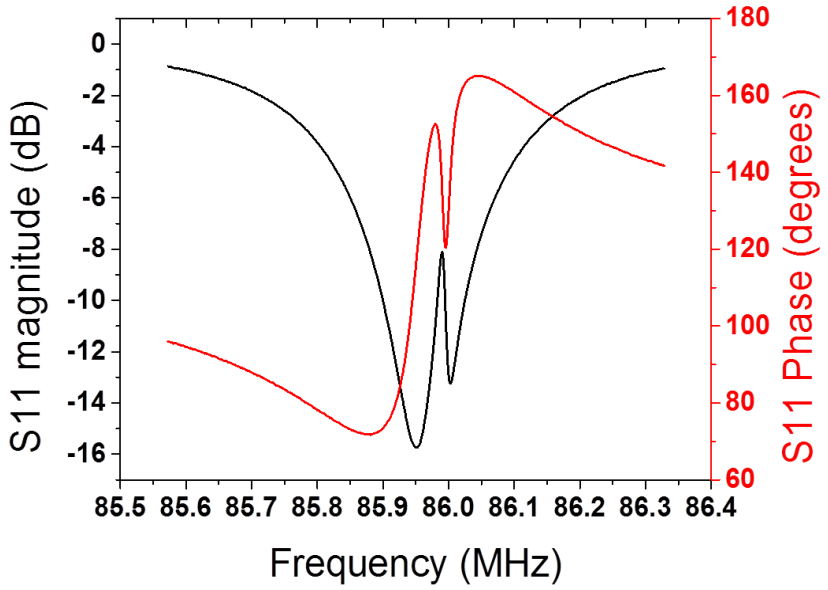

Figure 3.2.9 – The S11 reflection response of the coupled detector anetnna and QCM system for a separation distance d=0 mm

The QCM center peak magnitude (a) and phase (b) are shown in figure 3.2.10 at several values of applied magnetic field. This data is collected at d=0 mm. Frequency shifting of the center peak is clearly visible in both the frequency and the phase response of the coupled system as a function of applied magnetic field. The color map plots shown to the left of figure 3.2.10 show the frequency (x-axis) versus magnetic field (y-axis) spectra for the QCM peak normalized to zero applied bias field for separation distances of d=0,7,21 and 45 mm. The color contrast as a function of applied bias field indicates a shift in resonant frequency around 86 MHz. The contrast becomes significantly reduced as the separation distance decreases. This is due to the

expected decrease in the amount of the QCM impedance which is reflected into the detector antenna. Beyond separation distances of 45 mm the QCM peak is no longer resolvable.

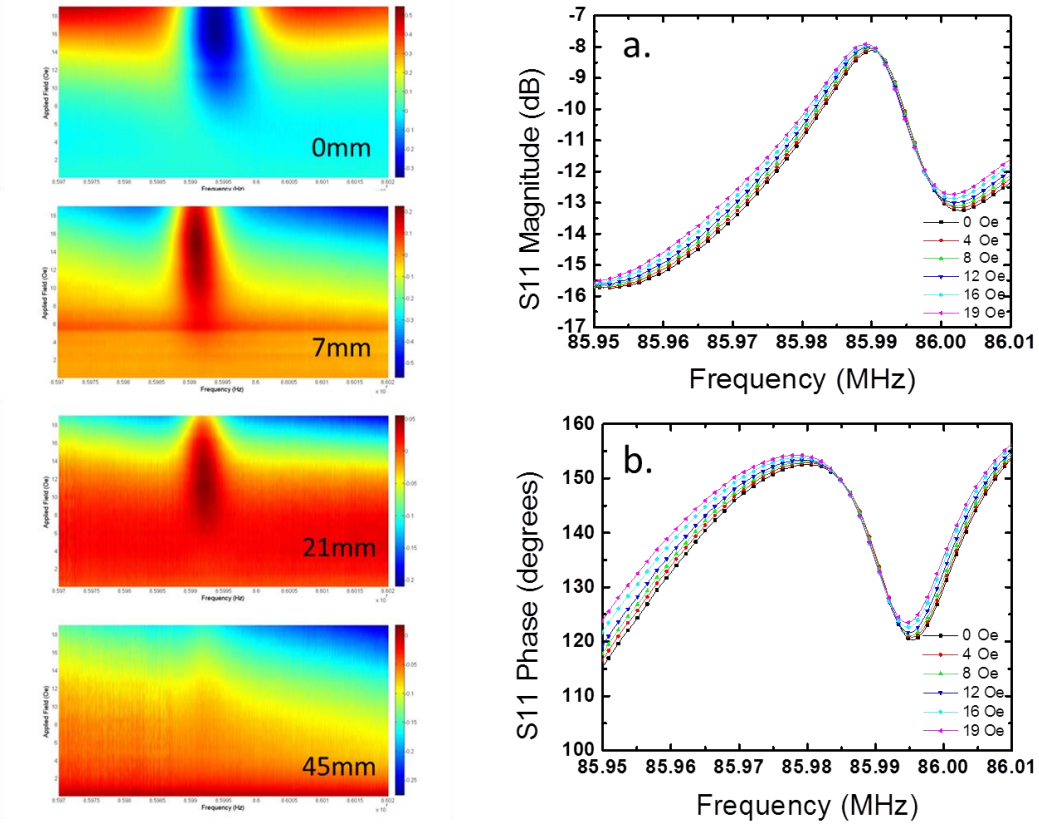

Figure 3.2.10 – Color map of the wirelessly detected frequency shifting behavior of the magnetometer at various separation distances. The magnitude (a) and phase (b) of the coupled system at various applied magnetic fields.

The frequency shift of the QCM is found by connecting the test system directly to the QCM test board without the use of the wireless system components. The transmission spectra are recorded and the peak minima measured from the reflected magnitude is extracted from the data as a function of the applied bias field. Similarly the frequency shift of the QCM using the wireless

test system shown in figure 3.2.8 can be extracted from the maxima of the reflection spectra as a function of applied magnetic field. A comparison of the frequency shifting characteristic for both the direct and wireless (d=0) measurement are shown in figure 3.2.11.a. Both curves follow the same general behavior indicating the wireless measurement method is accurately detecting the frequency shift of the device. These can also be compared against the magnetostriction behavior of the Metglas film shown in figure 3.2.11.b as measured using a laser Doppler vibrometer at Pennsylvania State University. The frequency shifting curves closely match the field dependence of magnetostriction as would be expected for the force frequency effect.

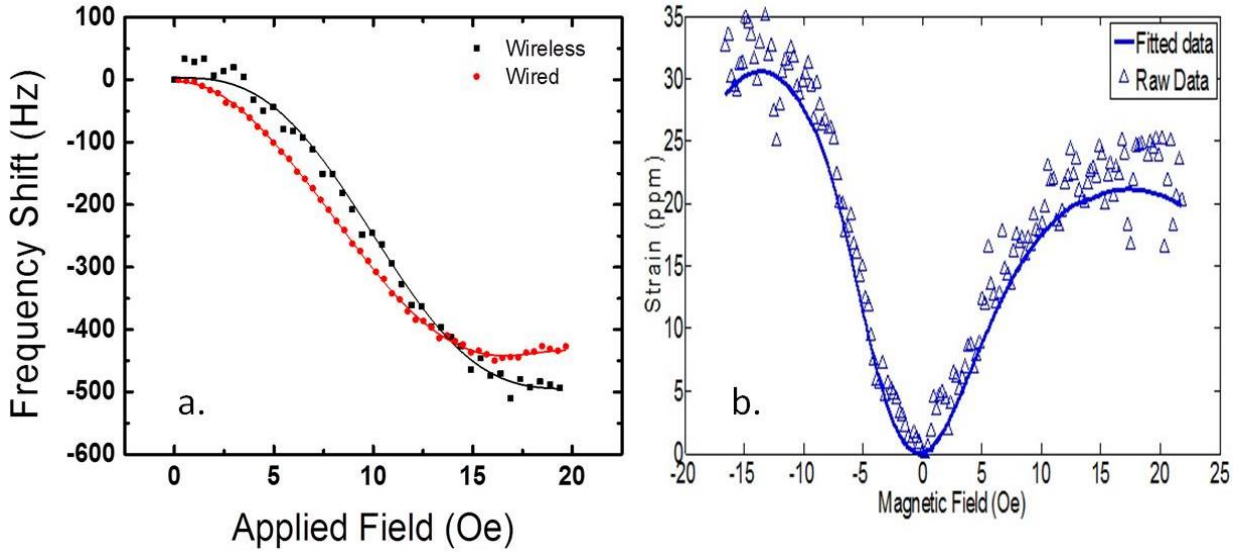

Figure 3.2.11 – a. The extracted frequency shift for the same QCM magnetometer device measured directly (red) and wirelessly (black). b. The magnetostriction curve of the Metglas film measured using a laser Doppler vibrometer (Penn State University).

The frequency shifting characteristic of the system for separation distances above d=0mm require the use a peak fitting algorithm to extract the center frequency. This is due to the

reduction in the peak magnitude (and quality factor) of the reflected QCM peak making a clear frequency maxima difficult to obtain. The system can be represented by two Lorentzian frequency distributions frequency (f) dependence

$$G(f) = 1 - \frac{I_{loop}}{1 + (\frac{f - f_{loop}}{\gamma_{loop}})^2} + \frac{I_{QCM}}{1 + (\frac{f - f_{QCM}}{\gamma_{QCM}})^2} \quad [Eq. 3.2.2]$$

Where I is the peak magnitude of the detector loop or QCM resonance, f is the center frequency of the loop or QCM and γ is the full width half maximum (FWHM) of the loop or QCM. Using a least squares method, the distribution in equation 3.2.2 is fitted to the system reflection magnitude and f_{QCM} and γ_{QCM} are extracted as a function of applied magnetic field for each separation distance. The extracted center frequency is shown as a function of applied field in figure 3.2.12.a for separation distances of d=0,7,21 and 45 mm. The observed behavior for each separation distance is seen to closely follow that of the experimentally recorded magnetostriction curve shown in figure 3.2.11.b. This indicates that the fractional frequency shifting magnitude does not depend on the separation distance between the detector antenna and the QCM. By taking the instantaneous values of the frequency shifting response, an average sensitivity value of 49.1Hz/Oe is found. The quality factor of the fitted peak (γ_{QCM}) is shown in figure 3.2.12.b. A decrease in the measured quality factor from 6600 to 5400 is observed with increasing applied field. This is due to the increase in the ratio between lossy (real) impedance components of the QCM/loop network to the lossless reactive components as the amount of power driven through the QCM is reduced with separation distance.

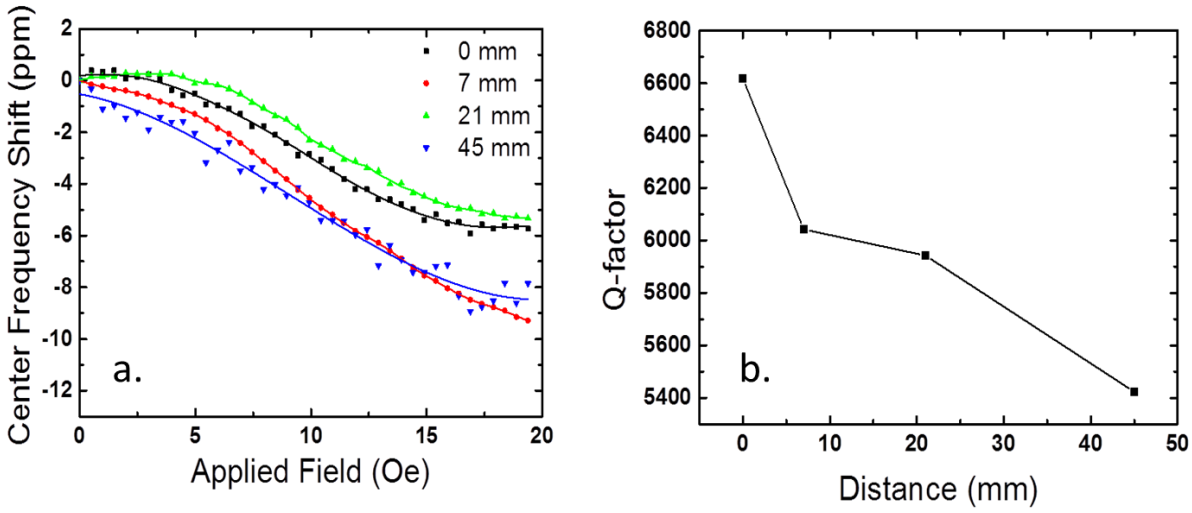

Figure 3.2.12 – a. The center frequency shift of the QCM as a function of applied bias field extracted using a multi Lorentzian frequency distribution for various separation distances. b. The extracted quality factor of the QCM as a function of separation distance.

The limit of detection of the wirelessly detected QCM device is measured by applying a low frequency AC magnetic field of decreasing magnitudes superimposed onto a static bias field. The bias field is selected such that the magnetometer is operating at the most sensitive point where the incremental changes in applied field will result in the largest changes in the QCM center frequency. The magnitude of the static bias field is selected to be 10 Oe. The power supply which drives the Helmholtz coil is modulated at 0.5 Hz about the static bias current value using square wave modulation. The phase response for the QCM is collected at the center frequency of the device at a sampling frequency of 33Hz. The phase shift as a function of time is shown in figure 3.2.13.a for three AC field amplitudes. The square input signal is clearly visible in the phase response at the lowest field amplitude of 20 μT. To detect lower amplitude signals, the time domain phase response of the QCM can be transformed into frequency domain using fast

Fourier transformation. The FFT of the phase response to a 7 μT input field is shown in figure 3.2.13.b for both the direct and wirelessly measured cases. It is seen that the 0.5 Hz peak in the wireless data is observed just above the noise floor (~5 mdeg). Fields below 7 μT produce phase magnitudes which are in the noise floor of the VNA. The directly measured case exhibits larger phase shifts in response to the same magnitude field input despite the identically nature of the observed frequency response shown in figure 3.2.11.a. The phase sensitivity is found to be approximately 1 mdeg/μT for the wireless case while the direct measurement produces 3.3 mdeg/μT.

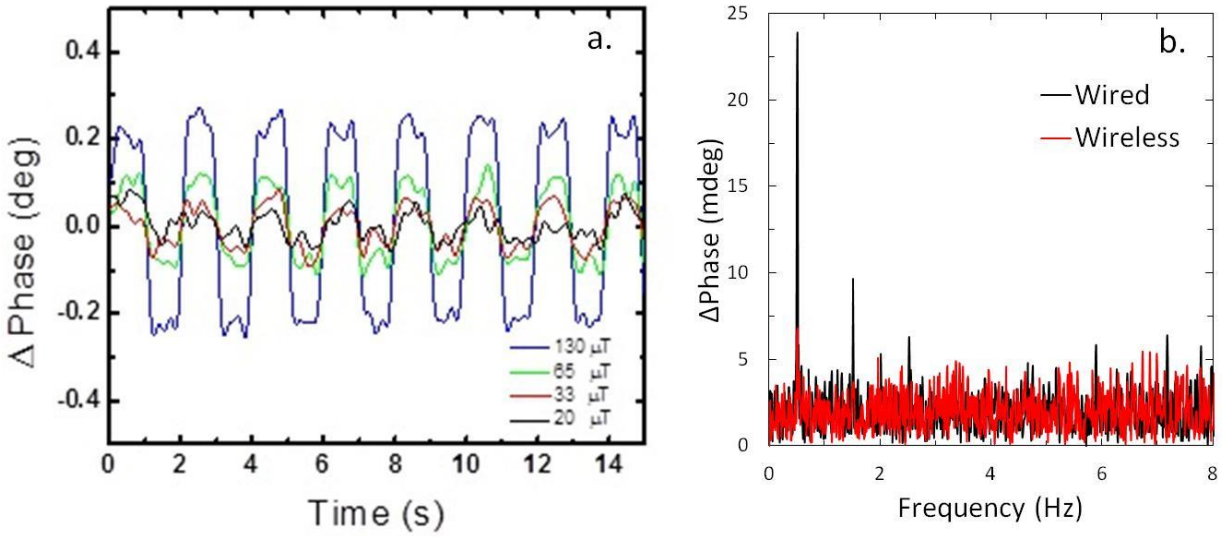

Figure 3.2.13 – a. The phase versus time response of a wireless QCM device for a 0.5 Hz square wave magnetic field input of various magnitudes. b. The frequency domain spectra of the phase response of the sensor for both direct and wireless connection for a 7 μT input field.

This is reduction in the phase sensitivity is due to the decreased phase slope when using the wireless test system. This decrease in the phase slope of the reflected power occurs due to the

superposition of phase response of the resonant loop and the QCM network. Figure 3.2.14.a shows the derivative of the phase spectra for the wired and wireless cases. A decrease from 10 mdeg/Hz to 4 mdeg/hz is observed when the system is measured wirelessly which is relatively close to the 3.3 times reduction in the magnetic field sensitivity shown in figure 3.2.13.a for an AC field magnitude of 130 μT. The phase magnitude becomes negative in the wireless case which indicates that the phase will shift down for positive applied fields in the wireless case while it will shift up in the case of the wired measurement. This is demonstrated in figure 3.2.14.b in the phase shift time response of the sensor for both wired and wireless measurement. It is seen that the two sets of phase shifts corresponding to wired and wireless test data are inverted with respect to one another.

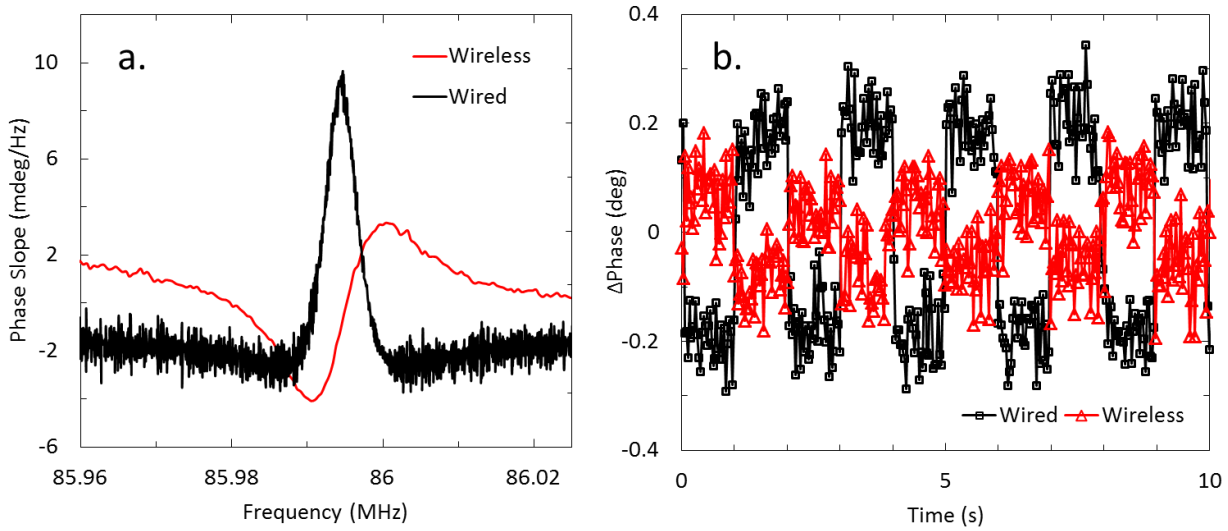

Figure 3.2.14 – a. The derivative of the phase response for the case of wireless and wired measurements of the QCM magnetometer. b. The phase shift time response of the QCM magnetometer for both the wired and wireless method of measurement for an input field amplitude of 130 μT.

VI. Conclusion

In this section the remote detection of a magnetometer operating on the force-frequency principle in quartz/Metglas multiferroic composites is demonstrated. A device is constructed which uses the frequency shifting mechanism found in bent oscillating piezoelectric plates to sense the magnetostrictive strains in a Metglas film. This device is packaged and tested in a wireless measurement system designed to detect the resonance of the quartz oscillator using a remotely located detector antenna. By tracking the location of the resonant peak of the magnetometer measured through the reflection of the detector antenna, the field dependent frequency shift is observed. This shifting behavior closely follows the shift measured by directly connecting to the oscillator device and both correspond well to the field dependence of the magnetostriction in the Metglas film. The effect of separating the detector and magnetometer device by a controlled distance was recorded and frequency changes were found to be consistent across all distances measured. The average maximum frequency sensitivity of the device is found to be 49.1 Hz/Oe. The limit of detection using a time based phase measurement is then characterized and found to be 7 μT. Discrepancies between the phase response for wired and wireless measurement techniques are analyzed and found to closely reflect the phase slope characteristics of the reflection response.

While the sensitivity of the device studied in this section is not as large as have been reported for similar devices [107] at 83.3 Hz/Oe, the concept of wireless sensor measurement can be applied across a range of systems with improved field sensitivities. This represents the first account of a wireless magnetic field sensor which can be detected at long distances up to 45 mm away and in a completely passive fashion. This advancement can potentially allow for the placement of a variety of remotely measured QCM type sensors in environments inaccessible to typical RF

measurement systems such as the human body. Furthermore, the small physical dimensions and compatibility with CMOS processing imply that such wireless sensors can be manufactured in large arrays which can provide spatially resolved sensing information. By frequency addressing each sensor, the entire sensing array can be measured in parallel with a single excitation antenna. This demonstration broadly impacts the use of nanoscale in situ sensor systems across a wide range of potential applications.

Chapter 4: Conclusion

In this work the use of strain mediated multiferroic composites was studied in the context of chip scale sensor technology based on the manipulation of magnetic fields. This approach has demonstrated the potential to improve on the energy efficiencies and device footprint of existing technologies which rely on Oersted fields to control magnetism. In Chapter 2 the use of multiferroic composites was studied for use as an electrically small antenna system. A unique analysis using Maxwell's equations and linear piezomagnetic constitutive coupling was used to compare the radiation efficiency of a radiating magnetoelastic block to a current carrying wire loop. This analysis demonstrated significant improvement in the radiation efficiencies for the magnetoelasic system for certain materials and sizes. Using this analytical technique materials were selected for experimental devices based on the predicted performance. A practical antenna structure was designed based on surface acoustic wave transducer technology through the use of finite element simulation. Magnetoelastic resonators and SAW IDT transducer geometries are optimized to maximize the output power produced by the multiferroic antenna. A fabrication process is developed to build SAW based antenna test structures using common MEMS and CMOS fabrication techniques. Using the developed processes, SAW antennae operating at 150 MHz and 300 MHz are constructed using lithium niobate substrates and nickel as the magnetoelastic layer. A measurement system is designed specifically to meet the requirements of a magnetoelastic antenna and sources of measurement noise are systematically uncovered and removed. Transmission coupling is not observed in the nickel/LiNbO3 SAW antenna devices due to the expected low output powers produced by the nickel magnetoelastic material. It is expected that other optimal material systems should produce output efficiencies above the noise floor of the current measurement.

In Chapter 3 the use of multiferroic laminates was applied to the field of chip-scale magnetometers. First a magnetometer operating on the delta-E effect in magnetoelastic materials was examined for its potential to detect nano-Tesla level magnetic fields in very compact footprints with industry established manufacturing processes. A mechanical probing technique based on surface acoustic wave propagation through a magnetoelastic film was shown in finite element simulations to resolve very small changes in the elastic modulus of the film. Using the guidance provided by the numerical results, a device was fabricated using lithium niobate substrates and nickel thin films. The highly stressed films deposited using evaporation showed no frequency dependence on applied magnetic fields while the thickest electroplated film showed over 1 MHz shift in the SAW center frequency when under magnetizing conditions. The thick film devices demonstrate very large fractional velocity tuning coefficients of about 0.7% and the corresponding delta-E coefficient is 5.3% which agrees with reported literature values for bulk nickel. The frequency sensitivity of the thick film is 8.2 kHz/Oe which, with modest frequency noise figures, can achieve field resolution in the nano-Tesla range. Lastly the remote detection of a QCM based magnetometer was explored using micromachined quartz and sputtered Metglas laminates. A high sensitivity magnetometer is constructed based on the force-frequency effect found in shear mode beams which experience flexure forces while in a cantilever type configuration. A quartz substrate is thinned to 19 μm using reactive plasma etching and a Metglas thin film is sputtered onto the top surface which applies bimorph type bending forces on the quartz oscillator. The oscillator is milled using a focused ion beam to release the device into a freely flexing cantilever arrangement. The device is tested remotely and passively in an anechoic chamber using a series of antennae to excite the QCM and reflect its impedance properties into the near field where they are detected using a larger resonant loop antenna. The phase and

frequency sensitivity are collected for various excitations and detector to device separation distances. The frequency shifting response is found to be invariant of the separation distance and is detectable up to a 45 mm distance from the device. The frequency sensitivity of the magnetometer is 49.1 Hz/Oe.

The results presented in this work demonstrate the vast potential that multiferroic laminate systems offer to the electronic devices marketplace. With the constant demand for higher sensitivities and lower power consumption in these ever shrinking types of systems, multiferroic transduction shines in its ability to fulfill these requirements with favorable scaling characteristics bound only by the limitations of current CMOS fabrication techniques. This firmly situates these types of material systems to become a champion technology for the future of small scale magnetic motors, memory devices and, as has been demonstrated in the present work, sensors.

1. References

[1] M. Bohr. 14nm Process Tehcnology: Opening New Horizons. IDF14 SPCS010. Intel (2014)

[2] C. Cavallaro, A.O.D. Tommaso, R. Miceli, A. Raciti, G.R. Galluzo and M. Trapanese. IEEE Transactions on Industrial Electronics. Vol. 52, No. 4 (2005)

[3] B.D. Cullity and C.D. Graham. Introduction to Magnetic Materials (John Wiley & Sons, Inc. 2009)

[4] T. Ikeda. Fundamentals of Piezoelectricity. Oxford University Press (1996)

[5] H. Hertz. Electric Waves. (Macmillian and Company 1893)

[6] J. Clerk Maxwell. Phil. Trans. R. Soc. Lond. 155 459-512 1865

[7] C.A. Balanis. Antenna Theory Analysis and Design. (John Wiley and Sons, Hoboken, New Jersey 2005)

[8] K.B. Alici and E. Ozbay. Journal of Applied Physics 101, 083104 (2007)

[9] A. Erentok and R.W. Ziolkowski. Microwave and Optical Technology Letters. Vol. 49 No. 6 (2007)

[10] T.J. Warnagiris. IEEE Transactions on Antennas and Propagation. Vol. 46 No. 12 (1998)

[11] E.E. Altschuler. IEEE Transactions on Antennas and Propagation. Vol. 50 No. 3 (2002)

[12] S.R. Best. IEEE Transactions on Antennas and Propagation. Vol. 52 No.4 (2004)

[13] A. Erentok and R.W. Ziolkowski. IEEE Transactions on Antennas and Propagation. Vol. 56 No. 3 (2008)

[14] K.V. Caekenberghe, N. Behdad, K.M. Brakora and K. Sarabandi. IEEE Antennas and Wireless Propagation Letters. Vol. 7 (2008)

[15] S. Lim and H. Ling. Electronics Letters. Vol. 42 No. 16 (2006)

[16] R.W. Ziolkowski. IEEE Antennas and Wireless Propagation Letters. Vol. 7 (2008)

[17] Y.X. Liu, J.G. Wan, J.M. Liu and C.W. Nan. Journal of Applied Physics 94, 5118 (2003)

[18] TD. Onuta, Y. Wang, C.J. Long and I. Takeuchi. Applied Physics Letters 99, 203506 (2011)

[19] S. Marauska, R. Jahns, C. Kirchhof, M. Claus, E. Quandt, R. Knochel and B. Wagner. Sensor and Actuators A 189 (2013) 321-327

[20] TD. Onuta, Y. Wang, S.E. Loftland and I. Takeuchi. Advanced Materials 27 (2015) 202-206

[21] S. Marauska, R. Jahns, H. Greve, E. Quandt, R. Knochel and B. Wagner. J. Micromch Microeng. 22 (2012) 065024

[22] I. Lopatina and I. Lisnevkaya. Ferroelectrics 1994. Vol. 162. 63-68

[23] J. Ryu, S. Priya, A.V. Carazo and K. Uchino. J. Am. Ceram. Soc. 84[12] (2001) 2905-2908

[24] K. Zhang, L. Zhang, L. Fu. S. Li, H. Chen and Z.-Y. Cheng. Sensors and Actuators A **200** (2013) 2-10

[25] R.V. Petrov, A.S. Tatarenko, S. Pandey, G. Srinivasan, J.V. Mantese and R.Azadegan. Electronics Letters Vol. 44 No. 8 (2008)

[26] G.M. Yang. X. Xing, A. Daigle, M. Liu, O. Obi, J.W. Wang, K. Naishadham, and N.X.Sun. IEEE Transaction on Magnetics Vol. 44 No. 11 (2008)

[27] J. Lou, D. Reed, C. Pettiford, M. Liu, P. Han, S. Dong and N.X. Sun. Applied Physics Letters 92, 262502 (2008)

[28] Y-Y. Song, J. Das, P. Krivosik, N. Mo, C.E. Patton. Applied Physics Letters 94, 182505 (2009)

[29] N. Benatmane, S.P. Crane, F. Zavaliche, R. Ramesh and T.W. Clinton. Applied Physics Letters 96, 082503 (2010)

[30] M. Liu, O. Obi, J. Lou, S. Li, X. Xing, G. Yang and N.X. Sun. J. App. Phys. 109, 07D913 (2011)

[31] S. Li, M. liu, W. Shao, J. Xu, S. Chen, Z. Zhou, T. Nan, N.X. Sun and J-G. Duh. Journal of Applied Physics 113, 17C727 (2013)

[32] S. Li, H. Du, Q. Xue, X. Gao, Y. Zhang, W. Shao, T. Nan, Z. Zhou and N.X. Sun. Journal of Applied Physics 115 17C723 (2014)

[33] J. Das, Y-Y. Song, N. N. Mo, P. Krivosik and C.E. Patton. Adv. Mater. 21 (2009) 2045-2049

[34] J. Lou, M. Liu, D. Reed, Y. Ren and N.X. Sun. Adv. Mater. 21 (2009) 4711-4715

[35] Y. Hui, T. Nan, N.X. Sun and M. Rinaldi. Journal of Microelectromechanical Systems. Vol. 24 No. 1 (2015)

[36] T. Nan, Y. Hui, M. Rinaldi and N.X. Sun. Scientific Reports 3:1985 (2013)

[37] G. Srinivasan. Annu. Rev. Mater. Res (2010) 40:153-78

[38] D. Labanowski, A. Jung, S. Salahuddin. Applied Physics Letters 108, 022905 (2016)

[39] A. Kamra and G.E.W. Bauer. Solid State Communications 198 (2014) 35-39

[40] L. Dreher, M. Weiler, M. Pernpeitner, H. Huebl, R. Gross, M.S. Brandt and S.T.B. Gonnenwein. Physical Review B 86, 134415 (2012)

[41] J. Lou, R.E. Insignares, Z. Cai, K.S. Ziemer, M. Liu and N.X. Sun. Applied Physics Letters 91 (2007) 182504

[42] W. Wang, K. Lee, I. Woo, I. Park and S. Yang. Sensors and Actuators A 139 (2007) 2-6

[43] G. Feuillard, M. Lethiecq, Y. Janin, L. Tessier and L. Pourcelot. IEEE Transactions on Ultrasonics, Ferroelectrics, and Frequency Control. Vol. 44, No. 1 (1997)

[44] H. Meier, T. Baier and G. Riha. IEEE Transactions on Microwave Theory and Techniques, Vol. 49, No. 4 (2001)

[45] A.J. Slobodnik. Proceedings of the IEEE, Vol. 64, No. 5 (1976)

[46] P.S. Cross, W.H. Haydl and R.S. Smith. Proceedings of the IEEE. Vol. 64, No. 5 (1976)

[47] R. Aigner. IEEE International Ultrasonics Symposium Proceedings. (2008) 10.1109/ULTSYM.2008.0140

[48] M. Hoummady, A. Campitelli and W Wlodarski. Smart Mater. Struct. 6 (1997) 647-657

[49] K. Wetzlar. Leveraging Anisotropy to Enhance Multiferroic Transduction. Dissertation UCLA 2015

[50] S. Tiwari, P. Nordeen, Q. Xu, Z. Yao, Y.E. Wang, G.P. Carman and R.N. Candler. Hilton Head Workshop. Abstract and Poster Presentation (2016)

[51] R.C. O'Handley. Modern Magnetic Materials (John Wiley & Sons, Inc. 1999)

[52] S.W. Meeks and J.C. Hill. Journal of Applied Physics 54(11) (1983)

[53] L. Sandlund, M. Fahlander, T. Cedell, A.E. Clark, J.B. Restorff and W. Wun-Fogle. Journal of Applied Physics 75, 5656 (1994(

[54] M.B. Moffett, A.E. Clark, M. Wun-Fogle, J. Linberg, J.P. Teter, E.A. McLaughlin. J. Acoust. Soc. Am. 83(3) (1991)

[55] J. Gao, A. Yang, Y. Chen, J.P. Kirkland, J. Lou, N.X. Sun, C. Vittoria and V.G. Harris. Journal of Applied Physics 105, 07A323 (2009)

[56] K. Fukamichi, T. Satoh, T. Masumoto. Journal of Magnetism and Magnetic Materials 31-34 (1983) 1589-1590

[57] I.H. Gul, A. Maqsood. Journal of Alloys and Compounds 465 (2008) 227-231

[58] C. Modzelewski, H.T. Savage, L.T. Kabacoff and A.E. Clark. IEEE Transactions on Magnetics. Vol. Mag-17, No. 6 (1981)

[59] K.K. Mohaideen and P.A. Joy. ACS Appl. Mater. Interfaces 4 (2012) 6421-6425

[60] M.I. Bichurin, D.A. Filippov, V.M. Petrov, V.M. Laletsin, N. Paddubnaya and G. Srinivasin. Physical Review B 68, 132408 (2003)

[61] B. Adolphi, J. McCord, M. Bertram, C-G. Oertel, U. Merkel, U. Marschner, R. Shafer, C. Wenzel and W-J. Fisher. Smart Mater. Struct. 19 (2010) 055013

[62] J-H. Yoo, G. Pelligrini, S. Datta and A. Flatau. Smart Mater. Struct. 20 (2011) 075008

[63] J. Lou, M. Liu, D. Reed, Y. Ren and N.X. Sun. Adv. Mater. 21 (2009) 4711-4715

[64] S.F.Xu, H.P. Zhang, W.Q. Wang, S.H. Guo, W. Zhu, Y.H. Zhang, X.L.Wang, D.L. Zhao, J.L. Chen and G.H. Wu. J. Phys. D: Appl. Phys. 41 (2008) 015002

[65] A.K. Nigam and A.K. Majumdar. Physica 95B (1978) 385-390

[66] C. Kittel, Introduction to Solid State Physics (John Wiley & Sons, Inc. 2005)

[67] J.G. Gaultieri, J.A. Kosinski and A. Ballato. IEEE Transactions of Ultrasonics, Ferroelectrics, and Frequency Control, Vol. 41 No. 1 (1994)

[68] A. Ballato. Piezoelectricity: Venerable Effect, Modern Thrusts. ARL-TR-70 (1994)

[69] C. Campbell. Surface Scoustic Wave Devices for Mobile and Wireless Communications. (Academic Press, 1998)

[70] X. Li, R. Zhang, N. Huang, T. Lu and W. Cao. Journal of Applied Physics 106, 054110 (2009)

[71] K.H. Choi, J.H. Oh, H.J. Kim. IEEE Ultrasonics Symposium (2001) 161-163

[72] R. Zhang, B. Jiang and W. Cao. Applied Physics Letters. Vol. 82 No. 5 (2003)

[73] R.S. Weis and T.K. Gaylord. Applied Physics A 37, 191-2003 (1985)

[74] G. Kovacs, M. Anhorn, H.E. Engan, G. Visintini and C.C.W. Ruppel. IEEE Ultrasonics Symposium (1990) 435-438

[75] Clariant Corporation AZ nLOF 2000 Series i-Line Photoresists (2002)

[76] T. Ryhanen, H. Seppa, R. Ilmoniemi and J. Knuutila. Journal of Low Temperature Physics. Vol. 76 Nos. 5/6 (1989)

[77] J.R. Kirtley, M.B. Ketchen, K.G. Stawiasz, J.Z. Sun, W.J. Gallagher, S.H. Blanton and S.J. Wind. Applied Physics Letters. 66, 1138 (1995)

[78] L.N. Vu and D.J. Van Harlingen. IEEE Transactions on Applied Superconductivity. Vol. 3, No. 1 (1993)

[79] J. Dechert, M. Mueck and C. Heiden. IEEE Transaction on Applied Superconductivity. Vol. 9, No.2 (1999)

[80] J.R. Kirtley, M.B. Ketchen, C.C. Tsuei, J.Z. Sun, W.J. Gallagher, L.S. Yu-Jahnes, A. Gupta, K.G. Stawiasz, S.J. Wind. IBM J. Res. Develop. Vol. 39, No. 6 (1995)

[81] J.R. Kirtley and J.P. Wikswo Jr. Annu. Rev. Mater. Sci. (1999) 117-148

[82] P. Ripka. Sensor and Actuators A 106 (2003) 8-14

[83] F. Primdahl. J. Phys. E: Sci. Instrum., Vol 12, 1979

[84] D.F. He, M. Tachiki and H. Itozaki. Review of Scientific Instruments. 80, 036102 (2009)

[85] P. Ripka, M. Vopalensky, A. Platil, M. Doscher, K.M.H. Lenssen and H. Hauser. Journal of Magnetism and Magnetic Materials 254-255 (203) 639-641

[86] M. Vopalensky, P. Ripka and A. Platil. Sensors and Actuators A. 106 (2003) 38-42

[87] J. Vcelak, P. Ripka, J. Kubik, A. Platil and P. Kaspar. Sensor and Actuators A. 123-124 (2005) 122-128

[88] B.S. Berry and W.C. Pritchet. AIP Conference Proceedings. 34, 292 (1976)

[89] P.M. Anderson III, Journal of Applied Physics. 53, 8101 (1982)

[90] K.B. Hathaway and M.L. Spano. Journal of Applied Physics. 55, 1765 (1984)

[91] L.M. Malkinski. Journal of Magnetism and Magnetic Materials 140-144 (1995) 2169-2170

[92] P.T.Squire. Meas. Sci. Technol. 5 (1994) 67-81

[93] E. Hristoforou. Meas. Sci. Technol. 14 (2003), R15-R47

[94] E.M. Simpson and W.P. Robbins. IEEE Transactions on Magnetics, Vol. MAG-16, No.5 (1980)

[95] B.D. Zaitsev, A.V. Ermolenko and V.A. Fedorenko. IEEE Transactions on Ultrasonics, Ferroelectrics and Frequency Control. Vol. 45, No. 2 (1998)

[96] A.K. Ganguly, K.L. Davis, D.C. Webb, V. Vittoria and D.W. Forester. Electronics Letters Vol. 11 (1975)

[97] V. Koeninger, Y. Matsumura, H.H. Uchida and H. Uchida. Journal of Alloys and Compounds, 211/212 (1994) 581-584

[98] P. Smole, W. Ruile, C. Korden, A. Ludwig, E. Quandt, S. Krassnitzer and P. Pongratz. Proceedingd of the 2003 IEEE International Frequency Control Symposium and PDA Exhibition Jointly with the 17th European Frequency and Time Forum. (2003)

[99] J.M. Chicharro, A. Bayon and F. Salazar. Journal of Magnetism and Magnetic Materials. 202 (1999) 465-472

[100] A.L. Morales, A.J. Nieto, J.M. Chicharro and P. Pintado. Journal of Magnetism and Magnetic Materials. 322 (2010) 1952-1961

[101] A.L. Morales, A.J. Nieto, J.M. Chicharro, P. Pintado, G.P. Rodriguez and G. Herranz. Journal of Magnetism and Magnetic Materials. 322 (2010) 3584-3594

[102] F.A. Doljack and R.W. Hoffman. Thin Solid Films. 12 (1972) 71-74

[103] E. Klokholm. Journal of Vacuum Science & Technology. 6 138 (1969)

[104] D.C. Jiles. J. Phys. D: Appl. Phys. 28 (1995) 1537-1546

[105] D.P. Bulte and R.A. Langman. Journal of Magnetism and Magnetic Materials. 251 (2002) 229-243

[106] G. Hatipoglu and S. Tadigadapa. Journal of Applied Physics. 118 034508 (2015)

[107] G. Hatipoglu and S. Tadigadapa. Applied Physics Letters. 107 192406 (2015)

[108]G. Hatipoglu and S. Tadigadapa. IEEE Transducers (2015) 807-810

[109] P. Sun, Y. Jiang, G. Xie, X. Du and J. Hu. Sensors and Actuators B. 141 (2009) 104-108

[110] R.D. Vaughan, R.M. Carter, C.K.O O'Sullivan and G.G. Guilbault. Analytical Letters. Vol. 36, No. 4 (2003) 731-747

[111] K. Reihmhult, K. Yoshimatsu, K. Risveded, S. Chen, L. Ye and A. Krozer. Biosensors and Bioelectronics 23 (2008) 1908-1914

[112] G. Hatipoglu and S. Tadigadapa. Journal of Microelectromechanical Systems. Vol. 25, No. 1 (2016)

[113] A.D. Ballato. Proc. 14th AFCS. (1960) 89-114

[114] E.P. EerNisse. Proc. 29th AFCS, (1976)

[115] A. Ballato, E.P. EerNisse and T. Lukaszek. Proc. 31st AFCS, (1977)

[116] P.C.Y. Lee, Y.S. Wang and X. Markenscoff. J. Acoust. Soc. Am. Vol. 59, No. 1 (1976)

[117] P.C.Y. Lee, Y.S. Wang and X. Markenscoff. J. Acoust. Soc. Am. Vol. 57, No.1 (1975)

[118] H. Ogi, H. Naga, Y. Fukunishi, M. Hirao and M. Nishiyama. Anal. Chem. 81 (2009) 8068-8073

[119] M. Thompson, S.M. Ballantyne, L.E. Cheran, A.C. Stevenson and C.R. Lowe. The Analyst. 128 (2003) 1048-1055

[120] H. Ogi, K. Motoshisa, T. Matsumoto, K. Hatanaka and M. Hirao. Anal. Chem. 78 (2006) 6903-6909

[121] H. Ogi, K. Hatanaka, Y. Fukunishi, H. Nagai, M. Hirao and M. Nishiyama. Japanese Journal of Applied Physics. 48 (2009)

[122] *Fundamentals of Quartz Oscillators.* Application Note 200-2. Hewlett-Packard Company (1997)

[123] P. Kao, D. Allara and S. Tadigadapa. Meas. Sci. Technol. 20 (2009)

[124] R. Kambale, DY. Jeong and J. Ryu. Adv. Cond. Matt. Phys. (2012) 824643

[125] J.S. Blakemore, Solid State Physics (Cambridge University Press, 1994)

[126] K.R. Williams, K. Gupta and M. Wasilik. Journal of Micrelectromechanical Systems, Vol. 12 No. 6 (2003)

[127] K.R. Williams and R.S. Muller. Journal of Microelectromechanical Systems. Vol. 5 No. 4 (1996)

[128] M. Madou, Fundamentals of Microfabrication (CRC Press LLC 1997)

[129] L.W. Martin, S.P. Crane, Y-H. Chu, M.B. Holcomb, M. Gajek, M. Huijben, C-H. Yang, N. Balke and R. Ramesh. J. Phys.: Condens. Matter 20 (2008) 434220